N°d'ordre NNT : 2022EMSEM022

THESE de DOCTORAT DE L'UNIVERSITE DE LYON

opérée au sein de

l'Ecole des Mines de Saint-Etienne

Ecole Doctorale N° 488

Sciences, Ingénierie, Santé

Spécialité de doctorat : Sciences et Génie des Matériaux

Soutenance prévu publiquement le 29/09/2022, par :

Mariam ASSI

Conception d'alliages pour la fabrication additive

Devant le jury composé de :

Joubert, Jean-Marc	Directeur de recherche	CNRS, PIMM, Paris	Rapporteur
Peyre, Patrice	Directeur de recherche	CNRS, ICMPE, Thiais	Rapporteur
Poquillon, Dominique	Professeure des universités	CIRIMAT, Université de Toulouse	Examinatrice
Cao, Trong-Son	Ingénieur-chercheur	ArcelorMittal Global R&D, Maizieres-lès-Metz	Examinateur
Favre, Julien	Chargé de recherche	LGF, MINES St-Etienne	Co-encadrant de thèse
Tancret, Franck	Professeur des universités	IMN, Université de Nantes	Co-directeur de thèse
Fraczkiewicz, Anna	Directrice de recherche	LGF, MINES St-Etienne	Directrice de thèse
Rigal, Emmanuel	Ingénieur-chercheur	CEA-LITEN, Grenoble	Invité
Desrayaud, Christophe	Professeur des universités	LGF, MINES St-Etienne	Invité

Spécialités doctorales	Responsables	Spécialités doctorales	Responsables
SCIENCES ET GENIE DES MATERIAUX	K. Wolski Directeur de recherche	MATHEMATIQUES APPLIQUEES	M. Batton-Hubert
MECANIQUE ET INGENIERIE	S. Drapier, professeur	INFORMATIQUE	O. Boissier, Professeur
GENIE DES PROCEDES	F. Gruy, Maître de recherche	SCIENCES DES IMAGES ET DES FORMES	JC. Pinoli, Professeur
SCIENCES DE LA TERRE	B. Guy, Directeur de recherche	GENIE INDUSTRIEL	N. Absi, Maitre de recherche
SCIENCES ET GENIE DE L'ENVIRONNEMENT	V. Laforest, Directeur de recherche	MICROELECTRONIQUE	Ph. Lalevée, Professeur

EMSE : Enseignants-chercheurs et chercheurs autorisés à diriger des thèses de doctorat (titulaires d'un doctorat d'État ou d'une HDR)

ABSI	Nabil	MR	Génie industriel	CMP
AUGUSTO	Vincent	MR	Génie industriel	CIS
AVRIL	Stéphane	PR	Mécanique et ingénierie	CIS
BADEL	Pierre	PR	Mécanique et ingénierie	CIS
BALBO	Flavien	PR	Informatique	FAYOL
BASSEREAU	Jean-François	PR	Sciences et génie des matériaux	SMS
BATTON-HUBERT	Mireille	PR	Mathématiques appliquées	FAYOL
BEIGBEDER	Michel	MA	Informatique	FAYOL
BILAL	Blayac	DR	Sciences et génie de l'environnement	SPIN
BLAYAC	Sylvain	PR	Microélectronique	CMP
BOISSIER	Olivier	PR	Informatique	FAYOL
BONNEFOY	Olivier	PR	Génie des Procédés	SPIN
BORBELY	Andras	DR	Sciences et génie des matériaux	SMS
BOUCHER	Xavier	PR	Génie Industriel	FAYOL
BRUCHON	Julien	PR	Mécanique et ingénierie	SMS
CAMEIRAO	Ana	PR	Génie des Procédés	SPIN
CHRISTIEN	Frédéric	PR	Science et génie des matériaux	SMS
DAUZERE-PERES	Stéphane	PR	Génie Industriel	CMP
DEBAYLE	Johan	MR	Sciences des Images et des Formes	SPIN
DEGEORGE	Jean-Michel	MA	Génie industriel	Fayol
DELAFOSSE	David	PR	Sciences et génie des matériaux	SMS
DELORME	Xavier	PR	Génie industriel	FAYOL
DESRAYAUD	Christophe	PR	Mécanique et ingénierie	SMS
DJENIZIAN	Thierry	PR	Science et génie des matériaux	CMP
BERGER-DOUCE	Sandrine	PR	Sciences de gestion	FAYOL
DRAPIER	Sylvain	PR	Mécanique et ingénierie	SMS
DUTERTRE	Jean-Max	PR	Microélectronique	CMP
EL MRABET	Nadia	MA	Microélectronique	CMP
FAUCHEU	Jenny	MA	Sciences et génie des matériaux	SMS
FAVERGEON	Loïc	MR	Génie des Procédés	SPIN
FEILLET	Dominique	PR	Génie Industriel	CMP
FOREST	Valérie	PR	Génie des Procédés	CIS
FRACZKIEWICZ	Anna	DR	Sciences et génie des matériaux	SMS
GAVET	Yann	MA	Sciences des Images et des Formes	SPIN
GERINGER	Jean	MA	Sciences et génie des matériaux	CIS
GONDRAN	Natacha	MA	Sciences et génie de l'environnement	FAYOL
GONZALEZ FELIU	Jesus	MA	Sciences économiques	FAYOL
GRAILLOT	Didier	DR	Sciences et génie de l'environnement	SPIN
GRIMAUD	Frederic	EC	Génie mathématiques et industriel	FAYOL
GROSSEAU	Philippe	DR	Génie des Procédés	SPIN
GRUY	Frédéric	PR	Génie des Procédés	SPIN
HAN	Woo-Suck	MR	Mécanique et ingénierie	SMS
HERRI	Jean Michel	PR	Génie des Procédés	SPIN
ISMAILOVA	Esma	MC	Microélectronique	CMP
KERMOUCHE	Guillaume	PR	Mécanique et Ingénierie	SMS
KLOCKER	Helmut	DR	Sciences et génie des matériaux	SMS
LAFOREST	Valérie	DR	Sciences et génie de l'environnement	FAYOL
LERICHE	Rodolphe	DR	Mécanique et ingénierie	FAYOL
LIOTIER	Pierre-Jacques	MA	Mécanique et ingénierie	SMS
MEDINI	Khaled	EC	Sciences et génie de l'environnement	FAYOL
MOLIMARD	Jérôme	PR	Mécanique et ingénierie	CIS
MOULIN	Nicolas	MA	Mécanique et ingénierie	SMS
MOUTTE	Jacques	MR	Génie des Procédés	SPIN
NAVARRO	Laurent	MR	Mécanique et ingénierie	CIS
NEUBERT	Gilles	PR	Génie industriel	FAYOL
NIKOLOVSKI	Jean-Pierre	Ingénieur de recherche	Mécanique et ingénierie	CMP
O CONNOR	Rodney Philip	PR	Microélectronique	CMP
PICARD	Gauthier	PR	Informatique	FAYOL
PINOLI	Jean Charles	PR	Sciences des Images et des Formes	SPIN
POURCHEZ	Jérémy	DR	Génie des Procédés	CIS
ROUSSY	Agnès	MA	Microélectronique	CMP
SANAUR	Sébastien	MA	Microélectronique	CMP
SERRIS	Eric	IRD	Génie des Procédés	FAYOL
STOLARZ	Jacques	CR	Sciences et génie des matériaux	SMS
VALDIVIESO	François	PR	Sciences et génie des matériaux	SMS
VIRICELLE	Jean Paul	DR	Génie des Procédés	SPIN
WOLSKI	Krzystof	DR	Sciences et génie des matériaux	SMS
XIE	Xiaolan	PR	Génie industriel	CIS
YUGMA	Gallian	MR	Génie industriel	CMP

Acknowledgement

First I would like to deeply thank the jury members in general for the fruitful scientific discussion we had during the defense, and to Dr. Jean-Marc Joubert and Dr. Patrice Peyre in particular for reviewing this manuscript.

I would like to express my gratitude to my thesis director Anna Fraczkiewicz, who was present to guide me in my scientific adventure since I arrived in France for my master's degree at the end of 2017. This work would not have been possible without her and her vast knowledge and experience in metallurgy, which still impresses me every time.

I would also like to thank my co-director Franck Tancret, who has always been there for me despite the distance (Saint-Etienne – Nantes)! Thank you Franck for all your advice and help and for the opportunity to discover the world of material informatics, and to work on such a rich topic.

A special thank you to my tutor Julien Favre. We started this journey side by side, and I had the chance to learn a lot from you. Your door was always open for me and my questions; scientific or not, and I truly appreciate all the time we spent talking and discussing.

I would also like to thank Christophe Desrayaud, for all the help provided in the field of additive manufacturing. Thank you to Pauline (and her lynx eyes) for making 3D printing possible.

And a warm thank you to all the colleagues at Mines Saint-Etienne and the lab's technicians: Claude, Michael, Gilles Blanc, Marilyne, Sergio, Claire, Max, Nathalie, Christophe. I learned a lot thanks to all of you!

I would also like to thank all the PhD students and post-docs: Ahmed, Ayoub, Alixe, Aman, Antonin, Ayobami, Clara, Dinesh, Ebert, Elia, Jihene, Jolan, Lisa, Margaux, Mathieu, Michella, Mohamad, Roland, Safa, Sandra, Zineb and everyone with whom I crossed paths! I wish you all the best for the future.

A special thanks to my dearest friends who made the whole adventure bearable: Rim, Maria & Anthony, Frederic. You were like my second family.

I would also like to thank all my friends in Lebanon who have always been there for me, despite the distance.

Last but not least, I take the opportunity to express my deepest gratitude to my family: my parents and my brothers. Your love is the reason I am able to carry on in life no matter how hard it gets. I wouldn't be here without you and I love you so much. Bhebkon.

Abstract

The recent developments in the field of metallic additive manufacturing (AM) processes for the production of high-performance industrial products remains restricted by the limited availability of reliably processable or printable alloys. So far, most of the alloys being printed by AM are commercial alloys which have been previously optimized for different processing techniques. One of the ambitions of the domain would therefore be to design new alloys that are specifically adapted to such processes, allowing to minimize the defects in final products and optimize their properties. This means an optimization of certain material characteristics which should allow to reduce the presence of defects currently seen in AM-fabricated parts such as hot cracking, porosity, surface roughness, residual stresses and distortions, etc.

Within the scope of this thesis, a computational design of new austenitic alloy compositions, optimized specifically for AM is proposed. This method is based on a set of computational tools including Bayesian machine learning (ML) algorithms combined with calculation of phase diagrams (CALPHAD) and physical models, integrated in a multi-objective genetic algorithm (GA). In this context, several material-dependent criteria are reviewed and their effect on the mentioned defects is identified. Then, the implementation of a genetic algorithm yields a set of optimal alloys. Experimental validation is carried out on one selected composition. The selected alloy was investigated in the as-cast condition, as an atomized powder and as specimens built by Selective Laser Melting (SLM). The printability of the alloy is assessed and compared to existing commercial alloys.

Résumé

Les développements récents dans le domaine des procédés de fabrication additive (FA) métallique pour la production de produits industriels à hautes performances restent limités par la disponibilité d'alliages pouvant être traités ou imprimables de manière fiable. Jusqu'à présent, la plupart des alliages imprimés par FA sont des alliages commerciaux qui ont été préalablement optimisés pour différents procédés de fabrication. L'une des ambitions du domaine serait donc de concevoir de nouveaux alliages spécifiquement adaptés aux procédés de FA, permettant de minimiser les défauts des produits finaux et d'optimiser leurs propriétés. Ceci impliquerait une optimisation de certaines caractéristiques du matériau permettant de réduire la présence des défauts actuellement observés tels que la fissuration à chaud, la porosité, la rugosité de surface, les contraintes et distorsions résiduelles, etc.

Dans le cadre de cette thèse, une conception de nouvelles nuances d'alliages austénitiques, optimisées spécifiquement pour la FA, est proposée. La démarche repose sur un ensemble d'outils de calcul comprenant des algorithmes bayésiens d'apprentissage automatique combinés à des calculs de diagrammes de phases par la méthode CALPHAD et à des modèles physiques, intégrés dans un algorithme génétique multi-objectifs. Dans ce contexte, plusieurs critères dépendants du matériau sont examinés et leur effet sur les défauts mentionnés est étudié. Ensuite, la mise en œuvre d'un algorithme génétique a produit un ensemble d'alliages optimaux. Une validation expérimentale est alors réalisée sur une composition sélectionnée. L'alliage sélectionné est étudié à l'état coulé puis de poudre atomisée, et sous forme d'échantillons construits par fusion laser sélective (SLM). L'imprimabilité de l'alliage est évaluée et comparée aux alliages commerciaux existants.

Nomenclature

Table of contents

Introduction

The world of production is in constant development and advancement. Every few years we witness either the birth of a new a production technique or a huge development in an existing one. In the last few years we have seen a tremendous interest in Additive Manufacturing (AM) techniques. Compared to conventional manufacturing processes, AM technologies offer a set of advantages. For instance, in technologies starting from a metallic powder, AM allows to produce complex geometries in almost their net-shape by user-defined computer aided design (CAD) data without tools or molds, lowering the need for post-processing thus raising opportunities to economize material and reduce time and cost. As a result, AM techniques for fabricating metal alloys have become demanded by different metal-parts producing industries, such as the biomedical, automobile and aerospace industries. In fact, the number of publications related to new AM techniques, or to the development of existing ones, has increased enormously over the last decade. The growth in the metal AM market was estimated at almost 900% during the period of 2013-2018, in which the number of sold Laser-Powder Bed Fusion (L-PBF) machines increased from 300 in 2013 to 1800 in 2017 [1].
Nevertheless, despite the presented advantages, the additive nature of these processes and their associated complex thermal histories result in many difficulties, making it challenging to produce dense and strong components. The presence of defects, such as porosity and cracks, the existence of residual stresses or the as-solidified microstructure, can significantly deteriorate the mechanical properties of the produced components compared to conventionally processed parts.
A lot of effort has been put into studying the effect of the process parameters in an attempt to ameliorate the process outcome. However, this large effort was not accompanied with a similarly paced one in the alloy design part, and there still exist very few studies that focus on optimizing the alloy composition to enhance the overall properties of AM products.

Indeed, it is admitted that the performance of components can be optimized if the used alloy is specifically adapted to the process by which it is manufactured. Conventionally, the technique for developing new alloys has mostly been a process of trial and error. This approach, despite being successful, has limitations, especially when the number of alloying elements is high. Recently, several advances in the scientific domain were keystones for the evolution of alloy design, such as the improvement of physical models for describing composition-property relationships, and the significant increase in computing power. The latter has also aided in the remarkable evolution of Machine Learning (ML) algorithms, which currently serve as an excellent exploitation tool for available experimental data, in the field of materials science in general, and for alloy design in particular. Subsequently, computational alloy design became more and more present in the literature.
Austenitic materials, such as austenitic stainless steels, offer many advantages, which makes them one of the most widely used structural materials. These alloys are known for their excellent corrosion resistance and high ductility. Currently, they are one of the main materials used and

studied in AM, as they account for almost one third of all publications in metal AM literature. Nevertheless, the studied compositions are most often conventional alloys that have been previously optimized for different processing techniques, such as casting and forging, and the studies focused on AM-specific compositions are rare.

To design compositions specifically for AM, several design requirements, based on the structural stability of the alloy, mechanical properties, surface properties, etc., must be taken into account. To predict the nature and amount of phases present in the alloys, computational tools are available to calculate phase diagrams in multicomponent systems, within the framework of the CALPHAD (CALculation of Phase Diagrams) method. These tools are based on the thermodynamic basis of minimizing the Gibbs free energy and rely on developed thermodynamic databases constructed from both experimental and theoretical works. In recent years, several alloy design approaches based on the combination of CALPHAD for phase prediction and physical or machine learning (ML) models for the prediction of mechanical properties have been developed. Additionally, work has also been carried out on the utilization of genetic algorithms (GAs) to automate and accelerate the optimization of computational alloy design.

This work proposes a contribution to such alloy design approaches. After a review of the most frequent defects and problems encountered in AM, along with their causes, material-dependent criteria are derived, which can be assessed by the combined use of computational thermodynamics, physical and ML models for the prediction of relevant alloy characteristics. The latter will constitute a set of design objectives and constraints for which a multi-objective genetic algorithm will be used to perform an automatic optimization and propose a set of optimized compositions. To validate the method, an alloy will be selected, produced as a powder, processed by AM and experimentally assessed in terms of defects, microstructure, physical and mechanical properties.

1 State of the art

1.1 Additive manufacturing

1.1.1 A brief history of additive manufacturing

Additive manufacturing (AM), commonly referred to as 3D printing, can be defined according to the American Society for Testing and Materials (ASTM), as the: "*Process of joining materials to make objects from 3D model data, usually layer upon layer, as opposed to subtractive manufacturing methodologies, such as traditional machining*" [2]. This definition can be broadly applied to all classes of materials including polymers, metals, ceramics, etc.

The concept behind "additive" manufacturing dates back way before the recent commercialization of AM machines. Indeed, the idea of adding layers or depositing materials to fabricate parts is seen in ancient repairing and manufacturing processes, such as welding or material/film deposition. In fact, the earliest example of welding goes back to the Bronze Age, where evidence of small gold circular boxes made by pressure welding lap joints is found. In the Iron Age, eastern Mediterraneans and Egyptians welded pieces of iron together. There is also evidence of iron parts welded by hammering that is estimated to date back to Middle Ages [3]. However, welding as we know it today was developed much later; one of the earliest patents of welding was given to De Meritens in 1881 for his work on using arc-generated heat to weld lead plates, at the Cabot Laboratory in France. Similarly, thin films deposited on top of a surface have a documented history of more than 5000 years. However, the deposition of powder or material layers is a more recent activity, first reported in early 1800s [4]. All of these techniques were keystones for the development of presently available AM processes.

The first commercial use of AM emerged in 1984, patented under the name of stereolithography (SLA) by Charles Hull [5]–[8]. From there, evolutions in this domain started happening at a fast pace. In 1988, Scott Crump invented the Fused Deposition Modelling, and in 1990, the first commercial Selective Laser Sintering (SLS) machine became available. From simple prototypes and limited size structures, to 3D printed concrete houses, aero engine components, turbine blades and heat ex-changers, the AM market exponentially evolved [9]. The detailed history of this evolution can be found elsewhere [10].

1.1.2 Opportunities and limitations of additive manufacturing

AM processes give rise to a host of advantages and additional benefits over traditional and conventional processes. From the point of view of applications, AM offers advanced geometrical customization with decreased manufacturing complexity and cost. It allows the production of complex 3D components directly from the design, therefore cutting the need for expensive forms such as punches, dies or casting molds. By doing so, it can also significantly reduce the part count by eliminating the need to assemble several components and might reduce post-processing cost

[11]. Additionally, AM processes allow a rapid change in the design in cases where a certain correction is required due to a discovered flaw, or simply if an optimization of the component shape is desired.

Despite the constant innovations and advances in this domain, AM processes still cannot fully compete with conventional manufacturing techniques, and this is attributed to several reasons. Depending on the type of components and the family of materials used to build the part, there exist limitations in size and expected productivity (production time) which hinder the fabrication of large objects, or conversely, very thin objects. For example, an investigation by Wang *et al.* on stainless steel 316L concluded that fabricating parts with small geometric features, such as plates thinner than 0.2 mm, cylinders smaller than 0.3 mm in diameter, overhanging round holes less than 0.5 mm in diameter, and inclined overhanging planes at an angle of less than 30°, is not possible with SLM and results in geometrically distorted parts [12]. Moreover, although AM processes are expected to provide significant cost reductions in terms of post-processing in the future, there remains a very high initial cost that must be taken into consideration. The cost of powder additive manufacturing equipment is high, especially considering the price of accessories and materials required for operation. Moreover, in the case of metals, producing powders of satisfactory quality is very expensive as well. In addition, the reduction of material loss expected thanks to the additive nature of these processes (compared to subtractive methods where removed material is often lost), may be decreased by difficulties in powder reuse and recycling. Finally, an important limiting point lies in the quality of the final components produced by AM. The parts often show the presence of several imperfections and defects which can significantly limit their performance and deteriorate their properties. This point will be further discussed later. In spite of such drawbacks, AM remains attractive in a number of applications; some processing techniques will be reviewed hereafter.

1.1.3 Major additive manufacturing processes

3D printing is currently widely spread in different application domains and used to fabricate a wide range of materials. Earlier, the application concentrated mainly on polymers due to the fact that a lower processing temperature is needed compared to metals or ceramics, and the properties of the material are less depending on processing. Later, with the technological advancement of different apparatuses, AM became widely present in the metallic alloys fabrication world as well.

There exist different types of AM technologies for fabricating metals; an overview is shown in Figure 1.1. Processes can be classified depending on the feedstock form (powder, wire, sheets...), and on the primary heat source: laser beam (L), electron beam (EB)… The most widely used AM processes for metals are Powder Bed Fusion (PBF) and Directed Energy Deposition (DED) which are capable of fabricating parts starting from a metallic powder [13]. DED works by depositing material onto a base through a nozzle. The powder material fed to the nozzle is melted as it is being

deposited. This procedure is done repeatedly, until the layers have solidified and created (or repaired) the part.

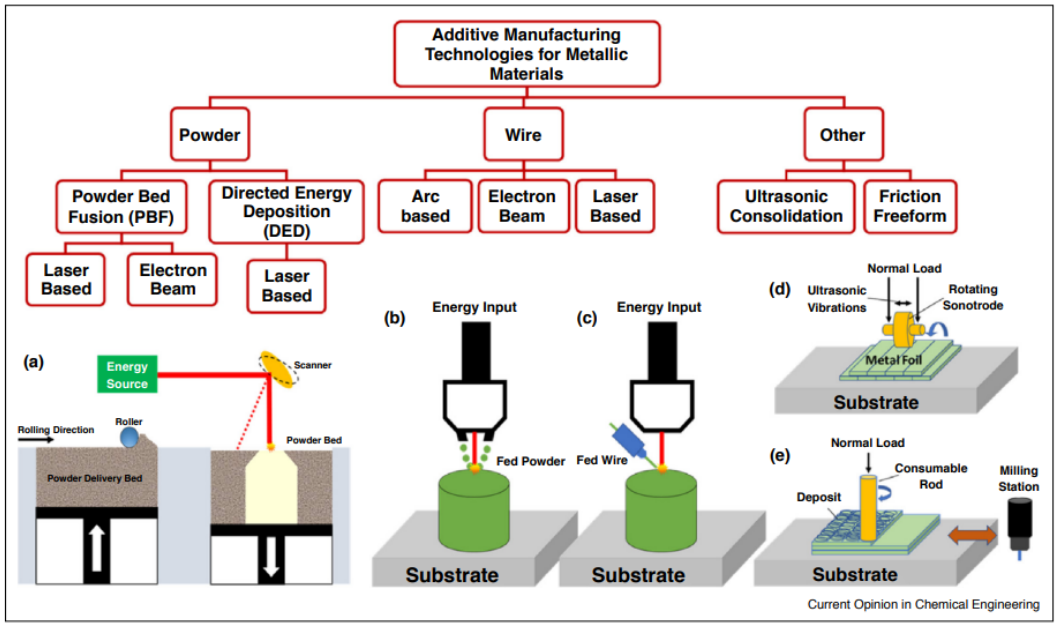

Figure 1.1 Different additive manufacturing technologies for metallic materials based on feedstock form and fabrication processes and their corresponding schematics where (a) is PBF, (b) DED, (c) wire-based deposition, (d) ultrasonic consolidation and (e) friction freeform [14]

For PBF, two processes are distinguished: Selective Laser Melting (SLM, also referred to as L-PBF), and Electron Beam Melting (EBM). In SLM, a moving heat source —a laser— is used to consecutively melt layers of powder which are added, or "spread" using a spreading roller device (see Figure 1.2). The built piece grows in the "building direction" (red arrow in Figure 1.2). The thickness of the spread layer is one of the process parameters and must be chosen by the user. The movement of the laser on the substrate is set according to what is called the "scanning strategy". A summary of the commonly used scanning strategies is shown in Figure 1.3. The offset distance between adjacent melt tracks (scans) is called the hatching distance (h). This is done under a shielding gas atmosphere (Ar or N_2) to avoid oxidation. EBM is performed in a similar manner, except that the heat source is an electron beam and the building is done under vacuum.

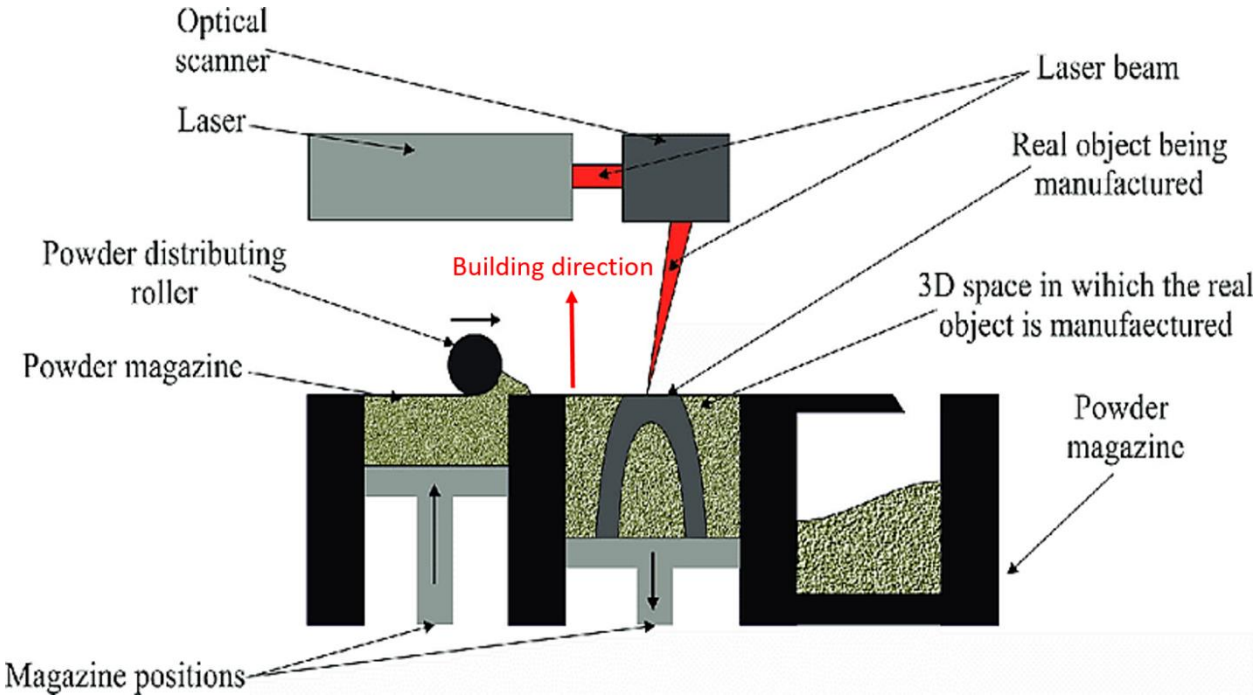

Figure 1.2 Schematic of the Selective Laser Melting (SLM) device [15]

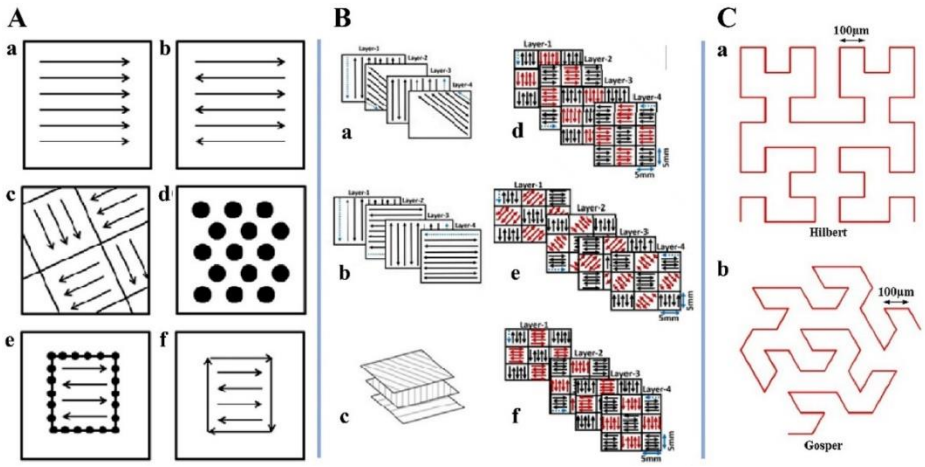

Figure 1.3 (A) Different scan strategies used in the L-PBF process. (a) unidirectional or concurrent fill, (b) bi-directional, snaking, or countercurrent fill, (c) island scanning, (d) spot melting, (e) spot melting contours with snaking fill, and (f) line melting contours with snaking fill. (B) Schematics illustrating scan patterns of successive layers with (a) 45° alternating, (b) 90° alternating, (c) 67° alternating, (d) chessboard scanning, and chessboard scanning with adjacent chessboard block scanned in (e) 45° and (f) 90° rotated direction. (C) Examples of fractal scan strategies of (a) Hilbert and (b) Gosper. [16]

All of the process parameters mentioned above must be optimized as to obtain the best possible results for the printed material, and they all play a role in the quality of the final component, as it will be shown later. An important value usually considered in SLM is the Volumetric Energy Density (VED, or E_v) (i.e. energy per volume unit) transferred to the material, defined as:

$$E_v(J.\,mm^{-3}) = \frac{P\ (W)}{V\ (mm.\,s^{-1})\ \times h\ (mm)\ \times d\ (mm)} \quad 1.1$$

where P is the laser power, V is the laser scan speed, h is the hatching distance and d is the thickness of the powder layer.

Table 1.1 shows a comparison between the processing parameters and product features of DED and PBF (SLM and EBM). In general, the DED process offers higher productivity but leads to a worse surface state (high roughness). For PBF processes, EBM is better for processing brittle materials (such as intermetallics) because they are sensitive to thermal shock. The effect of the latter is lessened in EBM because of the lower cooling rate, as the chamber and the substrate can be preheated to reduce thermal gradients. However, EBM generally has reduced accuracy compared to SLM due to the slightly wider beam. The parts developed by SLM also require less finishing (due to its lower roughness) compared to those built by DED or EBM.

Finally, the choice of a given process depends on the geometry, material, production time, as well as on the type of application and specifications of the required part.

Table 1.1 Comparison of process parameters for powder-fed DED and PBF for metallic components [17]

Process	**DED**	**PBF**	
		SLM	EBM
Heat source	Laser	Laser	E-beam
Building atmosphere	Ar/N_2	Ar/ N_2	vacuum
Power [W]	100-3000	50-1000	
Speed [mm.s^{-1}]	5-20	10-1000	
Max. feed rate [g.s^{-1}]	0.1-1.0	-	
Layer thickness [µm]	100-2000	20-100	
Max. build size [mm^3]	2000 × 1500 × 750	500 × 280 × 320	
Production time	High	High	
Dimensional accuracy [mm]	0.5-1.0	0.04-0.2	
Surface roughness [µm]	~ 300	25-30	20-50

1.1.4 Microstructure of additively manufactured parts

During PBF processes, the deposited metal powder undergoes rapid melting and solidification with a cooling rate in the order of 10^5-10^6 K/s. Then, the solidified layer might be partially re-melted and subjected to several rapid heating and cooling cycles as additional layers are deposited and melted on top of each other. This particular thermal history results in a microstructure which differs from that of the conventionally prepared material [18].

The size and shape of the grains in AM parts are greatly affected by the cooling rate of the solidifying material. Higher cooling rates will lead to a finer grain structure (a large undercooling induces a high nucleation rate and grains have shorter times to grow), which is why a fine structure is usually observed for the very first layers. However, as the layer height increases during building, the cooling rate of the material decreases, explaining why grains become coarser. As for the grain shape, columnar grains that grow epitaxially are mostly reported in the literature [19]–[23], usually elongated in the direction of the thermal gradient (see example in Figure 1.4). Equiaxed structures are much rarer because of the high thermal gradient [17].

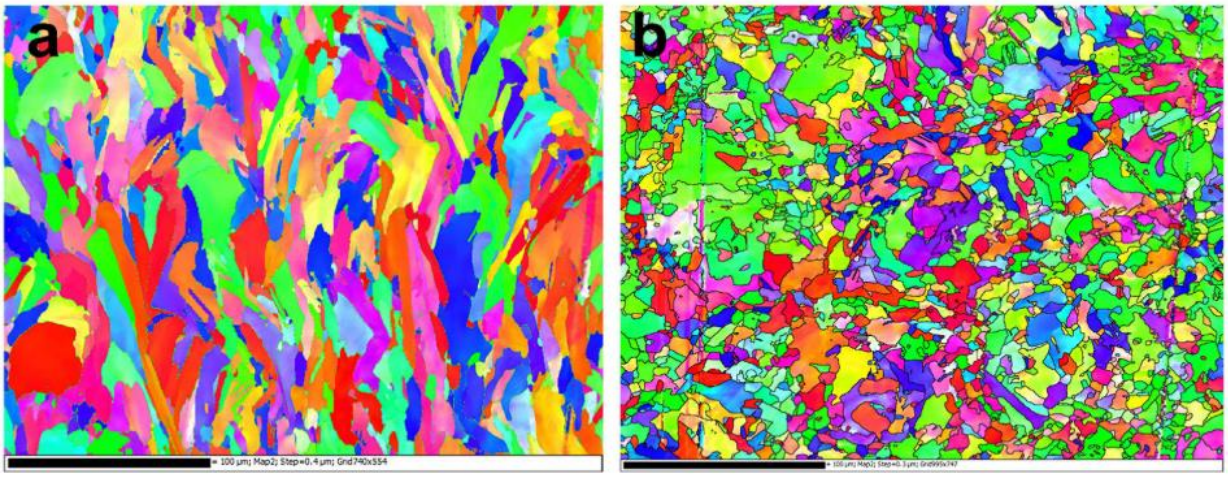

Figure 1.4 EBSD maps (inverse pole figure: blue is 111, green is 101 and red is 001) for 316L fabricated by SLM where in (a) the building direction is vertical, and (b) the plane of the image is perpendicular to the building direction [24]

Generally, the size and shape of grains depend on processing parameters, namely the heat source power and scanning speed, but also the type of shielding gas. Nezhadfar *et al.* [25] have shown that the use of a nitrogen atmosphere during the fabrication of 17-4 PH stainless steel introduces slightly lower temperatures but high cooling rates compared to an argon atmosphere. This was attributed to the higher thermal conductivity of nitrogen (~0.02 W/mK) compared to argon (0.016 W/mK). This leads to a finer microstructure, which has been shown to increase the hardness

of the specimens. Similarly, Amano *et al.* [26] have shown that the use of helium, which has an even higher thermal conductivity (~0.142 W/mK), can further increase the cooling rate, leading to a finer microstructure and slightly higher mechanical properties in the case of a Ti-6Al-4V alloy (Figure 1.5).

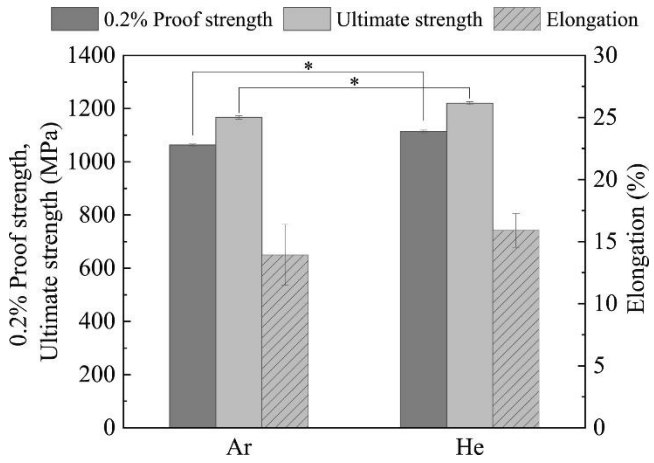

Figure 1.5 Tensile properties of Ti-6Al-4V alloy specimens fabricated by SLM under Ar or He flow [26]

1.1.5 Defects in additive manufacturing

As mentioned before, one of the main limitations of AM technologies is related to the presence of defects in the produced parts. These defects can come from several factors, starting from the initial composition of the material, the used powder and its quality, the process itself, or a combination of all of the mentioned. In this section, an overview of the different types of defects frequently observed in metal parts produced by AM will be shown. The effect of the powder and the process will be discussed separately in the following two sections, and a more detailed study of the effect of the chemical composition on each of these defects will be discussed thoroughly in Chapter 4.

1.1.5.1 Residual stresses and distortions

As the material heats and cools down during AM, it undergoes thermal expansion and contraction that are not uniform due to local heating, implying strain gradients in the part. The so generated strain incompatibility leads to stresses in the part that can be detrimental to its quality in several ways. First, if this stress exceeds the local yield stress (YS) of the material, plastic deformation occurs which leads to residual stresses, shape distortions and geometrical defects. Second, if this stress locally exceeds the ultimate tensile stress (UTS) of the material, cracking might occur; this will be described in the next subsection.

Geometric defects include warping of the surface (see Figure 1.6) or shrinkage in size of the final component. Although the severity of shrinkage depends a lot on the processing parameters, it can reach 2-3% in volume [27]. Mousa [28] investigated the "curling" phenomenon, i.e. a combination of shrinking and warping that yields a curved profile of down-facing surfaces intended to be flat. Curling is usually associated to an uneven shrinkage between the top and the bottom of the part.

Figure 1.6 Example of surface warping in material fabricated by SLM.

Additionally, geometrical distortions can happen in the form of "super-elevated edges", which are elevated ridges of the solidified material at the edges of the successive layers. Yasa *et al.* [29] studied this effect (see Figure 1.7) and attributed it to surface tension forces. This defect has a significant impact on the quality of the product as it worsens the surface topology and the dimensional accuracy of the part. It can also have an effect on the AM machine itself: when super-elevated edges stick out from the powder layer, they may interfere with the powder deposition system (roller), increasing its wear and negatively affecting the powder bed uniformity [30].

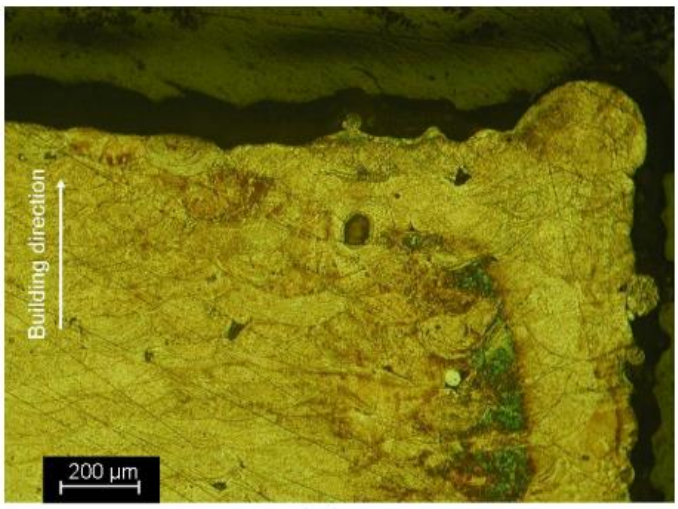

Figure 1.7 Example of elevated edges seen in parts fabricated by SLM [29]

1.1.5.2 Cracking

Figure 1.8 shows different types of cracking observed in SLM parts. Different sources of cracking exist; a more thorough study of some cracking mechanisms will be presented in Chapter 3. A particular case of cracking is a phenomenon called delamination (shown in Figure 1.8 c), where cracks originate and propagate between adjacent layers (inter-layer cracking). This happens when the residual stresses exceed the binding ability between the deposited layer and the previous one [30].

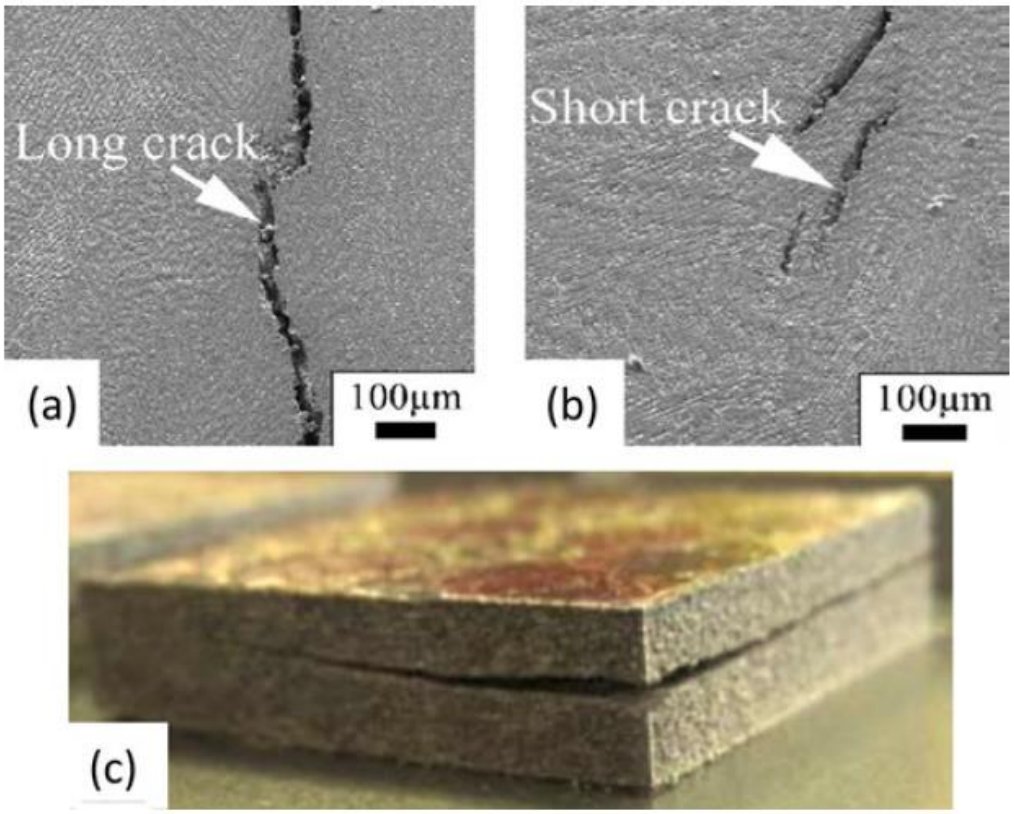

Figure 1.8 Examples of layer delamination and cracking in SLM [17] *where a) and b) show long and short cracks respectively and c) shows a delamination crack*

1.1.5.3 Porosity

One of the common defects observed in AM products is the presence of porosities and voids [31]–[33], which generally have a detrimental effect on the mechanical properties of the final part [34]. Three main mechanisms by which these defects are produced have been identified.

(a) Keyhole porosity

Two main melting modes can be distinguished during AM: conduction mode and keyhole mode. The melting mode depends on the intensity of the laser, or power density (laser power / laser spot size). In conduction mode, the power density is just high enough to melt the metal. When the laser density is higher (i.e. enough to go beyond melting and provoke vaporization), melting starts happening in a keyhole mode. In this mode, the vaporizing metal creates an expanding gas that pushes the meltpool outward. This creates a keyhole, or cavity from the surface down to the bottom of the meltpool. As the laser moves across the scanning track, the keyhole creates a deep and narrow weld. This keyhole remains open if the scanning speed is below a certain threshold that depends on the material type [35]. However, under certain conditions, keyholes may become unstable. Figure 1.9 shows an illustration of how the formation and collapse of these keyholes may cause the entrapment of vapor, leading to the presence of voids, which explains why in most cases these voids have a spherical shape [36]. This phenomenon was also observed by in-situ X-ray imaging [37], [38].

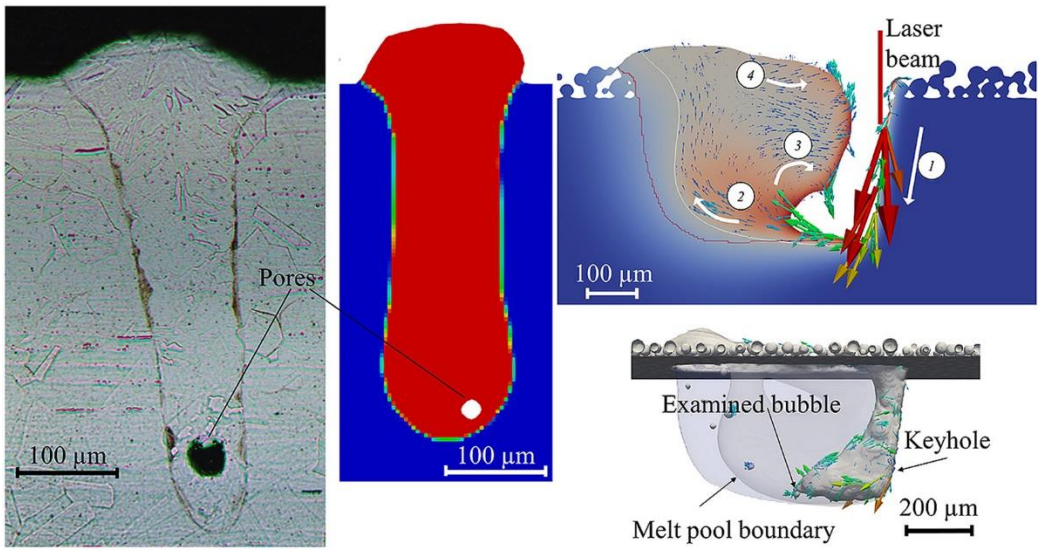

Figure 1.9 Representation of the formation of pores due to the collapse of unstable keyholes [39]. *Right images show the formation of a keyhole during the laser scan and left image shows a microscopic observation of the pore in the final material.*

(b) Porosity due to gas entrapment

Pores may also be due to the entrapment of gas from the atmosphere, as in most AM processes an inert shielding gas (such as Ar or He) is used to prevent oxidation. These gases are known to be insoluble in metal, thus any bubble created in the molten pool will remain trapped in the solidified metal as a pore unless it can outflow from the molten pool. This can lead to the type of porosity

shown in Figure 1.10. In an attempt to decrease this effect, certain authors replaced the inert shielding gas by a reactive one, such as nitrogen in the case of stainless steels. For example, Elmer *et al.* showed that A36 steel and 304L stainless steel displayed a strong correlation between the choice of the shielding gas and porosity levels during laser welding, where medium to high levels of porosity (1.19% for A36 and 3.6% for 304L) were observed in Ar atmosphere compared to little to no porosity when N_2 was used instead [40]. However, the choice of using N_2 as a shielding gas increases the content of this element in the final material because of its high solubility in the austenitic structure. Moreover, this element has two other effects: (i) it is an austenite stabilizer and (ii) it increases the strength of the stainless steel. Yet, due to its volatility, it remains difficult to control its exact content.

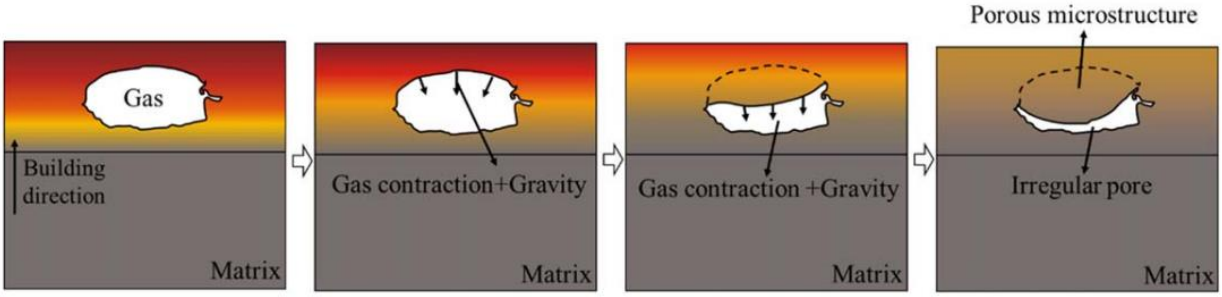

Figure 1.10 Schematic diagram of the formation of pores due to gas entrapment [41]

(c) Porosity caused by lack of fusion

Finally, voids can also be the result of an inadequate penetration of the molten pool in a deposited layer, either on a previously deposited layer or on the substrate [42]–[44]. In fact, these voids are much more harmful than the spherical voids caused by the gas molecules. Their size can reach 50 µm in diameter [18], [43]. Adequate fusion and inter-layer bonding for different alloys can be studied by considering a non-dimensional "lack of fusion index", LF, defined by [43]:

$$LF = \frac{d}{h} \qquad 1.2$$

where d is the penetration depth of the molten pool and h is the thickness of a layer of material deposited onto the substrate or previously deposited layer. In order for a deposited layer to bond properly with a previous layer, it is necessary that the penetration depth of the molten pool, d, exceeds the layer thickness h (i.e. LF ≥1).

1.1.5.4 Surface roughness and balling

High surface roughness is one of the defects currently seen in AM parts. Roughness might lead to long and costly post-processing depending on surface state and the shape of the desired product.

The two dimensional surface roughness S_a can be defined as [45]:

$$S_a \approx \frac{1}{NM}\sum_{i=1}^{N}\sum_{j=1}^{M}|f_{ij}| \qquad 1.3$$

where f_{ij} is the deviation of surface height at point of coordinates i-j from the mean height over the profile, with the assumption that the overall surface is level and N×M is the number of measured deviations f_{ij} over a given surface.

Several phenomena affect the quality of the surface of the printed parts. Among them, the "stair step" effect (i.e. a stepped approximation by layers of curves and inclined surfaces) originates form the part and process design (i.e. layer thickness) but is still a main concern despite the effort put into controlling this problem by minimizing the layer thickness and using an appropriate scan strategy.

Additionally, surface roughness can be caused by the phenomenon of "balling", or melt-ball formation. The latter occurs when the molten material solidifies in the shape of spheres instead of solid layers, which is a severe obstruction to interlayer connection [46]. Surface tension is what drives the balling phenomenon. When the value of the surface tension is high, it prevents the molten material to wet the underlying layer, creating spherical balls on the surface. When this occurs, the final surface is rough and bead-shaped, which produces an irregular layer deposition and can have detrimental effects on the density and surface quality of the part. Figure 1.11 illustrates this phenomenon. Additionally, in case the balling is quite severe, the spheres protruding from the powder layer may interfere with the movement of the roller that deposits the powder for subsequent layers and lead to other troubles such as the exaggerated wear of the machine and inhomogeneity of powder distribution in each layer [47].

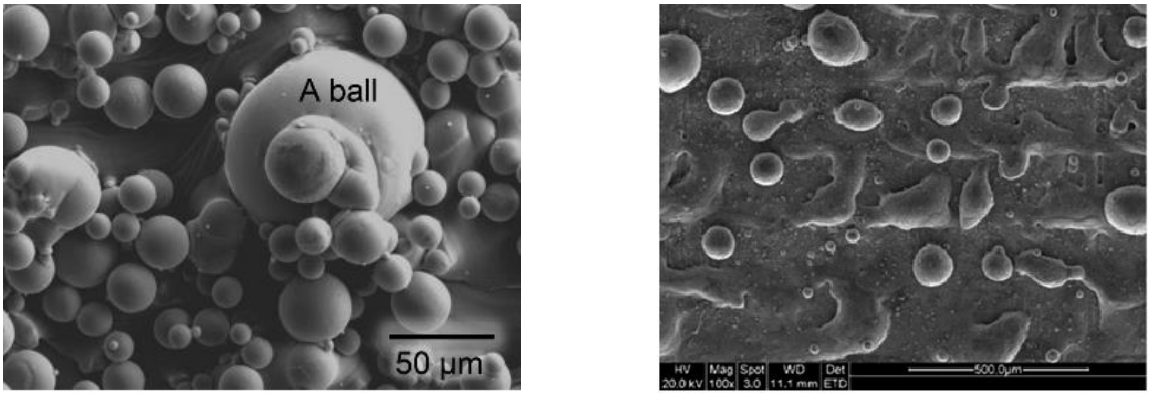

Figure 1.11 Examples of metal balls formation in SLM [48]

1.1.5.5 Vaporization and change in composition

The high temperatures reached during AM can lead to pronounced vaporization of elements from the meltpool. Evidence of the vaporization phenomenon was reported in literature. Figure 1.12 [49] shows an image in which a metal gas vapor was captured during the SLM printing of 316L, as well as several phenomena associated with it. Evaporation causes a hydrodynamic instability of the molten zone by fluctuating the height of liquid. Additionally, it drives the powder towards the sides of the scanned track, leading to powder denudation which is when particles get cleared in the vicinity of the laser track (as shown in Figure 1.12). Such clearing of powder causes uneven thickness and unstable melting, and can lead to surface roughness and porosity. Finally, as shown in the captured image of Figure 1.12, ejection of liquid metal droplets can take place. These droplets can either fall on the scanned track or somewhere else on the powder bed. In both cases, they can be a source of defects.

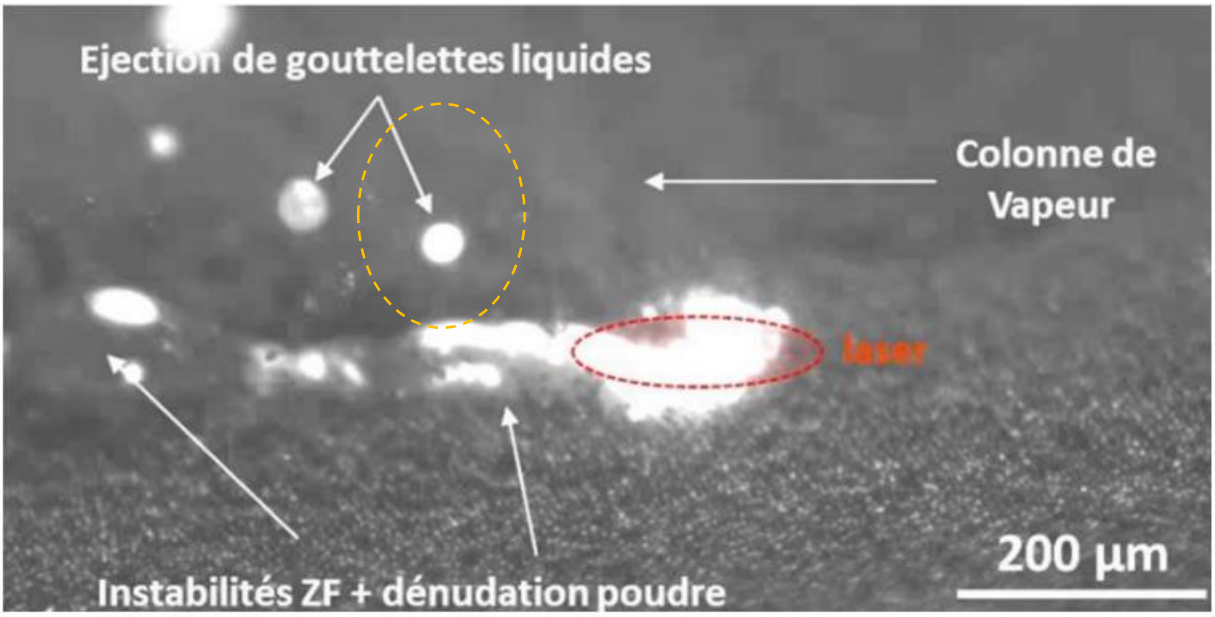

Figure 1.12 Evidence of gas vapor in SLM of 316L [49]

Additionally, depending on the difference in the volatility of the elements, selective vaporization might take place, which can change the overall composition of the alloy, and consequently affect the properties of printed components. Several authors have investigated this effect. For example, Yakout *et al.* [50] compared the composition of the powder before printing to the composition of the printed parts for 316L and showed that the concentration of Ni, Mn and (slightly) Cr decreased and subsequently the concentration of Si, Fe and Mo increased, as shown in Table 1.2.

Table 1.2 Material composition in wt.% of virgin powder and cubes of 316L stainless steel produced by SLM [50]

	Fe	Cr	Ni	Mo	Mn	Si
powder	67.59	17.13	10.69	1.62	1.84	1.13
produced by SLM	68.21	17.05	8.66	2.79	1.35	1.94

1.1.5.6 Spattering

Spatters are liquid metal particles ejected from the meltpool, which can be caused by vaporization as mentioned above. Indeed, the phenomenon of evaporation discussed in the previous section has an effect on laser absorption [51] which, combined with complex fluid motions, contributes to the ejection of spatters from the meltpool. When these ejections collide with each other, or with the powder, larger and irregular particles can be generated via coalescence or sintering. In a broader definition, the solid particles that blow out while the laser is moving can also be called spatters. The size of these spatters varies and can reach tens of micrometers (see Figure 1.13), depending on the "violence" of the meltpool dynamics affected by the laser density. Spatters lead to uneven layer thickness and increase the surface roughness.

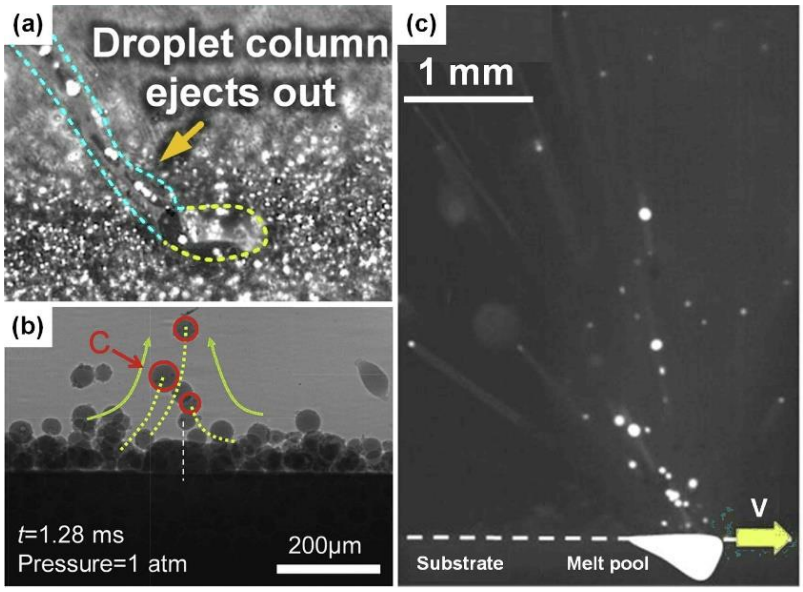

Figure 1.13 Spatters observed by high-speed imaging [52]

1.1.5.7 Impurities and contamination

Impurities include, as a broad definition, inclusions, contamination from other materials (used in the same machine) and surface oxides (formed during solidification) [53], [54]. Although in SLM a shielding gas is applied to avoid oxidation, even low levels of residual oxygen (0.1–0.3%) in the atmosphere can lead to the formation of oxides. In some cases, these oxides can be trapped inside the material and finally affect the properties of the produced part. Zhang *et al.* [55] argued that in some cases it might be unavoidable. The authors showed that even by using an argon gas with a 99.9999% purity, oxides in the form of Cr_2O_3 and Al_2O_3 were still found in Ni-based superalloy IN718 parts produced by AM.

1.1.6 Powder related defects

The fabrication of the powder and its corresponding characteristics also play a significant role in the quality of the final built components. There exists several methods of powder production; a full review can be found elsewhere [56]. The most widely used method to produce a metallic powder is gas atomization (see Chapter 3 for details), as this method provides spherical powders suitable for AM processing. In gas atomization, a molten stream of metal is disintegrated into droplets by a high-pressure gas flow. Droplets then "free-fall" inside a tower, solidify in the atmosphere and the resulting particles are collected at the bottom of the tower. To protect against oxidation, the atomization process is usually performed under a shielding gas (Ar or N_2). The prior melting of the starting material can be performed under vacuum or in a gas atmosphere. The method of melting and choice of atomization gas can significantly influence the powder cost and quality.

1.1.6.1 Effect of powder characteristics

To study powder related defects, several powder characteristics must be taken into consideration as they play a role in the packing density and flowability of the powder during printing, thus affecting the final quality of AM parts [57]–[61].

(a) ***Morphology/shape***

Concerning the particle shape, a spherical morphology is preferred for AM processes as it is associated with a higher packing density and a better flow [16]. Low packing density can lead to the presence of internal voids in AM parts.

(b) Mean size and size distribution

As for the particles size and particle size distribution (PSD) requirements, it varies depending on the AM process. In particle measurement, it is common to generate a cumulative distribution of particle sizes. Values for d_{10}, d_{50} and d_{90} sizes, for which the cumulative function is equal to 10%,

50% and 90% respectively, are mostly used to characterize the PSD. Figure 1.14 shows the usual required PSD ranges for different AM processes. Generally, the powder used for SLM has a size distribution in the range of 15 µm to 65 µm [62]. Very fine particles can decrease powder flowability and lead to agglomeration, but at the same time big particles might bring higher levels of internal porosity. In fact, among other authors, Rabin *et al.* [63] characterized a centrifugally atomized 304 stainless steel powder and showed that the gas concentration and porosity increased with increasing particle size.

Usually, gas-atomized powders have a log-normal size distribution. This distribution, especially with the presence of small particles, may have different effects. Wider PSDs, biased towards fine particles, lead to higher layer densities [61], as it can be argued that the addition of small particles can fill the voids between large ones [64]. Yet, it is important to note that while this might improve density, wider PSDs are usually also correlated with a lower powder flowability. Quantifying this compromise into a criterion is not obvious, and further investigations to correlate the PSD with process parameters optimization is needed.

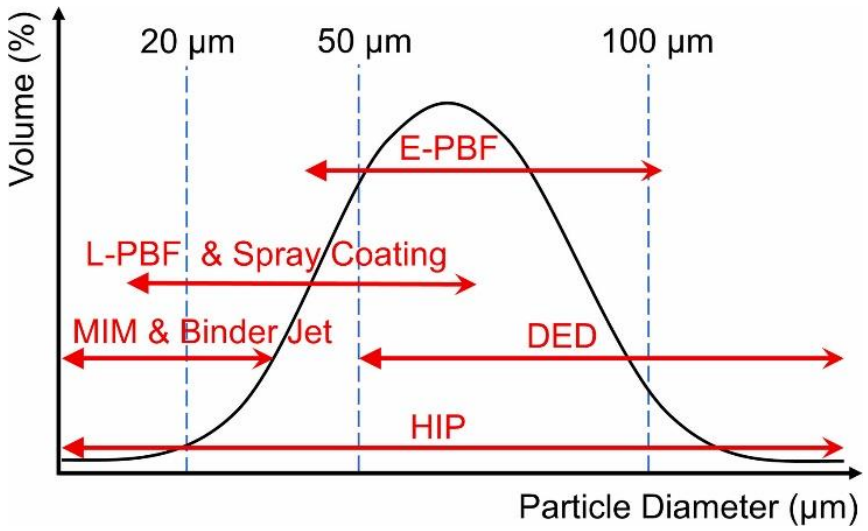

Figure 1.14 Schematics of the powder size distribution (PSD) for as-produced atomized powder (black curve) which shows volume distribution percentage against the particle diameter. L-PBF (SLM) and E-PBF(EBM) stand for laser and beam powder bed fusion, DED is directed metal deposition, HIP is hot isostatic pressing and MIM is metal injection molding [65]

(c) Powder porosity

The density –or porosity– of the powder particles themselves is another important factor. Internal voids in feedstock powder can remain in AM parts, especially voids that are caused by the entrapment of gas bubbles. Although it is sometimes possible to "release" this gas upon melting, in many cases it remains stuck in the meltpool and leads to porosity in the final built component.

(d) Surface contamination

The powder composition, including the level of impurities and inclusions within feedstock materials, affects the composition of the built material and plays a role in determining the properties of the produced part (mechanical properties, corrosion resistance…). Additionally, the formation of oxide layers on the powder particles may prevent their melting and therefore require an increase of heat input. Figure 1.15 illustrates this phenomenon. The presence of oxide layers can also potentially lead to balling as it is more difficult to melt highly oxidized powders since particles tend to keep their spherical shape, causing poor wetting of the substrate.

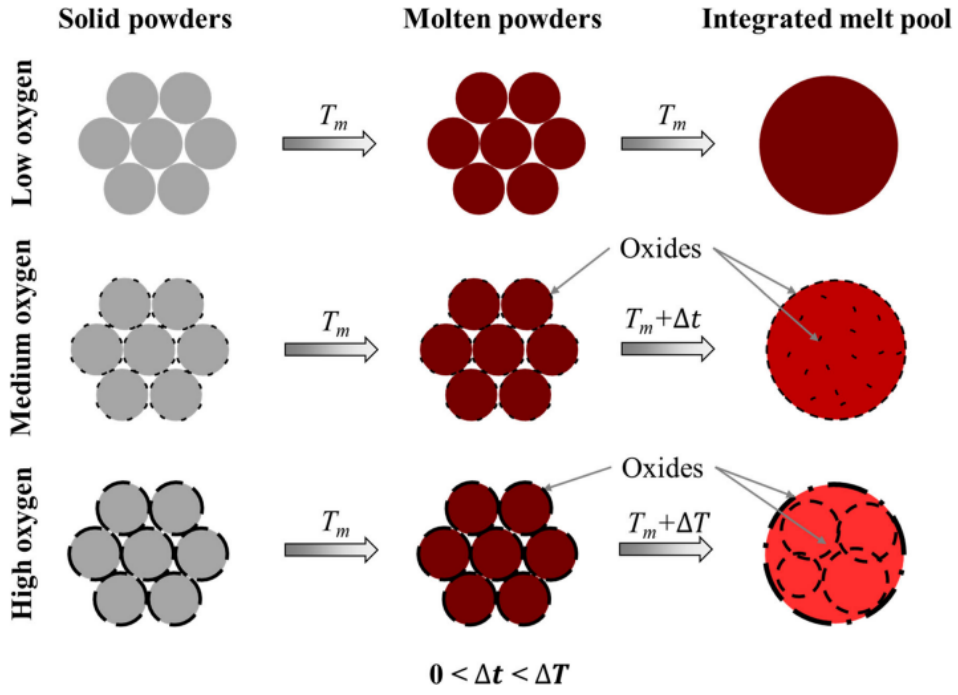

Figure 1.15 A schematic illustration of the effect of a surface oxide layer on powders. In the presence of oxides, a higher temperature is required to improve the wetting and integrate with other liquid for forming one melting pool [66]

1.1.6.2 Effect of powder mixing

Although using pre-alloyed feedstock is the most common option in AM, there has been some work on using a pre-mixed powder from available elemental powders and performing *in situ* alloying in PBF processes [67]–[73]. The technique of *in situ* alloying opens up a wide range of composition-adjustment possibilities to any alloy whose powder might be difficult to produce. These studies showed the possibility of AM part production using pre-mixed powders that has the

chance to compete with pre-alloyed powdered materials. As a perspective, performing *in situ* alloying can allow the possibility of manufacturing components with composite and composite-like structures [74], or steering the material microstructure in three dimensions inside the component during its manufacturing [70], [75], [76]. Thus, the creation of "gradient materials" becomes possible, a kind of a "4^{th} dimension", corresponding to a controlled compositional gradient, being added. However, there remains a clear challenge of achieving homogeneous microstructures and compositions from AM of pre-mixed powders, as new intermetallic compounds and phases might form during the PBF. Wimmer *et al.* [77] presented an investigation of the influence of mixing an aluminum (AlSi10Mg) alloy powder with a 316L stainless steel powder during SLM. They concluded that additives in the powder considerably affect important key characteristics of the SLM process like the maximum temperature values. Additionally, the authors demonstrated how the addition of AlSi10Mg decreased the chemical homogeneity of the built part. Another important conclusion is that despite the very different vaporization temperature and surface tension of aluminum, spatters formation was not changed, so it may be only weakly dependent on alloy composition.

Finally, despite the promising aspects of *in situ* fabrication of alloys, for the moment it remains far from perfection, especially compared to the results of pre-alloyed powders.

1.1.7 Process related defects

Process-induced defects are related to the interaction between the beam, the powder, and the previously melted layer of material, and are affected by the choice of the processing parameters.

1.1.7.1 Effect of scanning strategy

The scanning strategy term describes the spatially moving pattern of the heat source (laser, electron beam…) used to melt the deposited powder. The scanning strategy varies by different scanning directions, sequence, vector rotation angle, vector length, scanning speed, and hatch space [78]. Yet, the way to optimize the scanning strategy is poorly reported in literature, and varies a lot depending on the material properties, such as conductivity, specific heat, or ductility.

Van Elsen *et al.* [79] showed that the scan strategy has an effect on the temperature distribution over the surface. Hence, applying one scan strategy rather than another can lead to a significant modification of residual stresses. For example, Carter *et al.* [80] have shown that the "island" scan strategy (resembling a checkerboard pattern, see Figure 1.3 a-c) used for building nickel base superalloy CM247LC with SLM results in a heterogeneous structure with regions of higher susceptibility to extensive cracking. The authors showed that using a simple "back-and-forth" scan strategy allows to produce a more homogeneous structure. Additionally, if the chosen strategy is not well adapted, it may cause the generation of super-elevated edges. Yasa *et al.* [29] investigated this effect and compared the edge height of 316L parts built with SLM using four different scan

patterns: unidirectional (horizontal and vertical), or alternating (at 45° and 90° angles). Their results show that the highest edge height values are seen with the grid scanning (alternating 90°), and the lowest value is for horizontal unidirectional scan.

1.1.7.2 Effect of processing parameters: concept of a processing window

Generally, the most studied SLM process parameters in literature are the laser power, the scan speed, the hatch distance (also referenced as scan spacing) and the powder layer thickness. These values are used to determine the volumetric energy density (VED) transferred to the material, defined in Equation 1.1. Most often, the layer thickness is fixed for a given machine, depending on the expected resolution and surface finish. Yet, this value has a direct effect on the quality of the built part. It is currently admitted that a thin powder layer is favorable for the continuity of the scan track, and better for avoiding the balling phenomenon [47]. Among the studies on the effects of processing parameters, most of the available literature focuses on the effect of laser power and scan speed [81]–[83]. This helps in identifying the concept of a "processing window" which usually corresponds to good quality of the final part. Figure 1.16 shows an illustration of the processing window.

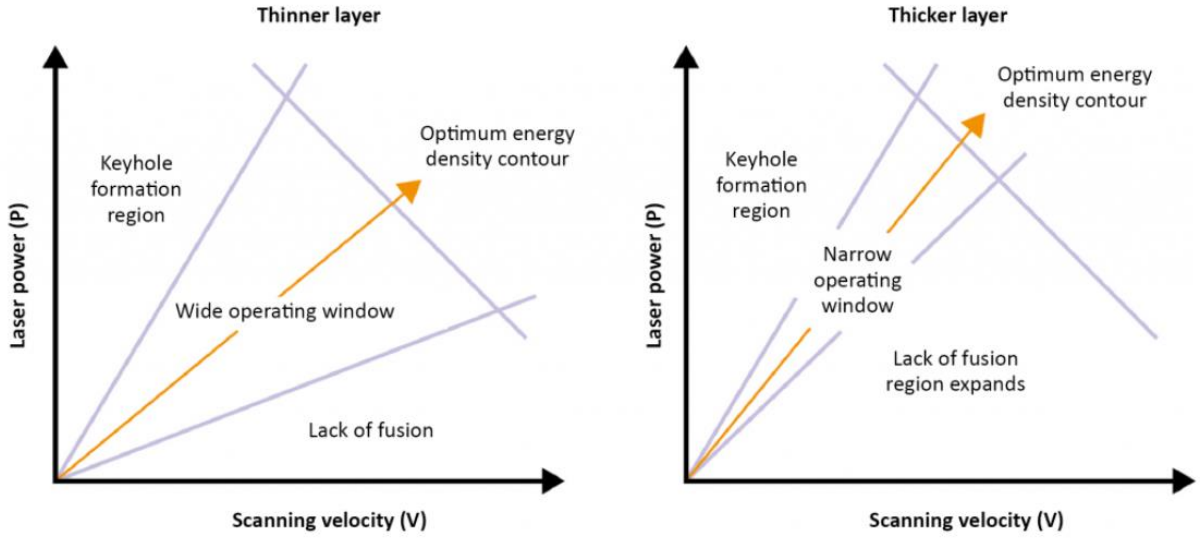

Figure 1.16 A schematic illustration of the processing window of AM. See text for details [84]

As it is shown, at high scanning speeds and low laser powers, there is a risk that the material does not fully melt. This leads to defects such as "lack of fusion" porosities. On the other hand, at high powers and low speeds, there is a risk of overheating the material, which causes deeper energy penetration and leads to the formation of keyholes. Therefore, to print a part with a good quality,

it is necessary to find the window in which the energy from the laser is high enough to fully melt the powder, without penetrating too deeply into previously built layers and overheating them. This "balanced" ratio is what is defined as the optimum energy density contour in Figure 1.16. However, there exist limitations to how high the power and speed can be increased, beyond which the meltpool becomes unstable, and phenomena such as balling and spatter formation (ejection of molten particles from meltpool) are seen [47].

Recently, Heiden *et al.* [85] have investigated the effect of several processing parameters on the microstructure and density of 316L fabricated by SLM. Figure 1.17 illustrates their results. These authors have shown how the grain size changes with the processing parameters. The figure shows the shift from fine, rather equiaxed grain sizes on the bottom right of the process map (low VED) to larger, more elongated grains at higher laser power and slower scan speed combinations (higher VED). It is also shown that lower laser powers can lead to an increase in porosity, impeding the growth of grains during solidification. The authors demonstrated that there is not one specific ideal process set for each machine. Alternatively, there are several combinations of process parameters to achieve similar goals: their observations and analyses further support the idea and the importance of a processing window. The authors have also shown that increasing the VED increases the part density, and improves top and side surface finish. Yet, this effect is limited, as too high values of VED lead to keyholing effects and unstable meltpools.

The processing window also depends on material properties, which will be detailed later. Overall, a wide processing window is always preferable, to be able to fabricate parts with highly flexible parameters (i.e. a "robust" process) and a high productivity. Therefore, materials which exhibit wider processing windows are considered to have a relatively higher printability.

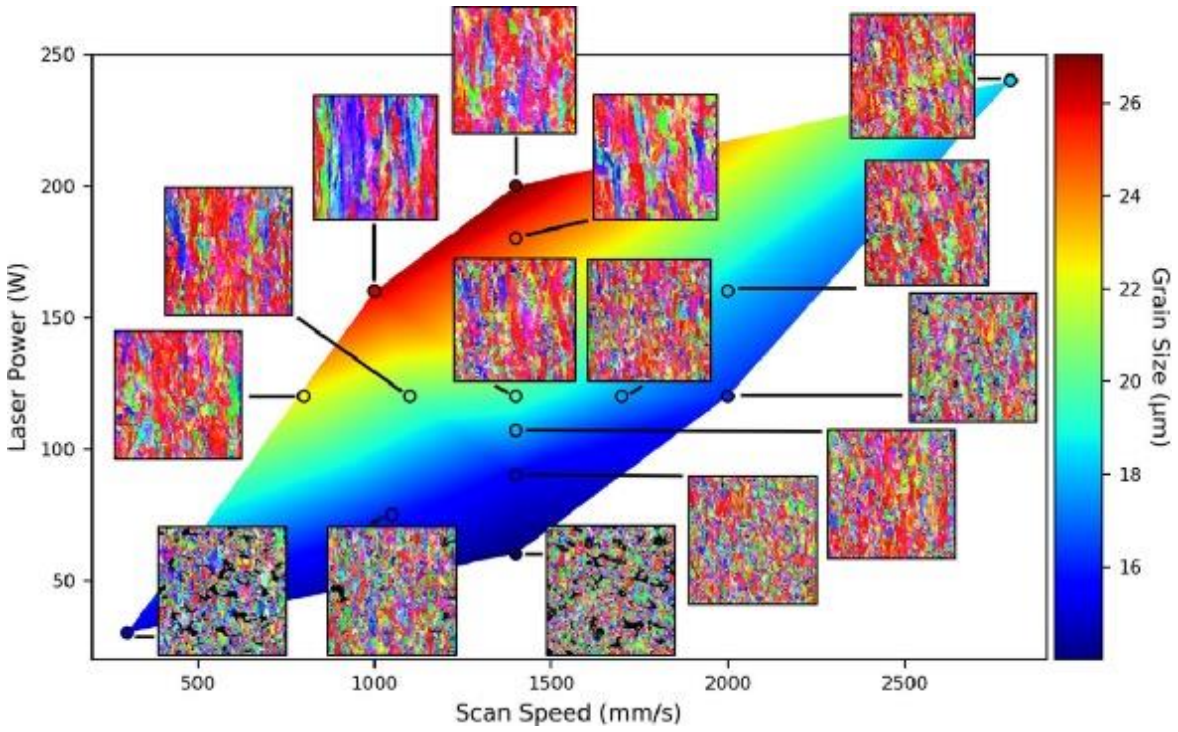

Figure 1.17 Microstructural process map highlighting changes to grain size at varying powers and scan speeds for 316L built by SLM [85]

1.1.8 Materials in additive manufacturing: need for AM-specific materials

The rapidly growing AM industry of metallic alloys uses and studies the major part of existing materials in fusion-based processes. Figure 1.18 shows the proportion of publications studying different alloy categories in AM between 2007 and 2017; it is interesting to note that about 200 studies were already annually published in this field, and this number has been systematically growing since then. Generally, the main alloy categories that are studied in AM were then titanium alloys (mostly Ti-6Al-4V), steels (largely stainless steels 316, 420, 17–4 PH and tool steel H13), aluminum alloys (mainly AlSi10Mg and AlSi12 and less commonly 7075, 6061, and 2000 series), nickel superalloys (mainly alloys IN 718 and 625). Several other groups of alloys, such as high entropy alloys [86], magnetic materials [87], [88], Co-Cr [89], [90] and tungsten alloys [91], [92], had also been tested for PBF processes. A rough but more recent literature analysis seems to indicate similar trends.

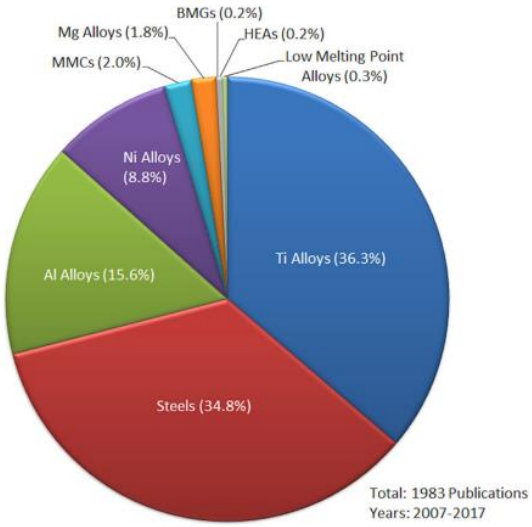

Figure 1.18 Pie chart of (2007–2017) publications of different alloy systems in AM [93]

Nevertheless, all of these alloys were previously optimized for different processing techniques with a specific set of thermo-mechanical processing histories, which explains why fabricating these alloys with AM can lead to many troubles. As an example, undesirable solid-state phase transformations were observed in the EBM of the IN 718, due to the fact that the powder bed temperature that produces crack-free material coincides with the temperature at which the phase transformations occur [94]. Therefore, the particularity of AM necessitates that the alloy compositions be tailored to its specific thermo-chemical and thermo-mechanical aspects, such that less effort is put into finding the optimal parameters resulting in defect-free parts or, in other words, such as to obtain wide processing windows.

1.2 A special focus on austenitic materials

In the previous sections we have mentioned the need for new alloys that are specially customized for AM. The focus of our study will be on designing austenitic materials owing to the excellent properties that can be associated with such alloys, like a high ductility and a high corrosion resistance. The approach will notably focus on austenitic stainless steels, but it is envisioned to widen the potential compositional range to that of materials presenting a face centered cubic (FCC) structure with contents of alloying elements that can be found in so-called "high entropy alloys". In this section, a short overview of austenitic materials such as stainless steels and high entropy alloys will be given, in addition to a review on their current use in AM.

1.2.1 Austenitic stainless steels

1.2.1.1 Definition and overview

Steels in general, and stainless steels (SS) in particular, are frequently the "standard" against which new emerging structural materials are compared. Indeed, the large family of steels remain one of the most successful materials. There exist many reasons for this dominance of steels; one of them may be attributed to the variety of microstructures that can be generated by solid-state transformations, leading to a wide range of properties [95], but their low cost –iron being the less expensive of all metals– also largely contributes to their success.

Stainless steels are generally defined as iron-based alloys with a minimum amount of chromium of approximately 11 wt.%, needed to give the alloy its "stainless behavior", or corrosion resistant characteristics. This is due to the formation of a passive film of chromium oxide. These alloys can be fabricated and formed in conventional ways, like casting, rolling, forging, extrusion, drawing, powder metallurgy techniques, etc. They can be further shaped by machining and they can as well be joined by different techniques such as welding, brazing, soldering and adhesive bonding [95].

Stainless steels can be divided into different families depending on their crystal structure(s), e.g. ferritic, martensitic, austenitic or duplex (austenitic plus ferritic). Some stainless steels can be precipitation-hardened by an appropriate heat treatment. These categories are dictated by the chemical composition of the alloy as well as the manufacturing process [96], [97]. Their properties largely depend on the composition of the alloy and on the heat treatment applied. Generally, stainless steels cover a very large range of mechanical properties, with a yield stress (YS) and ultimate tensile stress (UTS) which can vary between 200 and 1600 MPa, and between 400 and 1800 MPa, respectively. The elongation may reach and overcome tens of percent, but is generally lower for the most resistant grades.

Austenitic stainless steels (ASS) represent the largest stainless steel family in terms of the number of existing alloys (up to 70% of overall produced stainless steels). Austenitic steels are nonmagnetic, and they have an FCC crystal structure, similar to that of iron at high temperatures

(911-1392 ˚C). These alloys can possess excellent formability, ductility and toughness, even at cryogenic temperatures.

To represent the different grades of ASS, it is common practice to consider the AISI 304 grade as a starting composition. Figure 1.19 shows the evolution of several grades, seen as evolutions from the 304 in terms of alloying elements. The use of a grade or another depends on the targeted application. For applications where a high strength is required, grades 201 and 202 are generally used (increased Mn and N contents, and lowered Ni content). For increasing the pitting corrosion resistance, Mo is usually added (grades 316 and 317). To decrease the risk of intergranular corrosion, the limitation of carbon content (< 300 wt.% ppm) is a current solution, as in the L-series (316L, 304L, 317L, "L" standing for "low carbon").

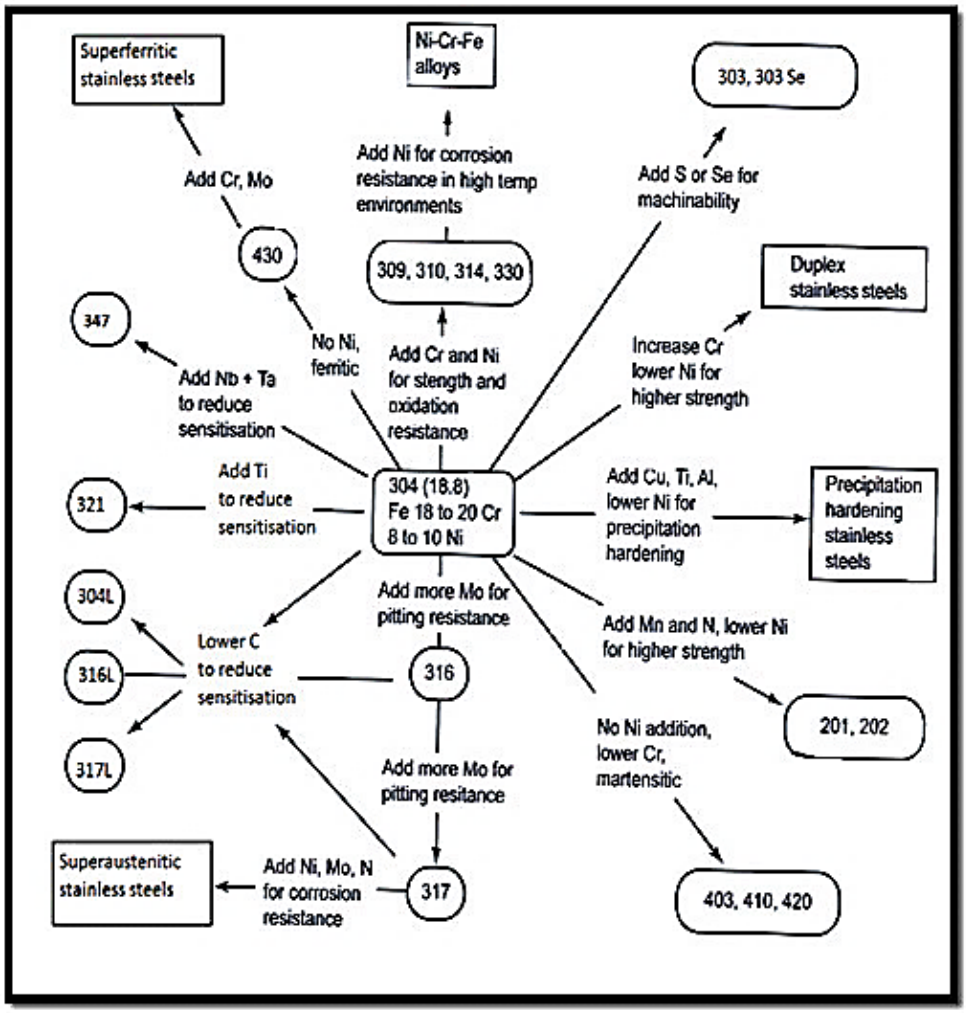

Figure 1.19 Map of different grades of stainless steels as a function of alloying elements, represented as evolutions from alloy 304 in the center [98]

1.2.1.2 Austenitic stainless steels in AM

The most intensively studied stainless steels in laser additive manufacturing techniques are so far the 304L and 316L grades. Both of these grades possess a good weldability, which benefits the processing by AM technologies. Generally, they develop a microstructure with a columnar dendritic primary structure and a cellular substructure [99]–[102]. Typically, a strong crystallographic and morphological texture aligned along the building direction is observed [103], [104]. The grain size of the materials produced by AM (10 - 50 µm) is usually finer than that of their cast equivalents (up to hundrends of µm) [24], [105], [106].

Consequently, the mechanical properties of ASS produced by AM are quite different from those produced by conventional manufacturing techniques. Table 1.3 shows different reported values of the tensile properties of 316L produced by SLM compared to conventional processes. As we can see, the UTS of 316L produced by SLM varies between 500 MPa [107] and 760 MPa [108], compared to 570 MPa for the wrought material [109]. Correspondingly, the elongation varies between 9.2% and 66.5% for the material built with SLM, compared to ~50% in wrought condition.

Table 1.3 Room temperature tensile characteristics of 316L grade produced by SLM, compared to the conventional material. YS stands for yield stress, UTS for ultimate tensile stress and A% for elongation to fracture. Horizontal and vertical refer to the building direction of the tensile sample.

Orientation	Heat treatment	YS (MPa)	UTS (MPa)	A(%)	Reference
Produced by SLM					
Horizontal	None	528	659	16.6	[110]
Vertical	None	444	567	8	[110]
Horizontal	None	580	684	36.3	[111]
Vertical	None	554	580	25.7	[111]
Horizontal	None	423	695	41	[112]
Vertical	None	397	564	35	[112]
Horizontal	None	557	591	42	[113]
Vertical	None	602	664	30	[113]
Horizontal	None	435	504	16	[107]
Vertical	None	438	528	10	[107]
Horizontal	None	500	620	46	[114]
Horizontal	None	490	685	51	[115]
Horizontal	None	650	760	30	[108]
Vertical	None	520	680	28	[108]
Conventional					
	annealed	170	485	40	ASTM A276
	annealed	241	586	50	[116]

1.2.2 High entropy alloys

1.2.2.1 Definition and overview

For thousands of years, the development of alloys was mainly based on one principal element, with an addition of alloying elements in limited concentrations. This was based on a general knowledge of metallurgy, derived mainly from empirical experience of mixing. Most often, high additions of elements in a given matrix made of a principal metal lead to the presence of secondary phases, which can be beneficial when just hardening effects occur, or harmful when their presence leads to a brittleness of the material. This latter phenomenon can be feared in the case of formation of many intermetallics [117].

In 2004, Yeh *et al.* [118] presented a new approach to design alloys with multiple principal elements in equimolar or near-equimolar concentrations. In the same year and almost in parallel, Cantor [119] presented a paper in which the central regions of multicomponent alloys phase spaces were investigated for the first time. The authors mainly focused on multicomponent transition metal alloys, and showed that some of them exhibit a surprisingly high degree of solid state solubility. Particularly, the equimolar CoCrFeMnNi alloy, which is now known as the Cantor alloy, was shown to solidify as a single FCC phase, stable over a large range of temperatures (down to about 600°C).

According to thermochemistry, for a phase transformation to occur spontaneously, the Gibbs free energy G of a system in the final state must be lower than that in the initial state, i.e. ΔG must be negative. The Gibbs free energy can be described according to Equation 1.4:

$$G = H - TS \qquad 1.4$$

where T is the absolute temperature, and S and H are the entropy and enthalpy of the system, respectively.

The entropic factor is, among others, made of the configurational entropy, S_{conf}. According to Boltzmann's hypothesis, the configurational entropy of a solid solution containing n elements ~~in~~ can be calculated as follows [120]:

$$S_{conf} = -R \sum_i X_i \, ln(X_i) \qquad 1.5$$

Where X_i is the mole fraction of element i and R is the gas constant (8.314 $J.mol^{-1}K^{-1}$).

Obviously, the relations 1.4 and 1.5 show that, unless the enthalpy of the system is positive and very large, alloys containing many elements in significant contents (ideally, equimolar) will yield to the formation of unique random solid solutions rather than mixtures of phases because of their high configurational entropy. This concept was the basis for the development of the so-called "high entropy alloys" (HEAs). The latter have first been described as those composed of five or more principal elements in equimolar ratios. The definition was then widened to a range of molar

fractions of all elements between 5 and 35 at.%, as it was shown that in such case the configurational entropy remains high enough to compensate a potentially high mixing enthalpy. An alternate definition classifies the alloys based on their configurational entropy values [121] into Low Entropy Alloys (LEAs) (S_{conf} < 0.69 R), Medium Entropy Alloys (MEAs) (0.69 R < S_{conf} < 1.61 R) and HEAs (S_{conf} > 1.61 R), where R is the gas constant. However, this simple criterion based on the number of alloying elements is not sufficient to predict single-phase, solid-solution formation in multi-element alloys. In fact Otto *et al.* [122] have shown that, in several five-element alloys, only one did not contain multiple intermetallic phases, suggesting that configurational entropy is not a useful predictor (at least not the only one) of which alloys can form simple solid solutions. In addition to configurational entropy, other entropic contributions such as vibrational, electronic, and magnetic entropy contributions must be taken into account [123], [124]. Another issue with this definition is that the initial analysis was performed at the melting point, whereas most alloy microstructures tend to be characterized at room temperature. And it is well known that the microstructures at room temperature and high temperatures can be different depending on several aspects, such as diffusion coefficients, phase transformation kinetics and cooling rates.

Since its discovery, a large number of papers published in this field presented single-phased HEAs [121], [125]–[135] and indicated that the formation of a solid solution is decided to a large extent by the proper choice of elements used for making the alloy. Several HEAs have been shown to present superior properties, such as a combination of high yield strength (thanks to the high lattice distortion of the multi-concentrated solid solution) and ductility [136], good microstructural stability and retained mechanical strength at elevated temperatures [137], [138], strong resistance to wear [139], fatigue [140], corrosion, and oxidation [141].

1.2.2.2 High entropy alloys in additive manufacturing

Many authors have studied the possibility of producing HEAs by AM processes. Their studies mainly focused on the effect of the process parameters on the microstructural and mechanical properties of parts produced by AM.

The CoCrFeNi alloy system has been the most studied overall. One of the earliest works on this alloy was performed by Brif *et al.* [86], where authors investigated the possibility of producing an equiatomic CoCrFeNi HEA by SLM, starting from a pre-alloyed gas-atomized powder. Their results were very promising, since a single FCC solid solution, exhibiting a homogeneous composition and very good mechanical properties with a UTS of 745 MPa and an elongation of around 30%, comparable to those obtained for industrial stainless steels, was obtained. Kuzminova *et al.* [142] investigated the $Cr_{21}Fe_{21}Co_{23}Ni_{35}$ MEA and showed that the obtained yield stress of the as-built material (YS about 590 MPa) is almost twice that of its traditionally prepared equivalent, such as hot rolled (YS about 300 MPa) [143]. The authors also investigated the effect of the laser energy density (VED) on porosity formation. An almost perfectly dense

material, with a value of porosity as low as 0.09% was obtained for a VED of 250 J/mm^3. Yet, the quality of built parts seemed to be strongly depending on VED: a porosity of 1% was measured for a VED of 100 J/mm^3, reaching 12% for a VED of 1500 J/mm^3.

Zhou *et al.* [144] investigated the $C_{0.05}$CoCrFeNi HEA elaborated by SLM with the aim of further enhancing mechanical properties. The alloy was successfully produced and a complete dissolution of carbon in the material was achieved: phase analysis showed a single FCC phase. The authors measured promising mechanical properties, with a yield stress of 656 MPa and an UTS of 797 MPa. The obtained microstructure varied with the processing parameters, but overall was typical of materials produced by SLM, with columnar grains having an average size of 40-50 μm. Similarly to previously discussed studies, authors have also shown that the density of the produced specimens is greatly influenced by the choice of the processing parameters.

The addition of other alloying elements to the CoCrFeNi system was also studied. For example, Fujieda *et al.* [145] studied the fabrication of $Co_{1.5}CrFeNi_{1.5}Ti_{0.5}Mo_{0.1}$ HEA by SLM, and reported a density of around 99.3% and excellent mechanical properties of as-built parts, with a tensile strength reaching 1170 MPa with an elongation around 25%. The authors attributed this strength to the fine crystal grains which is often a characteristic of materials produced by AM. However, these results were the outcome of an optimization of quite a wide range of processing parameters: laser power (160–270 W), laser scanning speed (540–1350 mm/s), and hatch spacing (80–120 μm), resulting in optimal values for an energy density of 61.5 J/mm^3.

Although much rarer, the CoCrFeMnNi alloy system was studied in AM as well. Li *et al.* [146] succeeded to print the Cantor alloy with SLM, with a relatively high density of 98.2% and a UTS of 601 MPa (VED = 74 J/mm^3), but more detailed observations revealed the presence of microcracks and micropores. Their results showed that all produced samples present a single FCC phase, like the powder. Figure 1.20 shows the chemical analysis done by the authors where a homogeneous distribution of Co, Cr, Fe, and Ni elements can be seen while Mn seems to segregate slightly at the boundaries between weld passes.

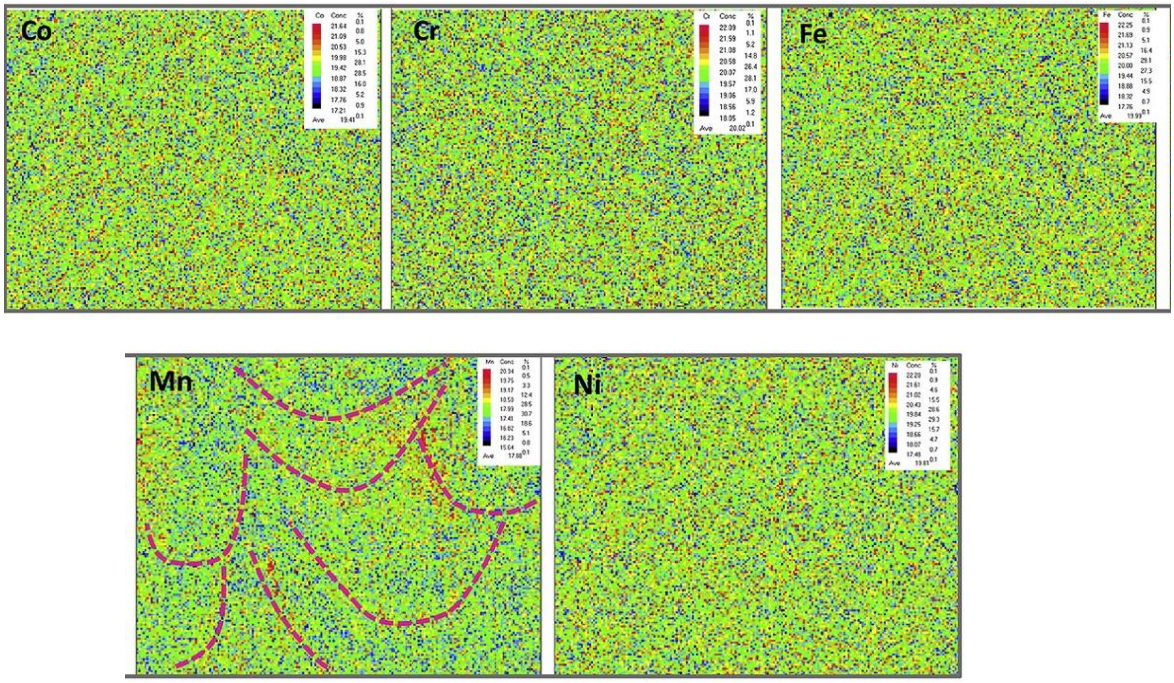

Figure 1.20 Electron Probe Microanalyzer element maps of CoCrFeMnNi fabricated with SLM with the observation plane parallel to the building direction [146]

In summary, it seems that additive manufacturing methods is a promising way to process austenitic HEAs. The combination of the high solid solution strengthening from the HEA (due to the high lattice distortion) and the small grain size from the AM rapid solidification results in interestingly high mechanical properties. As an illustration, Figure 1.21 shows the variation of the yield strength and elongation of several HEA alloy systems produced by different AM techniques compared to several conventional alloys, and overall, it is encouraging to see that higher levels of strength can be achieved without a significant loss of elongation to fracture. These preliminary results encourage the exploration of similar alloy systems by AM.

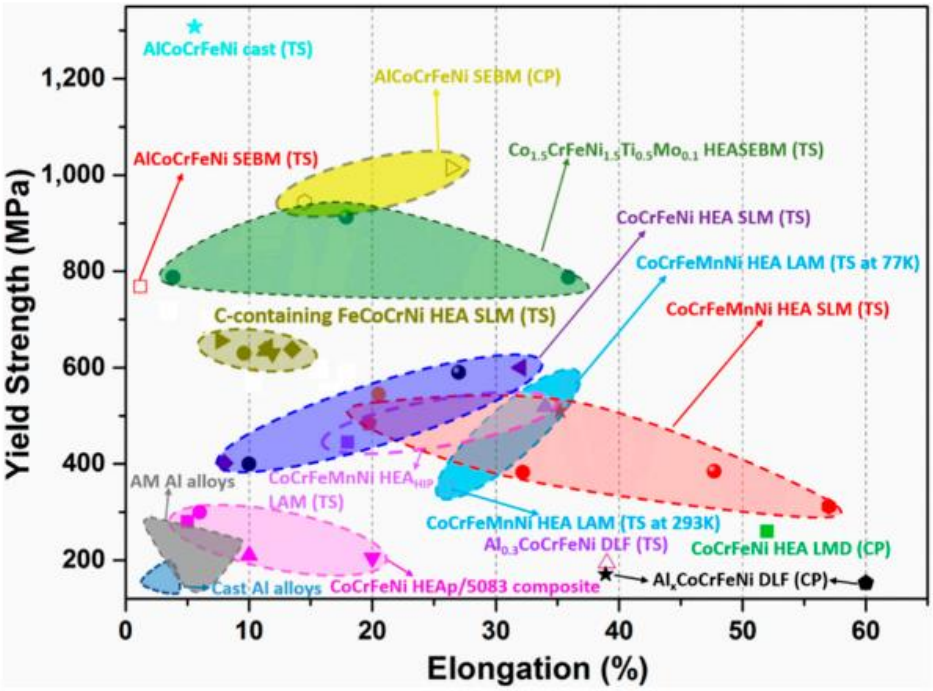

Figure 1.21 Yield strength vs. elongation for various HEAs using various AM methods where TS is tensile and CP is compression [147]

1.3 Alloy design for additive manufacturing

Over the course of the first twenty years in metal AM developments, the materials aspect has been mainly concurred by deploying conventional materials using these processes [148]. Currently, the AM market dynamics pushes researchers into focusing on highly performant components, made with alloys that are known to be adapted to the specific application. This explains why the majority of literature focuses on the exploration of currently existing alloys, which can present promising results when produced with AM processes, for instance 304L and 316L for the stainless steels family, AlSi10Mg and AlSi12 for Al-based alloys, Ti-6Al-4V for Ti-based alloys, In 718 for Ni-based alloys, among others. Nevertheless, several works have been undertaken in order to propose new compositions which are better adapted to the AM processes.

Thapliyal *et al.* [149] proposed a new Al-Ni-Ti-Zr alloy which exhibited a good printability and good as-built tensile properties (YS of 266 MPa) but a rather limited elongation of 17%. The authors have shown that the alloy produces crack-free parts over a wide range of processing parameters, compared to conventional Al alloys which are known to be highly susceptible to hot cracking. The authors based their design strategy on the addition of transition metals which would form metastable $L1_2$ tri-aluminides precipitates (Al_3X-based; X being Sc or Zr), acting as sites for heterogeneous nucleation, thus forming fine equiaxed grains which decrease the cracking

susceptibility. The content of the added elements, as the authors explain, was limited by their effect on the solidification range of the alloy. While this led to good results, the approach focused mainly on the control of the cracking susceptibility of the alloy, but did not include other detrimental defects, such as porosity or surface quality.

Recently, Ackers *et al.* [150] proposed a novel design approach to design titanium alloys. The authors used thermodynamic calculations to determine the equilibrium structure of the alloy over a range of temperatures. To avoid hot cracking, the authors set a constraint on the solidification range of the material (between 50 and 300 K). The surface tension of the alloys was also a criterion in the proposed approach. For the latter, the authors used equations and values specific for commercial alloys to estimate it, and alloys having surface tension values in the range of 1.5 - 1.7 mN/m were disregarded to lessen balling effects. The authors included a specific experimental step up to test several possible interesting compositions to be built with PBF, and retained the specific process conditions associated with them. Despite taking into account surface defects in addition to phase structure and cracking susceptibility, similar to [149] the authors did not include considerations of pore formation.

Assessment of the printability of stainless steels have also been studied in literature. Shortly after the start of our work, Sabzi *et al.* [151], [152] proposed a defect prevention method by combining material-dependent properties, such as the solidification range of the alloy for controlling cracking, the thermal expansion for controlling the level of residual stresses, solid solution hardening for ensuring strength and process parameters to control the keyholing effect. The authors validated their results on 316L and showed good agreement with the model. They also showed an improved printability compared to other versions of the alloy, which usually contain defects. Nevertheless, the applicability of their method was limited to a range which is close to the nominal composition of 316L, rather than a wider exploration of largely different compositions.

The presented works show very promising results. However, there remains a need for a method that focuses specifically on the material composition, and that simultaneously takes into account a large number of material-depending phenomena and characteristics at the origin of defects currently observed in AM parts. One could mention mechanisms of porosity formation, selective evaporation and loss of elements, etc...

1.4 Motivation and objectives

The field of additive manufacturing is constantly evolving. The processes of additive manufacturing have gained interest in many engineering domains and there is currently a need to develop more alloys that are adapted to such processes. Indeed, we have shown that most of the alloys that are currently built with AM processes were initially developed to give optimal results for different processing techniques. Despite the interesting results obtained with such alloys in AM, their fabrication requires an optimization of a large set of parameters over wide ranges. Additionally, it remains difficult to fabricate defect-free components without compromising between different aspects such as the mechanical performance of the alloy, its surface quality, etc. As briefly mentioned, the response to processing, as well as the quality and properties of additively manufactured materials, depend on alloy composition. Hence, ensuring process robustness through a widening of processing windows, minimizing defects, maximizing surface quality, as well as obtaining good mechanical properties, should be addressed by designing new alloy compositions that are tailored for AM processes.

In recent years, several authors presented successful approaches to design new compositions based on the combination of various computational tools. This includes the use of computational thermodynamics for predicting phases [153] and other physical models for predicting material properties [154]–[157]. However, depending on the targeted property, physical models might not always be available. In such case, the use of machine learning algorithms to build and train models from existing data became widely used [158]–[168]. Computational thermodynamics and different property predictive models combined with an optimization algorithm were used to accelerate material discovery and alloy design [169]–[176].

The aim of this work is to rely on such alloy design approach to find new austenitic alloys that are optimized for the process of additive manufacturing. Due to the continuity in composition that exists between austenitic stainless steels and FCC HEAs, we primarily focus on the design of steels, yet a larger compositional space is allowed. Thus, the possibility to end up with, if not proper HEAs, rather “multi-concentrated steels or alloys” is envisaged. The design method will focus solely on material-dependent criteria. The latter will be discussed and the associated predictive tools will be presented as well. Finally, the models will be validated with an experimental evaluation: an alloy with a composition selected from within the obtained optimized set of alloys will be elaborated and tested regarding its microstructure and principal characteristics, in link with our alloy design criteria.

This manuscript is structured in six chapters, completed by a general conclusion and several appendices, which bring supplementary elements and results obtained in this work.
The present Chapter 1 (“State of the art”) has presented an overview of AM processes and has focused on defining the defects currently observed in parts produced by AM and analyzing their causes. The most commonly used austenitic alloys in AM have been reviewed as well. A thorough analysis of the physical phenomena behind such defects will be discussed in Chapter 4, which will

allow to define a set of material-dependent criteria and requirements for AM-specific alloy design. Depending on the criteria, appropriate prediction tools will also be defined. All the numerical tools and experimental methods used will be described in Chapter 2 (“Numerical methods”) and Chapter 3 (“Experimental procedures and methods”) respectively. In Chapter 4 (“Phenomena considered for alloy design and associated criteria”), design criteria will be translated into a set of objectives to be either minimized or maximized –depending on the characteristics looked for– and of certain constraints to be respected. Then, these objectives and constraints will be used in the framework of a multi-objective optimization approach, meaning that the best possible compromises between targeted characteristics will be looked for, while ensuring that all designed alloys meet the requirements that have been set. A numerical optimization tool –a genetic algorithm– will be used to accomplish such a task. The employment of this algorithm and an analysis of the obtained results followed by the selection of one composition will be presented in Chapter 5 (“Multi-objective optimization and selection of alloy for experimental validation”).

Finally, the results of experimental validation of the model will be presented and discussed in Chapter 6 (“Experimental evaluation of the selected alloy”). The selected alloy will be fabricated and characterized in different states: as-cast, in powder form and produced by selective laser melting. The microstructural, mechanical, surface and thermal properties of the alloy will be evaluated and compared to existing data for other austenitic alloys such as 316L, 304 and the CoCrFeMnNi Cantor alloy.

2 Numerical methods

The design method used in our approach is based on the combination of several numerical tools as previously stated. This chapter describes them, including computational thermodynamics, machine learning, multi-objective optimization as well as multi-criteria decision analysis.

2.1 Computational thermodynamics

The thermodynamic equilibrium of a chemical system corresponds to the lowest value of its Gibbs free energy. Therefore, to efficiently make use of thermodynamics for multicomponent systems, it was necessary to develop analytical mathematical descriptions of Gibbs energy as a function of its variables. The most famous and commonly used modeling approach in thermodynamics is the CALPHAD method, which stands for CALculation of PHAse Diagrams, first led by Kaufman [177].

This method can provide a reliable estimate for the majority of relevant thermodynamic properties required for the description of the phases forming in materials and their stability. It allows to estimate properties like the enthalpy, entropy and therefore Gibbs free energy of all the potential phases as well as their chemical potential or activity [178]–[182].

Using CALPHAD, and by specifying the material composition as well as temperature and pressure, it is possible to calculate or estimate the type, composition and fraction of phases at equilibrium, provided that the Gibbs energy of all phases can be expressed as a function of composition and conditions, and that an algorithm is able to find what repartition of elements in potential phases leads to the lowest possible value of the Gibbs free energy of the system.

The evaluation of the model parameters is carried out in a hierarchical structure successively from those of pure elements, binary interaction parameters to ternary and multicomponent interaction parameters. Interactions of higher order than three can usually be neglected, so that CALPHAD can in principle work from descriptions of unary, binary and ternary data only. Parameters are stored in databases that can be specific to different categories of alloys, depending on the list of elements and potential phases they can form, i.e. there are thermodynamic databases specialized in steels, or in nickel alloys, etc. Such databases are then exploited by CALPHAD software to determine phase equilibria through the numerical minimization of G. The main computational tools or commercially available software and databases for industrially important materials are reported and available in [183] [184]–[186]. There are also recent developments of open source codes and softwares, such as OpenCalphad [187], [188], PyCalphad [189], and Thermochimica [190].

In our study, we used the Thermo-Calc software and its associated Python programming interface; TC-Python. The latter is a Python language-based software development kit (SDK) available along with Thermo-Calc. It allows the coupling of Thermo-Calc with other software programs.

Thermo-Calc includes several databases which are constantly under development and improvement. In this work, we have decided to explore mainly iron-rich alloys; indeed, as will be seen later, even the widening of our allowable composition domain towards HEAs will lead to alloys in which iron has the highest concentration. In this respect, all considered alloys will lie within the compositional ranges covered by the iron-based alloys database TCFE10. The latter contains thermodynamic descriptions for 29 elements and 308 binary, 269 ternary, and 77 quaternary systems. It also includes several quinary systems.

Thermo-Calc allows to perform equilibrium calculations (e.g. to predict the nature and composition of phases in a given alloy at a certain temperature), which can also be used to simulate solidification paths according to Scheil-Gulliver (or just "Scheil") assumptions. This model states that, during solidification of an alloy, (i) the liquid is always homogeneous due to fast diffusion and convection, (ii) solid state diffusion is negligible so that, once a solid phase has been formed, it keeps its composition until the end of solidification, and (iii) the liquid-solid interface is always at thermodynamic equilibrium. Scheil calculations are implemented in Thermo-Calc using a simple algorithm: temperature is initialized to a high enough value so that the alloy is completely liquid, and temperature is then reduced by small steps. At each step, an equilibrium is calculated, the solid phases are stored apart and the next step is calculated for a material that would have the composition of the remaining liquid. This is repeated until there is no more liquid.

By default, a Scheil calculation allows to calculate:

- The solidification range of an alloy
- Phases formed during solidification and their associated fractions and compositions

The CALPHAD method can nowadays be thought of as an essential tool for the discovery of new materials. It has shown great potential to design different types of multi-component alloys. Tancret [172] used CALPHAD aided alloy design to optimize Ni-base superalloys. Xu *et al.* [174] used CALPHAD to design ultra-high strength (UHS) stainless steels combining criteria based on thermodynamic, thermokinetic and mechanical principles. Examples of the design of high-performance aluminum alloys using CALPHAD has also been reported [191]–[194], as well as magnesium alloys [195], high entropy alloys (HEAs) [169], [175], [196]–[204], and Co-base superalloys [205].

2.2 Machine learning meta-models

Over the course of years, the physical modelling of material properties has made a huge progress. Nevertheless, physically modelling properties which could depend on numerous factors such as the material composition, microstructure, heat treatments, etc., can easily become very complicated and require the fitting of a significant number of parameters for functions that, in addition, would probably not be valid over the whole range of conditions. Hence, less complicated approaches were needed to model such nonlinear correlations. Fortunately, for many properties large databases of existing experimental measurements are already present in literature. The availability of such data makes it possible to utilize data-driven machine learning algorithms, which can model in a naïve way the correlation between input and output values. The fitted function can be non-linear, can adapt to complex input-output relations in a very flexible manner without any prior knowledge, and can take interactions between inputs into account. Once trained, or learnt, from data, the model can predict the output for a new set of inputs. In our case, this would mean predicting the modelled property of an alloy that has a new composition. The most popular tools for such data mining are artificial neural networks, but many others exist, like Gaussian processes, genetic programming, support vector machines, etc.

Several works on the use of Machine Learning (ML) approaches in the field of alloy design exist. Attempts to approach the problem of acquiring knowledge by machine using various methods date back to the 1950s, and the earliest works on integrating such methods in the field of materials science began in the late 1990s [206]–[208]. With time, ML algorithms evolved in complexity and became more and more present in this domain. More recently, Shen *et al.* [162] worked on finding a relation between composition, processing parameters, working conditions and mechanical properties of maraging steels using a ML model. Xiong *et al.* [159] used a ML algorithm to develop a model describing the glass-forming ability and elastic moduli of bulk metallic glasses. Möller *et al.* [161] showed that it is possible to use a ML model to develop hard magnetic materials. Other authors used a combination of various ML algorithms to simultaneously optimize several material properties, such as the work of Zhang *et al.* [163] on the design of ultrahigh-strength high entropy alloys. Similarly, Wang *et al.* [165] incorporated a set of ML algorithms to develop iron based soft magnetic materials. Khatavkar *et al.* [166] employed ML models for Co- and Ni-based superalloys development. Other authors combined ML prediction models with ML clustering algorithms, such as the work of Wen *et al.* [200] to produce HEAs with higher degrees of hardness. These are just a few examples, as there are now hundreds or thousands of papers on the use of ML to model the properties of materials.

In this work, we use a particular ML tool, Gaussian process regression [169], [209] (GPR, also known as Kriging, Gaussian spatial modeling, Gaussian stochastic process). It is a method that can be used to model a complex relationship between an output and several inputs that cannot reasonably be approached by a simple linear model. GPR has a statistical nature that gives it an

advantage over other non-statistical machine learning methods in that, in addition to predicting a mean value, it also provides a variance, or an error estimate, for predictions.

Details of the mathematical description of this method can be found in Appendix C.

Generally, when ML algorithms are constructed, they learn from a specific provided dataset. If sufficient care is not taken, the model can learn all the noise and irrelevant information as well as the actual trends contained in the data. This could cause "overfitting", i.e. the model fits too closely to learnt data but is unable to perform well when subjected to new unseen data. To avoid this, several methods of estimating the overall performance of a ML algorithm exist. One of the most commonly used methods is the K-fold cross validation, which is detailed below.

2.2.1 K-fold cross validation

The principle behind K-fold cross validation is shown in Figure 2.1. The dataset is divided into K folds, and each time the model is trained on K-1 folds and tested on the remaining fold. By calculating the accuracy of predictions on testing sets, it is possible to have an idea on the predictability of the model as well as discovering the weak points at which it fails (indicators of precision will be presented later). After training the model K times and calculating the corresponding prediction accuracy, the average of the latter serves as an indication on the global performance of the model. The predicted values should also be recorded for a better visualization of the prediction compared to the real values. The KFold package from the Scikit-learn Python module was used [210].

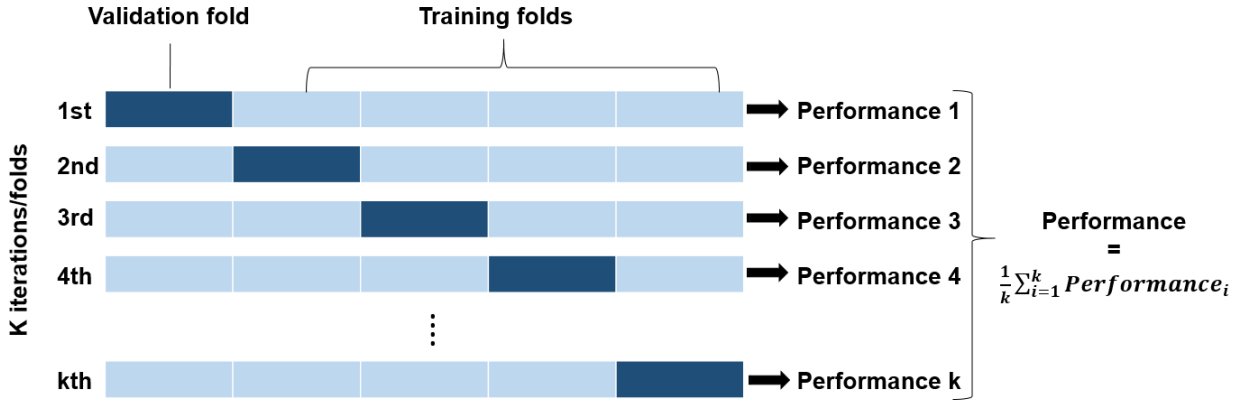

Figure 2.1 Schematic of a K-fold cross validation process

2.2.2 Evaluation metrics

The most commonly metrics used for evaluating the quality of regression machine learning algorithms are the Mean Squared Error (MSE), the Root Mean Squared Error (RMSE), the Mean Absolute Error (MAE) and R^2 (or "R-squared"), defined as follows:

- Mean Squared Error (MSE):

$$MSE = \frac{1}{n}\sum_i (y - \hat{y})^2$$

- Root Mean Squared Error (RMSE): which is the square root of the MSE
- Mean Absolute Error:

$$MAE = \frac{1}{n}\sum_i |y - \hat{y}|$$

- R-squared (R^2):

$$R^2 = 1 - \frac{\sum_i (y - \bar{y})^2}{\sum_i (y - \hat{y})^2}$$

where y is the actual experimental value, $\bar{y}$ is the corresponding mean value and $\hat{y}$ is the predicted one, while i denotes the i^{th} data point among n. The model parameters are adjusted to obtain a large R^2, a small MSE, a small RMSE and a small MAE.

2.3 Multi-objective genetic algorithm (MOGA) for optimization

2.3.1 Multi-objective approach

Engineering problems usually require the optimization of a set of objectives simultaneously, which can sometimes be antagonist and/or interdependent. In alloy design, one would for instance want to optimize simultaneously strength, ductility, corrosion resistance and cost. When such a task is associated to a large space of input variables –which could be, in alloy design, compositional variables–, a manual search approach would be extremely tedious and, in many cases, inefficient. Therefore, it is common practice to consider numerical methods and algorithms to find the best set of solutions, often referred to as Pareto-optimal solutions. For example, Figure 2.2 shows a problem with two objectives (f1 and f2) to be minimized, with solutions illustrated as squares. One can see that in such problems, there is not usually a single optimal solution, but rather a set of solutions for which none is better than the other, and the choice includes a tradeoff between objectives that is user-dependent. The solutions belonging to the "Pareto front", shown as a red line in Figure 2.2, are said to be non-dominated, since no solution would be better than others on

both objectives. Reciprocally, all solutions not belonging to that front are called dominated ones, since, in all cases, a better solution can be found. For instance, for point C on the Figure 2.2, both points A and B would be better on both objectives.

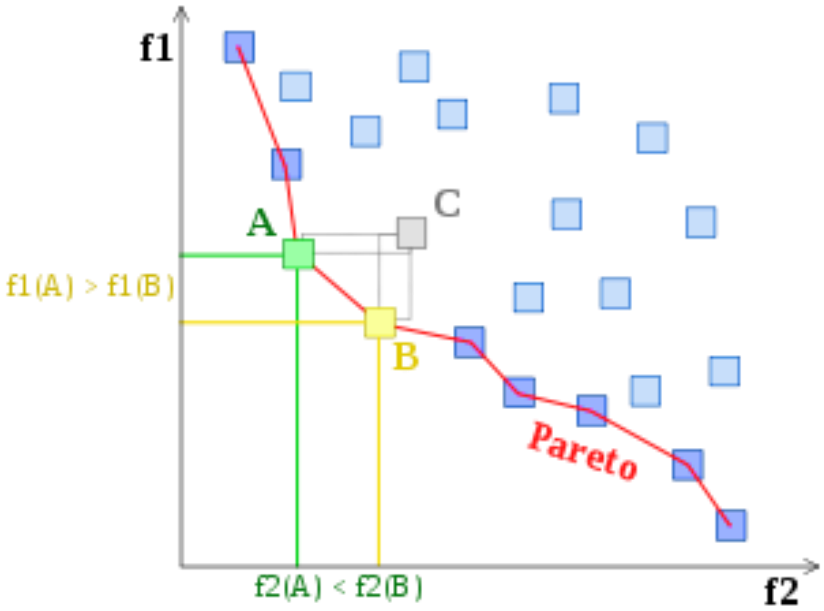

Figure 2.2 Schematic showing the Pareto front of two objectives to be minimized, as well as the concepts of dominated (C) and non-dominated (A and B) solutions

In multi-objective problems, the Pareto front is no longer a line, but a surface for three objectives and even a hypersurface for a higher number of objectives. This explains the need for numerical methods to solve such problems. Among these methods, evolutionary optimization algorithms have been widely used because they have been shown to be able to generate a set of solutions allowing an approximation of the Pareto front, even for complex relations between inputs and outputs.

These algorithms, as their name implies, rely on the concept of evolution of a population of individuals, which are described by a set of genes. To explain this in terms of a metallurgical problem, the different individuals would be different alloys, and the genes would be their compositions. Before starting the algorithm, a group, of typically tens or hundreds of individuals, is created, with random genes; in our case these would be alloys with random compositions. The process then includes an evaluation of the individuals (alloys), based on a set of defined objectives and constraints. In our case, the objectives are material properties which we wish to either minimize or maximize. On the other hand, constraints can be numerical or categorical values, used to define the “acceptability”, or “feasibility” of the alloy. They can be in the form of equalities or inequalities; ex: material property X must be greater than, less than, or equal to a certain value, or

belong to a certain range, etc. Based on the results of evaluation, individuals are sorted, or "ranked" according to their feasibility (constraints) and optimality (objectives). The least interesting individuals are then discarded, whereas the best ones are kept and used to generate new individuals by mathematical operations called mutation (some randomly picked genes of randomly selected individuals are randomly altered) and reproduction, or crossover, consisting in mixing randomly the genes of pairs of individuals (called "parents") to produce new individuals called "offsprings" or "children", a given child possessing half of the genes of its parents. The so-obtained new population, called a generation, is then evaluated again, and the process is repeated iteratively, generation after generation. This provokes an evolution of the population towards individuals having a better performance with respect to objectives and constraints, i.e. towards the Pareto front. A number of studies used GA for the development and optimization of steels. One of the earliest works on alloy design using GA dates back to early 2000s, where Mahfouf *et al.* [211] used a combination of ML models and GA to optimize the chemical composition and heat treatment conditions of steels, as to obtain better mechanical properties such as UTS and A%. Similar work was previously done by Tenner [212] where the author presented an "automated" alloy design of steel based on ML and GA to optimize compositions, for the purpose of increasing UTS, proof stress, impact energy and elongation.

Das *el al.* [213] used ML to develop a relationship between mechanical properties of steel such as YS, UTS and elongation with the composition and rolling process parameters. The author then proposed a GA optimization of the tensile properties of thermomechanically processed high strength low alloy (HSLA) steel plates. Reddy *et al.* [214] proposed a method to design medium carbon steels based on the combination of ML and GA to optimize composition and heat treatment parameters for the desired mechanical properties. Joo *et al.* [215] combined a ML model with a genetic algorithm to find domains of input parameters (composition and hot-rolling process parameters) which correspond to different target properties (UTS, tensile elongation..). Xu *et al.* [216] presented a computational alloy design approach for precipitation-hardened Ultra High Strength (UHS) stainless steels. The authors worked on optimizing alloy compositions as well as some key heat treatment parameters to obtain desired microstructures. Chatterjee *et al.* [217] used a combination of ML models and GA to design a TRIP assisted steel in which the silicon concentration is kept low. Lu *et al.* [218] worked on improving the creep strength and maintaining a low activation under irradiation, using a high-throughput computational alloy design model coupling thermodynamics, precipitate-coarsening kinetics and GA.

There exist also several studies with a focus on Ni-based superalloys. Tancret [153] combined CALPHAD calculations with GA to design creep-resistant and affordable superalloys. Similarly, Menou *et al.* [171] presented an alloy design method based on a multi-objective genetic algorithm combined with CALPHAD and ML-prediction models to design affordable nickel-based superalloys.

Examples of GA for the design of other types of materials exist as well, such as HEAs [169], [170], Ti-based alloys [219], [220] and Al-based alloys [221].

Many GAs exist, with different ways of mathematically defining and parametrizing them. In our study, we used the Non-Sorting Genetic Algorithm II (NSGA-II), which is one of the most popular genetic algorithms used for solving multi-objective problems. The pymoo: Multi-objective Optimization in Python was used [222]. Detailed explanation of this method can be found in Appendix A.

2.3.2 Multi-criteria decision analysis: the PROMETHEE approach

Multi-objective optimization will result in a set of Pareto-optimal solutions. Without any preference from the user, none of these solutions can be classified as "better" than another since they are non-dominated, i.e. each one of them is better than all others on at least one objective.

Nevertheless, there exists several methods to guide the user to select a specific solution. This selection will be user-dependent, as it requires the manual setting of several parameters, representing the user preferences [223]. One of the these methods is the Preference Ranking Organization Method for Enrichment Evaluation (PROMETHEE) method [224] which will be further explained in this section.

Let us consider A: a finite set of n possible alternatives (or solutions; in our case alloys) $\{a_1, a_2, \ldots, a_i, \ldots, a_n\}$ and $\{g_1(.), g_2(.), \ldots, g_j(.), \ldots, g_k(.)\}$ a set of evaluation criteria (or objectives; in our case material properties), as shown in Table 2.1.

The studied criteria can be set to be maximized or minimized, and the decision-maker is expected to find a solution that best fulfill the requested criteria.

Table 2.1 Evaluation table for multi-criteria problems

a	**$g_1(.)$**	**$g_2(.)$**	**…**	**$g_j(.)$**	**…**	**$g_k(.)$**
a_1	$g_1(a_1)$	$g_2(a_1)$	…	$g_i(a_1)$	…	$g_k(a_1)$
a_2	$g_1(a_2)$	$g_2(a_2)$	…	$g_i(a_2)$	…	$g_k(a_2)$
⋮	⋮	⋮	⋮	⋮	⋮	⋮
a_i	$g_1(a_i)$	$g_2(a_i)$	…	$g_i(a_i)$	…	$g_k(a_i)$
⋮	⋮	⋮	⋮	⋮	⋮	⋮
a_n	$g_1(a_n)$	$g_2(a_n)$	…	$g_i(a_n)$	…	$g_k(a_n)$

To apply the PROMETHEE method, two types of information should be taken into consideration:

- Information between the criteria, i.e. defining the relative importance of criteria
- Information within each criterion, i.e. determining the link between the calculated objective and the level of satisfaction it brings to the user

(a) Between the criteria

Providing information between criteria means setting a relative importance for each criterion by assigning a non-negative weight for each one (see Table 2.2) with the sum of the weights being 1. This weight should be independent from the measuring unit. The higher the weight, the more important is the criterion, and the higher its effect on the decision-making, which will be explained later.

Table 2.2 weights of relative importance between criteria

$g_1(.)$	$g_2(.)$	…	$g_j(.)$	…	$g_k(.)$
w_1	w_2	…	w_i	…	w_k

(b) Within each criterion

The PROMETHEE preference structure is based on pairwise comparisons. Let us consider two solutions a and b, and their associated objective function values for the criterion $g_i(.)$: $g_i(a)$ and $g_i(b)$. In this case, the difference between the evaluations of two alternatives on this particular criterion is:

$$d_j(a,b) = g_j(a) - g_j(b)$$

For a small difference it is possible to set a small preference to the best alternative or no preference if the decision-maker considers that this difference is negligible. But in general, the larger the difference, the larger the preference. In fact, this preference can be quantified in a function F varying between 0 and 1 with respect to the difference d_i. This implies that for each criterion, the decision-maker has a function:

$$P_j(a,b) = F_j[d_i(a,b)] \quad \forall\, a,b \in A$$

If we consider that the criterion is set to be maximized, the defined function will give preference of a over b for a positive deviation above a threshold value d, as illustrated in Figure 2.3.

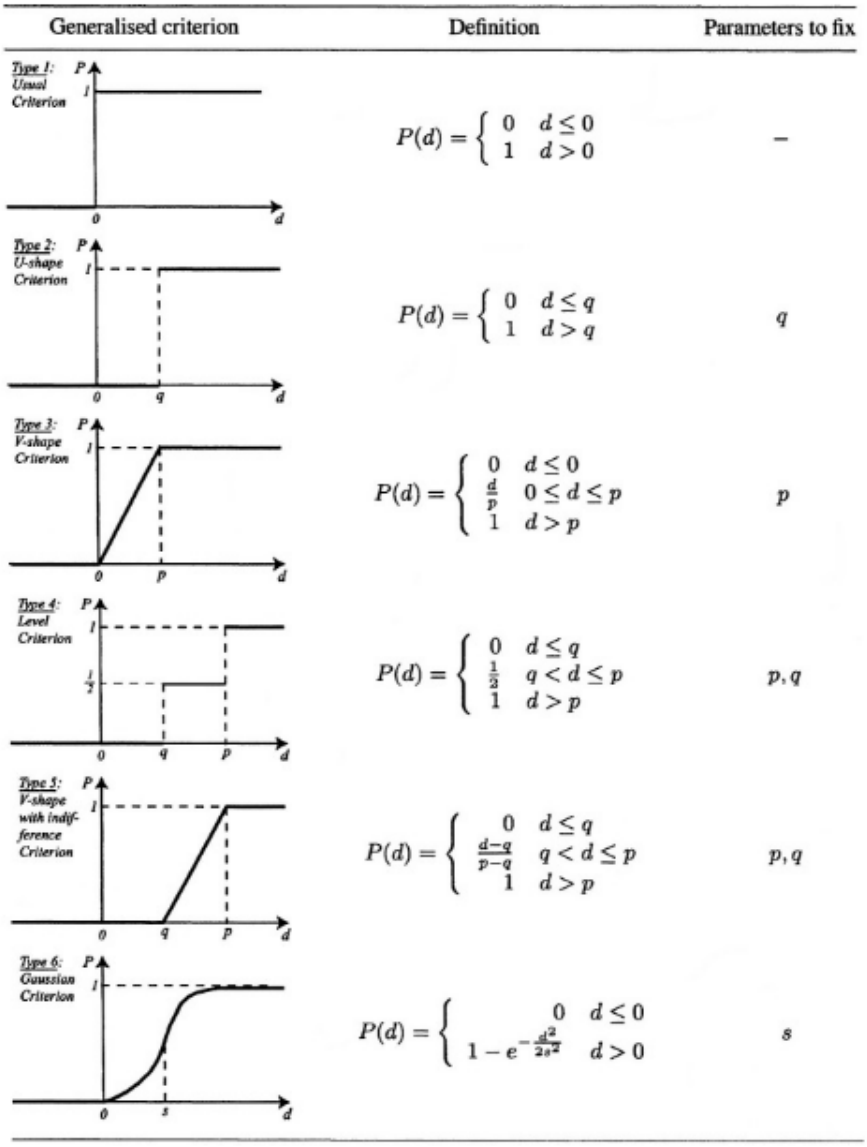

Figure 2.3 Types of preference functions [224]

There exist several types of preference functions (see Figure 2.3), and a typical choice is usually a V-shape preference function with an indifference criterion enlarged in Figure 2.4. The use of this function allows to say that for the considered criterion, between two solutions a and b, if the difference between the evaluations of the two criteria is below a threshold value *q*, no preference is made (*q* is thus called the indifference threshold). For instance, it makes sense that if $d_j(a,b)$ is below the prediction accuracy of the function $g_j(.)$, this difference is neglected, hence *q* should be of the order of the predictive uncertainty. If the difference is between this lower threshold *q* and an upper threshold *p* (called the strict preference threshold), the preference is assigned a value between 0 and 1 that grows linearly with *d*. Finally, if the difference is above the threshold *p*,

solution a is given a preference value of 1 over solution b. Setting the values of q and p can be useful depending on the studied function.

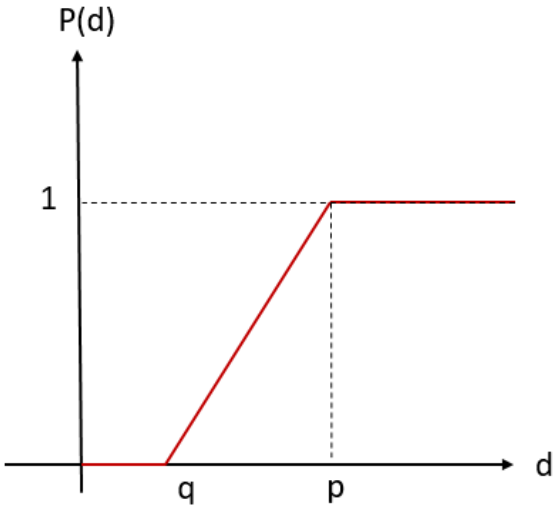

$$P(d) = \begin{cases} 0 \; if \; d \leq q \\ \dfrac{d-q}{p-q} \; if \; q < d \leq p \\ 1 \; if \; d > p \end{cases}$$

Figure 2.4 Example of a V-shape preference function with indifference criterion

Once the evaluation table (Table 2.1) is given, and the weights and the generalized criteria are defined, the PROMETHEE procedure can be applied. To do that, two values must be defined: the aggregated preference indices and outranking flows.

2.3.2.1 The aggregated preference

The above approach allows to quantify how much a solution is considered superior to another, on a given criterion or objective. It is now necessary to quantify how better a solution is over another, considering all criteria simultaneously, which is called the aggregated preference. For every two solutions a and b belonging to the set of solutions A, the aggregated preference indices are defined such that:

$$\pi(a,b) = \sum_{j=1}^{k} P_j(a,b) w_j$$

$$\pi(b,a) = \sum_{j=1}^{k} P_j(b,a) w_j$$

$\pi(a,b)$ and $\pi(b,a)$ are expressing to which degree a is preferred over b and b is preferred over a respectively, considering simultaneously all objectives j from 1 to k. Because of the nature of

multi-criteria problems, there will always be criteria for which a is preferred over b, and vise-versa. The following rules can be admitted:

$$\pi(a,a) = 0$$

$$0 \leq \pi(a,b) + \pi(b,a) \leq 1$$

The closer $\pi(a,b)$ is to zero, the weaker the global preference of a is over b. And the closer it is to one, the higher the preference is. These two values must be calculated for each pair of solutions within the whole set of solutions.

2.3.2.2 Outranking flows

The above-defined aggregated preferences allow comparisons between pairs of solutions, but do not provide a global view, or ranking, of all solutions. This can be made by calculating so-called outranking flows. For every solution a, competing against (n-1) other solutions, two quantities should be calculated:

a) The positive outranking flow:

$$\emptyset^{+}(a) = \frac{1}{n-1} \sum_{x \in A} \pi(a,x)$$

This expresses how "powerful" solution a is compared to all others.

b) The negative outranking flow:

$$\emptyset^{-}(a) = \frac{1}{n-1} \sum_{x \in A} \pi(x,a)$$

This expresses how "weak" solution a is compared to all others.

Now that these two values are calculated for each individual in the solution set, the actual ranking of solutions can be done.

2.3.2.3 PROMETHEE II complete ranking

There are several ways of exploiting outranking flows to produce an overall ranking of solutions. The one chosen here, that has proved its efficiency in a number of situations, is called PROMETHEE II. For that, a net outranking flow should be considered:

$$\emptyset(a) = \emptyset^{+}(a) - \emptyset^{-}(a)$$

Using this value, a direct comparison between all solutions can be done. Therefore, a is preferred over b if $\emptyset(a) > \emptyset(b)$. If $\emptyset(a) = \emptyset(b)$, then a and b are indifferent.

With this complete ranking, all solutions become comparable.

Although the PROMETHEE method has been used to solve multi-criteria problems in materials science, most of the existing literature focuses on the ranking of already existing —or industrial— alloys. Maity & Chakraborty [225] used PROMETHEE to classify ten existing tool steels based on a set of criteria representing their performance such as cost, hardness, resilience, Young's modulus, thermal conductivity, abrasion resistance and machinability. Chatterjee & Chakraborty [226] compared the PROMETHEE method with three other decision making tools for a problem of selecting existing gear alloys, based on several properties: surface and core hardness, tensile strength and fatigue life according to a surface stress or a bending. The authors showed that the results of the different methods are very close. Anojkumar *et al.* [227] used PROMETHEE to classify five existing stainless steels for piping applications, according to seven criteria: cost, yield strength, tensile strength, elongation at break, hardness, corrosion resistance and abrasion resistance. Again, the approach produces a classification close to that provided by other tools. Similarly, Peng & Xiao [228] used PROMETHEE for the selection of an alloy intended for rolling bearings according to nineteen physicochemical criteria, including cost, density, hardness, coefficient of thermal expansion, thermal conductivity and corrosion resistance. All of these studies focus on finding the optimal choice between a set of already existing alloys, rather than selecting a novel designed composition. Therefore, for some of these studies it was possible that the set included alloys that were dominated, and could thus be excluded directly without the recourse to a mathematical decision method. Moreover, for most of the mentioned studies, the number of alloys to be ranked and chosen from remains low (about ten alloys).

In our study, this method will be applied to rank a set of entirely novel alloys following a process of computational alloy design. The alloys will all be non-dominated with respect to each other since they will be generated by a multi-objective optimization algorithm. Materials selection will therefore be made on truly incomparable Pareto-optimal candidates, whereas published works were made on sets of (real) alloys in which some were dominated. Additionally, as will be seen later, the size of the set of alternatives will be of the order of 100, i.e. much larger than that of most reported decision-making problems in the field of materials. This approach remains original, and there seems to exist only one example of such application [229].

2.3.2.4 GAIA plane

One of the associated tools of the PROMETHEE method is the Geometrical Analysis for Interactice Aid (GAIA) visual representation. This tool allows the representation of the n-solutions of a k-dimensional space by projecting the information on a plane, to make it easier to visualize and analyze. This plane is termed the "GAIA plane" and is a projection of both solutions and criteria axes (see Figure 2.5), based on the principal components analysis (PCA) method. PCA is a tool used to reduce multi-dimension distribution of data, typically into two or three-dimensions (to be able to visualize) while keeping the information loss to a minimum. This method allows to define a set of "principal components", which are basically a linear combination of the original dimensions. These components represent the directions of the data that explain maximum variance,

i.e., the dimensions that capture most information of the data. The high variance of a dimension means a large dispersion of the data points along it, indicating a higher level of information and significance in differentiating between data.

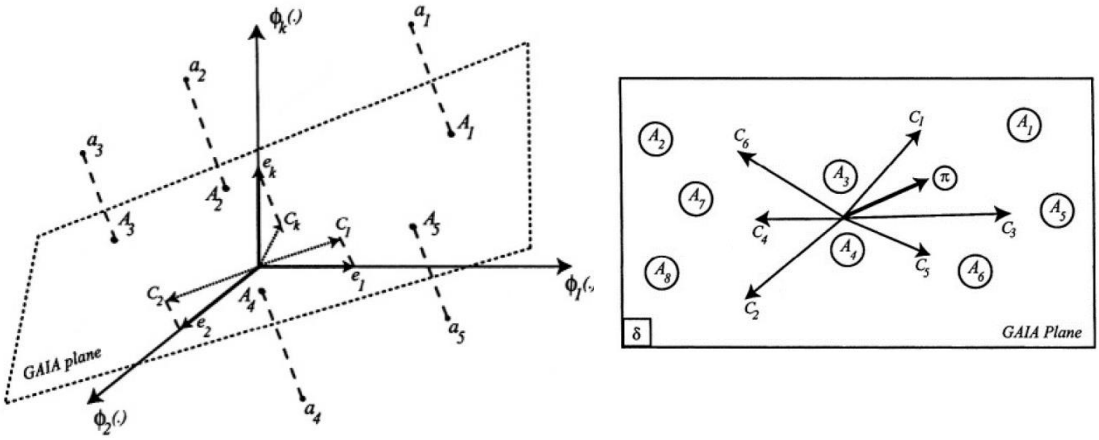

Figure 2.5 Visual representation of alternatives/solutions (A_n) and Criteria (C_n) on a GAIA plane

This projection allows a visual representation of the solutions and criteria, as shown in Figure 2.5. Several information can be inferred from the GAIA plane based on the following properties:

1- The length of a criterion axis is related to its discrimination power with respect to the other criteria; the longer the axis, the more discriminating the criterion is in decision making.
2- A similar orientation of axes means similar preferences of the corresponding criteria, therefore indicating a positive correlation between the respective criteria.
3- Criteria which have oppositely oriented axes (angle ~180 °) express conflicting preferences, i.e. a negative correlation between associated criteria.
4- Orthogonal axes (angle ~ 90 °) signify that the corresponding criteria are independent (not related to each other).
5- The closer the points of the solutions are to each other, the closer the corresponding solutions are.
6- Solutions that perform well on a particular criterion will have a representative point which is located in the direction of the corresponding criterion axis.

Hence, the GAIA tool can provide useful information on the discriminating power of the different criteria in decision making through an observation of their associated lengths, the conflicting or correlated aspects of the different criteria based on their similar or opposite orientation, as well as the performance of the different solutions with respect to the multiple criteria based on their respective position in the projection plane. This method also makes it easy to determine visually which solutions (in our case alloys) perform better in which criteria.

3 Experimental procedures and methods

As will be exposed later, in the last stage of our study, one composition from within an optimized set of alloys was selected for experimental validation of our design method. This selected alloy was first cast using a cold crucible method at École des Mines de Saint-Étienne (MINES) labs. The alloy was then fabricated in powder form in the labs of Université de Technologie de Belfort Montbéliard (UTBM). Finally, the material was produced by SLM in the labs of École Nationale d'Ingénieurs de Saint-Étienne (ENISE). At each stage, the material was characterized and evaluated microstructurally and mechanically. This chapter describes the experimental procedures applied.

3.1 Powder fabrication and characterization

3.1.1 Gas atomization

The powder used in this study was produced in UTBM labs by gas atomization under argon atmosphere.

Gas atomization is a method to produce powder particles which consists in atomizing a molten metal filament into fine droplets by disintegrating them using a high pressure gas flow (see Figure 3.1). The liquid droplets solidify by convective heat exchange in an atomizing chamber with a protective gas (Ar in our case) to produce the powder. Liquid metal atomization using a “de Laval” nozzle allows a laminar flow of the gas around the molten metal filament. As a result, a good control of the droplet size and of the distribution of the elaborated powder can be ensured, so that micronic powder particles with a narrow size distribution and a spherical shape can be obtained.

Four batches of powder, of 5 kg each, were produced in agreement with the specifications for the SLM process. Sieving was performed after the atomization step to target a specific granulometry.

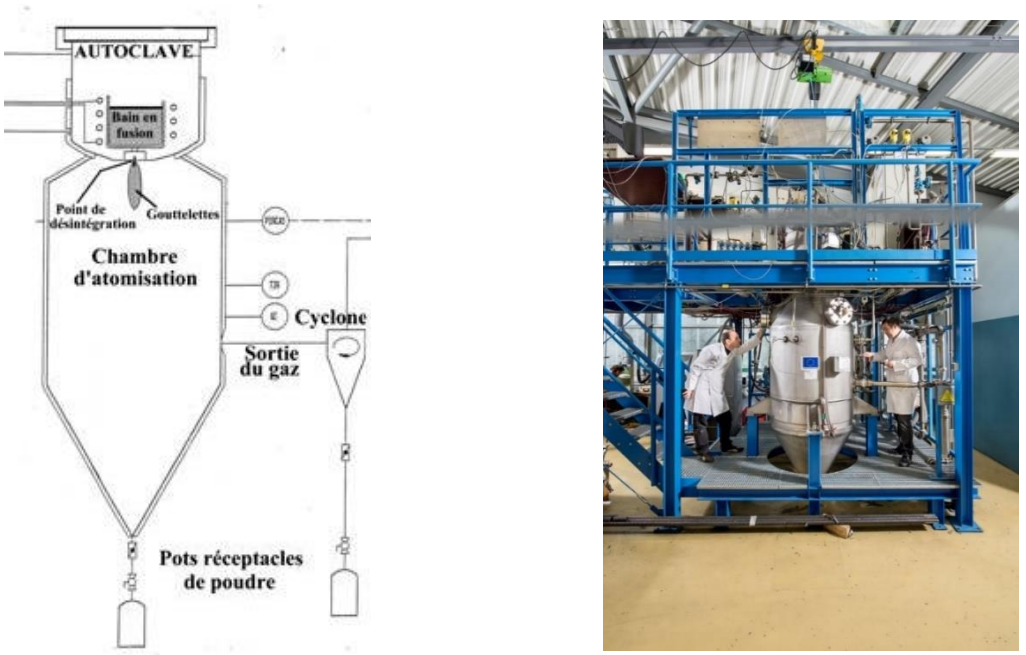

(a) (b)

Figure 3.1 a) Schematic of a gas atomization chamber b) gas atomizer in UTBM lab

3.1.2 Particle granulometry

The particle size distribution was determined at UTBM by dry laser diffraction, with a Malvern MasterSizer 3000 particle sizer. The powder is carried in the measurement cell using a gas flow, and the laser light scattering provides an estimation of the size of the particles. The analyzes are carried out twice to ensure a good repeatability. The pressure of air inside the machine must be chosen as to separate the particles in order to correctly measure their sizes, and for a sufficiently high level of pressure, powder aggregates may break. To verify this, the measurement was done at two pressures (0.1 and 3.5 bar) to test the agglomeration of the powder. Almost identical results were obtained at different pressures and for different measurements, confirming the low fraction of aggregates in the powder.

3.2 Selective laser melting

The samples were constructed on a ProX DMP 200 LPBF device from 3D Systems. This machine is equipped with an Nd YAG type laser source operating at near-infrared spectrum ($\lambda = 1064$ nm), with a variable power P (max. 300 W). The laser beam is transported by an optical fiber to a group

of focusing lenses. The laser beam then enters the chamber through the lenses, which then direct energy to areas of the building substrate, following a pre-written program. The scanning strategy selected was -45/+45° compared to the orthogonal axis of the specimens.

The powders are layered by a roller on a building platform with a size of 140 × 140 mm^2. The main characteristics of the machine are indicated in Table 3.1. The specimens were disposed in staggered rows on the building platform, with a building sequence oriented in the opposite direction of the Ar gas flow, to prevent the deposition of spatters.

This device is also equipped with a sensor which continuously assesses the level of oxygen in the chamber. This machine has been used to print several grades of materials, including 316L steel, AlSi12 aluminum alloy, Ti-6Al-4V titanium alloy and IN 718.

Table 3.1 Technical characteristics of ProX DMP 200 machine and the parameters ranges used in our study

		This study
Laser power	Max: 300 W	**120-250 W**
Laser speed		**1000-1200 mm/s**
Layer thickness	20 µm to 100 µm	**30 µm**
Gas	Nitrogen or argon	**Argon**

3.3 Microstructure observations

3.3.1 Samples preparation

For all observations, surfaces were prepared by manual grinding with SiC paper (P240 - P1200). The specimens were then polished using a polishing felt lap and 1 µm diamond suspension. Final polishing was obtained by using Buehler Mastermet 2 colloidal silica. The so obtained state of the surface was generally satisfactory for further observations by scanning electron microscopy or X-Ray Diffraction (XRD), with some occasional pits. SLM samples were further electropolished with a solution of 6% $HClO_4$ and 94% ethanol at 30 V for 45 s with a Struers LectroPol-5 machine.

3.3.2 Scanning electron microscopy

A Scanning Electron Microscope (SEM) Zeiss SUPRA55VP was used for microstructure observations in backscattered electrons (BSE) mode operated at 20 kV. The same microscope was used for electron backscatter diffraction (EBSD). The EBSD technique provides a map of the local

crystalline orientation of the grains. The technique relies on the analysis of the backscattered electrons diffraction diagrams to determine the crystalline orientation. EBSD analysis was carried out with a conventional tilt angle of the specimen of 70°, a working distance of 15 mm, and a step size between 0.06 and 0.1 μm. The EBSD data were analyzed with the HKL Channel5 software (Oxford Instruments NanoAnalysis, version 5.11.10405.0). Grain boundaries were set as a change in orientation over 15° and subgrain boundaries as between 2° and 15°.

Local chemical composition was analyzed by using SEMs equipped with Energy Dispersive Spectrometers (EDS): JEOL 6500F SEM equipped with silicon diode detector Princeton Gamma tech, and Zeiss SUPRA55VP SEM equipped with Oxford SDD detector XmaxN 80.

3.3.3 X-ray diffraction

Crystal structure and phase identification for samples in different states were determined using an X-ray diffractometer (XRD) X'Pert Pro MPD PANALYTICAL with Cu K_α radiation operated at 40 mA and 45 kV. Divergence slits at 0.5° were set for the incident beam, and a graphite monochromator and a Miniprop point detector were used for the diffracted beam. The analyzed angle was between 10° and 120° with a step size of 0.03°, and a counting time of 25 s/step.

3.4 Mechanical properties

3.4.1 Vickers hardness

Vickers hardness was measured under a load of 10 kg. At least eight equally spaced indents were made on a clean and polished surface and the average values were calculated.

3.4.2 Tensile tests

Tensile tests were performed with an Instron 1186 machine on flat specimens with the dimension shown in Figure 3.3, at the strain rate of 10^{-3} s^{-1}. All tests were performed at room temperature. The tensile specimens produced by SLM were wire-cut then machined at the laboratories of MINES. All samples were tested in the as-machined state without prior surface polishing. The size of samples was measured with a caliper (error range of 0.02 mm). The elongation was measured by a clip-on extensometer with an initial gage length of 10 mm.

Mechanical characteristics of the samples, yield stress (YS), ultimate tensile stress (UTS) and uniform elongation to fracture (A%), have been evaluated from the engineering stress-strain curves. In fact, the so-calculated YS value corresponds to the proof stress at 0.2 % of permanent plastic deformation. The UTS value was calculated as the maximal measured force and the uniform elongation to fracture is the sample elongation at the UTS point.

3.5 Porosity measurement

3.5.1 Archimedes method

Density measurements were made using the so-called Archimedes method. The device used was a digital weighing system (Mettler AE240) equipped with a solid sample weighing module. This technique is based on the principle of Archimedes (ASTM B962).

The sample is weighed in air and then in a liquid, providing the measurement of apparent masses M_{air} and M_{liquid}. Knowing the density of the liquid (ρ_{liquid}, which varies with temperature) and of the air (ρ_{air}), it becomes possible to calculate the density of the sample ρ_{sample} according to equation 3.1:

$$\rho_{sample} = \frac{M_{air}}{M_{air} - M_{fluid}} \times \left(\rho_{fluid} - \rho_{air}\right) + \rho_{air} \qquad 3.1$$

To estimate the porosity fraction of the sample, the measured density must be compared with the theoretical density of the material. For accuracy, the measurements were repeated three times and with different liquids: demineralized water, ethanol and acetone.

3.5.2 Helium pycnometry

Helium pycnometry measurements were performed on a Micromeritics AccuPyc 1330 device. This technique gives access to the density of a sample (in massive or powdery state) after the measurement of its volume, the latter incorporating closed porosity. The measurement process consists in placing a sample in a tank whose volume V_1 is calibrated and perfectly known, at atmospheric pressure P_a. This tank is then filled with helium at a pressure P_1. The gas is then expanded to a pressure P_2 in another atmospheric pressured empty vessel (called expansion), of a volume V_2.

The pycnometer measures the volume of a displaced gas from a primary tank (V_{tank}) at a pressure P_1 to an expansion tank ($V_{expansion}$) at a pressure P_2. The pressure variation permits to determine the volume of the sample (V_{sample}) and the application of Boyle-Mariotte law allows calculating this volume with equation 3.2:

$$V_{sample} = \frac{V_{tank} - V_{expansion}}{\frac{P_1 - P_a}{P_2 - P_a} - 1} \qquad 3.2$$

The mass is measured accurately beforehand and, knowing the volume of the sample, it is possible to calculate its density. In the case of helium pycnometry, several purge cycles are previously

performed to remove all the air present in the tank and in the open pores of the sample. Then ten successive measurements are made while keeping the tank closed and airtight.

3.6 Surface roughness

The surface topography was analyzed using a confocal microscope 'ALICONA Infinite Focus'. Rectangular areas (0.8×5 mm^2) were analyzed on the top surface of printed specimens. Then 2D profiles were filtered with a short-wavelength cut-off L_c = 800 µm Gaussian filter (ISO 4287). Various surface roughness parameters were quantified, but the S_a parameter, describing the mean of the absolute value of the difference in height of each point compared to the average altitude, was mostly considered in our case.

3.7 Dilatometry

Dilatometric testing was carried out in a SETARAM Setsys Evolution 16/18 dilatometer under argon atmosphere to avoid oxidation during continuous heating and cooling at a fixed rate of 5° C/min. The samples were cut into cubes of dimensions $10\times10\times10$ mm^3, and the surfaces were sanded to ensure a suitable contact of the displacement sensor. The sensor is able to detect a length variation down to around 0.01 µm for a selected measuring range of +/- 2 mm. The measurements are corrected with a blank experiment to account for machine artifacts. Data acquisition and processing were done with the associated software CALISTO.

3.8 Chemical composition

The chemical composition of the material in the as-cast state was measured by X-ray fluorescence spectroscopy using a Fischerscope XAN-FD spectrometer. The measurements were repeated eight times and averaged over the values.

The chemical composition of the powder was measured at Bureau Veritas Laboratories by optical emission spectrometry (OES) of an inductively coupled plasma (ICP), or ICP-OES. The carbon content was measured by combustion infrared absorption (CIR).

The oxygen content in the powder and in the samples produced by SLM was measured using inert gas analysis (IGA) with an oxygen/nitrogen analyzer of the brand LECO model TC436.

4 Phenomena considered for alloy design and associated criteria

4.1 Introduction

The design of novel alloys means finding the right combination of alloying elements and their corresponding proportions that will give the material all the wanted properties. To proceed with this, it is first vital to define the requirements and desired properties, and translate them into criteria —or objectives. The second step is to define the appropriate model, including the computing tool, that will allow to predict this value for new compositions.

To design austenitic alloys for additive manufacturing, it is necessary to take into consideration all the defects currently seen in additively manufactured metallic alloys. The list of these defects was discussed in section 1.1.5. Obviously, the process parameters largely affect the majority of these defects and the quality of the final component can be significantly enhanced by the sole optimization of these parameters. However, in this work, we focus on the effect of the chemical composition and the role it plays in all of the discussed phenomena, with an aim of improving the quality of parts as well as the robustness of the process.

Firstly, the criteria must be solely material-dependent. In other words, it means that calculated criteria should, whenever possible, be representative of the behavior of the material, or of trends relative to certain characteristics, irrespective of processing conditions or, at least, within wide enough processing windows.

Secondly, it is important to physically understand the effect of each feature on the overall result. Although some properties are known to play a key role in defining the printability of an alloy, it is not always clear in what way varying this property affects it. As an example, varying the thermal conductivity of the material could be problematic and have a direct effect on the size of the processing window of the material. Indeed, with highly conductive materials, the extraction of heat from the meltpool through conduction is fast and hence the energy loss is high. It has been shown that this leads to a small process window as it could, coupled with other parameters, lead to phenomena such as balling, porosity and finally crack formation [230]. This is the case of pure copper for example [231], [232]. On the other hand, in order for metal powder particles to melt, an appropriate efficiency of heat transfer is necessary. Therefore, a “sufficiently high” thermal conductivity is necessary to ensure the consolidation process of a metallic powder [233]. Similarly, several other properties can provoke similar effects. Thus, sometimes it is necessary to define a range of variation rather than a strict optimization direction for the property. Conversely, in many other cases, the effect of the studied characteristic is not fully understood or/and cannot be fully separated from other material characteristics. In such a case, studying the interaction between these different properties might be complicated and it may not be completely feasible to mathematically

express it based on physical principles. It is therefore not advised to consider such properties among the objective functions.

In this chapter we propose a set of material-dependent criteria which we will later use as objectives or/and constraints in the multi-objective optimization problem. The choice of these criteria will be detailed and further discussed along with the necessary tools needed to predict or estimate them, and their corresponding limitations. Such tools can be physically-based, or rely on machine learning when no physical model exists or would be too complicated to establish, while sufficient data is available. Specifically, the following criteria are considered:

- Targeting an austenitic structure: role of alloying elements on the final structure
- Avoiding solidification cracking: studying the effect of solidification conditions
- Tackling vaporization: preventing pores and deviation from targeted composition
- Minimizing residual stresses: preventing distortions and cracking due to residual stresses
- Controlling the effects of surface tension: preventing balling, spattering and delamination by increasing the wetting of the material by the meltpool
- Ensuring a high strength: searching for increasing the solid solution strengthening of the alloy

4.2 Targeting an austenitic structure

For reasons exposed in section 1.2, it is here envisioned to design austenitic alloys (stainless steels, and possibly more concentrated alloys), so that the first goal is to ensure the microstructure will be mainly constituted of austenite, i.e. of an FCC solid solution. Phase formation can be addressed by computational thermodynamics (e.g. CALPHAD) under equilibrium conditions (see section 2.1), but additive manufacturing produces out-of-equilibrium microstructures resulting from complex liquid-solid and solid-solid phase transformations paths, leading to different constitutions and to potentially microsegregated states. Indeed, the fast solidification and cooling rates in AM processes can affect the nature of the phases that are present compared to cast, forged and/or annealed alloys. The phase transformations during solidification or in solid state can be modified by:

- The solidification rate which can change the redistribution of solutes (microsegregation) and therefore the local chemical composition of the material
- The cooling rate after solidification which, if too fast, can prevent diffusion and inhibit certain solid state phase transformations

To be able to control the final microstructure, it is important to consider the effect of material chemistry on phase transformations. In general, in steels, two different phases may be observed at the beginning of solidification, δ-ferrite (body-centered crystal structure) or γ-austenite (face-centered crystal structure), fiercely depending on the alloying elements. The latter can therefore be classified into two categories based on the type of phase they tend to promote:

- α-stabilizers: elements that stabilize the ferritic phase (ex: Cr, Mo, Si...)
- γ-stabilizers: elements that stabilize the austenitic phase (ex: Ni, Mn, C...)

The content of these elements in the alloy notably affects the solidification path, which will be discussed in the next subsection. To illustrate the effect of δ and γ-stabilizers on the phases present at equilibrium, Figure 4.1 shows a comparison between the effect of chromium and nickel addition to iron. Any Fe-Cr alloy would first solidify as ferrite, whereas Fe-Ni alloys containing more than ~ 5 wt.% Ni would first form austenite. The α or γ– stabilizing elements contents of the material can be translated into the nature of the phases after solidification. To quantify this, CALPHAD can be used as a guide but, as will be discussed later, it cannot fully take into account the strong out-of-equilibrium features of rapid solidification.

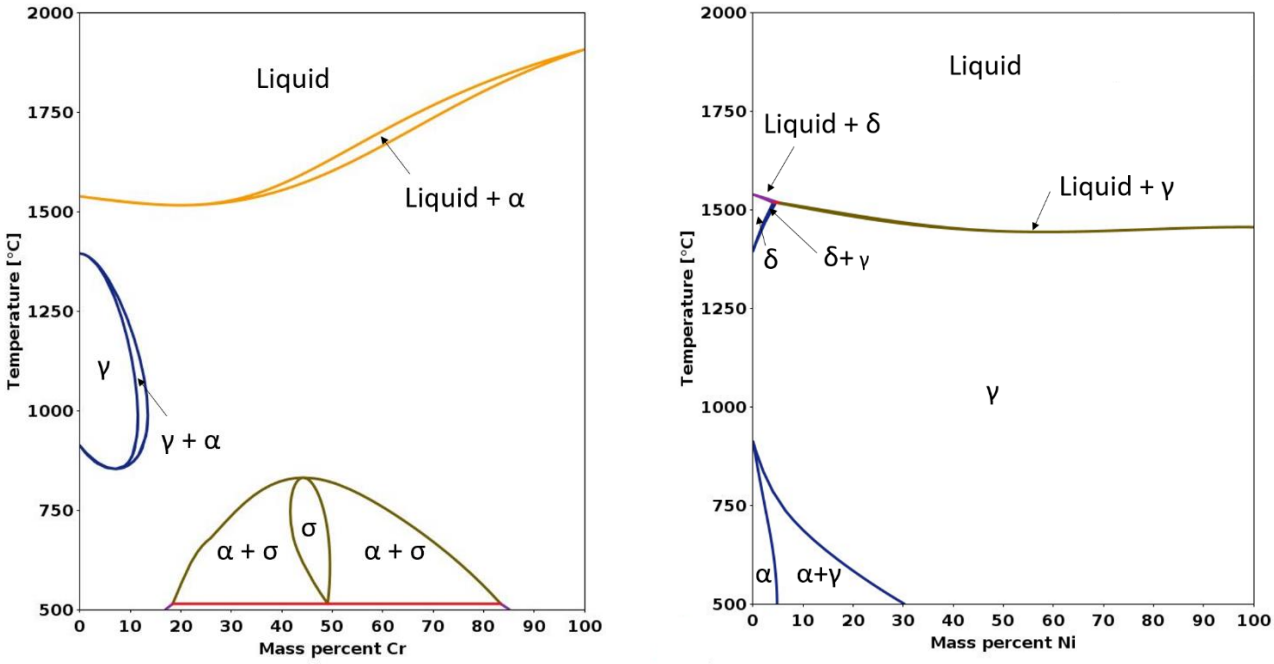

(a) (b)

Figure 4.1 Equilibrium phase diagrams of a) Fe-Cr and b) Fe-Ni, calculated using Thermo-Calc software

Besides, it is a common practice to define the equivalent power of different alloying elements in the preferential formation of phases, relative to those of Cr and Ni, through quantities named the "chromium equivalent" (Cr_{eq}) and the "nickel equivalent" (Ni_{eq}). Several equations to calculate these values have been proposed; a summary is provided in Table 4.1.

A low Cr_{eq}/Ni_{eq} ratio (< 1.25-1.3) implies the solidification will happen in austenite, and inversely a high ratio (> 1.8-1.95) will imply a solidification in ferrite. As for intermediate values, or the case for which there is a lot of both α and γ– stabilizing elements, it will in fact lead to a mixed solidification due to the redistribution of solutes –or microsegregation– taking place during solidification. The present phases will also depend on their stability range with temperature.

Table 4.1 Summary of different Cr_{eq} and Ni_{eq} equations provided by different authors; all element contents are expressed in wt.%.

Relationship	Cr_{eq}	Ni_{eq}
Schaeffler [234]	Cr + Mo + 1.5Si + 0.5Nb	Ni + 30C + 0.5Mn
Modified Schaeffler [235]	Cr + Mo + 1.5Si + 0.5Nb + 5V + 0.75W	Ni + 30C + 0.5Mn + 30N + 0.3Cu + Co
Schneider [236]	Cr + 1.5Mo + 2Si + 1.75Nb + 0.75W	Ni + 30C + 0.5Mn + 30N + 0.3Cu
Newhouse[236]	Cr + 4Mo + 6Si + 5Nb + 1.5W + 11V	4Ni + 2Mn + 40C + 30N + 2Co
Kaltenhauser *et al.* [237]	Cr + 4Mo + 6Si + 4Nb + 2Al + 11V + 8Ti	Ni + 2Mn + 40C + 40N
WRC [238]	Cr + Mo + 1.5Si + 0.5Nb	Ni + 30C + 0.5Mn
Ezaki *et al.* [239]	Cr + 4Mo + 6Si + 5Nb + 1.5W + 11V + 12Al + 8Ti	4Ni+2Mn+40C+30N+Cu+2Co
Balmforth and Lippold [240]	Cr + 2Mo + 10(Al+Ti)	Ni + 35C + 20N
Ryu and Yu [241]	Cr + 2Mo + 0.8Si + 2Nb + W + 1.7Al + 60B + 2Ti + Ta	2Ni + 0.4Mn + 0.6Co + 0.6Cu + 20N + 20C
Hull [242]	Cr +1.21Mo + 0.48Si + 2.27V + 0.72W + 2.2Ti + 0.14Nb + 0.21Ta + 2.48Al	Ni + 0.11Mn – $0.0086Mn^2$ + 0.14Co + 0.44Cu +18.4N + 24.5C

Many studies aimed at developing empirical diagrams to predict the final microstructure, notably in welded metals, from alloy composition. One of the most used diagrams is that of Schaeffler [234], which was later on modified by Delong [235]. With the Schaeffler-Delong diagram it is possible to predict the final microstructure in as-welded stainless steels by plotting the calculated values of Cr and Ni equivalents. With the years, more complex steel compositions have been developed, and more authors studied the effect of different elements on the stabilization of either austenite or ferrite, which led to the various equations of the Cr and Ni equivalents shown in Table 4.1. One of the main differences between the first Schaeffler equations and the majority of the

equations which were later proposed is the strong effect of N on the stabilization of austenite. Similarly, α-stabilizing elements such as Al, Ti, V and W, which can eventually have a stronger stabilization power than Cr (coefficient > 1) were initially overlooked, probably due to the fact these elements were not normally added to steels at that time.

In our case, to account for the effect of as many alloying elements as possible, the Hull equations/diagram [242] is taken into consideration.

This approach can serve as a simple tool to estimate the phases present after solidification. It will aid in a rapid prior classification of compositions into potentially acceptable (i.e. mainly austenitic after solidification, called "feasible") and unacceptable ("unfeasible") alloys. This step can save unnecessary and computationally heavy thermodynamic calculations which, in turn, may not provide a prediction of all final phases (austenite, ferrite, martensite) in a straightforward and reliable manner.

Figure 4.2 shows the Hull diagram with the feasible space defined with green dashed lines. The aim would be to limit as much as possible the search space to alloys that have a fully austenitic microstructure after solidification and cooling down to room temperature. The feasible space is set according to two boundaries, a limit on the ferrite content and another on the martensite content. Unlike the case of martensite, which we wish to completely avoid for reasons of brittleness, the boundary with ferrite is given a margin of around 5%. This choice is based on the fact that different several known austenitic alloys, which are in fact fully austenitic experimentally, lie in this region of the diagram. Therefore, setting a strict limit of feasibility according to the line between Austenite (A) and Austenite+Ferrite (A+F), would be very restrictive to the search and lead to disregarding some possible austenitic compositions that might lie in this region. In fact, Figure 4.2 shows the scatter (between 0 and 5% ferrite) of several experimental alloys on the Hull diagram: 304, 316 [243], 316L-5Mo-5Ni [244] and SSW2 [243] (see Table 4.2 for compositions). In other words, it is important to account for the error range of this diagram.

Therefore, the green lines refer to 0% of predicted martensite and 5% of predicted ferrite respectively.

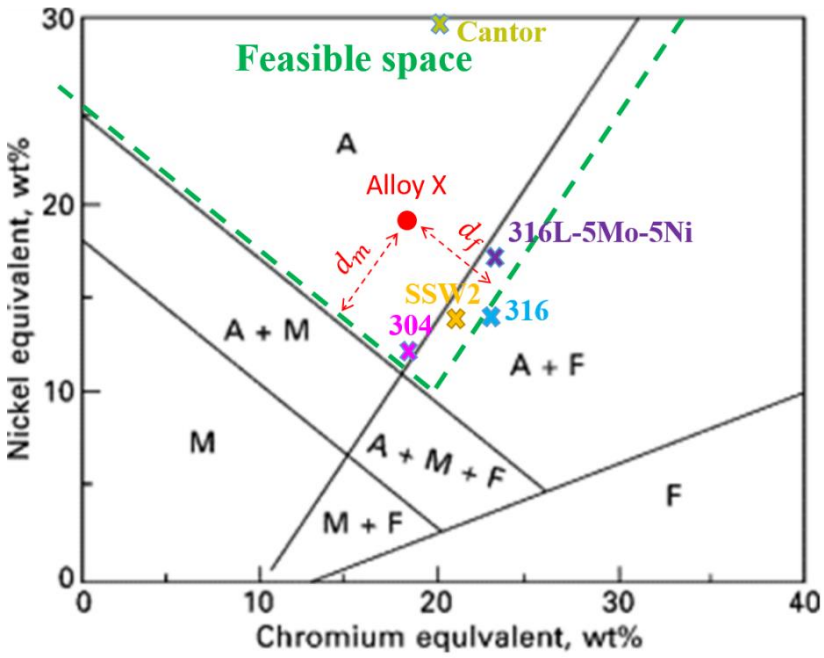

Figure 4.2 Hull diagram with a definition of the feasible search space defined in our study; A stands for austenite, F is ferrite and M is martensite

To favor the search of alloys which are definitely within the austenitic region, in addition to the feasibility constraint, an objective function is set, based on the distance of the alloy to the ferrite and martensite boundaries (illustrated by d_m and d_f from a random alloy X on Figure 4.2). To favor alloys that are as far as possible from the boundaries, the objective was set to maximize the smallest among both distances.

Table 4.2 Chemical composition in wt.% for several austenitic stainless steel alloys

Alloy	Fe	Cr	Ni	Mn	Mo	Co	Si	W	C
304	77.4	18.5	9	2	-	-	1	-	0.07
316 [243]	66.3	17.5	11.7	0.9	2.2	0.2	0.6		0.05
316L-5Mo-5Ni [244]	60.7	15.3	15.8		7.3	-	0.9		0.03
SSW2 [243]	68.2	16.7	10.8	0.7	1.1	0.1	0.6	1.1	0.08
Cantor	19.9	18.5	20.9	19.6	-	21	-	-	-

4.3 Avoiding solidification cracking

The problem of solidification cracking, or hot cracking, has been widely studied in conventional manufacturing techniques like casting and welding. The knowledge from welding literature can be particularly interesting due to the acknowledged similarities with AM techniques. For example, it is known that non-weldable superalloys are often subjected to hot cracking with AM [245]. Nevertheless, AM processes comes with their own features and particularities, thus in some cases certain weldable alloys can still undergo hot cracking when fabricated with AM [246], [247]. This indicates that although the similarities between the two families of processes allow to make useful analogies, it is also important to take special care when dealing with AM processes and consider their individualities. Despite the huge effort made to completely understand this phenomenon, the effects of the different thermal, metallurgical and mechanical factors complexly interacting to create it, are still not fully described. Nevertheless, there exist some rules, criteria or trends that can be exploited to try to avoid or at least minimize the risk of solidification cracking. In this section, we focus solely on the material-dependent criteria. This includes the solidification temperature range as well as the nature of phases that form during solidification.

4.3.1 Effect of solidification temperature range

The solidification temperature range is of one of the main characteristics which affect the cracking susceptibility of an alloy. There exist several theories which explain this effect, such as the shrinkage-brittlness theory first proposed by Bochvar in 1947, and the strain theory proposed by Pellini in 1952 [248]. Later, in 1960, Borland proposed a “generalized theory” based on the two previous ones, while defining a “critical solidification range” during which the material is most susceptible to solidification cracking. Figure 4.3 illustrates this phenomenon.

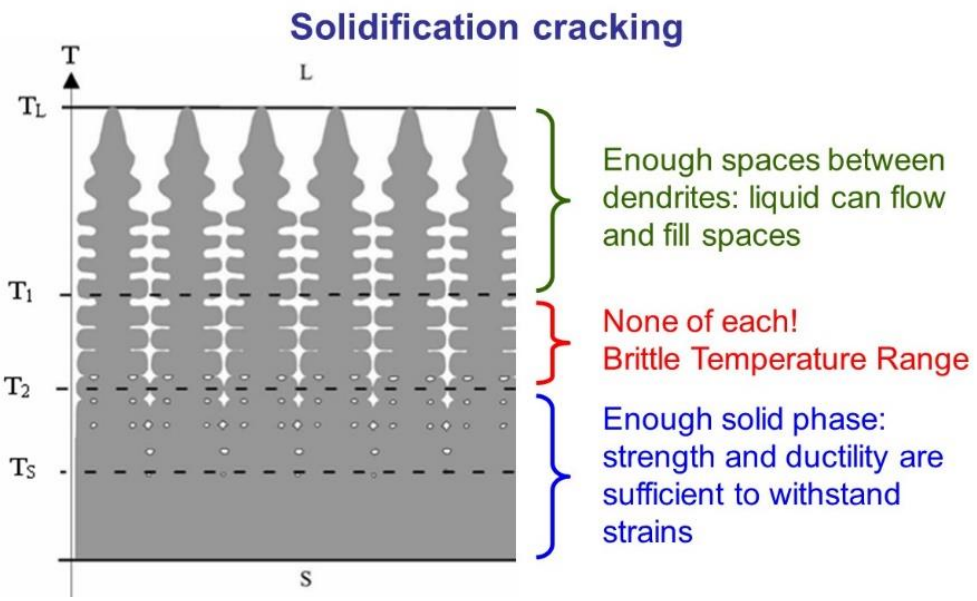

Figure 4.3 Schematic showing the brittle temperature range of a solidifying material where S is solid and L is liquid.

At the highest temperatures of the solidification range (higher than a certain value T_1 that will be defined later), enough liquid is available to flow and fill spaces between forming dendrites or grains, or "heal" cracks that may form. At the opposite, for the lowest temperatures of the solidification range (lower than a certain value T_2), enough solid phase is present such that the strength and ductility of the material are sufficient to withstand strains. Between T_1 and T_2, decohesion along interdendritic liquid films can occur, that cannot be filled by flowing liquid, thus defining the so-called critical temperature range (CTR) or brittle temperature range (BTR).

In alloys, cracking susceptibility is considered to be the highest at the composition where the "effective interval" is the largest [249]. Based on this, the calculation of the solidification temperature range can be used to quantify the cracking susceptibility of an alloy. More specifically, the CTR or BTR as defined above, must be considered [250], [251]. Definitions vary between sources, but the CTR is generally defined as the difference between the temperatures at which certain fractions of solids have been formed; several values can be found, but the choice made here corresponds to fractions of solids between 95% (T_1) and 99% (T_2), since they seem to be the most frequently reported ones [151], [152], [171].

It must be noted that, in steels, solidification cracking susceptibility is usually worsened by impurities, such as sulphur and phosphorus, as they tend to form low melting point phases, thus extending the solidification range of the alloy [22], [23]. They have other effects that will be discussed later. However, in what follows we shall assume that all alloys react in a similar way to such effects and that standard levels of impurities will be present in all alloys, so that the calculated

trends of evolution of the CTR with steel composition will be relevant for alloy design. The method to calculate the CTR will be described later.

4.3.2 Effect of solidification path

The final microstructures of stainless steel welds usually contain a variety of complex austenite/ferrite structures. These structures are controlled by both the solidification behavior and the subsequent solid state transformations [252]. As already stated, the final microstructure can be approached by the Hull diagram or similar tools, but the solidification path that leads to it may also depend on composition and cooling rate. Figure 4.4 shows how the variation of the composition (by varying Cr_{eq} and Ni_{eq}) and of the solidification rate affects the solidification path of the alloy.

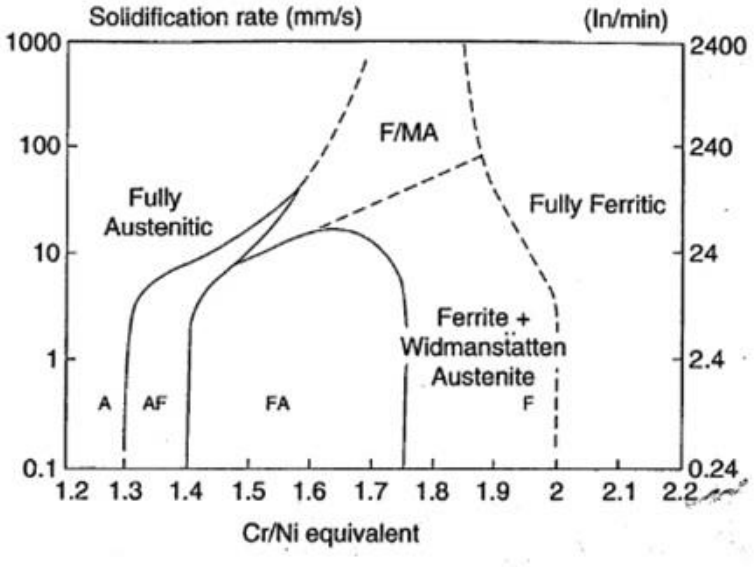

Figure 4.4 Effect of solidification rate and Cr/Ni equivalent ratio on the solidification path of stainless steels [238].

There exist in fact four solidification and solid-state transformation possibilities for stainless steel weld metals [248] (summarized in Table 4.3):

- Solidification mode A: The solidification occurs as primary austenite, and the microstructure is fully austenitic at the end of solidification.
- Solidification mode AF: After the solidification of primary austenite, some ferrite forms via a eutectic reaction.
- Solidification type FA: The solidification occurs in primary ferrite. Then, some austenite starts forming later. In this case, the austenite forms via a eutectic [253] or a peritectic [254], [255] reaction.

- Solidification type F: The metal solidifies completely in ferrite and the microstructure is fully ferritic at the end of solidification. After the metal cools down below the ferrite solvus, austenite might form within the microstructure. The amount of austenite that might form depends again on the composition and cooling rate.

Table 4.3 Solidification types, reactions and resultant microstructures for stainless steel weld metals. L stands for liquid, F is ferrite and A is austenite; "eut" and "per" indicate eutectic and peritectic reactions, respectively [248].

Solidification mode	**Reaction**	**Cr_{eq}/Ni_{eq}**
A	L → L+A → A	< 1.25-1.3 [151], [236]
AF	L → L+A → L+A+$(A+F)_{eut}$ → A+F_{eut}	> 1.25-1.3 < 1.4-1.48
FA	L → L+F → L+F+$(A+F)_{eut/per}$ → F+A	> 1.4-1.48 [151], [256] < 1.8-1.95
F	L → L+F → F → F+A	> 1.8-1.95

Concerning processes with high solidification rates, different studies have shown that the FA or F modes can significantly lower the hot cracking susceptibility, compared to A and AF [256]–[263]. In fact, Brooks *et al.* [252] argue that since solidification cracking is mainly associated with grain boundaries, factors that affect the nature of the interdendritic regions should be relevant to cracking behavior. The latter is of course affected by the phases formed and their order. According to the authors, one of the major factors that make FA/F modes preferable and more resistant to cracking is actually related to the smaller solidification temperature range of primary ferrite than that of primary austenite, which reduces the critical temperature range. As discussed in section 4.3.1 above, this shortens the range in which strains are increasing in the presence of a mushy zone and therefore lowers the cracking susceptibility. This effect should be, however, captured by the CTR criterion. Another important reason is related to the higher solubility of harmful impurities (S, P…) in ferrite compared to that in austenite, which results in less segregation during primary ferrite solidification. Although in our case we assume to be working in a somewhat ideal situation where the content of such impurities is decreased to a minimum, Figure 4.5 shows how the cracking behavior of several austenitic stainless steels is controlled by the S+P impurity content as well as the Cr_{eq}/Ni_{eq} ratio. In fact, Bollinghaus *et al.* [264] mentioned that as the ratio of Cr_{eq}/Ni_{eq} approaches 1.48, the impurity content of S and P which leads to cracking becomes much higher, and above this value (~1.48) cracking becomes rare even for somewhat high impurity contents (> 0.2 wt.%). Indeed, this value corresponds to the range at which the solidification mode changes from A or AF to FA or F (see Table 4.3).

Therefore, we assume that by setting a constraint on the solidification mode to be FA, we will be able to increase the cracking resistance of the searched compositions. The details of the set constraints and objectives will be given in the next section.

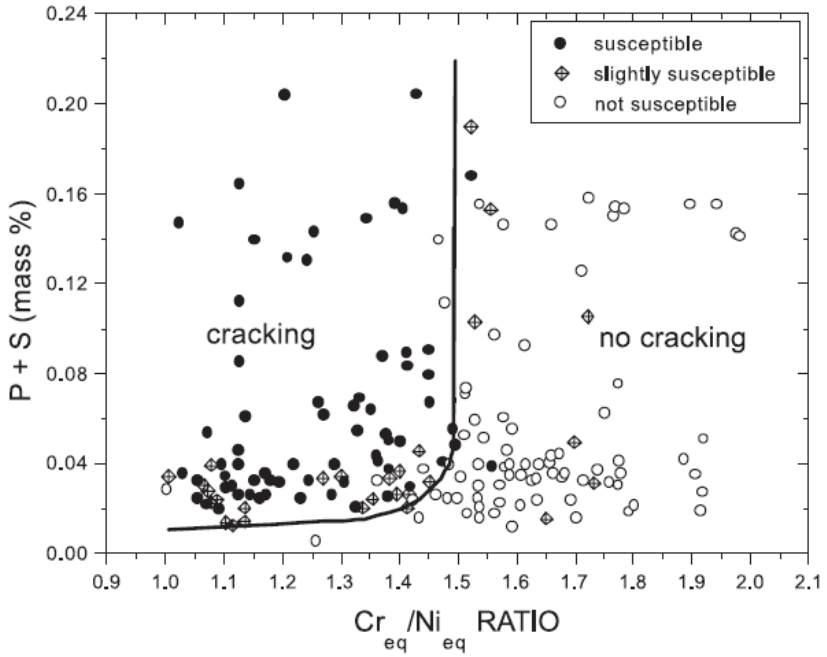

Figure 4.5 Solidification cracking behavior in austenitic stainless steel welds as a function of Schaeffler Cr_{eq}/Ni_{eq} ratio and P+S levels [265].

4.3.3 Scheil-Gulliver solidification simulation: a tool for solidification criteria

Two important material-dependent criteria are therefore considered for avoiding solidification cracking in the designed alloys: the critical solidification temperature range (CTR) which must be minimized, and the solidification path mode which should be Ferrite-Austenite.

As mentioned before, the rapid heating and cooling in AM processes results in out-of-equilibrium solidification conditions. These conditions can be approximated by the Scheil-Gulliver assumptions. As already stated, the Scheil-Gulliver model assumes that (i) the liquid is always homogeneous in composition, due to a fast diffusion of all elements in the liquid phase and to convection effects, (ii) diffusion of all elements in the solid phases is null, which is a fair approximation when cooling is fast enough, and (iii) that the liquid/solid interface is at thermodynamic equilibrium. This model is then seen as a good way to predict both the critical temperature range and the solidification path.

The Scheil-Gulliver solidification simulation (also just called “Scheil model”) from Thermo-Calc is used. This tool allows to calculate the full solidification range, the formed phases including their order and the evolution of their associated fractions. The obtained result can be presented graphically, as shown in Figure 4.6.

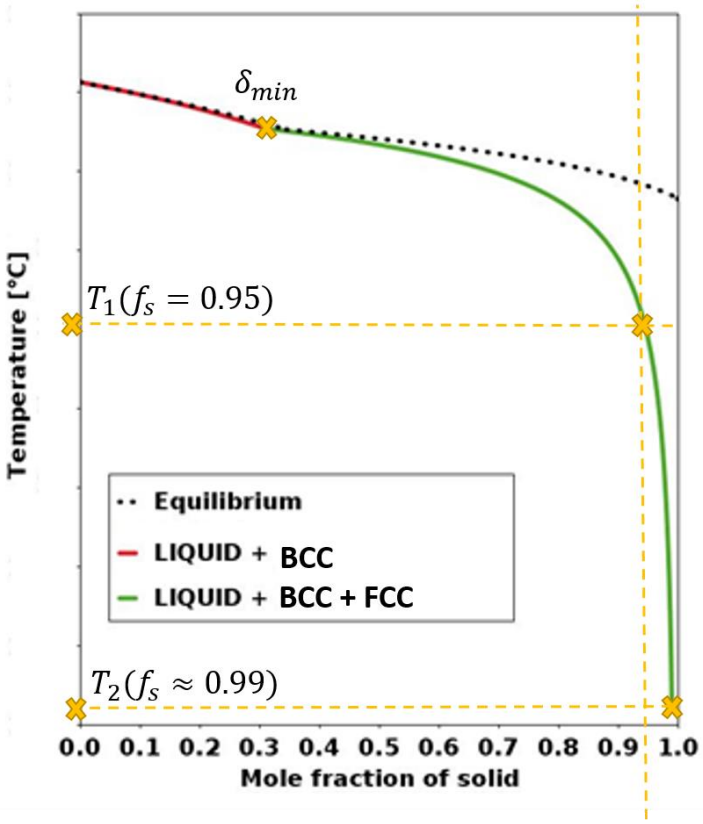

Figure 4.6 Example of a Scheil-Gulliver calculation for 316L by Thermo-Calc software version 2021 with TCFE10 database.

Starting from the simulation results, several values are calculated to define objectives and constraints.

First, to ensure that the solidification mode is FA, a constraint on the first phase formed during solidification is set to δ-ferrite. However, as we discussed in section 4.1, the final aimed microstructure is austenitic. Hence, it is necessary to set lower and upper limits on the fraction of δ-ferrite formed during solidification. Indeed, if too much δ-ferrite is formed, it may not fully transform into austenite during subsequent cooling. So, to guarantee that the benefits associated with the formation of δ-ferrite are present and to ensure that an almost complete solid state transformation of ferrite into austenite will be able to take place during cooling after solidification,

a target range is defined on the fraction of formed δ-ferrite. Based on bibliography [266]–[268], a minimum of 10% of δ-ferrite is set as a constraint, to reduce the risk of cracking. To set an upper limit, the Scheil-Gulliver results of several commercial austenitic alloys which solidify in an FA mode were taken into consideration. For example, the calculated δ-ferrite can reach 33% for 316L, and 35% for 304 whereas studies have shown that the final structure of the SLM-ed alloys is fully austenitic [269], [270]. Several tens of percent of δ-ferrite may thus be allowed. Besides, it must be reminded that the maximum amount of primary ferrite formed is expected to be regulated by the constraint set using the Hull diagram, as defined in section 4.1. A maximum value of 50% is chosen as a constraint for δ-ferrite calculated using Scheil model, ensuring a kind of redundancy in the criteria, but it is expected to be a weak constraint compared to that enforced by the criterion derived from the Hull diagram. Finally, to avoid the formation of undesired phases and intermetallics, a constraint is set to ensure that at least 99% of the phases at the end of solidification consist of δ-ferrite and austenite (i.e. only compositions with less than 1% of other phases are accepted).

The CTR is calculated as the difference between temperatures T_1 and T_2 at solid fractions of 95% and 99% respectively as shown in Figure 4.6 and is directly used as an objective function to be minimized.

A summary of the discussed objectives and constraints is shown in Table 4.4.

Table 4.4 Summary of the objectives and constraints put to satisfy the criteria of solidification cracking.

Value		**Type**	**Target**
CTR		Objective function	To be minimized
Order of phases		Constraint	Set to FA
Fraction of phases	δ-ferrite	Constraint	≥ 10% and ≤ 50%
	Austenite + δ-ferrite	Constraint	≥ 99%

4.4 Tackling vaporization

4.4.1 Avoiding porosity: understanding keyholing

During AM processes, the applied laser power and scanning speed are typically in the range of 10^2-10^3 W and 10^2-10^3 mm/s, respectively. This corresponds to an energy density within a typical range of 10-100 J/mm^3 depending on the layer thickness. SLM is characterized by two different melting modes: conduction and keyholing. These modes are separated by a threshold that is

dependent on temperature and speed of the laser. Below this threshold, the meltpool formation is mainly controlled by heat conduction, while above it, it becomes controlled by the metal gas pressure or "keyhole" mode. Indeed, high energy inputs can lead to very high temperatures of the molten pool, at which vaporization of certain alloying elements might take place. As the metal vaporizes, the gas pressure pushes the liquid metal outward, creating a keyhole-like shape. The presence of such hole and gas in the center of the meltpool may notably result in the formation of pores in the deposited metal. King *et al.* [271] determined a criterion for the occurrence of keyholing linking it to a ratio of the absorbed energy density to the enthalpy at melting. This ratio represents the excess energy that is neither lost by conduction during melting nor absorbed by melting. This excess energy contributes to the increase of the local temperature of the melt. The authors showed that at temperatures close to the boiling temperature T_b, the material becomes susceptible to keyholing. The threshold value for the excess energy is shown to be proportional to the ratio T_b/T_m (where T_m is the melting temperature). The higher this ratio is, the less susceptible the material is to keyholing. Nevertheless, T_b is significantly correlated to the melting temperature for most metals. Therefore, the possibility of increasing their ratio by changing the composition is quite limited.

To tackle this, another approach could be to directly consider the evaporation of elements. Indeed, as the keyhole formation is mainly caused by the vaporization of elements, a minimization of their vaporization flux should mitigate the keyhole problem. This will be addressed in the next subsection.

4.4.2 Loss of elements and change in composition

The tendency to vaporize, or the volatility, varies between different elements and so, at high temperatures, it is possible that a selective vaporization takes place. This could cause a deviation from the overall composition of the alloy which can affect its solidification microstructure as well as other properties such as its corrosion resistance and mechanical properties.

One way to approach this issue is to consider the volatility of individual elements within the meltpool. Equation 4.1 shows the Langmuir expression [272] for the vaporization flux of element i, J_i:

$$J_i = \lambda_c \frac{P_i}{\sqrt{2\pi M_i T}} \qquad 4.1$$

where P_i and M_i are the equilibrium vapor pressure and molecular weight of element i, respectively, T is the temperature and λ_c is a positive constant that accounts for the inevitable condensation of a portion of the vaporized atoms at atmospheric pressure. Usually a λ_c value of 1 is considered for vacuum conditions and, according to existing literature, it tends to over-predict

vaporization rates by up to an order of magnitude when used at atmospheric pressure [17]. Nevertheless, it will here be assumed that trends and relative fluxes are correct; indeed, what is important is that an alloy keeps its composition during processing, i.e. that the vaporization rates of elements are close to each other.

4.4.3 Criteria based on vaporization fluxes

Starting from Equation 4.1, it is possible to approach the problem of vaporization and its consequences on mass loss and change in composition from a material-dependent perspective.

By using the equations of vapor pressures for each element independently, it is possible to obtain an approximate value of J_i for each element. Doing so we can ensure that, globally, the total vaporization flux is minimized, by aiming at decreasing the sum of J_i over all elements. This should lessen the possibility of element vaporization and its effect on pore formation. In order to consider the problem related to change in composition, the variation (standard deviation) of the vaporization flux of different elements must be decreased as well.

To estimate the J_i for individual elements, we must estimate the value of their corresponding vapor pressure. To approach this, it is possible to estimate it at a specific temperature, using Alcock equations [273] in the form of a polynomial:

$$\log P_i = A_i + \frac{B_i}{T} + C_i \log T + \frac{D_i}{T^3} \qquad 4.2$$

where A_i, B_i, C_i and D_i are values depending on the element i; commonly used values are provided in Table 4.5 [273]. The equation is applicable within the indicated temperature range and the fitted coefficients depend on the state of the material (solid or liquid). Due to the limited available data, coefficients are available over limited temperature ranges, and sometimes for the solid or liquid state only, the latter being the ones needed. To overcome this problem, we will assume that the equations can be extended beyond the specified temperature ranges, and hold for both solid and liquid states. To verify these hypotheses, the vapor pressure calculated from Alcock equation at temperatures higher than the provided temperature range were calculated and compared to existing data. For instance, if we consider the example of Al, according to [274], it has a vapor pressure of 2 atm at 2610 °C, compared to 1.97 atm calculated using the Alcock equation. Additionally, the equations for liquid metals can be found for several metals but for other ones (W, Mo, Cr, Nb and Mn), only equations for the solid can be found. However, Figure 4.7, shows that, when equations are found for both the liquid and solid metal, they seem to give similar values over the range of temperatures of interest. Consequently, it is here estimated that the use of equations established

for solid state, when equations for the liquid are not found for the concerned metal, will still give a good estimation.

Table 4.5 Coefficients of vapor pressure equations for different elements ("m.p." stands for "melting point"). Alcock approach, see Equation 4.2, pressure being in atm and temperature in K.

Element i	A_i	B_i	C_i	D_i	Temperature range [K]
Fe solid	7.1	-21723	0.4536	-0.5846	298-m.p.
Fe liquid	6.347	-19574			m.p.-2100
Ni solid	10.557	-22606	-0.8717		298-m.p.
Ni liquid	6.666	-20765			m.p.-2150
Cr solid	6.8	-20733	0.4391	-0.4094	298-2000
Co solid	10.976	-22576	-1.028		298-m.p.
Co liquid	6.488	-20578			m.p.-2150
Mn solid	12.805	-15097	-1.7896		298-m.p.
Mo solid	11.529	-34626	-1.1331		298-2500
W solid	2.945	-44094	1.3677		298-m.p.
W solid	-54.527	-57687	-12.2231		2200-2500
V solid	9.744	-27132	-0.5501		298-m.p.
V liquid	6.929	-25011			m.p.-2500
Ti solid	11.925	-24991	-1.3376		298-m.p.
Ti liquid	6.358	-22747			m.p.-2400
Al liquid	5.911	-16211			m.p.-1800
Nb solid	8.822	-37818	-0.2575		298-2500

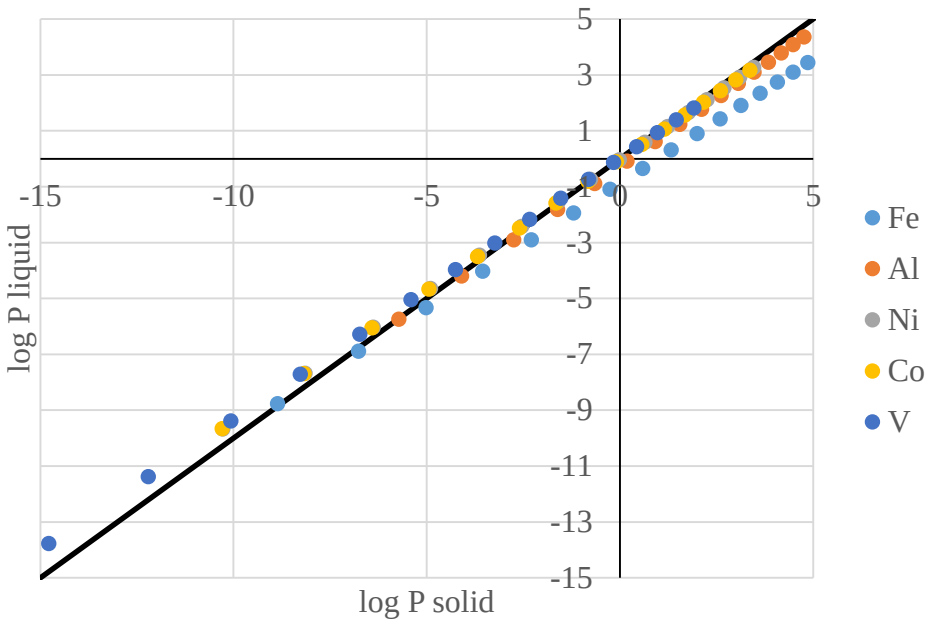

Figure 4.7 Vapor pressure values (in atm) obtained from Alcock equation established for liquid and solid states for several metals, when coefficients are available for both states; the solid line would indicate a perfect agreement between both values.

In our study, we set both the average vaporization flux of the elements as well as the standard deviation of their corresponding values as objectives to be minimized at the boiling temperature of the alloy estimated by a sum rule, respectively to avoid porosity through keyholing and to avoid compositional changes due to differential vaporization.

4.5 Controlling the effects of surface tension

4.5.1 Role of surface tension in AM processes

AM processes involve liquid metal, so that different properties of materials in this state are of practical importance and need to be studied. Among them, the surface tension (ST, γ) is crucial, as two different effects involving this property may be feared: (i) the ST value influences the conditions of wetting of the previously deposited solid phase by the liquid one; (ii) the absolute ST value and its variation with temperature contribute to the control of the meltpool stability and shape [275], and can play a role in balling, spattering, and in the formation of porosity due to keyholing through the phenomenon of Marangoni convection. The latter being a phenomenon that causes a convection motion driven by temperature-induced surface tension variations.

In the first case, the ST value influences the capability of the meltpool to form a continuous and stable seam. For high scanning speed and with a low deposited energy, the length of the meltpool increases compared to its diameter, resulting in the balling effect detailed in section 1.1.5.4. The larger ST is, the faster an instability in the melt is going to happen. To understand this dependence with ST, an analogy can be driven from Equation 4.3 [276]:

$$\tau \propto \sqrt{\frac{\rho R^3}{\gamma}} \qquad 4.3$$

with τ the characteristic time for the breakup of a fluid jet into drops, R the jet radius, ρ the fluid density and γ the ST value. It can be concluded that a decrease of ST would result in a larger time for breakup, possibly longer that the time for solidification, therefore resulting in the prevention of the balling effect. The decrease of ST would result, overall, in a better geometric stability of the seam.

In the second case, the variation of ST with temperature is contributing to the emergence of instabilities such as keyhole. Bayat *et al.* [277] demonstrated that the keyhole is intrinsically unstable and the transition from a shallow meltpool to a keyhole regime is in fact a result of a chain of multiple interconnected physical phenomena. The authors also showed that pores are generally formed due to the presence of cold zones with higher surface tension and insignificant recoil pressure (the pressure caused by the evaporation of metal on the surface of a meltpool). Khairallah *et al.* [278], [279] developed a model in which they considered the effect of both the recoil pressure and the Marangoni effects. They showed how, when the meltpool becomes deeper, there are higher chances of entrapping evaporated gas bubbles. In fact, especially for stainless steels, several studies have shown that the fluid flow within the meltpool is dominated by the force of Marangoni which is induced by the surface tension gradient ($d\gamma/dT$) of the molten metal [280], [281].

Therefore, a key factor governing the shape of the meltpool is the surface tension gradient with respect to temperature. This has also been seen in welding, as several studies report the change in the meltpool shape from wide and shallow to deep and narrow as the sign of the gradient changes from negative to positive [282] (see Figure 4.8).

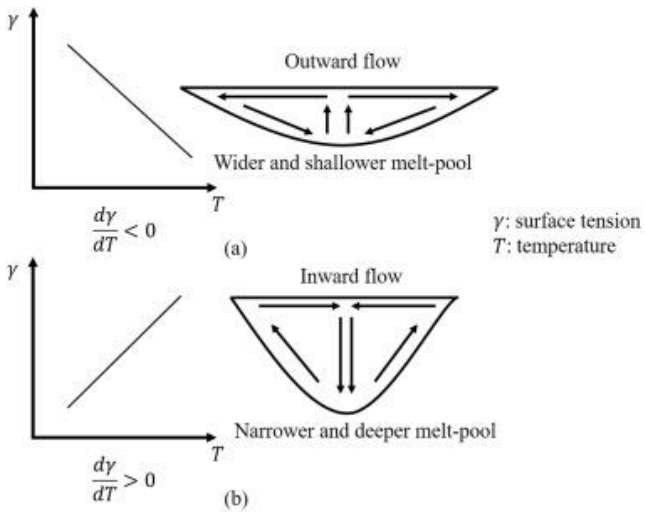

Figure 4.8 Effect of surface tension temperature gradient on the meltpool geometry where γ is the surface tension [282]

Hence the gradient of the surface tension could also be considered as a criterion to better control the shape of the meltpool. The possibility of calculating this value and its corresponding difficulty will be presented and discussed in the next subsection.

4.5.2 Theoretical models of surface tension

It is currently admitted that the ST value depends on the temperature of the liquid, pressure and chemical composition of the alloy [283], [284]. Generally, for a wide range of materials, ST decreases with temperature [285]–[288]. There is no general rule about alloying effects on ST in comparison to pure elements. Typical values in metals and alloys range between 0.4 $N.m^{-1}$ (e.g. Li at 453 K), and 2.5 $N.m^{-1}$ (e.g. W at 3650 K) [284].

Experimental measurement of surface tension in metallic alloys faces many challenges and is subjected to numerous risks of error. The difficulties come from several features. First, the measurements need to be performed in the liquid state, at high temperatures, facing an obvious risk of contamination (oxidation) that is difficult to be avoided. Moreover, real alloys currently contain impurities; some of them (S, O) have a significant effect on ST, decreasing its value even if present in very low contents [289]–[293].

The theoretical description of surface tension, based on alloys thermodynamics, started at the beginning of the 20^{th} century, with the first approaches proposed by Gibbs [294] and improved by Guggenheim [295], [296]. Finally, the Butler model proposed in 1932 [297] became the most known and used one to estimate ST from the chemical composition of the alloy.

Although it provides a fair estimation, the Butler model remains inaccurate in many cases, probably due to neglecting the atomic structure of liquid alloy surfaces [298]. Recently, Vermot des Roches *et al.* [299] have compared the results of ST calculations by the Butler model to

available experimental data on binary alloys; it was shown that it fails to accurately predict almost 40% of them. Other modeling approaches (Wynblatt *et al.* [300], Egry *et al.* [301], [302]) are sometimes successful in describing several binary systems such as Al-Au and Al-Ni. Yet, a general model, that would be able to describe all existing alloys, or at least the compositional ranges covered by the present study, is still missing.

Some authors proposed models relating the ST value in a given metallic matrix to the presence of different surface-active elements. An interesting approach was presented by Ghebiri *et al.* who proposed a semi-empirical model describing the oxygen content effect in different metallic liquids [303]. The authors assessed the predictability of their model by describing the effect of oxygen on the surface tension of several pure elements (Cu, Co, Ni…) and showed an agreement between the model predictions and experimental data.

Although several theoretical models have been proposed to describe the ST, mainly in binary systems [295], [297], [300], [304], and some authors have used them to estimate the ST values and their evolution for ternaries and multi-element alloys [305]–[307], both experimental studies and existing theoretical models mainly focus on simple systems. Rare are the results coming from alloys containing three or more elements, except experimental measurements in a few grades of industrial alloys, as austenitic stainless steels [308]–[310] and Ni-based superalloys [311], [312]. Besides, the lack of models for multicomponent systems is due to the difficulty in physically modeling the complicated behavior of ST when several elements are included and the large number of parameters it requires to assess.

4.5.3 ML model to predict ST

In our work, due to the lack of a reliable physical model, we propose a general machine learning (ML) model to predict the surface tension of metallic alloys. The model is based on a Bayesian algorithm, specifically Gaussian process regression (GPR). This work will be published [accepted; Journal of Materials Science], and all details on the database used as well as the construction steps and evaluation of the model can be found in Appendix C. Some of its main features are nevertheless reminded below.

To construct the model, it was necessary to build a database from available experimental measurements reported in the literature. In total, around 2200 data points were collected from approximately 70 articles. The data considered consist of purely experimental data, and although incorporating simulated data and data coming from other modelling approaches in the training set could potentially bring insightful outputs, it would require a more elaborate work. The elements considered are Ag, Al, Au, C, Co, Cr, Cu, Fe, Ge, Li, Mg, Mn, Mo, Nb, Ni, Si, Sn, Ta, Ti, W, Zn, and Zr. These data points are measurements recorded at different temperatures, for which around 520 points are for pure metals, 1257 for binary systems, 350 for ternary systems, and less than 140 points for quaternary and higher order alloys. Impurities such as oxygen, sulfur and phosphorus behave differently than the above-listed elements and would require a separate approach. Hence,

they were not included in the composition vector. It is assumed, being present in most alloys as non-controlled trace impurities with a "random" concentration, that their average role can already be captured thanks to the statistical nature of GPR, and that their influence would remain similar in designed alloys, so that the developed model will be used to predict the sole effect of alloying elements that are incorporated on purpose.

To evaluate the predictability of the model, a cross-validation was done. The average values of the evaluation metrics for both the training and the testing sets, computed with the ten-fold cross-validation method, are shown in Table 4.6.

Table 4.6 Machine learning model for surface tension prediction. Average and standard deviation values for different evaluation metrics using the ten-fold cross validation method [see [313] *in Appendix C]*

	test R^2	**train R^2**	**test MSE**	**train MSE**	**test MAE**	**train MAE**
Average	0.9783	0.9950	0.0237	0.0050	0.0581	0.0419
Standard deviation	0.0294	0.0003	0.0369	0.0003	0.0091	0.0008

It can be seen that the overall performance of the model is very good with an MSE average of around 0.02 and an R^2 value of 0.97. Figure 4.9 shows the cross-validation prediction results as well as the final prediction results of the model after training as a function of the real measurements. The majority of the points lie close to the line with slope 1, indicating a generally good prediction accuracy of the model. Nevertheless, there remains a few data points for which the model shows a relatively high error in prediction, especially in the cross-validation test results. Several of these points can be explained by the insufficiency of data to cover a particular material or specific compositional domains. For example, Mg and W-based alloys are only described with 14 data points each. Hence, it is unavoidable that the model fails to correctly predict these points when they lie within the testing set. The same could be said about Li and Zn, which are represented with 10 and 24 points respectively, especially that these points are located on the extremes of the database. Li and Mg have some of the lowest ST values of 0.39 and 0.55 $N.m^{-1}$ respectively at their melting temperatures, compared to 3 $N.m^{-1}$ for W. It is also normal to observe that the predicted value for the mentioned points is correct when the model is trained on the whole dataset, as shown in Figure 4.9 b. Of course, there remain a few points that still show a higher error even after training (see article in Appendix C for details and further discussion). However, for most of these points the error is below 0.3 $N.m^{-1}$, which remains moderate.

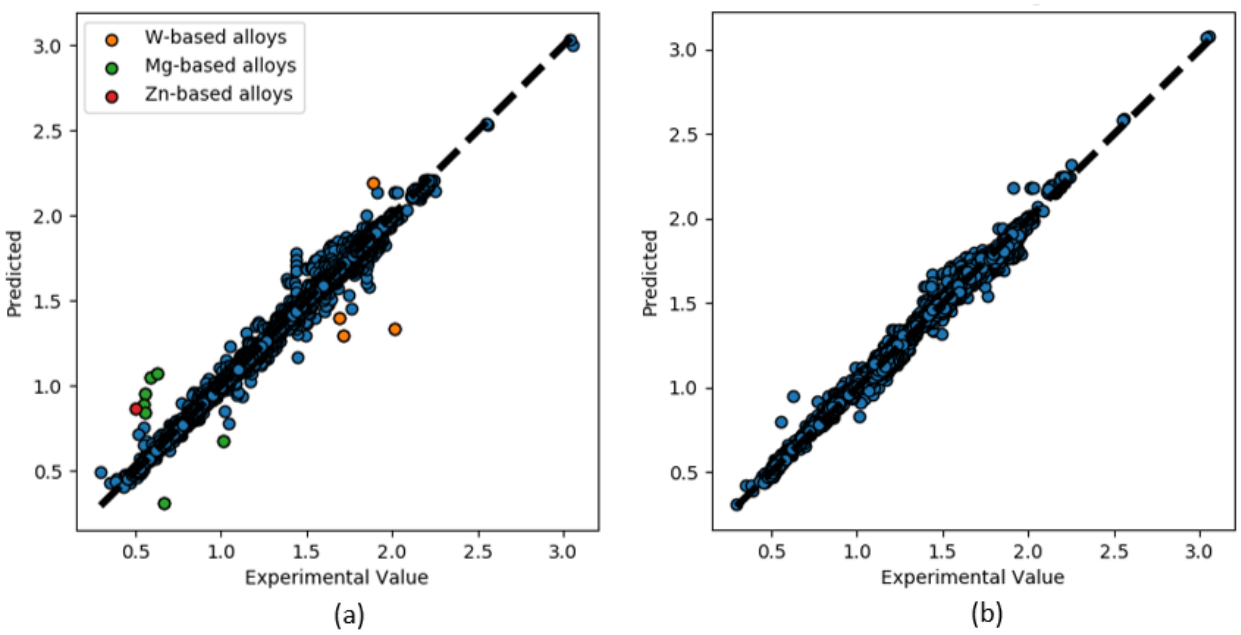

Figure 4.9 Predicted surface tension values (in N.m^{-1}) as function of the experimental values from literature for a) ten-fold cross validation b) the final trained model on the whole dataset [see [313] *in Appendix C].*

The detailed steps on the evaluation of this model for binary, ternary and higher-order systems are included Appendix C.

To discuss on the employment of this model in our optimization problem for alloy design, it is important to consider its generalization capability in the case of multi-element materials. For this purpose, the ability of the ML-GPR model to extrapolate towards the behavior of systems containing at least three elements, on the basis of data coming from simpler ones (since it has been built mainly from pure elements or binary systems, and to a minor extent from higher-order systems) was analyzed. Therefore, the ML-GPR model was trained again on solely pure materials and binary alloys. Then, the available experimental ST values of several ternaries and higher-order systems were used as test points. The results showed that it is possible to extend the model to higher-order systems as long as the compositional space of the lower order systems involved is sufficiently well described. The range to which it can be extrapolated could be individually discussed based on the statistical representation of the system on topic, but also with the help of the error bars provided by the algorithm. As a consequence, since it was assessed that a model learnt from unaries and binaries could make good predictions in the case of ternaries, it was assumed that the model learnt using all available data should be able to provide fair predictions of the trend of ST in the case of multicomponent alloys with a maximum error range of around 0.3 N.m^{-1} (see article in Appendix C).

On the other hand, the prediction of the ST dependency on temperature showed less satisfying results. To illustrate this, Figure 4.10 shows the variation of ST for the Cantor alloy as a function

of temperature. As it is shown, the variation in the ST value with temperature is very limited (less than ~0.1 $N.m^{-1}$), especially compared to the predicted error range (~0.3 $N.m^{-1}$). This indicates that the model may be less accurate for predicting the temperature effect on the trends of ST, and shall not be taken into consideration.

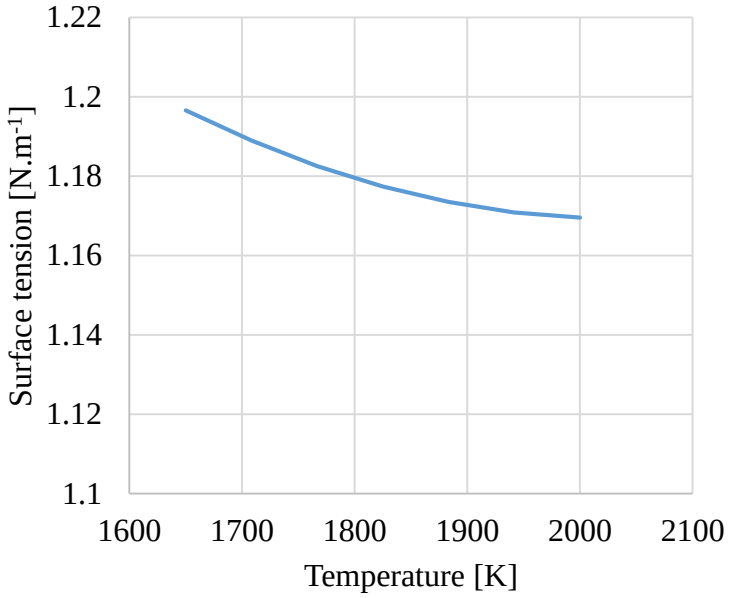

Figure 4.10 Predicted surface tension [$N.m^{-1}$] value for the Cantor alloy as a function of temperature [K].

Therefore, an objective to minimize the ST value predicted with this model is set. The ST value will be calculated at the liquidus temperature of the alloy, determined by Thermo-Calc.

4.6 Minimizing residual stresses

The successive addition and melting of layers in the process of SLM has a direct effect on the final level of residual stresses in the built component. Although the detailed description of the thermal history effect is complicated, there are certain material properties which have a direct influence on the residual stresses. The factors responsible for residual stresses in AM components are the spatial temperature gradient caused by localized heating and cooling as the heat source moves following the selected scan strategy, and the resulting thermal expansion and contraction of the material due to heating and cooling (illustrated in Figure 4.11), ending in an uneven distribution of plastic

strains (strain compatibility). The phenomenon can also be seen in fusion welding processes [271], [314]–[316].

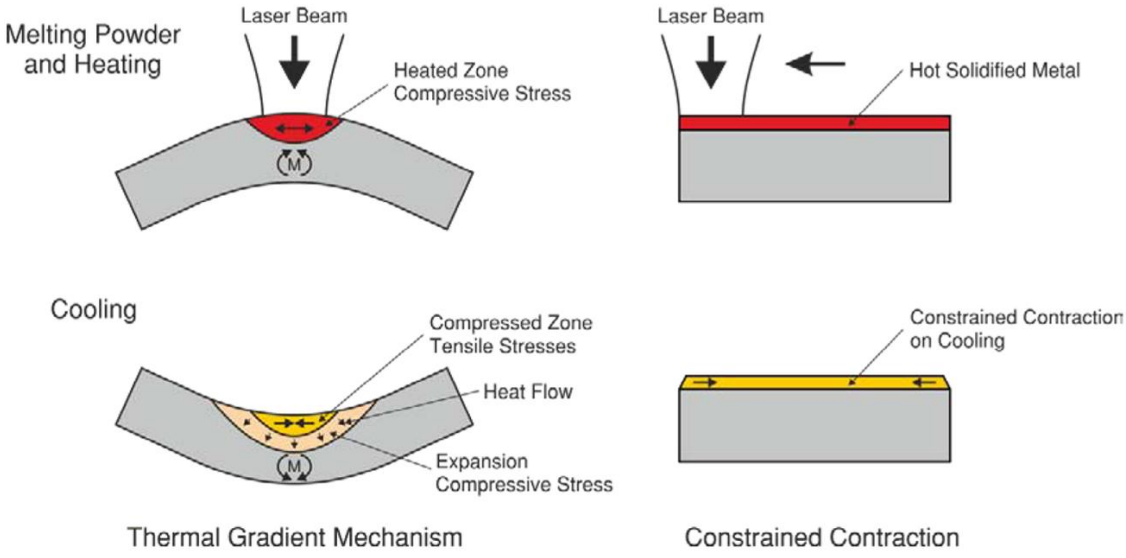

Source: Adapted from (Vollersten 1998); (Shiomi *et al.* 2004)

Figure 4.11 Schematic of the compressive and expansion forces in the heated zone [317].

The development of residual stresses depends on a set of phenomena related to processing and to material properties, including thermal expansion and thermal conductivity, as well as elastic and plastic properties. Complex descriptions exist [318]–[320] but, as a general rule and to focus on material properties, avoiding the risk of cracking [321] would require:

- a high thermal conductivity to reduce thermal gradients within the built part;
- a low coefficient of thermal expansion to minimize thermal strains that are proportional to it;
- a low Young's modulus, and, secondarily, a high Poisson's ratio, to minimize thermal stresses since, for given thermal strains, elastic stresses are proportional to E/(1-ν);
- a high fracture stress to be able to withstand high stresses without fracture.

Similarly to one of Hasselman's thermal shock resistance parameters for ceramics [322], this would be expressed as an index to be maximized [321] :

$$I = \frac{k.\sigma_f(1-\nu)}{E.\alpha_{CTE}} \qquad 4.4$$

where σ_f is the fracture stress, k is the thermal conductivity, E is the Young's modulus and α_{CTE} is the coefficient of thermal expansion.

This relies on the development of elastic stresses only, but it can be assumed that the trends it gives are correct.

However, the variation of the Young's modulus within the family of austenitic stainless steels is usually quite low. Indeed, the immense majority of austenitic stainless steels have a Young's modulus in the range 190-210 GPa, i.e. within +/- 5%. The Poisson's ratio is also only slightly dependent on composition.

As already stated, the thermal conductivity has a set of various effects in AM, so that maximizing it could be problematic and result in the formation of other defects, and in difficulties to reach a sufficient temperature with the laser to melt the material. With highly conductive materials, the extraction of heat from the meltpool through conduction is fast and hence the energy loss is high. It has been shown that this leads to a smaller process window as it could, coupled with other parameters, lead to phenomena such as balling, porosity and finally crack formation [230]. Therefore, it is considered that varying this material property may not bring the desired outcome, and it is here chosen to ignore it.

Finally, going back to the expression of Equation 4.4, as the strength will be considered as a separate criterion (see section 4.7) and the variation range of Young's modulus is not significantly important for stainless steels, the objective function is set as to minimize α_{CTE}. In addition to residual stresses and their impact on cracking, macroscopic distortions of built parts also largely depend on the coefficient of thermal expansion [321], so that trying to minimize it would act in the proper direction as well.
To estimate the coefficient of thermal expansion, a rule of mixtures is used following the approach of [323]. For the different elements i of the alloy, X_i being the element atomic fraction, α_{CTE} can be estimated by a simple rule of mixtures, as in Equation 4.5:

$$\alpha_{CTE} = \sum_i X_i \alpha_{CTE_i} \qquad 4.5$$

where α_{CTE_i} is the coefficient of thermal expansion of pure element i.
Values for the different elements considered in the search space of this study are given in Table 4.7. The values taken for the CTEs of individual elements are at room temperature. Therefore, the CTE of iron is that of ferrite. This will lead to underestimated CTEs for the austenitic alloys aimed at, but it will not impact our design strategy. Indeed, applying the linear equation 4.5 with any value for the CTE of the base element (iron) will give exactly the same trends as a function of the concentrations in other elements. Since we will aim at minimizing the CTE, the result will be semi-quantitatively identical.

Table 4.7 Coefficient of thermal expansion (10^{-6}/K) for several elements in the range of 300 K [324].

Element	Fe	Cr	Ni	Co	Mn	Mo	Al	Nb	Si	Ti	W	C
α_{CTE} (10^{-6}/K)	12.3	6.2	13.3	13.4	22	5.43	23	7.07	2.6	8.35	4.59	1.19

4.7 Ensuring strength

4.7.1 Physical models of solid solution hardening

As mentioned before, it is desired to maximize the strength of the material. In the absence of strain hardening, the yield strength, σ_y, of an alloy can usually be expressed as:

$$\sigma_y = \sigma_0 + \Delta\sigma_{HP} + \Delta\sigma_{PH} + \Delta\sigma_{SSH} \qquad 4.6$$

Where σ_0 is the yield stress of the single crystal of the main element, $\Delta\sigma_{HP}$ is the increase in strength due to the effect of grain size (i.e. Hall-Petch effect), $\Delta\sigma_{PH}$ is the precipitation hardening and $\Delta\sigma_{SSH}$ is the solid solution hardening. In this particular study, we have ignored the effect of precipitation since we are aiming at designing single phase steels. The effect of grain size is also excluded from the optimization criteria, since it is assumed to be mostly process dependent. The term left is the solid solution hardening.

Solid solution hardening originates from the interaction between solutes and lattice dislocations. When a dislocation moves in the crystal, the distortion it induces on the lattice interacts with the distortions around the substitutional solutes. In cubic materials, substitutional solutes distort the lattice geometrically due to the size mismatch between the atoms of the solute and the host, but also, chemically by introducing a different local bonding environment. In general, theories of solid solution hardening (SSH) can be mainly classified into two categories: strong-pinning and weak-pinning models [325], [326]. Strong-pinning models treat solutes as independent point obstacles which pin dislocations, therefore the effect of a solute atom in the crystal structure of solvent can be described in isolation, especially in the case of a low solute content. Dislocations can bow out between solutes, and can break free with the application of an additional stress. Models in this category include the ones proposed by Friedel [327] and Fleischer [328], [329]. The latter suggested that the SSH effect can be expressed as:

$$\Delta\sigma_{SSH} = \sum_i B_i X_i^{\frac{1}{2}} \qquad 4.7$$

where:

- X_i: content (atomic fraction) of solute i
- $B_i = 3\mu\varepsilon_i^{(\frac{3}{2})} Z$: depends on the shear modulus μ of the alloy, the mismatch parameter ε_i and a fitting constant Z; multiplier 3 stands for the Taylor factor
- $\varepsilon_i = |\eta_i'| + \alpha|\delta_i|$
    - $\eta_i'\ (elastic\ misfit) = \eta_i/(1 + 0.5|\eta_i|)\ ;\ \eta_i = d\mu/dX_i . 1/\mu$
    - $\delta_i\ (atomic\ size\ misfit) = da/dXi\ .1/a$

      a= cell parameter of the alloy

      α is a parameter that accounts for the difference in interaction forces between screw and edge dislocations and the solute atom; in general a value $3 < \alpha < 16$ is given for screw dislocations and $\alpha > 16$ for edge dislocations

On the other side, weak-pinning models, firstly proposed by Mott [330] and Labusch [331], [332], take into consideration the effect of randomly-distributed solutes on the dislocations. In this case, dislocations are subjected to a frictional effect due to constant interaction with solute atoms, as opposed to the blocking effect discussed in strong-pinning models. Similar to the expression of Fleischer, Labusch described the SSH effect in the following manner:

$$\Delta\sigma_{SSH} = \sum_i B_i X_i^{\frac{2}{3}} \qquad 4.8$$

where:

- X_i: solute content (atomic fraction) of component i
- $B_i = 3\mu\varepsilon_i^{(4/3)} Z$: constant depending on the shear modulus μ of the alloy, mismatch parameter ε_i and fitting constant Z
- $\varepsilon_i = (\eta_i'^2 + \alpha^2.\delta_i^2)^{0.5}$, with η_i' the same as above

There are many similarities between the two approaches and there are some works showing a good experimental fit to both expressions [333], [334]. However, there seems to be a larger number of works reporting a better agreement with the approach of Labusch [335]–[337]. As a matter of fact, Leyson and Curtin [325] assessed the domains of applicability of the two models concluding that the Labusch model, overall, better approaches the strengthening mechanisms for metallic alloys at temperatures and concentrations relevant to engineering applications.

In the case of highly concentrated alloys, several models have been proposed in literature as well. Toda Caraballo [338] proposed a model that relies on the concept of Labusch, but is more generalized to consider the local variation of the cell parameter in the crystal structure attributed to the local combination of different elements which causes a "lattice distortion" effect. The author's approach presents an improvement in the prediction of highly multi-concentrated alloys such as CoCrFeMnNi or AlCoCrCuFeNi systems, compared to the Labusch model.

Similarly, Walbrühl *et al*. [156] proposed a general SSH model for multicomponent alloys based on the Labusch model, but considering a non-linear composition dependence to the strengthening parameter by directly fitting the model to existing experimental data. Their results showed a better description for concentrated alloys with an overall accuracy of ±13%.

Finally, the approach of Labusch constitutes a basis for the development of SSH models for both binary as well as highly concentrated alloys. In our case, we remain within the domain of Fe-rich alloys, and the Labusch model is considered sufficient to describe the SSH for such alloys.

4.7.2 Solid solution hardening index: an approximation based on Labusch model

For reasons mentioned in the above subsection, in our study we will proceed by using the physical model of Labusch. To obtain an approximation of the solid solution strengthening value from this model, it must be accompanied by calculation of the misfit parameters for the different alloying elements involved.

According to Zander *et al.* [154], [339], solid solution hardening comes from the mismatch in size and modulus of the solute atoms, thus creating a strain field that can be defined as:

$$\epsilon_b \text{ (usually referred to as } \delta\text{i)} = \frac{db}{bdX_i} \qquad 4.9$$

$$\epsilon_S = \frac{d\Omega}{\Omega dX_i} \qquad 4.10$$

$$\epsilon_G = \frac{d\mu}{\mu dX_i} \qquad 4.11$$

where ϵ_b and ϵ_S are related to the atomic size misfit (usually referred to as δ_i), ϵ_G is related to the elastic shear modulus misfit, b is the Burgers vector, Ω the atomic volume, μ the shear modulus and X_i the atomic fraction of the solute.

The atomic size misfit value depends on the crystal structure; yet, b is always proportional to the lattice parameter a. Thus, replacing b in the previous equation gives:

$$\delta_i = \frac{da}{adX_i} \quad 4.12$$

For FCC crystals, $a = \frac{4r}{\sqrt{2}}$, with r the average atomic radius, which implies :

$$\delta_i = \frac{dr}{rdX_i} \quad 4.13$$

According to Vegard's law [340], the lattice parameter of a solid solution can be approximated by the weighted average of the lattice parameters of its separated constituents. In our case, as we are aiming at iron-rich alloys, we assume that Fe is the basis, or solvent element. As a consequence, by considering Fe as the solvent, the equivalent atomic radius r of the solution follows a weighted mean as well:

$$r = (1 - X_i)r_{Fe} + X_i \cdot r_i \quad 4.14$$

With r_i the atomic radius of the solute and r_{Fe} the atomic radius of the iron solvent. This implies that:

$$\frac{dr}{dX_i} = -r_{Fe} + r_i \quad 4.15$$

Then, by combining the previous equations, we obtain:

$$\delta_i = \frac{dr}{rdX_i} = \frac{r_i - r_{Fe}}{(1 - X_i)r_{Fe} + X_i \cdot r_i} \quad 4.16$$

This expression can be used to assess the capability of a solute element to increase the yield stress by solid solution strengthening.

As for the term of the elastic misfit, in general, the variation of shear modulus with composition is assumed to be linear [323], [341], and it will be assumed that the parameter η_i can be estimated as [342], [343]:

$$\eta_i = 2\frac{\mu_i - \mu_{Fe}}{\mu_i + \mu_{Fe}} \quad 4.17$$

where μ_{Fe} and μ_i are the shear moduli of solvent (Fe in our case) and solute, respectively. To simplify, the elemental shear modulus is taken for each element at its respective crystal structure.

Of course, the shear modulus changes with crystal structure (2-5%), but in this case this effect is ignored since elastic properties have been shown to mostly depend on composition [341], [344], [345].

Finally, by considering a value of 16 for α which is typically used for FCC alloys to account for the interaction of solute atoms with edge dislocations [346], is it possible to calculate a solid solution strengthening index according to Eq. 4.8, using the atomic radius and shear modulus values of elements provided in literature [347].

4.8 Summary of design criteria

The microstructure stability after solidification is the first criterion to be considered when designing austenitic stainless steels. It is necessary to control the phases present in order to be able to take benefit from the good properties of the material for the desired application. Based on this, the stability of phases was discussed in two steps. The first is to set a constraint for the feasibility of the researched alloys based on the **Hull diagram**. Secondly, the phases forming during solidification are also calculated using the Scheil module by Thermo-Calc in which a constraint is set as to accept a maximum of 1% as a sum of "undesired phases" (i.e. other than iron-based solid solutions) at the end of solidification. In addition to these two steps, the effects of alloying elements on the different discussed criteria in general, and on phase stability in particular, were also reviewed. Accordingly, the elements and their corresponding variation range will be further discussed in the optimization chapter.

The Scheil-Gulliver simulation will also allow us to calculate the set of solidification criteria to ensure a low cracking susceptibility for the designed alloys. This includes minimizing the **critical temperature range** (CTR) as well as constricting the solidification path of the alloy in the FA (Ferrite-Austenite) mode. Alloys solidifying in any of the other different modes will be considered infeasible. As for the CTR, it is set as an objective to be minimized.

To ensure a good strength, and a better resistance to thermal strains, the **solid solution hardening** of the alloy is set as an objective to be maximized. The value will be estimated using the Labusch solid solution model.

In addition to increasing the strength of the material, to ensure a low level of residual stresses in the final component it was seen that the **coefficient of thermal expansion** must be minimized. This will be calculated using a rule of mixtures (linear combination of the CTE of alloying elements).

To optimize the meltpool and surface stability of the designed alloys, several properties were taken into consideration. It was shown that the **vaporization fluxes** play a significant role in controlling the vaporization of elements from the meltpool. Vaporization, coupled with keyholing, can lead to

the entrapment of gas bubbles within the meltpool and could therefore induce porosity in the final component. For this reason, the average vaporization flux of the elements within the meltpool, calculated from the partial vapor pressures of the compositional elements, will be minimized as to avoid the formation of porosity due to the entrapment of evaporated gas bubbles. Similarly, the distribution of this value will also be minimized as to avoid a change in composition caused by the imbalance in the vaporization of the different compositional elements.

Finally, the **surface tension** of the designed alloys is considered. To avoid phenomena such as balling or swelling, the surface tension will be searched to be minimized. The surface tension is to be estimated using a Gaussian process regression model. Although the temperature gradient of the surface tension also plays a role in the final meltpool geometry, it will not be considered due to difficulties in accurately calculating this value.

It must be noted that, in all of the studied models, the goal is to minimize or maximize the predicted output as a function of composition, so that making a precise prediction of the exact value of the property is of secondary importance as long as correct trends are predicted. Therefore, any systematic bias in the modeling of properties would not affect the global optimization.

Finally, all the discussed objective functions and constraints will be incorporated in a genetic algorithm which will be further detailed in the following chapter.

5 Multi-objective optimization and selection of alloy for experimental validation

In the previous chapter we have defined the criteria that will be the basis to constitute a set of objective functions and constraints to design austenitic stainless alloys, optimized for AM processing. As stated, this calls for the use of a multi-objective optimization algorithm.

In this chapter we present the details of applying this algorithm, and its results, which will allow us to select an original composition for experimental validation.

5.1 Compositional search space

There is quite a large number of elements that are currently present in stainless steels. Each of them has a specific role and influences the material properties in some way. The different alloying elements and their effect have been extensively studied in literature [95], [348], see also section 1.2. An overview of the alloying elements found in about 500 industrial steels (iron-rich; containing at least 30 wt.% Fe) as well as their approximate compositional ranges is shown in Table 5.1.

Table 5.1 Alloying elements and their concentration ranges, from a database of ~ 500 iron-rich alloys [324].

Element	wt.%	Element	wt.%
Fe	30-100	N	0-1
Cr	0-30	Zn	0-4.5
Ni	0-35	Sn	0-2.5
Mn	0-23	V	0-0.5
Si	0-17	Se	<0.3
Mo	0-7	Ta	<0.1
C	<1	Pb	<0.3
Cu	0-4	B	<0.01
Co	0-20	Mg	<0.01
Al	0-2	Zr	<0.01
Ti	0-2.2	S	<0.4
Nb	0-1	P	<0.2
W	0-3		

In general, the main alloying elements for iron-rich austenitic materials are Ni, Mn and Co, since they tend to stabilize the FCC solid solution, as well as Cr to ensure a good corrosion resistance. The majority of the elements have a lower and upper bound depending on the final application of the alloy and therefore the desired properties. On the other hand, some elements are often present as impurities and are in most cases technologically unavoidable, such as sulfur and phosphorus. The content of these elements is sought to be limited to a minimum (usually < 20 ppm), and higher amounts are only added in very rare cases. For example, sulfur in higher amounts (up to 0.1-0.3 wt.%) is sometimes added to increase machinability, such as the case of AISI 303 alloy.

Other elements like Mg and Zr usually have a too low level to be considered in the composition and therefore they do not play a crucial role on the properties of the material. B is often added to to improve creep properties of stainless steels used at high temperatures, but is present in too small content to have an effect on the criteria considered in our study. Elements such as Cu and Sn are usually added in limited amounts as well, either to improve the corrosion resistance of the alloy or to increase strength through the formation of precipitates, which is out of the scope of our work. Despite nitrogen being a very interesting addition due to its high austenite stabilizing power and its positive effect on increasing the mechanical resistance of austenitic steels, there are technological difficulties associated with adding it while controlling its exact content in the final alloy, due to the nature of AM processes. Indeed, nitrogen may escape from the meltpool, so that a shielding gas containing N_2 should be used which, conversely, may lead to a too high concentration of nitrogen in the alloy. This is for instance a known problem in the welding of duplex stainless steels, which we want to avoid.

In this study, we decided to consider only iron-rich alloys, which is why a minimum amount of 30 wt.% of Fe was set. To ensure a good corrosion resistance of the alloy, including intergranular corrosion resistance, two compositional limits are set. First, the minimum content of Cr was set at 15 wt.%; second, the content of C was set to 200 wt. ppm, as in “low carbon” SSs. Indeed, increasing the chromium content and limiting the carbon content is a common practice in designing stainless steels, in order to avoid the intergranular precipitation of Cr carbides, accompanied by a depletion in chromium in the vicinity of carbides-containing interfaces. Currently, it is considered that in austenitic structures, a local chromium content above 11% is necessary to stabilize the protective Cr_2O_3 oxide. This approach is seen in the L series of industrial austenitic stainless steels where the content of carbon is usually limited below 300 ppm. Another essential element in the designed alloys is nickel. As previously shown in section 4.1, Ni is a strong austenite stabilizer and its addition expands the austenitic phase region.

Although no lower limit is effectively set for Ni, the criteria based on the Hull diagram to obtain austenitic structures, while having a minimum of 15 wt.% of Cr, imply that at least 10-12% of Ni is expected in the final material, but the optimization algorithm should find it automatically. Similar to Co and Mo, one drawback of Ni is its high price. Manganese and cobalt are also major alloying elements for which a high upper range (25%) is set for the compositional search space. Mn is an austenite stabilizer and a common solid solution strengthener used in austenitic alloys.

On the other hand, Mn is known to be highly volatile and has the tendency to form manganese oxides. Cobalt is also an austenite former; moreover, its addition can significantly enhance the strength of the austenitic matrix as well. However, this element has been often avoided for several reasons (high cost, low and risky availability, difficulties in recycling). Finally, elements such as Mo, V, Nb... are expected to increase solid solution hardening.

The search space selected for this study contains twelve elements and is presented in Table 5.2. Finally, out of the larger list of elements that are commonly added to austenitic materials, in our case we choose the elements which have significant effects on our design criteria, and for which the content is technologically possible to control without too much hassle. The range of their content varied from 0 wt.% (or 15 wt.% for Cr), up to a certain level which seemed reasonable according to the values already used in stainless steels (see Table 5.1), as well as in some high entropy alloys. For instance, the concentration in Ni and Cr is systematically lower than 35% for all the commercial grades, so the maximal concentration was set as this value. The maximal concentrations of the other elements are adjusted similarly based on the data coming from the commercial alloys population. No specific variation step for the inputs can be set in the algorithm we use, therefore we have set a manual threshold of 0.1% difference in elemental composition to compare the alloys afterwards, meaning that obtained compositions will be rounded up to the closest decimal percentage after optimization.

Table 5.2 The compositional search space considered for the optimization (in wt.%). The carbon concentration is fixed at 0.02 wt.% in all cases.

Element	**Fe**	**Cr**	**Ni**	**Co**	**Mn**	**Al**	**Ti**	**Nb**	**Mo**	**W**	**Si**
min	30	15	0	0	0	0	0	0	0	0	0
max	100	35	35	25	25	5	2	2	5	2	5

5.2 Implementing the NSGA-II algorithm

As shown in the previous chapter, the design of austenitic stainless steels implies a large number of objectives and constraints, and should therefore be considered in the frame of a multi-objective optimization problem. The latter in principle leads to a set of Pareto-optimal solutions rather than a single solution. Based on the definition of dominance, it can be said that without taking any additional information into account, none of these solutions can be considered “intrinsically better” than the other.

To tackle this problem, the NSGA-II algorithm (see section 2.3 and Appendix A for details) was used. There exist several approaches to set and/or optimize the parameters of a genetic algorithm; in our study, these parameters were chosen by considering the most widely used operators and associated parameter values, known to be able to tackle efficiently a vast range of optimization problems [349], while the population size (100 alloys) was chosen so as to keep a reasonable computing time.

Table 5.3 shows a summary of the set of objectives and constraints individually discussed in Chapter 4. The objectives are used to evaluate the individuals of the population —the different alloys—, and give them corresponding "scores" in order to select and rank them throughout the successive generations. On the other side, the constraints are used to evaluate the feasibility of alloys in terms of the user-set restrictions.

Table 5.3 Summary of the objectives and constraints set for the optimization.

Criteria	Constraint	Objective	Method of calculation
Austenitic structure	Belongs to feasible space on Hull diagram	Maximize distance from feasible space boundaries	Hull diagram: Cr_{eq} and Ni_{eq}
Solidification cracking	Solidification mode = FA 10% < δ-ferrite < 50% δ-ferrite + austenite > 99 % at the end of solidification	Minimize CTR	Scheil-Gulliver model
Surface tension		Minimize ST at liquidus	GPR-ML model
Coefficient of thermal expansion		Minimize CTE	Linear model
Solid solution hardening		Maximize SSH	Labusch model
Vaporization flux		Minimize average Minimize variance	Vaporization flux Langmuir equation

The algorithm flowchart is shown in Figure 5.1. In section 2.1 we stated that it is also possible to use the equilibrium phase calculations by Thermo-Calc to predict the phases at equilibrium over a range of temperatures. This approach was not included in the NSGA-II algorithm used as it was seen that the Hull diagram (using Cr_{eq} and Ni_{eq}) is a good tool to predict the as-built structure at

room temperature in the case of stainless steels produced by AM. Nevertheless, the equilibrium phase calculations are reintroduced after obtaining the results of the optimization. This additional filtering criterion will help us filter or prioritize alloys based on the range of stability of the austenitic phase.

At first, the choice of setting a go/no-go constraint based on the Hull diagram allows, if the alloy is non-feasible, its direct penalization, by arbitrarily setting all other criteria to very poor values, and non-feasible constraints. Therefore, penalized alloys are directly considered non-feasible. The aim of this step is also to avoid time-consuming computational thermodynamic calculations.

On the other hand, if the alloy is feasible, then a Scheil-Gulliver calculation by Thermo-Calc takes place. From this calculation, we obtain the solidification range, the phases formed during solidification and their respective order and fraction. If the alloy satisfies the constraints set based on the solidification mode, the range of δ-ferrite and the sum of austenite and δ-ferrite at the end of solidification, then calculation of the other criteria is done: CTE, vapor flux criteria, as well as the ST (at the melting temperature calculated in the previous step using Scheil model), otherwise it is penalized.

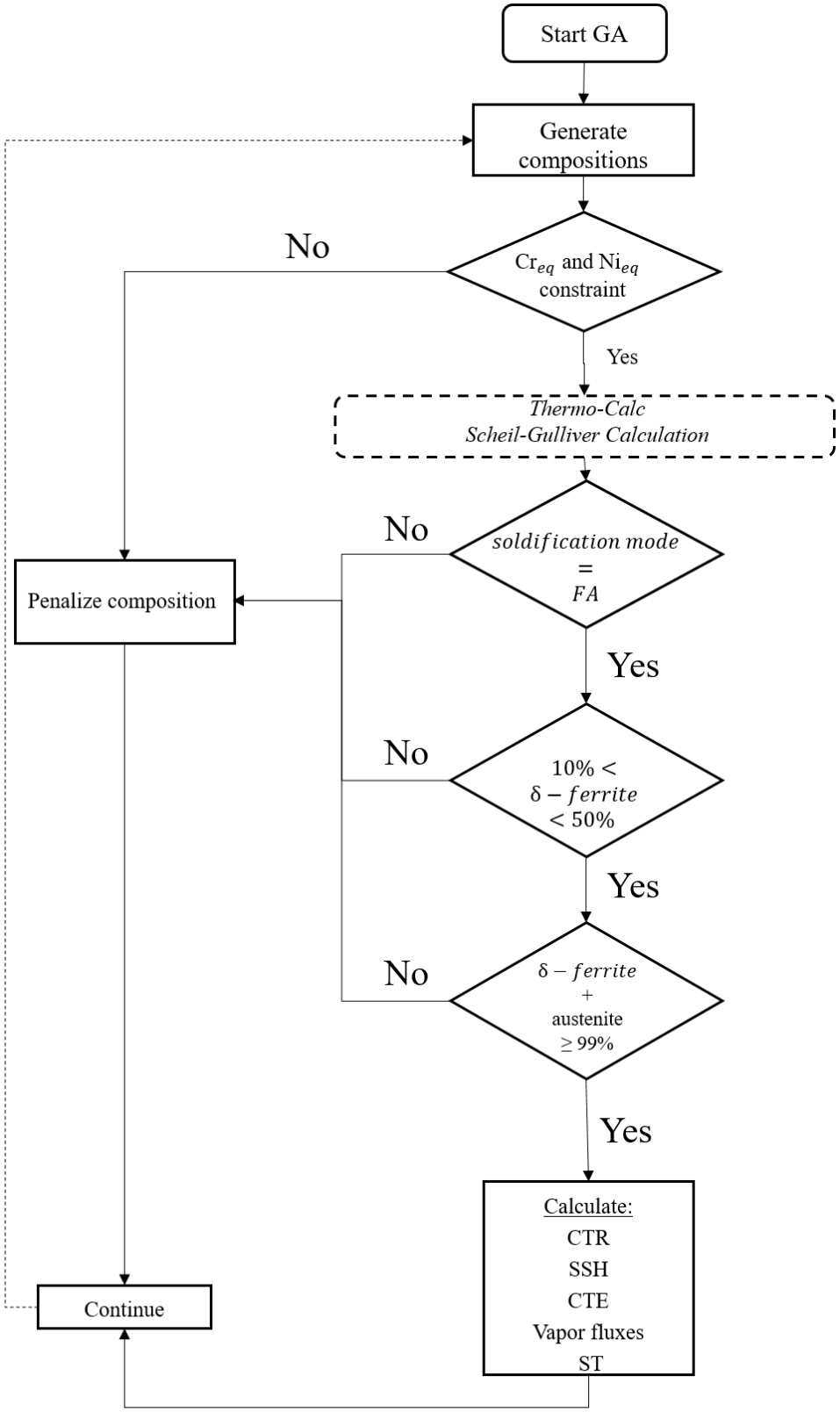

Figure 5.1 Flowchart of the applied algorithm where CTR is critical temperature range, CTE is coefficient of thermal expansion, SSH is solid solution hardening and ST is surface tension.

To use the optimization algorithm efficiently, it is also necessary to define a termination criterion. Several possibilities exist, and thorough explanation can be found elsewhere [350], [351]. In our case, we set a termination criterion based on the number of iterations (generations). Figure 5.2 illustrates the number of solutions (alloys) over the number of generations following four categories: dominated feasible ones (red line), dominated non-feasible (green line), non-dominated non-feasible (blue line), and non-dominated feasible (black line), the latter being the ones searched for.

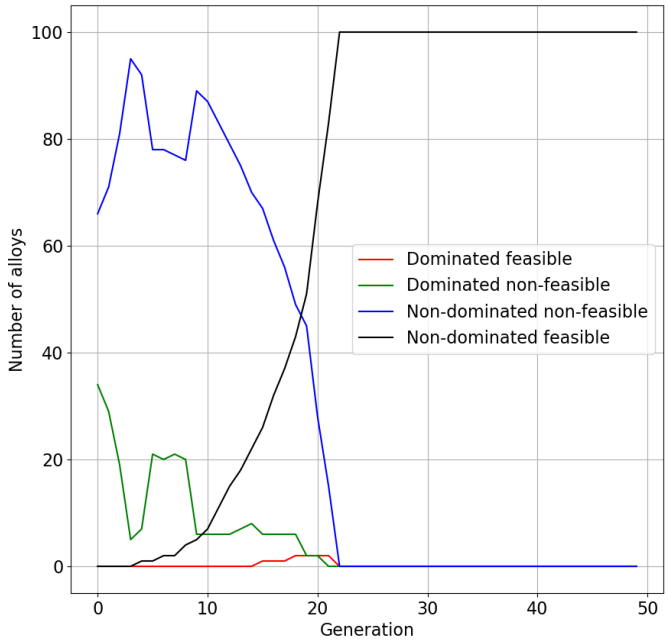

Figure 5.2 Evaluation of results of optimization with the NSGA algorithm: number of alloys on the Pareto front as a function of the generation number.

The number of non-dominated solutions is already quite high in the initial population, with 66 individuals at the generation 0. This is due to the high number of seven objectives: statistically, a solution can frequently become non-dominated on an objective, while it is dominated by some other solutions on other objectives. At the opposite, all of these solutions are non-feasible due to the four constraints. The algorithm has two effects when the number of generation increases. First, it can be seen on Figure 5.2 that the number of feasible solutions increase very rapidly. The blue curve indicates that non-feasible non-dominated solutions decrease rapidly, and reach 0 for the generation n°22. Then, the number of non-dominated solutions increases (given by the sum of the blue and black lines), while the number of dominated solutions decrease (sum of green and red). This evolution illustrates the right progression of the optimization process.

Based on Figure 5.2, one can see that the algorithm converges to an optimized population by eliminating both non-feasible and dominated solutions after the generation n°22. Beyond this generation number, all the solutions are non-dominated and feasible, and they may be possibly interesting solutions. After this point, however, the population keeps evolving, with "more optimal" solutions progressively replacing "less optimal" ones. The final number of generations was set to a larger value of 100 to ensure the convergence, while keeping a reasonable calculation time. This results in 10000 evaluations overall and 133 h of calculation time, to obtain a set of 100 optimized alloys.

5.3 Optimization results

In Figure 5.3, a composition overview of the different alloys found in the optimized population is shown. The majority of the alloys contains a high iron fraction, between 30 and 42 wt.%. Yet, it is interesting to note that the content of Fe does not exceed 50 wt.% in the large majority of optimized compositions. The amount of Cr is contained between 15 and 31 wt.%, Ni between 5 and 20 wt.% and Mn varies largely between 0 and 25 wt.%. A significant content of cobalt (between 5 and 20 wt.%) is to be noted in most of the alloys; its presence probably comes both from the criterion of high solid solution hardening and that of the austenitic structure stabilization. The content of cobalt is probably the most differentiating feature in our alloys, as compared to the existing austenitic SSs. Interestingly, the content of other elements is limited to only a few percent: Mo and Al do not exceed 2 and 4 wt.% respectively. As for the elements Nb, Ti and W, their average value remains below a fraction of a percent and can be considered as negligible. One could hypothesize that their strong tendency to primary segregation could go against the criterion of a low CTR value. Despite their probably high SSH power, these three elements are actually ferrite stabilizers, thus their presence increases the value of the Cr_{eq}, resulting in non-feasible compositions.

Finally, these results show that, in terms of chemical composition, the optimized alloys lie between concentrated alloys and conventional stainless steels. For this reason, in the following chapters, analyses of our results will be done in comparison with some "reference" alloys of both categories: commercial, wildly-used 304 and 316L ASSs, and the Cantor alloy ($Co_{20}Cr_{20}Fe_{20}Mn_{20}Ni_{20}$), considered as the model austenitic high entropy alloy.

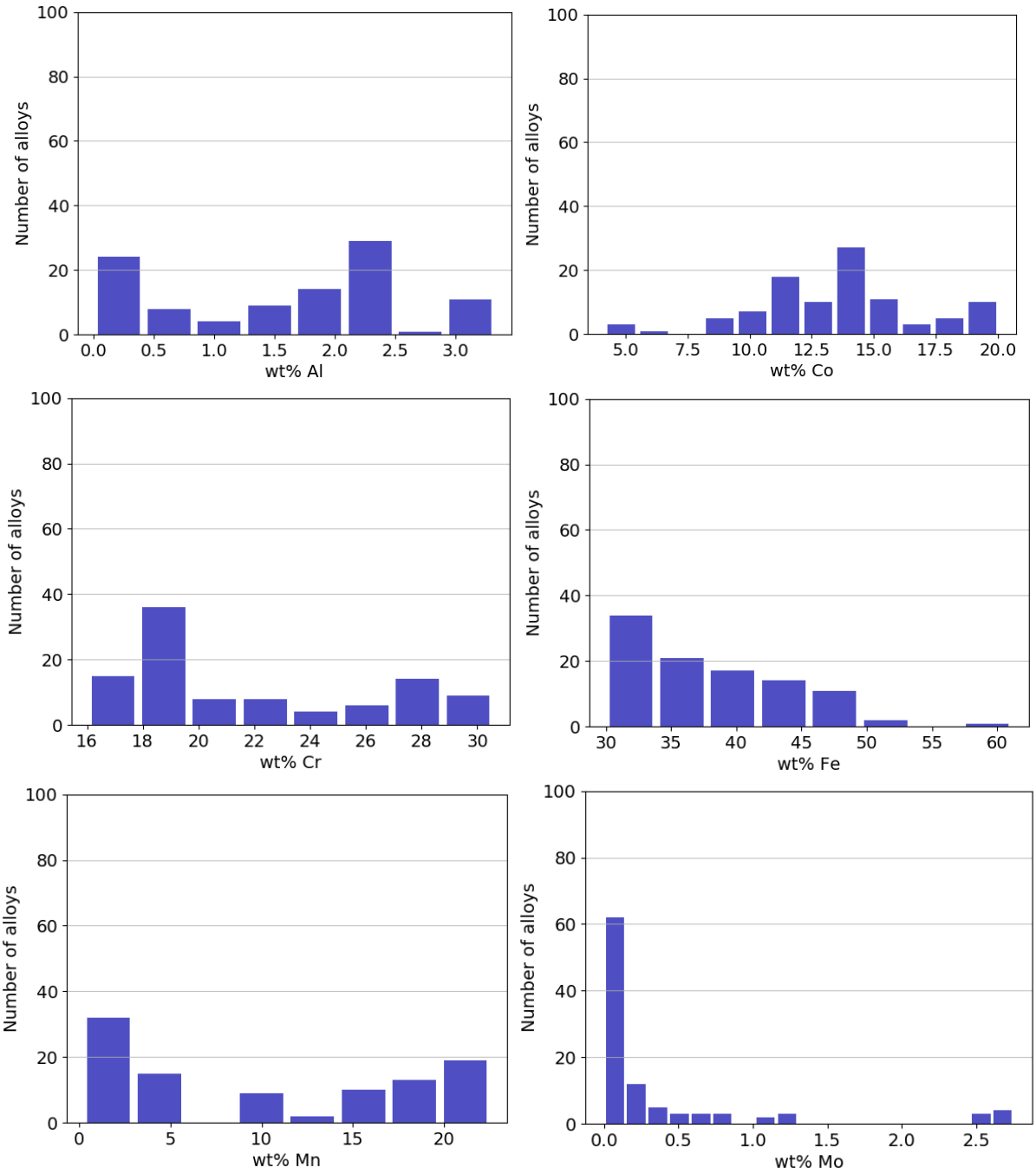
Number of alloys
wt% Al
wt% Co
wt% Cr
wt% Fe
wt% Mn
wt% Mo

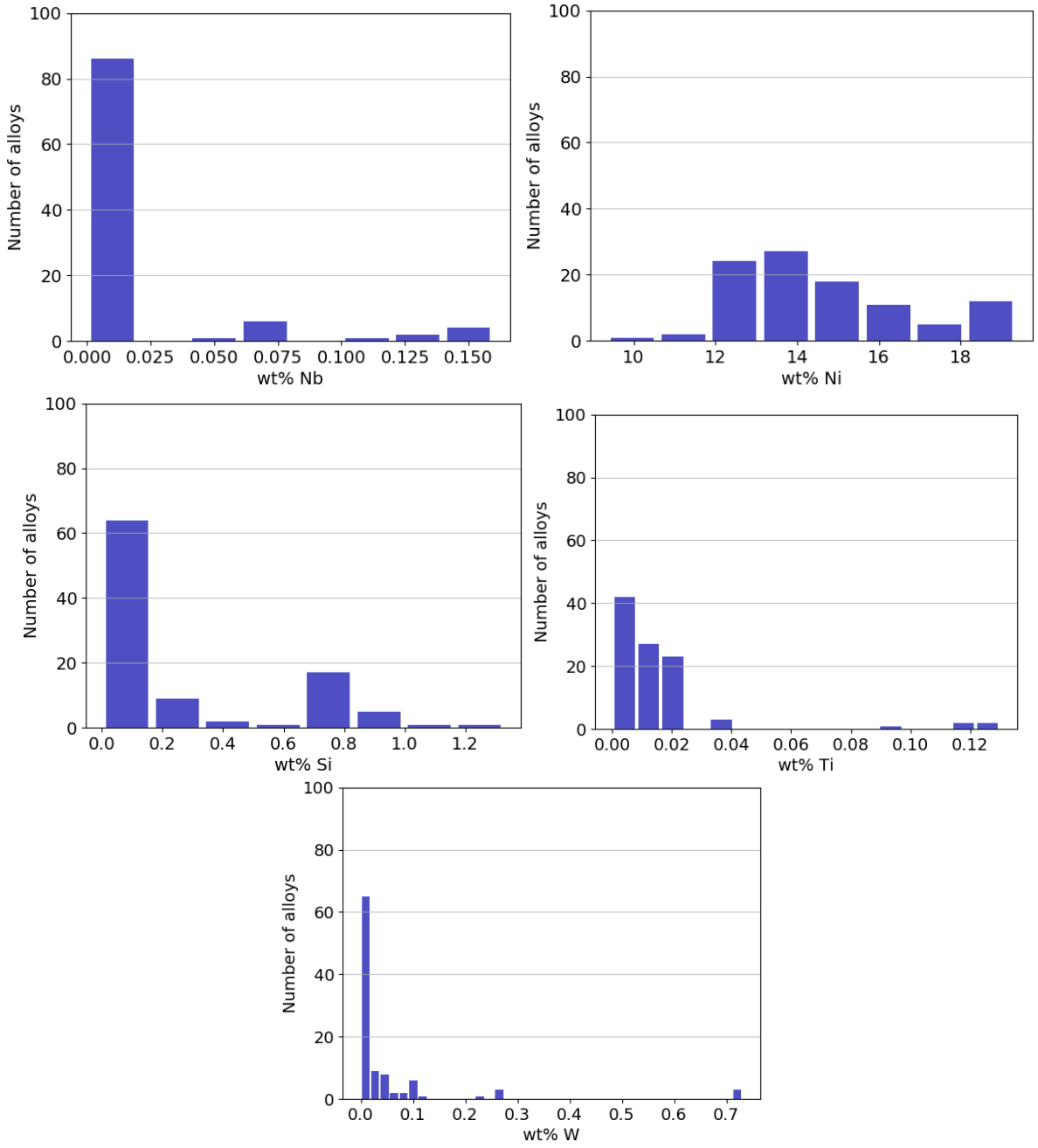

Figure 5.3 Distribution of element concentrations within the final optimized set of alloys.

In Figure 5.4, the distribution of the alloys in terms of their objective values is shown. For the critical solidification range (CTR) criterion, it is seen that the vast majority of the evaluated alloys have a value between 50 and 100 K. As for the amount of δ-ferrite calculated at the end of solidification, the majority of the alloys have its fraction between 0.4 and 0.5, which is basically on the upper range of the permissible values—or feasible space. As for what concerns the CTE,

the calculated values vary between 11 and 14 [10^{-6}/K]. In steels, the range of CTE is 10-19 [10^{-6}/K] depending on the alloy type. Therefore, the calculated values are within the usual range met for steels, and the minimization of CTE remains overall limited. To recall, the model used to predict the CTE is a law of mixtures of the CTE of individual elements, and it may result in an uncertainty. Nevertheless, almost half of the optimal alloys have a predicted CTE lower than 12.5 [10^{-6}/K], which can be considered overall as a rather low value. It is reminded that, as explained in Chapter 4, values of the CTE are underestimated for austenitic materials, but the obtained result of optimization should be correct, i.e. a minimization.

As for the criterion of surface tension, the values vary between 1.0 and 1.4 N.m^{-1}. This range is already lower than what is reported for steels (1.4-1.9 N.m^{-1}). However, when analyzing the ST values, one shall remain cautious. However, as presented in section 4.1, the exact predicted value of ST becomes less reliable when a large number and/or content of alloying elements is present. Therefore, when treating the ST values of the optimized alloys, which do indeed have a relatively high content of alloying elements, the predicted value of ST may have a high uncertainty. However, the variation trend of ST from one alloy to another should remain meaningful. Similar remarks can be made on the analysis of the solid solution hardening (SSH) criterion. The model that was used remains a comparative estimate of the real value, and must be used as a trend indicator rather than an exact prediction of the SSH value.

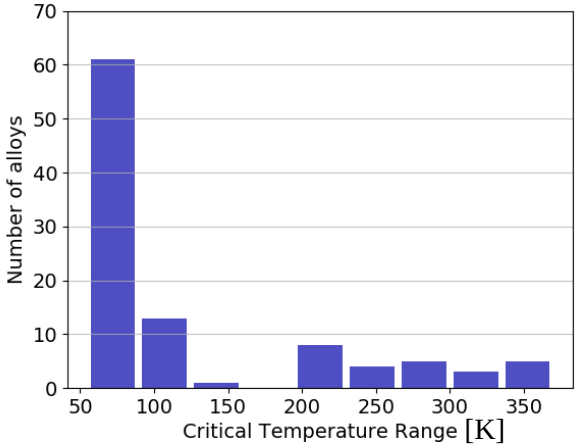
Number of alloys
Critical Temperature Range [K]

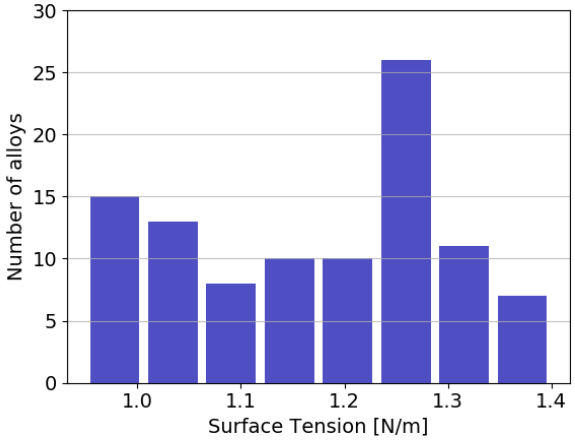
Number of alloys
Surface Tension [N/m]

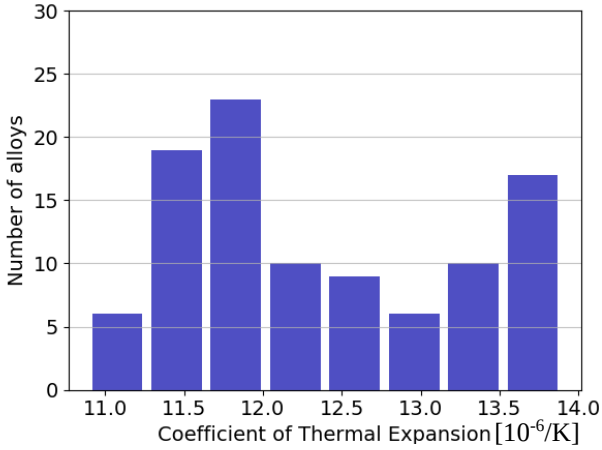
Number of alloys
Coefficient of Thermal Expansion [10-6/K]

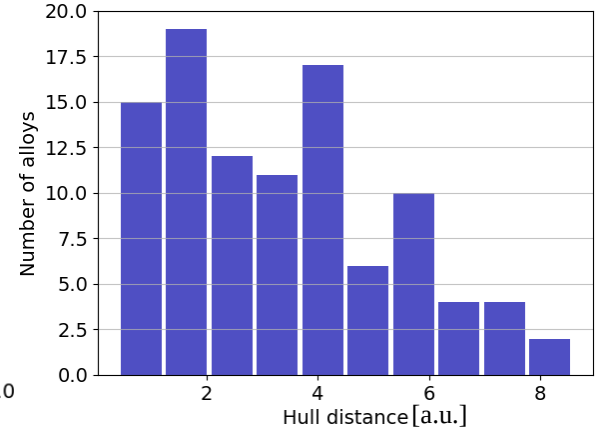
Number of alloys
Hull distance [a.u.]

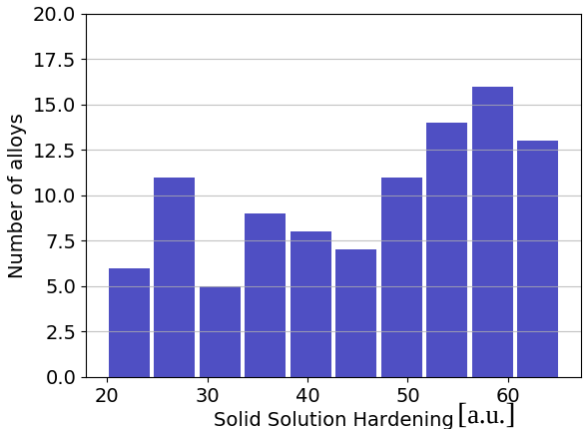
Number of alloys
Solid Solution Hardening [a.u.]

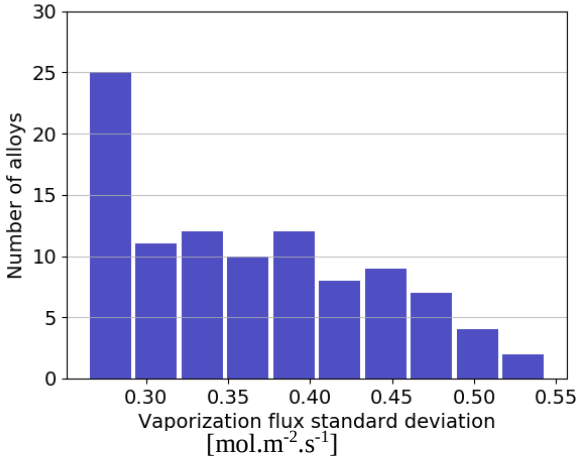
Number of alloys
Vaporization flux standard deviation
[mol.m-2.s-1]

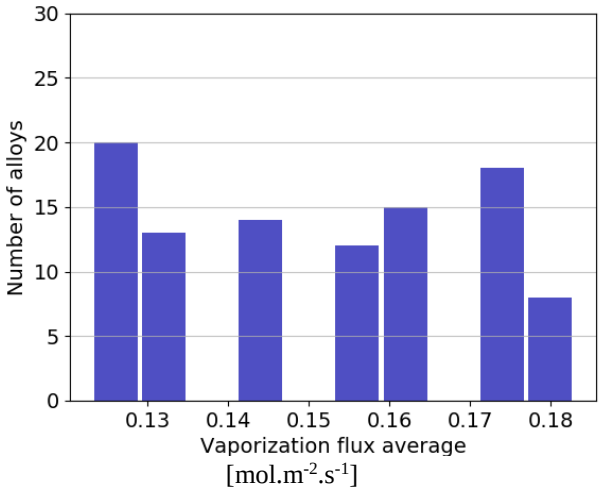

Figure 5.4 Distribution of objective function values within the final optimized set where a.u. means "arbitrary units".

Figure 5.5 and Figure 5.6 show the GAIA plane related to the multi-objective optimization problem. In the plane, the different axes, which originate from the center, represent the criteria, as projected in the reduced two-dimensional place (named U-V in this case). The squares named A_n, shown in Figure 5.6, represent the n different individuals (alloys) in the final optimal set obtained by the genetic algorithm calculation. The position of these alloys on the plane is based on their evaluations (value of objective functions) of the different criteria.

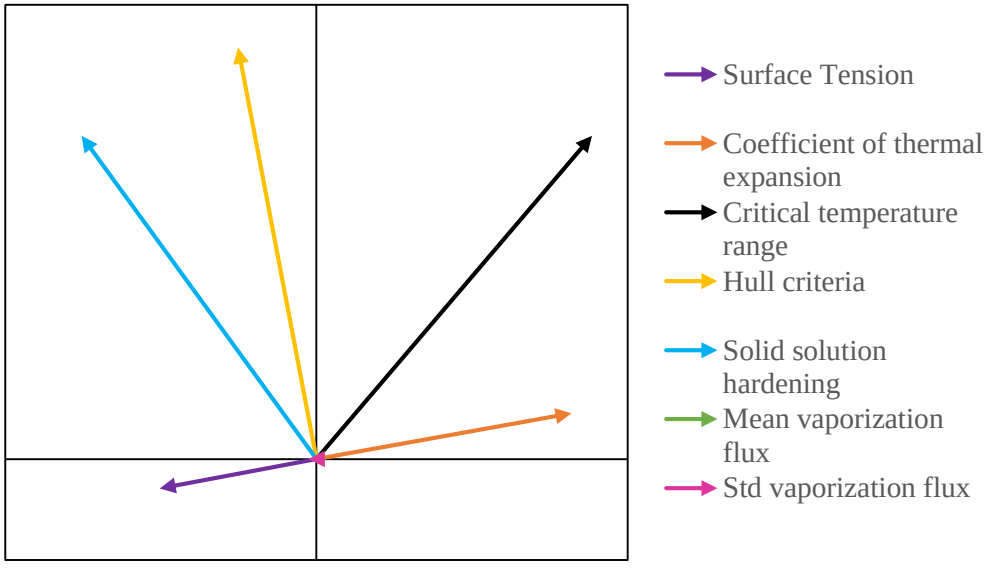

Figure 5.5 GAIA plane showing the projection of all criteria axes. Note that the axes of the vaporization fluxes average and standard deviation (pink and green arrows) have very short lengths.

Several information can be inferred from the GAIA plane.

First, the closer the alloys are to each other on Figure 5.6, the more their characteristics are similar.

Then, the lengths of the criteria axes project their importance in discrimination, such that the longer a criterion axis is, the more discriminating the criterion is. According to Figure 5.5, the critical temperature range, solid solution hardening and Hull criteria are the most discriminating in our design approach. They are followed by the surface tension and the coefficient of thermal expansion, while the mean and standard deviation of the vaporization flux are the least discriminating.

Finally, the orientation of the different axes shows how closely correlated the associated criteria are to each other in terms of preference. Perpendicular axes indicate independent criteria, an angle of 180^{o} indicates that the criteria have opposite preferences, whereas small angles indicate "similar orientation" and therefore similar preferences. By analyzing Figure 5.5, one can deduce that the criterion of CTR has a similar preference to CTE. A similar but less clear preference is seen between the CTR and the Hull criterion. On the other hand, we can see that the CTR is globally independent from the SSH and vaporization criteria while being conflicting (opposite preference) with the ST criterion.

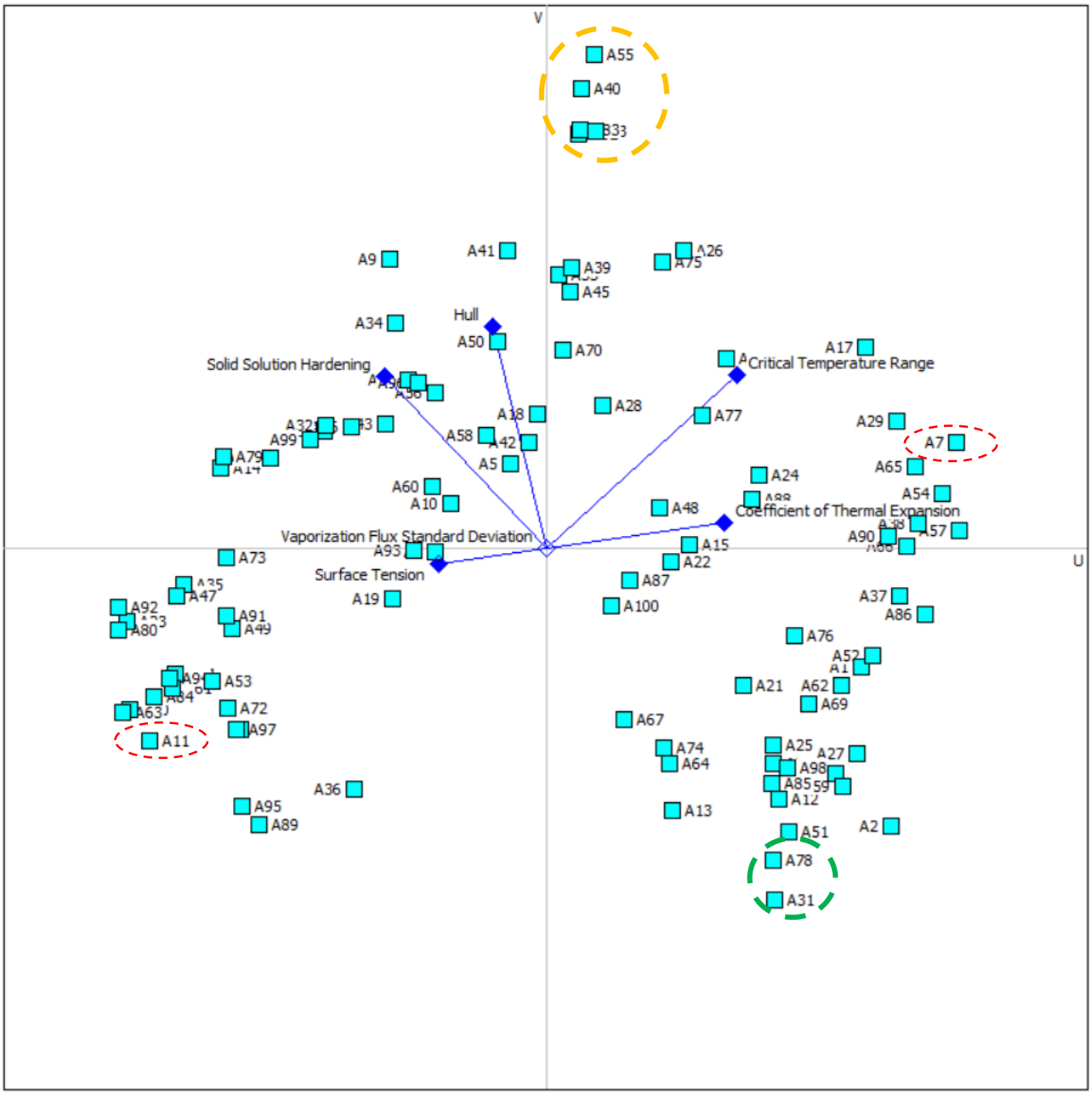

Figure 5.6 GAIA plane projection showing the relative position of the alloys in the optimized set with respect to criteria axes.

In fact, this can be explained by considering the opposing effect of certain elements on ST compared to CTR and CTE. To illustrate this, the correlation coefficients of the different alloying elements with the criteria is shown in the correlation heatmap of Figure 5.7. Each square in the heatmap shows the correlation between the corresponding variables. Correlation ranges from -1 to +1. Values closer to zero means there is no linear trend between the two variables. The closer the

correlation is to +1 the more positively correlated the variables; that is as one increases so does the other, and vice-versa for -1. We can clearly see that elements such as Mn, Si and Al contribute to decreasing the surface tension of the alloy, which indeed has been previously shown and discussed in section 4.1. Conversely, the presence of these elements have the opposite effect on the CTR and CTE as they tend to increase their values (for instance, pure Mn and pure Al have high CTEs of 22 and 23 10^{-6}/K, compared to very low ST at their melting points of 1.2 and 0.8 $N.m^{-1}$ respectively). On the other hand, the effect of these elements is not similar on the Hull criterion. Indeed, Mn is an austenite former while Al is a ferrite former. Therefore, they have opposite effects on the Hull criterion.

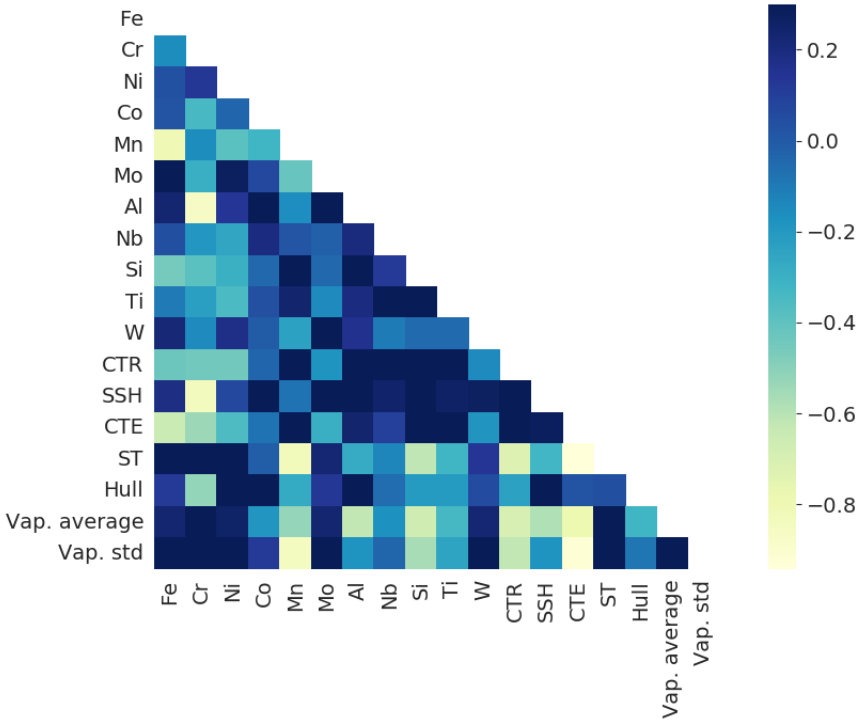

Figure 5.7 Color map showing the correlation between elements composition (wt. %) and objectives where: CTR is critical temperature range (K), SSH is solid solution hardening (arbitrary unit of SSH), CTE is coefficient of thermal expansion (10^{-6}/K), Hull is the Hull austenite criteria (distance) and Vap. average and std are the average and standard deviation of the vaporization flux respectively ($mol.m^{-2}.s^{-1}$).

This type of analysis can also be used as a tool to analyze correlations between elements. This information can be beneficial when certain restrictions are put on the type of alloying elements or their content, as it gives an idea of possible replacements. On the other hand, in many cases these correlations between elements can be a direct consequence of imposed constraints, such as the Cr_{eq} and Ni_{eq} values. Generally, increasing the content of ferrite formers automatically means that an increase in the content of austenite formers is necessary to stay within the feasible space. More specifically, to optimize the objectives while satisfying constraints, the algorithm was “forced” to

associate some elements (e.g. Al and Co, or Cr and Ni) whereas the addition of some elements would automatically penalize the presence of others (e.g. Al and Cr).

Finally, an important indication of the GAIA plane is the related locations of alloys with respect to the criteria axes. Indeed, to know which alloy performs best according to a certain criterion, one can look at the alloys towards which the criteria axes point on Figure 5.6. To illustrate this, let us consider two compositions A7 and A11 (red dashed circles) which are on the opposite directions of the CTR criterion axis: alloy A7 has a CTR of ~ 50 K while A11 has a CTR of ~ 400 K. Similarly, for other criteria, it is possible to directly visualize the alloys that perform better or worse depending on their relative position. Overall, alloys that are close to each other might have similar compositions (e.g. alloys in yellow circle), or similar performances (e.g. alloys in green circle).

5.4 Selection of a composition for experimental verification

After showing an overview of the alloys found in the final optimized set, in this section we further analyze results in order to choose one composition for experimental validation.

5.4.1 PROMETHEE results

As previously stated, multi-objective genetic algorithms yield a set of solutions, where none of them dominates the others. The whole set of obtained compositions can be found in the Appendix D. However, some multi-criteria decision aiding tools can be used to help the user select a solution based on certain preferences. In our case, the PROMETHEE method [223] was used as a first step. It is important to note that, as mentioned in section 2.3.2, the PROMETHEE method allows to set threshold values while defining the preference functions. The threshold values should be set respectively to the level of uncertainty associated to the criteria. For instance, a solution should be preferred over another one only if the difference on the criterion is above the error range.

Table 5.4 shows the preference function parameters (V-shaped with indifference threshold; see Figure 2.4) set for the criteria. Criteria were associated to a linear preference function with an indifference threshold (q) and a strict preference (p) such that:

- Below a difference “q” (e.g. at least of the order of the predictive error of the model), no distinction between two alloys is made; the user is indifferent to such difference.
- Beyond a certain difference “p” (which should be significantly high), a strict preference is made for one alloy over the other.
- Between both, a linear variation of the preference is set.

Several points must be considered in our case:

- For the CTR: a 5 K difference should not lead to a major distinction in the comparison between alloys, as this value is most probably lower than the confidence interval of the Scheil-Gulliver model of Thermo-Calc. Therefore, a difference of 5K between two alloys is considered insignificant.
- For ST: a difference of less than 0.2-0.3 $N.m^{-1}$ should not be regarded as significant to compare alloys, as it is the approximate error range of the model, as shown in section 4.5.3.
- For the CTE: similarly, considering the error range of the predictive model used, a difference less than 0.5 10^{-6}/K is considered insignificant.
- For Hull criterion: q was kept at 0 whereas p was set to 2; being the approximately minimum distance between ferrite lines on the Hull diagram (distance between "No ferrite" and "5% ferrite" – see Figure 4.2).

As for some other criteria, the values of q and p were rather set with a percentage difference than absolute value, as is common practice in multi-criteria decision analysis [352].

Table 5.4 Parameters of the V-shaped reference function set for the PROMETHEE method.

	CTR [K]	**ST [N/m]**	**SSH**	**Hull [distance]**	**CTE [10^{-6} K^{-1}]**	**Vap. flux average**	**Vap. flux std.**
q	5	0.3	5%	0	0.5	5%	5%
p	100	0.3	20%	2	1	20%	20%

5.4.1.1 Different scenarios: emphasis on selected criteria

The PROMETHEE makes it possible to assign a weight for each criterion, thus giving it a specific relative importance, with respect to the user's choice and the desired application. Changing the weights will lead to different "scenarios", leading to modification in ranking of the alloys. This further emphasizes the importance of the user-defined parameters in ranking the optimized alloys.

Following this approach, we will explore the effect of a weight change affected to one criterion at a time, while the weights of the other criteria are equal. It will help to understand the effect of the weight value on the selected alloy. The different scenarios to be tested are listed in Table 5.5, along with the associated weights for every criterion.

Table 5.5 Different scenarios for PROMETHEE ranking, depending on some weight values (weights are here indicated with values 1 or 2 for easy comparison, but for the calculation they are normalized such that their sum is one, as explained in Chapter 2).

	CTR	**ST**	**SSH**	**Hull**	**CTE**	**Vap. flux average**	**Vap. flux std.**	**Highest ranked alloy**

Scenario 1	1	1	2	1	1	1	1	A40
Scenario 2	1	2	1	1	1	1	1	A83
Scenario 3	1	1	1	1	1	2	1	A70
Scenario 4	1	1	1	2	1	1	1	A3
Scenario 5	2	1	1	1	1	1	1	A3
Scenario 6	1	1	1	1	1	1	2	A73

Depending on the favored criterion (i.e. the one with the highest weight), the ranking of the alloys changes. Table 5.6 shows the "top-ranked" compositions for the different scenarios and their respective ranking in all scenarios.

Table 5.6 Composition and ranking of alloys selected based on different scenarios for PROMETHEE.

	Element	**Alloy A40**	**Alloy A83**	**Alloy A70**	**Alloy A3**	**Alloy 73**
Composition (wt.%)	**Fe**	39.9	39.9	47.2	39.8	34.7
	Cr	17.8	17.8	18.0	17.8	17.7
	Ni	17.7	18.3	11.8	18.4	15.6
	Co	19.8	19.8	18.5	19.8	8.9
	Mn	0.3	0.7	0.4	0.7	20.1
	Mo	1.2	0.2	0.8	0.0	0.1
	Al	3.3	3.3	2.3	3.3	2.1
	Nb	0.0	0.0	0.0	0.0	0.0
	Si	0.1	0.0	0.9	0.0	0.9
	Ti	0.0	0.0	0.0	0.0	0.0
	W	0.1	0.0	0.0	0.0	0.0
	C	0.02	0.02	0.02	0.02	0.02
Rank (/ 100)	**Scenario 1**	1	2	6	4	9
	Scenario 2	7	1	9	3	8
	Scenario 3	6	2	1	3	9
	Scenario 4	4	2	10	1	14
	Scenario 5	3	2	7	1	21
	Scenario 6	11	5	10	6	1

In scenario 1, the strength criterion is favored. The resulting "top-ranked" alloy contains indeed a higher content of alloying elements which favor the SSH, such as Mo and Al (1.2 and 3.3 wt.% respectively). In scenario 2, where the ST criterion is favored, the first ranked composition is similar to the one previously discussed, but with a lower content of Mo which has a relatively high ST value. Let us note that both alloys have a high content of aluminum, previously identified as an element strongly decreasing the ST value in alloys. By favoring the average vaporization

criterion in scenario 3, the top alloy has a composition which is low in Mn (although not being much lower than the other discussed compositions), but a lower Ni content as well (~11.8 wt.%) which seems difficult to interpret. In the 4th scenario, the Hull criterion is favored, and the result is a composition rich in austenite-promoting elements (Ni, Co) with 18.4 and 19.8 wt.% respectively. The same composition is top ranked when we favor the CTR criterion in scenario 5. Finally, in scenario 6, when the distribution of the vaporization flux criterion is favored, the resulting alloy is much richer in Mn than all discussed alloys (~20 wt.%). Despite a higher volatility of Mn, an increase of its fraction compensates its relative loss by vaporization, resulting in a lower relative composition change. Overall, it is nevertheless seen that all of these specific compositions perform well in the different scenarios (all within top 20%).

Finally, the increase of certain weights results in an effective selection of the alloys with better performance for the associated criteria, and it shows the validity of the selection method. It also illustrates that the increase of a given weight would favor a specific criterion, however at the expense of the others since we are dealing with a Pareto-optimized set.

In this study, all the criteria have a first-order importance on the microstructure and on the occurrence of defects, as detailed on Chapter 4. Besides, we follow mainly an academic approach, aiming at demonstrating the possibilities of the method rather than targeting a specific application through a set of properties to be reached, so that there would be little justification to emphasize a specific criterion at the expense of others. Therefore, as a first step, equal weights would be a rational approach for the selection of an alloy.

5.4.2 Selected alloy

The aim is to select an alloy that will be compared to already existing industrial alloys, namely AISI 316L and 304 SSs. Comparing optimized alloys to 316L and 304 is particularly relevant, as these alloys are among the most studied stainless steels in additive manufacturing. Compared to commercial alloys, the selected alloy should be dominant from a multi-dimensional point of view. Comparison will also be made against concentrated alloys, mainly the Cantor alloy (equimolar CoCrFeMnNi).

In an attempt to find the best alternative overall, we attributed similar weights in PROMETHEE for all the criteria (i.e. a weight of 1/n for n criteria). The net outranking from the PROMETHEE method gives an idea on the overall comparison between individuals.

From the set of highly ranked alloys sorted by PROMETHEE, it was decided to choose one alloy for experimental validation, since we did not have the possibility to test more due to the limited time of the study.

Many of the alloys that are "highly ranked" according to PROMETHEE are quite similar in their composition, and selecting a specific composition becomes difficult. Therefore, at this stage, we propose to include an additional criterion to help the selection, that is the temperature range of austenite stability. As previously explained, for computational cost reasons this criterion was not included among multi-objective optimization criteria. However, the alloy must develop a fully austenitic microstructure, and a large stability domain of this phase would be desirable, to avoid any undesired phase transformation during any heat treatments following AM processing. This criterion helped on the ultimate sorting between alloys that are otherwise nearly equivalent on the basis of other criteria. To compare between the different designed compositions, equilibrium phase calculations by Thermo-Calc were done in order to evaluate the region of austenite stability and the temperature range, if present, for which the alloy is fully austenitic.

From the optimized alloys, one composition was chosen based on the previously discussed criteria, i.e. among the alloys highly ranked by PROMETHEE using the set of even weights, with an additional "manual" criterion linked to the equilibrium temperature stability range of austenite predicted by Thermo-Calc.

The selected alloy has the composition shown in Table 5.7. It contains a high content of Fe (42.1 wt.%) and incorporates Cr, Ni, Mn and Co, as well as a small percentage of Al. As for several of the optimized alloys, its composition is quite different from what we can typically find in austenitic stainless steels and is closer in nature to common HEAs, such as the Cantor alloy. In fact, the configurational entropy ($S_{conf} = -R\sum_{i=1}^{n} x_i \ln(x_i)$) of the selected alloy is equal to 11.27 $J.K^{-1}.mol^{-1}$ (~1.35R), which places it in the range of medium entropy alloys [353].

Table 5.7 Compositions in wt.% for several existing alloys compared to some designed alloys and to the selected alloy.

	Fe	**Cr**	**Ni**	**Mn**	**Co**	**Al**	**Mo**	**W**	**Si**	**C**	**N**
316L	68-67	16.5-18.5	10-13	2	/	/	2-2.5	/	1	0.03	0.1
304	71-72	17.5-19.5	8-10.5	2	/	/	/	/	1	0.07	0.1
Cantor	19.9	18.5	20.9	19.6	21	/	/	/	/	/	/

A7: Lowest CTR	34.6	30.6	19.3	10.7	4.7	0.1	/	/	0.1	0.02	/
A6: Lowest CTE	45.4	28.1	12.1	0.3	14.0	/	/	/		0.02	/
A5: Highest SSH	45.0	18.3	16.3	0.6	13.8	2.5	2.6	0.7	0.3	0.02	/
A3: Highest Hull	39.8	17.8	18.4	0.7	19.8	3.3	/	/		0.02	/
A16: Selected alloy	42.1	15.2	13.7	11.7	15	2.3	/	/		0.02	/

Especially, its content of Mn (11.7 wt.%) is much higher than the range found in conventional austenitic steels (usually ≤ 2 wt.%, with the exception of AISI 200 series where it can go up to 8 wt.%). Increasing Mn has been associated with lower ST values, which is expected to increase the flowability of the melt during printing and decrease the effects of surface defects such as balling. On the other hand, such a high content of Mn could be troublesome because of its high vaporization and oxidation tendency, which can lead to difficulties in both producing the powder in gas atomization and printing it, so assessing it experimentally would be interesting. The content of Co (15 wt.%) is also high as this element is almost never added to stainless steels. Co is expected to increase the solid solution hardening of the material and to stabilize its austenitic structure. The presence of Al is expected to lower the surface tension of the material. On the other hand, Al can lead to possible issues of oxidation. Finally, the number of alloying elements and their respective content of the selected alloy is quite different from compositions of conventional stainless steels.

Table 5.8 shows a comparison between the values of our defined objective functions between the selected material and several existing alloys. There are two main things to consider while comparing the different alloys manually: feasibility and evaluation scores. As shown in Table 5.8, by making a criterion-by-criterion comparison, we can see that the alloy is not dominant over the other alloys, i.e. it does not strictly perform better in every criterion. However, it is not dominated either. Compared to 316L and 304, the selected alloy performs better in all criteria except for the CTE. Compared to Cantor alloy, it performs better on all criteria except for the CTR. This comparison is done on the basis of the evaluation criteria only, but it is important to note that the feasibility of the alloy is determined by the set constraints. For example, despite not being dominated "criteria-wise", Cantor is not feasible because it does not have an "FA" solidification mode.

Table 5.8 Comparison of the calculated objective function values between the selected alloy, some other designed alloys and several existing alloys. Notes: the negative sign of the Hull criterion for 304 SS

indicates that it lies on the ferrite side of the ferrite-austenite boundary on the Hull diagram; it is reminded that calculated CTEs are underestimated.

	CTR [K]	ST [$N.m^{-1}$]	SSH [a.u.]	Hull [a.u.]	CTE [$10^{-6}/K$]	Vap. flux average [$mol.m^{-2}.s^{-1}$]	Vap. flux std. [$mol.m^{-2}.s^{-1}$]
316L	92	1.3	31.3	0.56	11.3	0.13	0.34
304	105	1.3	19.3	-0.32	11.3	0.12	0.3
Cantor	60	1.1	18.1	14.1	13.4	0.14	0.3
A7: Lowest CTR	54	1.4	24.9	1.14	11.7	0.17	0.38
A6: Lowest CTE	85	1.3	17.7	0.23	10.9	0.18	0.53
A5: Highest SSH	74	1.3	63	3.38	11.6	0.17	0.48
A3: Highest Hull	68	1.3	54.8	8.18	12.0	0.13	0.36
Selected alloy	77	1.0	43.9	6.35	13.0	0.12	0.25

The Scheil-Gulliver simulation and the amount of phases as a function of temperature for the selected alloy are shown in Figure 5.8 a and b respectively. As required, it is shown that the alloy first solidifies in δ-ferrite, and it is only after around 0.2 mole fraction is solidified that austenite starts forming so that, at the end of the Scheil-Gulliver solidification simulation, these phases constitute more than 99% of the material. The equilibrium phase diagram shows that the formed δ-ferrite (BCC) subsequently transforms into austenite (FCC) upon cooling, as assessed in section 4.3.2 through a comparison with other steels. According to this equilibrium calculation, the alloy is expected to have a single FCC structure between 957 and 1235 °C. Below approximately 950 °C, an ordered BCC phase of the B2 type (BCC #2) is expected to form at equilibrium. Nevertheless, the Cr_{eq} and Ni_{eq} suggest that according to the Hull diagram, the alloy is expected to be fully austenitic after solidification and cooling through a welding-type process. A very minor amount (< 0.005 %) of chromium-rich $M_{23}C_6$ carbides is also predicted below ~ 800°C. Due to the low carbon content of the alloy (0.02 wt.%), this is similar to what is found in "low carbon" stainless steels and should not provoke any sensitization to intergranular corrosion.

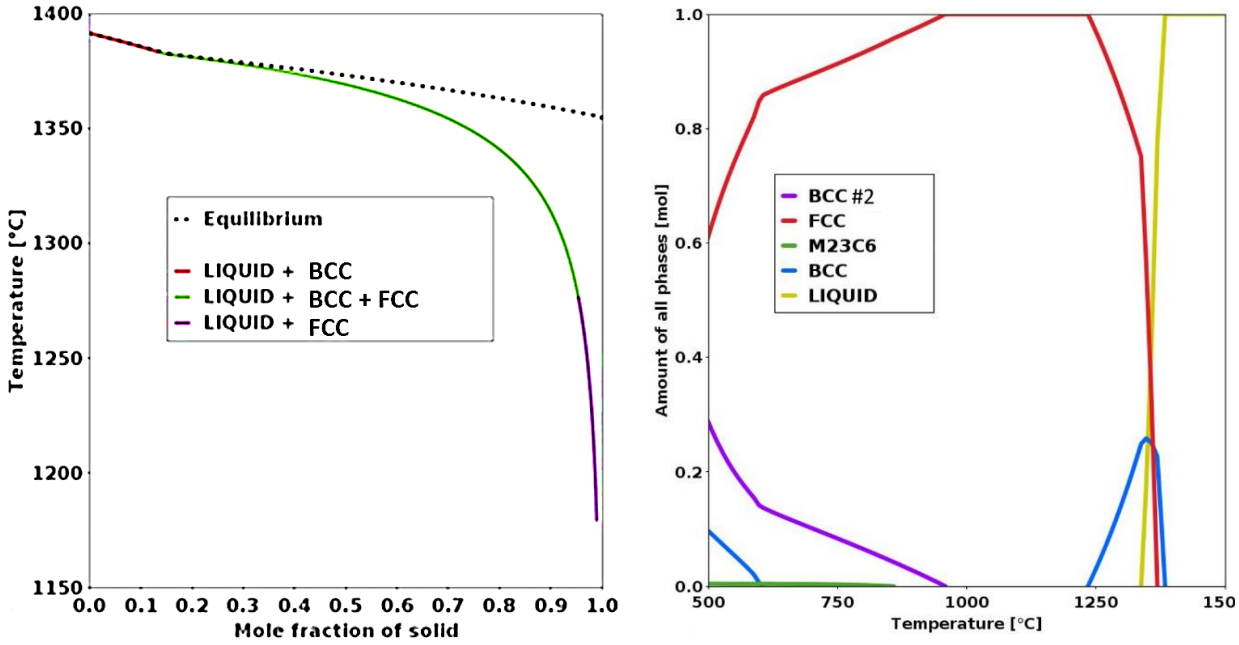

(a) (b)

Figure 5.8 a) Scheil-Gulliver and b) equilibrium Thermo-Calc predictions for the selected alloy.

In Figure 5.9, the composition of liquid phase as a function of temperature, calculated by Thermo-Calc, is shown. According to Scheil-Gulliver model, the composition of the remaining liquid changes through classical mechanisms of elements partition between solid and liquid phases. When the temperature decreases, liquid becomes depleted in Fe and enriched in Mn and Ni. The last liquid present at the end of solidification, at about 1160 °C, contains high amounts of manganese and nickel, while the iron content drops to less than half of its nominal value. This enrichment in Mn and Ni promotes the stability of austenite at the end of the solidification, in agreement with the solidification sequence illustrated on Figure 5.8 a. Overall, these thermodynamic analyses confirm that the alloy has good chances to be fully austenitic after printing.

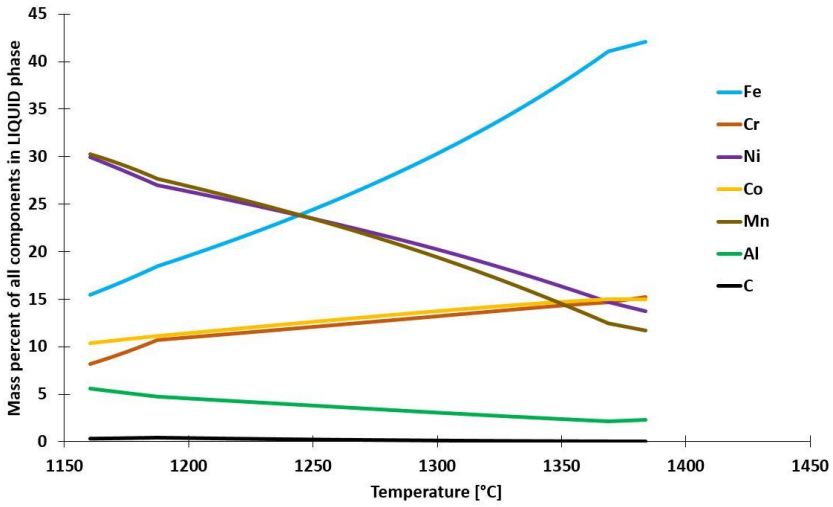

Figure 5.9 Change of chemical composition of the liquid during solidification of the selected alloy, according to Thermo-Calc using Scheil-Gulliver model.

5.5 Conclusion

The combination of different predictive tools (CALPHAD, machine learning model, physical and linear models) explained in Chapter 4, with the genetic algorithm NSGA-II, allowed a multi-objective optimization of austenitic materials compositions. After running the optimization algorithm, a set of non-dominated solutions was obtained. The analysis of the type of compositions designed shows that, in general, the optimized alloys lie between complex concentrated alloys and conventional stainless steels, notably concerning the iron content. With the help of the PROMETHEE method and additional CALPHAD simulations, we have chosen one alloy out of the optimized set to be experimentally evaluated. The alloy shows interesting predicted characteristics compared to presently available AM-processable austentitic stainless steels in terms of our defined criteria, and is expected to be easily printable and little susceptible to changes with the process parameters of AM.

In the following chapter, a global experimental evaluation of the selected alloy will be shown and discussed.

6 Experimental evaluation of the selected alloy

In this chapter, we will show and discuss the experimental evaluation results of the selected alloy, which will also be referred to hereafter as S_A for simplicity. This alloy was selected from the optimized set of alloys, as explained in the previous chapter. Its evaluation will follow several steps and it will be characterized in three different states: as-cast, as-atomized (powder form) and as-built by selective laser melting (SLM). These steps will allow the validation of our alloy design approach and will help to understand the overall behavior of the alloy.

6.1 Preliminary evaluation of selected alloy: as-cast state

6.1.1 Microstructure and phase stability

As a first step, a 300g ingot of S_A was produced by induction melting in a cold crucible at Mines Saint-Etienne to perform a preliminary evaluation of the phase stability and thermal properties of S_A in the as-cast form. The real chemical composition of the cast alloy is shown in Table 6.1 and compared to the nominal composition. A very good agreement between targeted and obtained contents of all elements are to be noted, with differences lower than 2 % (relative) for all elements.

Table 6.1 Selected alloy: nominal and real chemical composition (wt.%) of as-cast alloy. Chemical analyses were done by X-ray fluorescence spectroscopy. Carbon was not analyzed.

Element	Fe	Ni	Cr	Co	Mn	Al
Nominal	42.1	13.7	15.2	15	11.7	2.3
Real	41.9	13.9	15.0	15.1	11.8	2.3

The microstructural observations (Figure 6.1) show that the alloy solidified in a dendritic structure with a grain size of several hundred micrometers, eventually up to a millimetric diameter. On the basis of the SEM images, it can be supposed that the solidification results in a single phase material, as no contrast of a second phase is seen. Yet, this scale of observation does not exclude the presence of a minor secondary phase, especially if its morphology was small enough to approach the SEM spatial resolution (of the order of few tens of nanometers).

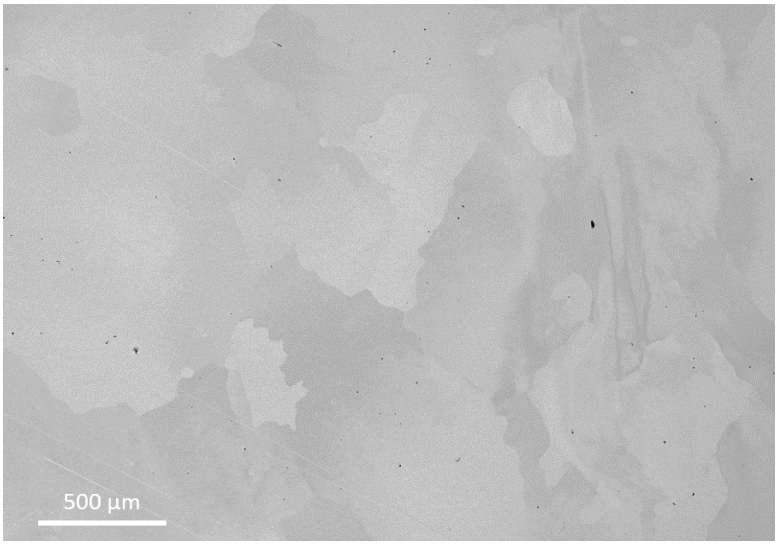

Figure 6.1 Secondary electron image of selected alloy in the as-cast condition.

To verify the homogeneity of distribution of elements in the alloy at the grain-scale, an Energy Dispersive X-ray Spectroscopy (EDS) analysis was performed in SEM. Figure 6.2 shows the EDS maps where primary segregation is observed: the interdendritic zones are enriched in Mn, Ni and Al, whereas Fe, Cr and Co are more concentrated in the center of dendrites. This observation confirms the predictions of solidification conditions with the Scheil-Gulliver simulation model (section 5.4.2). This behavior is typically seen in cast HEAs, such as the Cantor alloy [354] or $Cr_{15}Fe_{46}Mn_{17}Ni_{22}$ [355].

The density of the alloy, as measured with He pycnometer, gives a value of 7.71 g/cm^3, i.e. 99.7 % of its theoretical density, calculated with a rule of mixtures and equal to 7.73 g/cm^3. Thus, the metallurgical quality of the alloy seems satisfactory.

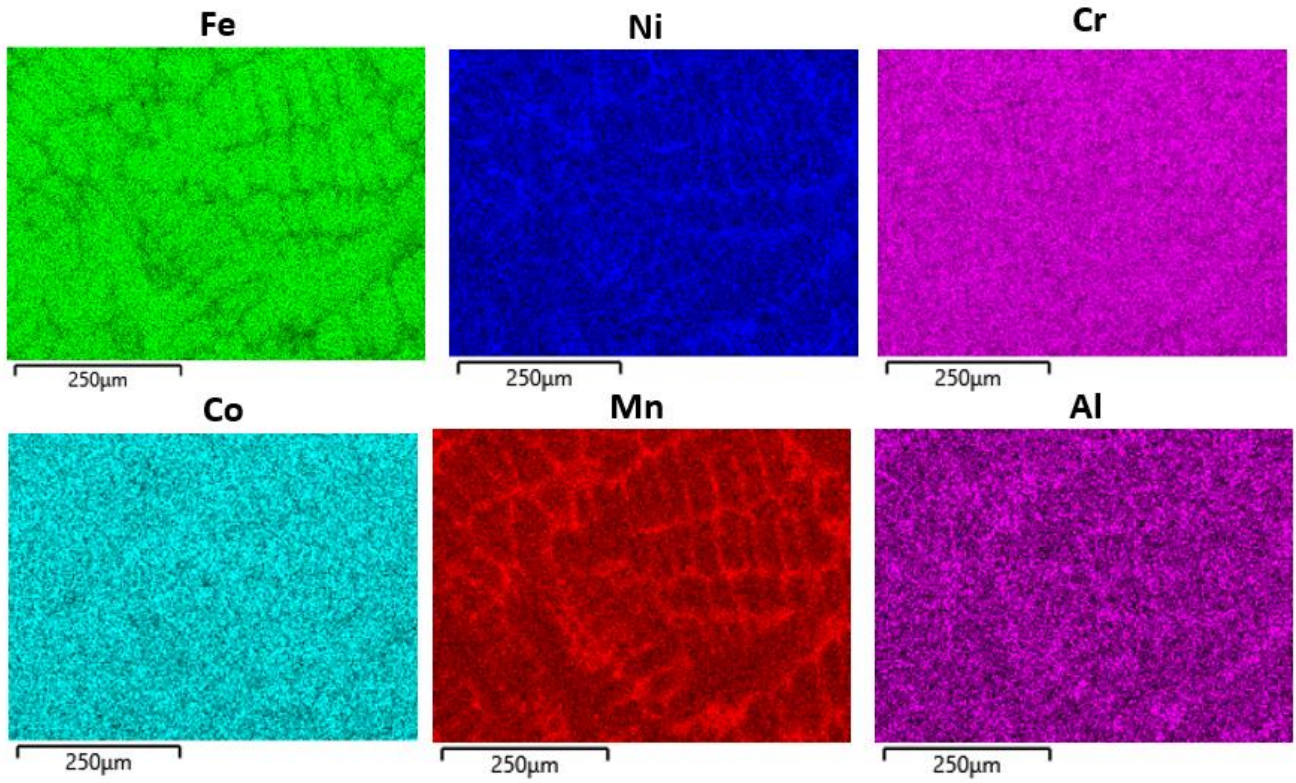

Figure 6.2 SEM-EDS maps of distribution of metallic elements in as-cast S_A, showing primary segregation

6.1.2 Mechanical properties

Initial evaluation of mechanical properties was first done by hardness measurements. In the as-cast state, the average hardness of S_A is equal to 112 ± 5 HV10 (as per Vickers with a test load of 10 kg).

Due to the limited amount of the as-cast alloy, only one tensile test was performed in this state, at room temperature. Figure 6.3 shows the stress-strain curve, from which a yield stress (YS) of about 225 MPa, an ultimate tensile strength (UTS) of about 455 MPa, and a uniform elongation of about 30 % can be measured. The total elongation, near 50 %, is the sign of necking and so of a good plasticity of the material. These values are similar to those provided for commercial austenitic stainless steels which generally have a YS around 200 MPa, a UTS in the range 500-700 MPa and an elongation at fracture A% close to 40% [95], [284], [356]. This result is satisfactory for our selected alloy, especially as it is obtained in its as-cast state.

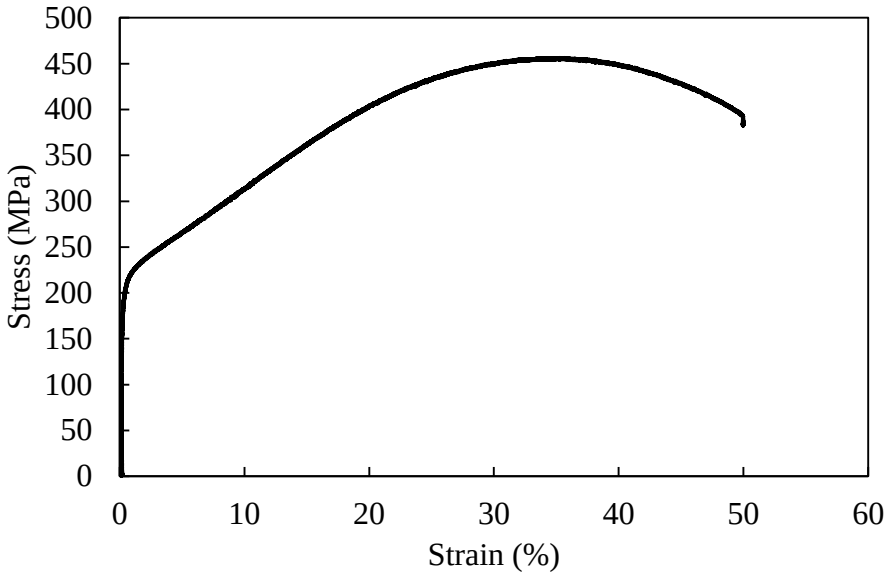

Figure 6.3 Room temperature tensile curve (engineering stress vs strain) of the selected alloy in as-cast state, with a strain rate of 10^{-3} s^{-1}.

6.1.3 Thermal expansion

The thermal expansion behavior was measured for S_A and for 316L (as reference) by dilatometry. The measurement was done in the range of 20 to 1000 °C with a heating rate of 5 °C/min. The used dilatometer can measure a length variation of 0.004 µm.

Figure 6.4 shows the evolution of the strain versus temperature curves for S_A and 316L between 20 and 1000 °C. As we can see, the expansion behavior of both alloys is very similar. Yet, above 600 °C, we observe a slightly higher strain variation for S_A compared to that of 316L. However, this variation is not significant enough compared to the measurement noise. These results are in agreement with our comparison between the predicted CTE values of the selected alloy compared to 316L, where it was expected that S_A will have a slightly higher CTE value. The average CTE values calculated based on the measured strain over the temperature range specified is around 22 10^{-6}/K and 23 10^{-6}/K for 316L and S_A respectively. These values seem to be overestimated (22 compared to 18-19 10^{-6}/K in literature for 316L), probably due to issues with the calibration of the dilatometry machine. Nevertheless, a comparison between the calculated CTE for both alloys shows that the difference remains limited (< 1 10^{-6}/K absolute, or < 5% relative), which is consistent with predictions.

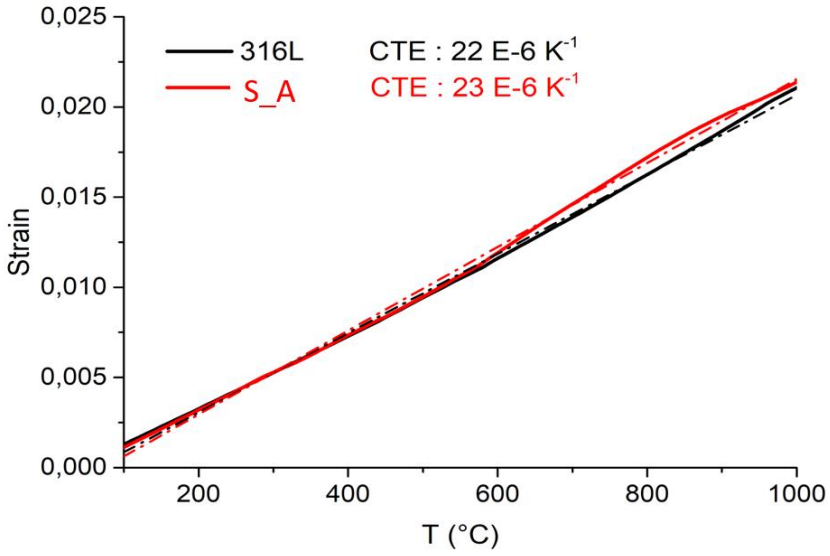

Figure 6.4 Strain as a function of temperature, as measured by dilatometry for the selected alloy and 316L

6.2 Characterization of powder in as-atomized state

After primarily satisfying results in terms of the phase stability, thermal and mechanical properties in the as-cast state, the selected alloy was produced in powder form following the gas atomization procedure described in section 3.1.1.

6.2.1 Chemical composition

Table 6.2 shows the chemical composition of the as-atomized alloy compared to the nominal composition. It can be seen that the composition slightly differs from that of the nominal composition. Namely, the analyses of the powder composition showed a significantly higher content of iron (45.9 vs 42) while the content of other metallic elements decreased. This decrease is more pronounced for Cr and Co. Interestingly, the loss of manganese, supposed to easily evaporate in liquid state, is relatively low. The carbon content is lower in the powder than expected (60 ppm vs 200 ppm). Finally, some oxygen is unavoidably present in the powder; for a series of measurements, its value varies from 53 to 280 ppm.

Table 6.2 Comparison between the nominal and as-atomized chemical composition (wt.% unless specified) of selected alloy

	Fe	Ni	Cr	Co	Mn	Al	C	O
Nominal	42	13.7	15.2	15	11.7	2.3	0.02	0
As-atomized	45.9	13.1	14.3	13.5	11	2.11	0.0064	53-280 ppm

This range of oxygen content is not surprising in atomized powders. For example, in stainless steel powders, an oxygen level between 110 and 610 ppm was reported in literature [357]. The oxygen level can be influenced by parameters of the atomization process and powder storage conditions. As to the scatter of the measured oxygen level in the studied case, no convincing hypothesis can be proposed. A series of nine measurements has been performed. All the samples of powder have been stored in the same conditions (under an inert gas) and are supposed to have a similar size distribution, hence a similar reactivity with gases. Yet, this latter powder characteristic seems to be the most probable reason of differences, due to possible higher absorption of oxygen, if some tested samples contained a higher fraction of finer powder with higher specific surface.

The differences between nominal and real composition of S_A, especially as to the proportions of alloying elements, may have a direct effect on the phases presence and their stability. Moreover, it can influence other properties that were optimized through the proposed alloy design process. Thus, it is necessary to re-calculate these properties accordingly, and evaluate if the fabricated powder corresponds to the quality of material we expected. This is also a way to test the "robustness" of our approach, in terms of sensibility of the optimized material properties to deviation from expected composition, current in industrial conditions of alloys fabrication.

The stability of austenite at room temperature was first checked, on the basis of Hull diagram. The relative decrease of contents of austenite and ferrite forming alloying elements is quite similar in the produced powder, and the increase in iron content have a small effect on the stability of phases. Thus, the new composition remains in our defined feasible space on the Hull diagram.

The solidification conditions have been re-calculated following the Scheil-Gulliver model and equilibrium phase diagrams estimated from Thermo-Calc calculations for both compositions. As we can see in Figure 6.5 a and b, the Scheil-Gulliver simulation for the modified composition shows that the alloy still solidifies first in δ-ferrite before forming austenite, satisfying the FA solidification mode constraint. The fraction of δ-ferrite formed is around 15%. Despite being lower than that predicted for the nominal composition (~20%), it is still within our defined constraints (10 to 50%). The small content of M_7C_3 carbide, theoretically present at the end of solidification in the S_A composition, is absent in the case of the real powder, due to the loss of carbon. The phase stability in equilibrium conditions undergoes only limited modifications in the real powder composition (Figure 6.5c and d). More interestingly, the solvus temperature of the ordered BCC B2 phase (BCC #2) decreases (870 vs 950°C), while that of α-ferrite remains almost the same.

Also, the negligible fraction of carbides previously expected to form below 750 ºC is even lower due to the lower content of C (64 ppm compared to 200 ppm in the nominal composition).

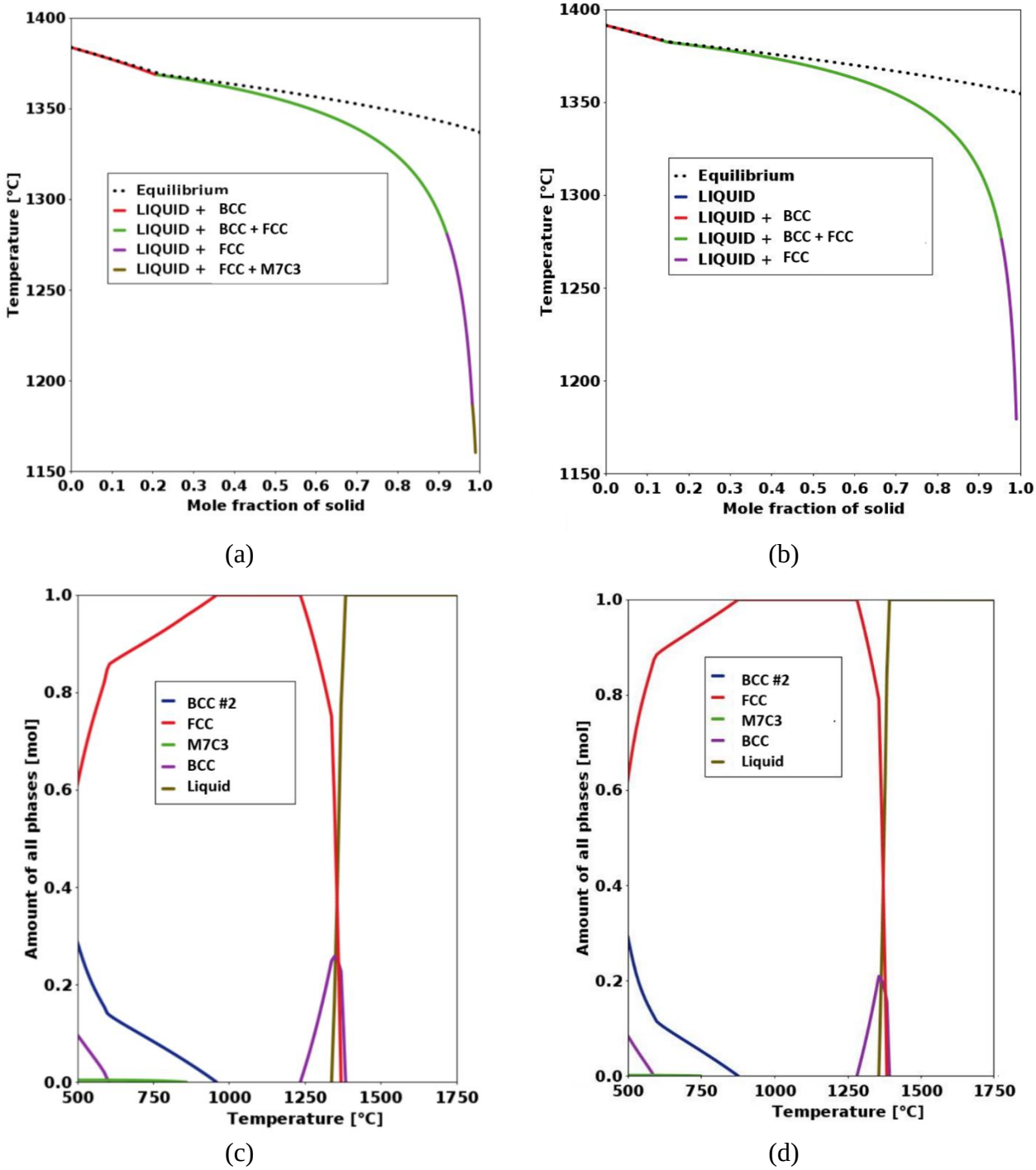

Figure 6.5 Solidification and phases equilibrium in the aimed (left) and fabricated powder (right) compositions. a-b) Scheil-Gulliver diagram; c-d) equilibrium phase diagram as a function of temperature. Thermo-Calc calculations

Finally, another quantity, coming from thermodynamic calculation and presented in Table 6.3, is the critical temperature range. Its value is slightly higher for the as-atomized composition: ~ 88 K compared to 77 K for the nominal one, but this remains rather low and should not affect printability.

Table 6.3 shows the results of calculation of all complementary physical properties of the alloy, used as criteria for alloy optimization. Comparison between nominal composition with that of atomized powder is satisfactory for all of them. Little to no difference in the values of the surface tension, vaporization flux average and standard deviation, and thermal expansion coefficient is seen. Alternatively, it is not surprising to see that the lower content of alloying elements overall will lower the solid solution hardening (SSH) from 44 to 42; yet, this value remains high and is considered as satisfactory for our purposes.

Table 6.3 Comparison between the calculated criteria values between the nominal (aimed) and as-atomized powder composition, where a.u. is arbitrary unit.

	CTR [K]	**Surface tension [$N.m^{-1}$]**	**SSH [a.u.]**	**CTE [10^{-6}/K]**	**Vap. flux average [$(atm/K.kg/mol)^{0.5}$]**	**Vap. flux [$mol.m^{-2}.s^{-1}$]**
Nominal	77	1.0	44	13.1	0.12	0.25
As-atomized	88	1.0	42	13.0	0.12	0.24

On the basis on all above presented data, it can be concluded that the difference in chemical composition has a minimal effect on the predicted properties of the alloy.

6.2.2 Size distribution

The particle size distribution is determined by dry laser diffraction according to the procedure described in section 3.1.2. In Figure 6.6, the size of powder is characterized by its volume (a) and number (b) distribution, respectively.

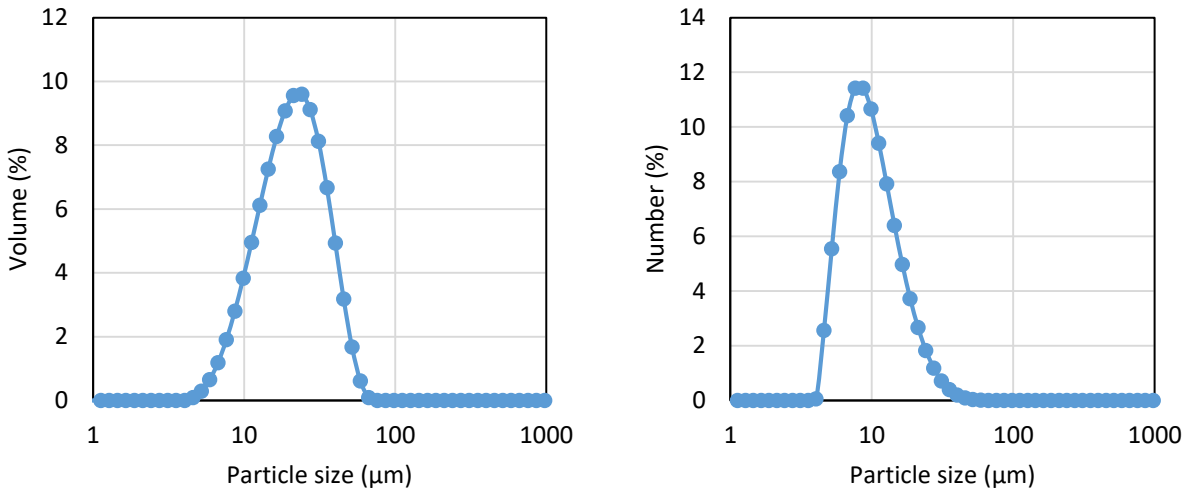

(a) (b)

Figure 6.6 Granulometry of as-atomized powder by a) volume and b) number as measured by dry laser diffraction method

The particle size is considered as "medium", with d_{10}= 11 µm, d_{50}= 22.1 µm and d_{90}= 40.1 µm. Medium sized particles are sometimes considered better than very fine-sized powders (< 10 µm) because they have a better flowability and have a lower tendency to agglomerate. For example, Meier *et al.* [358] have shown that for relatively fine-grained powders (median particle diameter 17 µm), cohesive forces dominate gravity forces by around two orders of magnitude which can lead to low quality powder layers. Here the powder granulometry is within the range of specifications of laser powder bed fusion processes (10-60 µm).

6.2.3 Microstructure and phase analysis

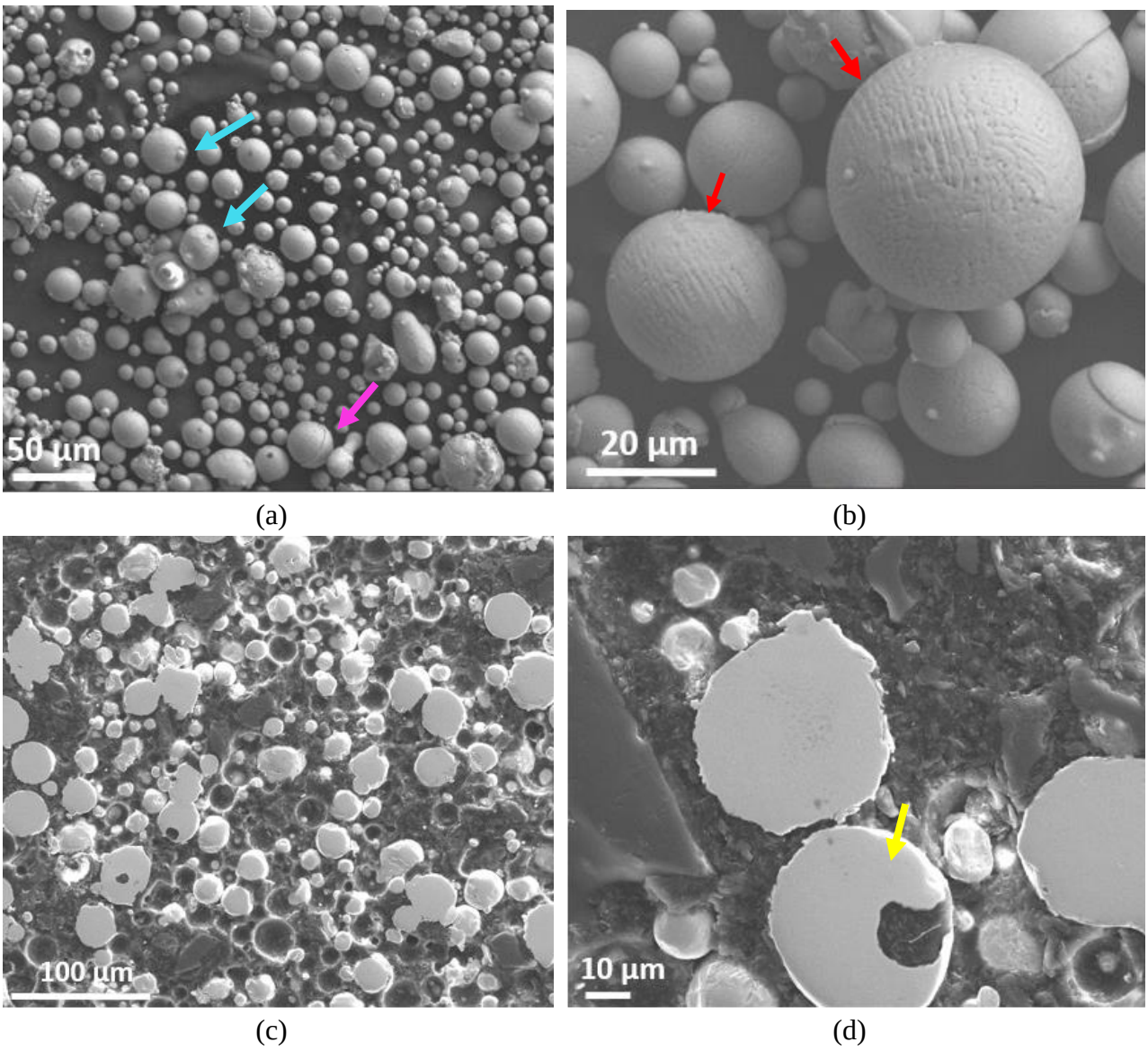

Figure 6.7. Microstructure of as-atomised powder. SEM images. a, b) overall observation of the powder shape and surface; c, d): cross-sections of powder particles.

Figure 6.7 shows SEM micrographs of the surface of the powder as well as its polished cross-section. The majority of the observed particles are spherical in shape (Figure 6.7 a and b), in agreement with what is expected from the atomization process. In cross-section images, Figure 1.7 c and d, more irregular shapes are observed: they are due to small particles collapsed on the surface of a bigger particle during atomization, leading to the presence of “caps” (pink

arrow in Figure 6.7 a) or “satellites” (blue arrows in Figure 6.7 a). Caps happen when a small liquid droplet hits a large cold particle during atomization, whereas satellites are due to the collision of a small cold droplet with a large hot particle (nearly-solidified). The size of the particles is in agreement with the granulometry measurements, with an average diameter of around 20 µm. On the surface of particles, a dendritic structure is currently observed (Figure 6.7 b, red arrow), which is characteristic of the rapid solidification during gas atomization. The cross-section images show the occasional presence of porosity inside some powder particles, especially those which are on the upper size range (≥ 40 µm), as shown in Figure 6.7 d (yellow arrow). The porosity of the powder is estimated using He pycnometry at around 1.8%. Generally, the shape of the pores can give insight on their possible origin. Spherial pores, as in Figure 6.7 d are usually caused by the entrapment of Ar gas bubbles during the atomization process. According to literature, e.g. Cunningham *et al*. [359], this type of porosity can be avoided if enough time is given for argon to escape from the melt. Yet, it is interesting to note that this type of porosity, compared to voids due to solidification shrinkage, is less detrimental to the final mechanical properties, and especially to ductility [18], [110], [360]. In fact, their presence is not associated to any chemical and potentially embrittling segregation, as it may be the case of shrinkage-caused pores.

X-ray diffraction (XRD) analysis was carried out to identify the phases in the powder; the results are shown in Figure 6.8. The observed peaks correspond to two phases. The main Face-Centered Cubic (FCC) phase corresponds to the austenite (γ) phase of iron with a theoretical lattice parameter a = 3.606 Å, according to the JCPDS PDF number 01-081-8775. The minor Body-Centered Cubic (BCC) phase, with a volume fraction estimated to 3%, corresponds to the ferrite phase of the iron whose theoretical lattice parameter is equal to a = 2.882 Å, (JCPDS PDF number 04-003-2920).

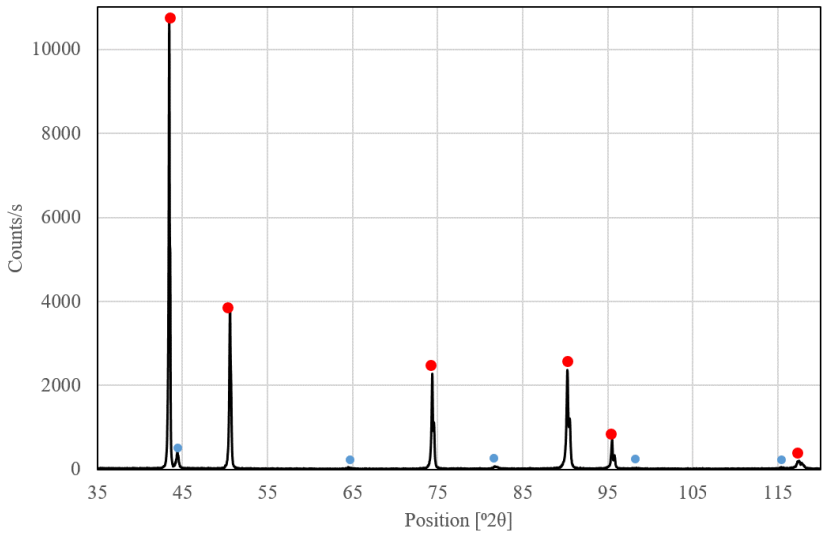

Figure 6.8 X-ray diffraction phase identification in as-atomized powder. Red points: austenite (JCPDS PDF ref 01-081-8775). Blue points: ferrite (JCPDS PDF ref 04-003-2920).

The origin of the ferritic phase in the powder structure should be questioned. In fact, at equilibrium (Figure 5.8), both high temperature δ-ferrite and low temperature α-ferrite may be present in the alloy. As the lattice parameter of both in test conditions (i.e. at room temperature) is the same, unless the phase composition is strongly different, it is impossible to distinguish between two variants of ferrite from sole diffraction measurements. Yet, due to the fast cooling rate in gas atomization of 10^2 to 10^4 K/s [361] (compared to 1−100 K/s for conventional manufacturing processes), it is likely that the observed ferrite is δ-ferrite rather than α-ferrite. Indeed, according to the Scheil-Gulliver simulation of solidification, δ-ferrite is the first solid phase to form. Under slow cooling, this phase should transform into austenite but, in an atomized powder, this transformation could be hindered by the high cooling rate.

6.3 Parts fabricated by selective laser melting

6.3.1 Sample construction

In the state of the art (Chapter 1), we have identified certain key parameters which influence the quality and properties of the final parts produced by SLM. The laser power and scanning speed, scanning strategy, hatching distance (HD) and the thickness of the powder bed are the parameters that mostly affect the microstructure and mechanical properties of built materials.

In general, all the process parameters have a first order influence and should be optimized. However, a sufficient level of optimization may be achieved by considering essentially the power and speed, at least during a preliminary work. Other parameters may be set to a constant value based on existing knowledge of behavior of similar materials and of characteristics of the machine used. Therefore, both constructor recommendations and the existing expertise of the technical staff operating the machine are sufficient in the starting stage of any study involving AM by SLM. Of course, a complete optimization would require an exploration of all the process variables to get the absolute best results and minimal defects, which is here mitigated by the fact that the alloy has been designed specifically to be tolerant to processing conditions and to minimize defects. Nevertheless, it is necessary to choose operating parameters, which can benefit from existing experience. In a previous experimental work in our laboratory [362], focused on the fabrication of 316L using the same SLM machine as we did, the optimal hatching distance was found to be equal to 60 µm, and the optimal thickness of the powder bed was 30 µm. These two values were kept for the current work. An additional variable to set is the focal distance: this parameter was shown to be extremely influent on the porosity rate in former works, as it controls the size of the laser spot waist and therefore the energy density. Default value is 0 mm; however, a significant improvement of the final parts quality was observed by shifting the focal distance to -6.0 mm, and therefore this latter value was here selected as a starting point.

Finally, the scanning strategy consisted in alternating layers at 45° and 225°, in agreement with the recommendations of the constructor. Thus, the present study focuses on two process parameters:

- the power of the laser (P),

- the scanning speed of the laser beam (V).

From these parameters, the volume energy density (VED) will be calculated.

This part aims to evaluate the influence of these parameters on the porosity of the built part and its surface state (roughness). The parametric interval studied is centered around the parameters provided by the machine manufacturer as well as the team experience with producing several grades of commercial stainless steel parts (such as 316L). The whole set of parameters is shown in Table 6.4.

In total, two building jobs could be performed for the parametric search. In the first plate, 28 cubes of dimensions $10 \times 10 \times 10$ mm^3 were built on a stainless steel substrate. An example of a substrate plate with printed specimens atop is shown in Figure 6.9. During the first job, different values of power and speed are tested: two levels of speed (1000 and 1200 mm/s) were selected, and the power was gradually increased from 120 to 250 W with a step of 6 W (2%). For each building job, the resulting part quality was quickly assessed by optical microscopy to select the optimal parameters for the next job. No major problems were encountered, and no apparent macroscopic cracks were observed.

Yet, for certain sets of parameters (see Table 6.4) the building process had to be stopped because of some important surface roughness or warping of the parts, resulting in the friction of the rolling device with the part. This difficulty concerned six built parts, with a power above 195 W. In addition, the observation of surface roughness by optical microscopy revealed a better surface quality for low power within the range 138-153 W, for a speed of 1200 mm/s. Therefore, a second job was carried out to refine the parametric search within these bounds.

Table 6.4 The set of processing variables tested for the first building plate where hatch spacing is 60 µm, layer thickness is 30 µm and focal distance is -6 mm

Visual evaluation	Sample #	P (W)	V (mm/s)
Fair	1	120	1000
Fair	2	126	1000
Fair	3	132	1000
Fair	4	138	1000
Fair	5	144	1000
Fair	6	150	1000
Fair	7	156	1000
Fair	8	162	1000
Fair	9	168	1000
Fair	10	174	1000
Fair	11	180	1000
Fair	12	186	1000
Fair	13	192	1000
Good	14	198	1000
Good	15	204	1000
Very good	16	**141**	**1200**
Very good	17	**150**	**1200**
Good	18	159	1200
Good	19	168	1200
Good	20	177	1200
Fair	21	186	1200
Building stopped	22	195	1200
Building stopped	23	204	1200
Building stopped	24	213	1200
Building stopped	25	222	1200
Building stopped	26	231	1200
Building stopped	27	240	1200
Building stopped	28	249	1200

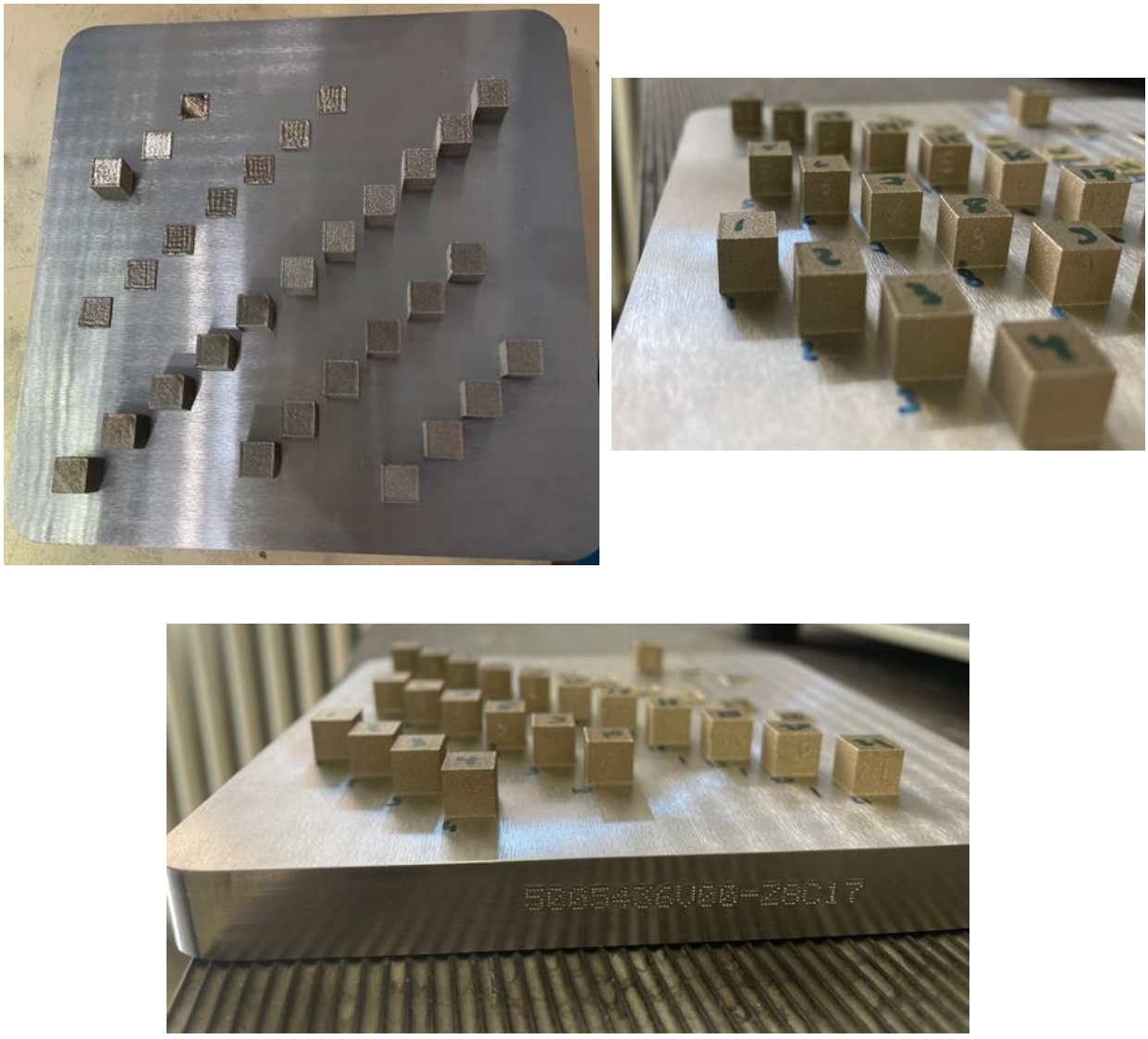

Figure 6.9 Top and side views of a standard build plate with built cubes (10 × 10 × 10 mm^3) printed atop it

During the second job, the speed value was selected at 1200 mm/s and kept constant, and the power was finely changed from 138W to 153 W with a step of 3 W (1%); for a finer parametric tuning, the focal distance was also slightly varied from -5.4 mm to -6.4 mm, with a step of 0.2 mm (see Table 6.5).

Table 6.5 Parametric search for the second building plate where laser speed is 1200 mm/s, hatch spacing is 60 µm and layer thickness is 30 µm.

Visual evaluation	Sample #	P (W)	f (mm)
Fair	2.1	138	-5.4
Fair	2.2	138	-5.6
Fair	2.3	138	-5.8
Fair	2.4	138	-6
Fair	2.5	138	-6.2
Fair	2.6	138	-6.4
Good	2.7	141	-5.4
Good	2.8	141	-5.6
Fair	2.9	141	-5.8
Good	2.10	141	-6
Fair	2.11	141	-6.2
Fair	2.12	141	-6.4
Fair	2.13	144	-5.4
Good	2.14	144	-5.6
Good	2.15	144	-5.8
Fair	2.16	144	-6
Good	2.17	144	-6.2
Very good	2.**18**	**144**	**-6.4**
Fair	2.19	147	-5.4
Good	2.20	147	-5.6
Good	2.21	147	-5.8
Fair	2.22	147	-6
Fair	2.23	147	-6.2
Good	2.24	147	-6.4
Good	2.25	150	-5.4
Fair	2.26	150	-5.6
Fair	2.27	150	-5.8
Fair	2.28	150	-6
Fair	2.29	150	-6.2
Fair	2.30	150	-6.4
Fair	2.31	153	-6

Finally, this allowed to choose the best parameters to construct the final samples for the microstructural and mechanical evaluation of the material in the third building job, presented in Table 6.6. These conditions were providing the best surface quality by optical microscopy.

Table 6.6 set of parameters chosen for the construction of the final parts in the third plate

P [W]	V [mm.s^{-1}]	f [mm]	Hatching distance [µm]	Layer thickness [µm]
144	1200	-6.4	60	30

Once the experimental campaign was completed, more quantitative characterization of the parts was carried out, including surface roughness, porosity fraction measurements, and microstructural analysis.

6.3.1.1 Effect of process parameters on surface roughness

To evaluate quantitatively the effect of process parameters on the quality of the samples, two properties were considered: surface roughness and porosity. The surface roughness of as-built cubes was measured according to the procedure described in section 3.6 (see Appendix B for microscopic images). Due to time limitations, only the top surfaces of the built samples were observed, nevertheless allowing a comparison with other materials printed in similar conditions.

Table 6.7 shows the average surface roughness (S_a) of the top surface of cubes built by SLM produced with different processing parameters. In all studied cases, the S_a values remain small and are contained in the range of 3.6 to 6.2 µm. These values are considered very good as the average reported surface roughness of SLM parts is usually between 5 and 30 µm [363]–[365]. This tends to demonstrate both the beneficial role of a low surface tension and the efficiency of our design strategy regarding this parameter.

No clear correlation between S_a and VED may be drawn but, in the studied range, the minimal surface roughness is measured for intermediate or high values of VED, between 80 and 113 J/mm^3.

Table 6.7 Relation between process parameters and the surface roughness values of the top surface of as-built cubes obtained by SLM

Sample #	P [W]	V [mm/s]	VED [J/mm^3]	S_a [µm]
1	120	1000	66.7	5.28
2	126	1000	70	5.51
3	132	1000	73.3	4.65
5	144	1000	80	4.3
6	150	1000	83.3	4.06
12	186	1000	103.3	5.97
15	204	1000	113.3	3.65
16	141	1200	65.3	6.22
17	150	1200	69.4	5.56
21	186	1200	86.1	3.9

6.3.1.2 Effect of process parameters on porosity

To evaluate the density of the printed cubes in plate 3 (with the processing parameters shown in Table 6.6), two different methods were used as described in section 3.5: Helium pycnometry and Archimedes density measurement.

For the Archimedes method, two different fluids were tested; de-mineralized water and ethanol. Note that the measured densities will depend to a large extent on the value of the actual density of the fluid at the time of measurement. However, as this value is not exactly known during the measurement, the density of the fluids was replaced by the corresponding theoretical value at the room temperature measured at the time of the experiment [366].

As shown in Figure 6.10, the measurements done with de-mineralized water lead to a higher porosity (2.5%) than those performed using pure ethanol (<0.1%), or measured with He pycnometry (1.7%). The difference in the porosity measured for the two fluids can be attributed to the difference in the surface tension of the fluid. It is assumed that a lower surface tension (e.g. ethanol compared to water) should allow the fluid to better wet the surface, thus yield a lower porosity. However, based on the microstructural analysis it seems that the measurements with ethanol underestimates the true porosity. Therefore, the porosity fraction is estimated between 1 and 2.5%.

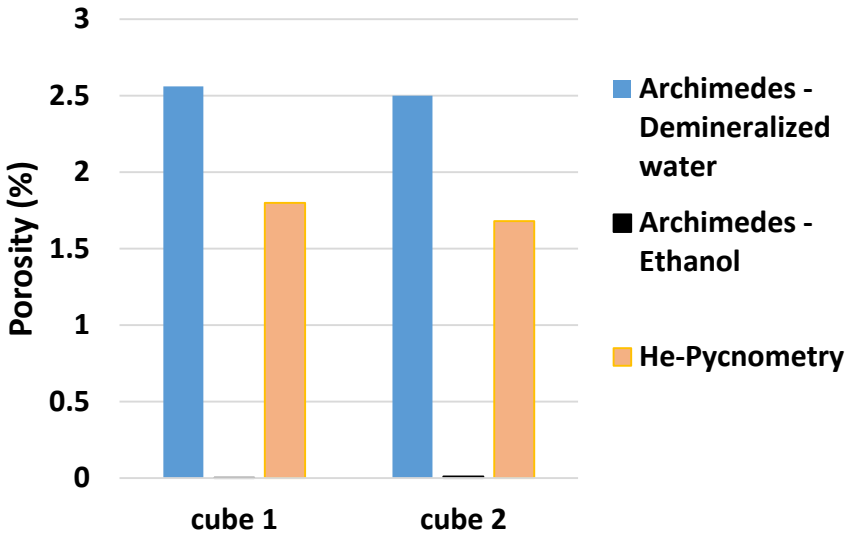

Figure 6.10 Porosity measurements of as-printed cube samples

Then, to study the effect of the processing parameters on the density, the He pycnometry method was chosen to estimate the porosity levels in the cubes built on plate 1.

Figure 6.11 shows the variation of porosity as well as average surface roughness (Sa) as a function of the energy density (VED) for several selected cubes. Overall, porosity varies between 1.3 and 1.8 %. Based on the graph, there seems to be a partial correlation between the porosity and surface roughness values. Both values seem to be higher at the extremities of the VED range tested. The lowest values recorded seem to be in the VED range of 80 to 113 J.mm^{-3}. All the so-built cubes present satisfactory quality, with a roughness below 6 µm and a porosity below 2 %.

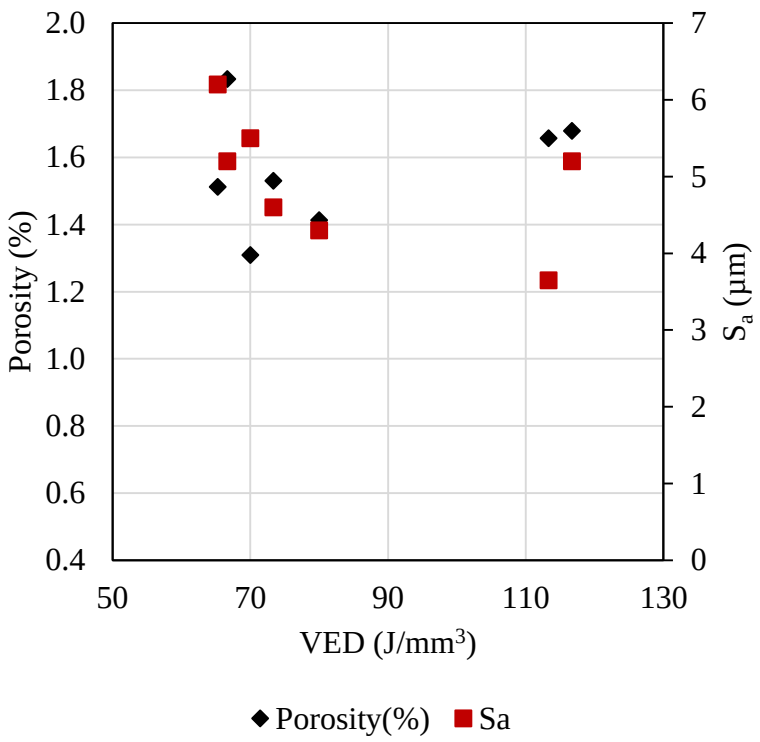

Figure 6.11 Porosity (%) and average surface roughness (S_a) measured as function of VED.

To compare with the values found in literature for stainless steels, Table 6.8 shows the porosity for 316L measured by different authors. Overall, the values vary in the range of 0.1-19.6%, depending on the set of processing parameters used. Note that best values given are usually the lowest porosity values observed after optimizing the process parameters over the tested parametric range. Therefore, we can see that the range of porosity measured in our case (< 1.8%) is comparable to some of the highly dense 316L parts reported in literature.

6.3.2 Chemical composition

Table 6.9 shows the chemical composition of the alloy as measured for the atomized powder and the samples as-built by SLM. Although the content of Fe, Cr and Ni seem to be higher in the SLM material compared to the powder, with a slightly lower content on Mn, the averaged values of repeated EDS measurements show that the compositions of the as-atomized power and SLM samples are close, indicating no significant variation or elemental loss. These primary investigations show that the S_A alloy does not exhibit strong elemental vaporization.

Table 6.8 Summary of density values of additively manufactured 316L parts measured by different authors, where P is laser power, V is laser speed, d is the layer thickness and h is the hatching space distance.

VED [J/mm^3]	P [W]	V [mm/s]	d [µm]	h [µm]	Porosity [%]	Ref
37.8-156.3	85-105	300	20-60	112-125	0.8-1.2	Yasa *et al*. [367]
33.3-88.9	104	300-800	30	130	0.5-0.7	Spierings and Levy [368]
88.2-137.2	100	300	30	81-126	1.1-1.6	Yasa *et al.* [369]
86.8	50	120	40	120	<1	Yadroitsev and Smurov [370]
55.3-110.5	105	380	20-40	125	0.2-0.75	Kruth *et al.* [371]
34.8-75.6	100	175-380	60	126	1.2-4.2	Kruth *et al.* [319]
--	105	380	N/A	125	0.8	Yasa *et al.* [100]
88.9-99.2	100	300	30	112-125	0.8-1.2	Yasa [372]
41.7-125	50	100-300	50	80	0.07-3.3	Liu *et al.* [373]
59.5	87	150	75	130	16	Dadbakhsh *et al.* [374]
145.8-546.9	175	80-200	100	40-60	1.5	Laohaprapanon *et al.* [375]

Table 6.9 The chemical composition (in wt.% unless specified) of the selected alloy in different states. Note that the carbon content was not measured in the as-built material, the content is assumed to be identical to that measured in the powder.

	Fe	Ni	Cr	Co	Mn	Al	C (ppm)	O (ppm)	Measured by
Nominal	42	13.7	15.2	15	11.7	2.3	200	-	
As-atomized	46.5	11.9	13.4	10.3	15.3	2.6	64	53-280	EDS
As-built	42.4	13.6	15.7	11.9	14.1	2.3	64	150	EDS IGA for oxygen

The amount of carbon cannot be measured quantitatively by EDS.

6.3.3 Microstructure and phase stability

After having identified the parameters giving the dense samples (Table 6.6), their microstructure was analyzed. As a reminder, during the analysis of the powder we noted the presence of the γ austenite phase (FCC) but also that of δ ferrite (BCC) in a small percentage. However, a post-SLM characterization by X-ray diffraction (XRD) (Figure 6.12), performed under the same conditions as for powder analysis, shows that only the austenite phase is present. This analysis was also confirmed by SEM-EBSD observations (Figure 6.13). This austenitic phase corresponds to an FCC structure reference (theoretical lattice parameter a = 3.605 Å). The ferrite phase observed in the powder is not detected in SLM samples. It is possible that the ferrite phase has formed and then transformed into austenite.

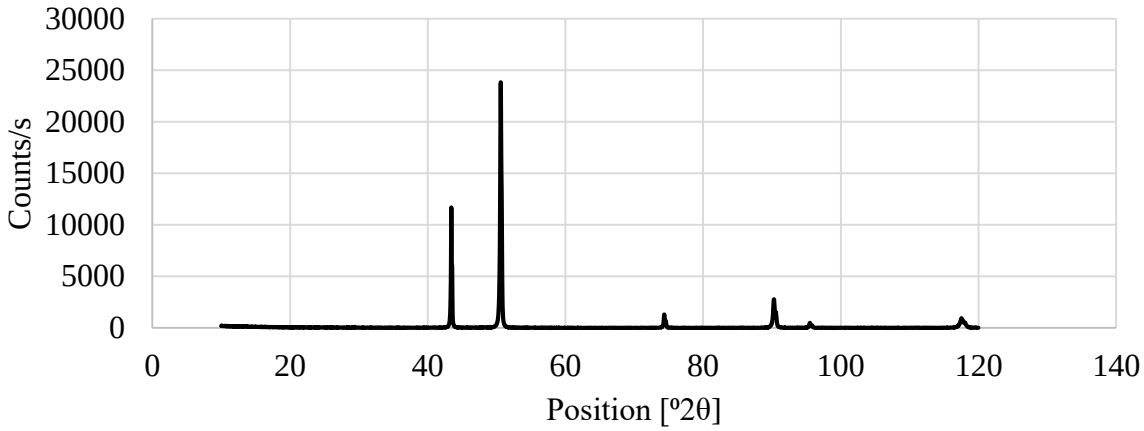

Figure 6.12 X-ray diffractometry of as-built SLM sample.

On the EBSD Inverse Pole Figure (IPF) map, large grains having the geometry of the melting pool are observed. Figure 6.13b illustrates the IPF map along the building direction (BD), on a cross-section of the specimen, with the scanning direction (SD) normal to the figure, and BD oriented to the top. High angle boundaries (>15°) are illustrated by black lines. Small variations of the IPF color code within grains indicate the existence of a substructure after solidification. This suggests that most of the FCC phase was directly formed during the solidification step. Hence, the solidification was probably liquid $\rightarrow \gamma$ for most of the observed austenite, in agreement with predictions.

One can notice that the microstructure is not constituted of long columnar grains, as it is sometimes met in 316L alloy [376], but the crystalline orientation of each successive layer differs from the previous one. This tends to prove that the solidification does not proceed by epitaxial growth between successive layers.

Figure 6.13c shows an IPF map along BD, with BD normal to the figure, and SD along the X and Y axis. This map confirms the existence of large grains in the meltpool, resulting in a microstructure following a grid pattern. The pole figure corresponding to the map 5.12c is shown on Figure 6.13d for {100} planes: this crystalline orientation is preferentially met along BD and SD axis, and it is close to a cube texture.

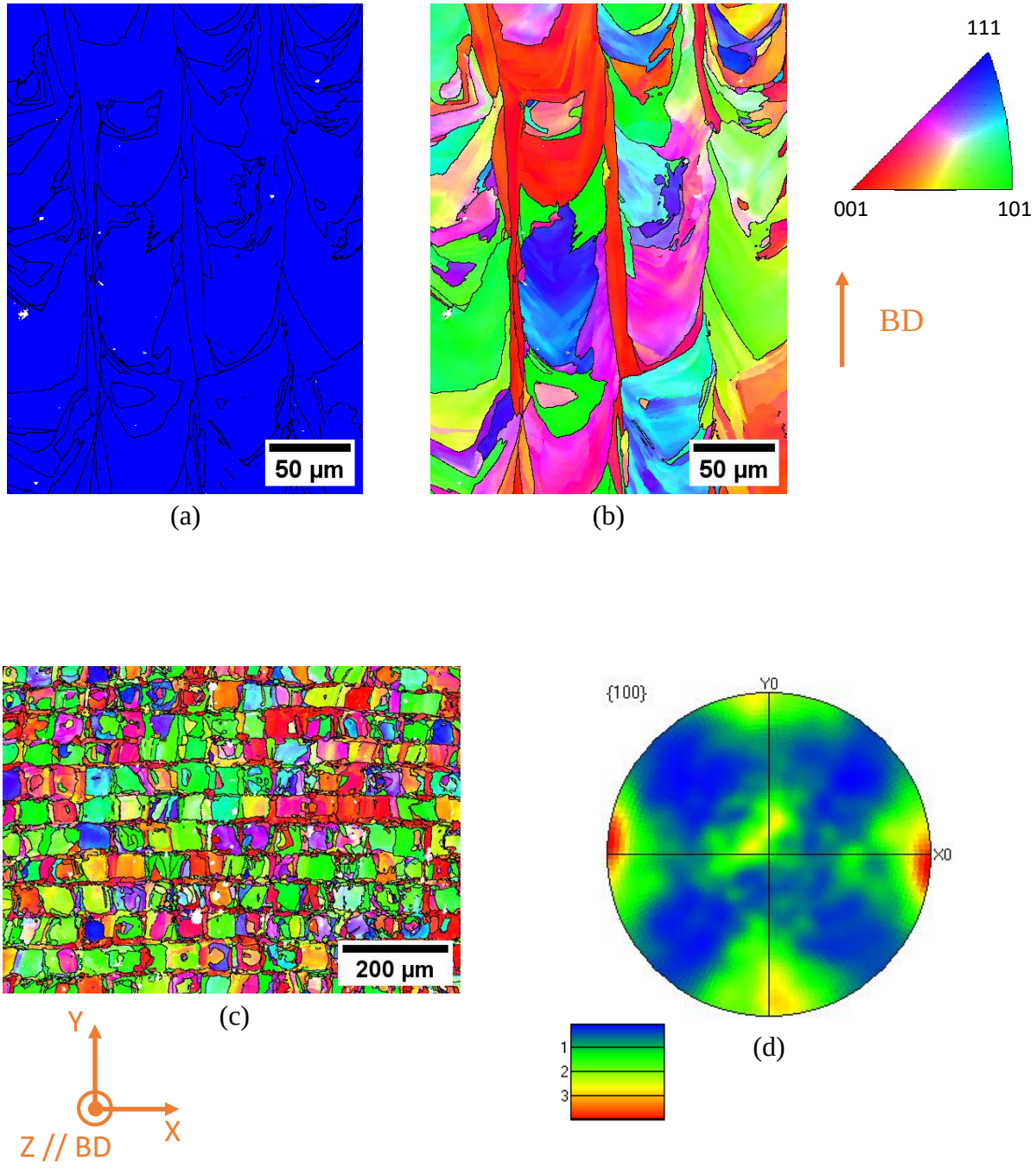

Figure 6.13 EBSD mapping of as-built SLM samples: a) Phase map showing the identification of FCC phase (blue color), b) and c) IPF-Z map indicating the crystalline orientation along the building direction (BD), d) Pole figure corresponding to the IPF map shown on c).

Moreover, the results of the EDS analysis of the as-printed samples shown in Figure 6.14 suggest a uniform distribution of elements indicating a homogenous composition without segregation of elements, except for the presence of Al-rich particles which will be discussed later. Such characteristics have been seen in several studies of materials built with SLM [377].

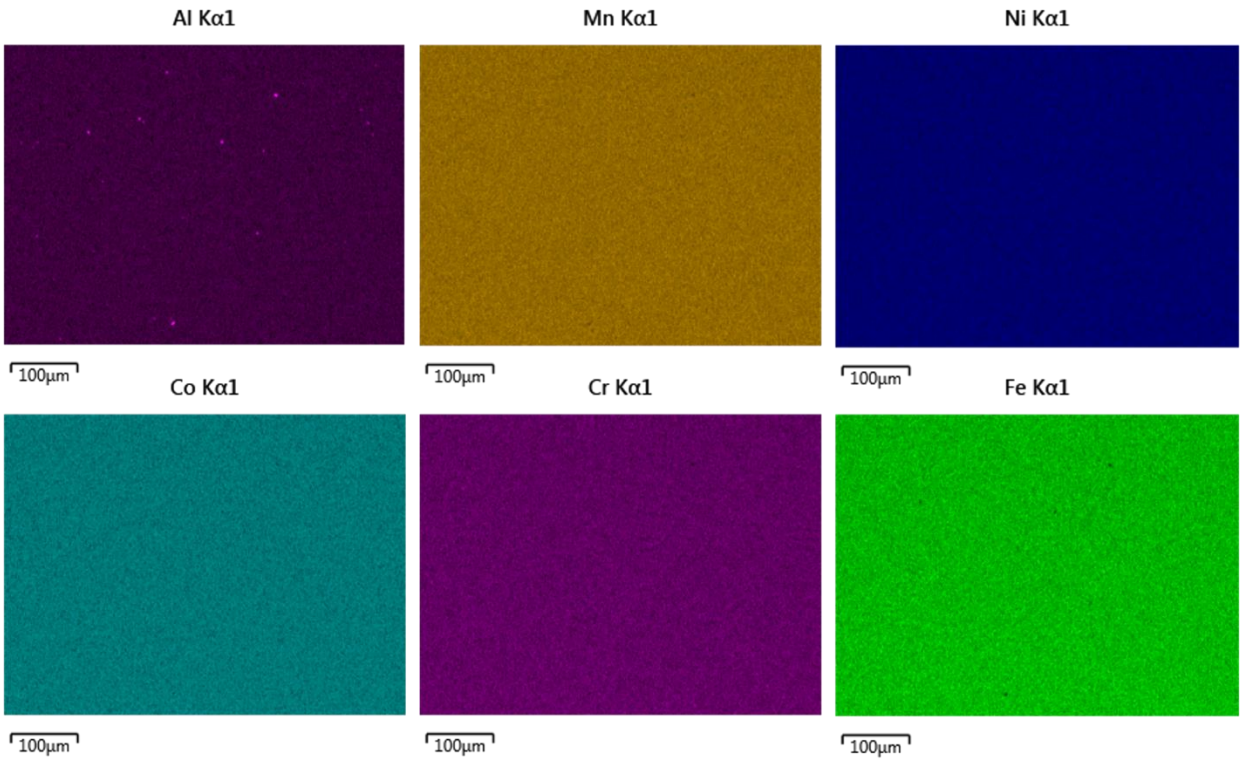

Figure 6.14 EDS mapping of SLM samples.

Figure 6.15 shows the SEM images of the SLM samples. These observations also indicate that the material is single phased.

Additionally, there were no signs of cracking over any of the observed surfaces. Nevertheless, the presence of pores was noticed. The observed porosity is spherical in shape, which suggests that it originated from the entrapment of Ar gas bubbles during the printing process, rather than from a lack of fusion. The frequency and size of pores differed between observed surfaces prepared by mechanical polishing or electropolishing, as the latter tends to enlarge surface pores (Figure 6.15 b). In general, analysis of the porosity based on 2D imaging is not optimal as it is limited to the investigated layer of the bulk sample, and can exaggerate the value compared to Archimedes method or He pycnometry [378].

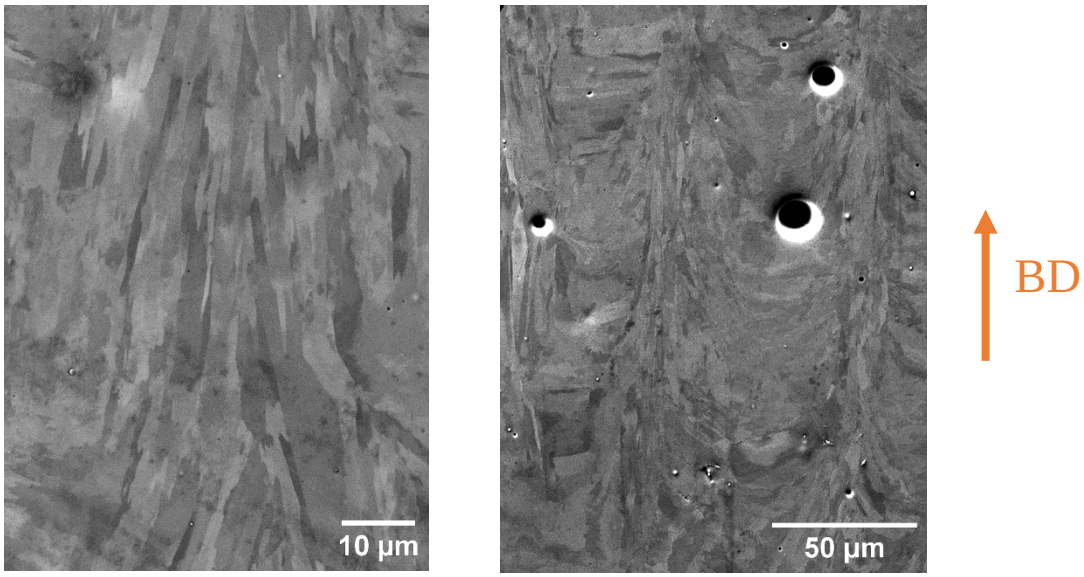

Figure 6.15 BS SEM images of SLM sample, where BD stands for building direction.

6.3.4 Mechanical properties

In the as-built state, the average hardness of the alloy is around 216 ± 6 HV10, almost twice the one (112 HV) measured in the as-cast material. This difference cannot come from the differences in chemical composition of both alloys, the solid solution strengthening value being only slightly affected by the composition deviation. The higher hardness in alloy built by SLM is probably due to the fine microstructure obtained and to the presence of a high density of dislocations, both resulting from the fast cooling rate.

Tensile tests were carried out according to the procedure described in section 3.4.2, at room temperature with strain rate of 10^{-3} s^{-1}. Specimens have been tested in the as-printed state. They were cut in the built part in two different orientations, with the tensile axis parallel or perpendicular to the building plane (called “horizontal” and “vertical”, respectively), in order to assess the potentially anisotropic behavior. For each orientation, three tests have been performed.

Figure 6.16 shows the results of the tensile tests. The main mechanical characteristics (YS, UTS and elongation to fracture), calculated from the stress-strain curves, are summarized in Table 6.10.

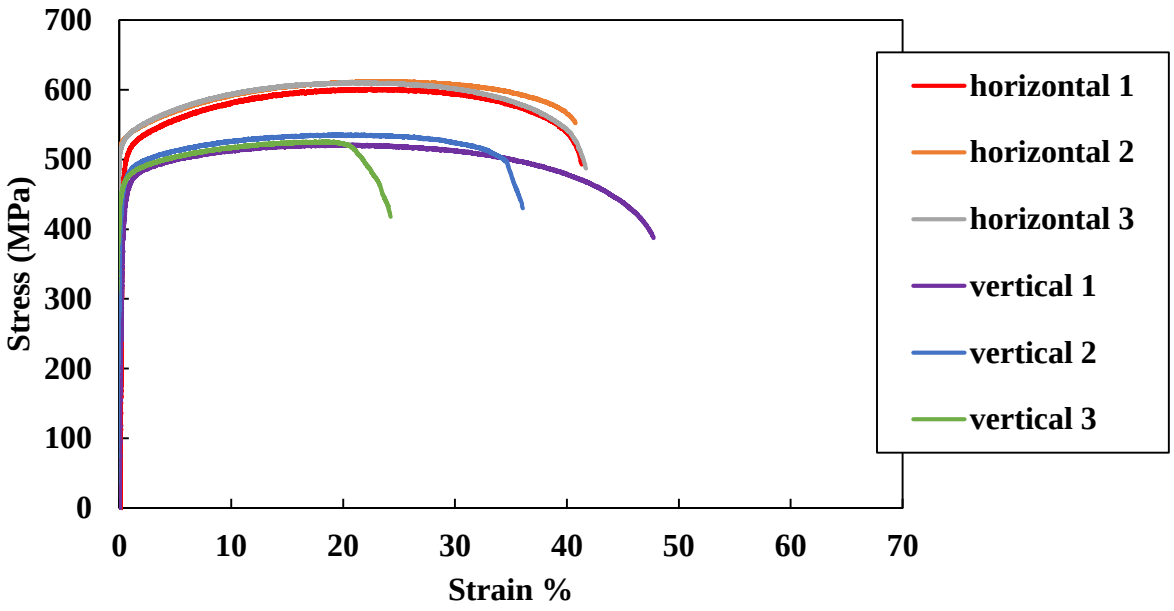

Figure 6.16 Engineering stress-strain curve for the tensile tests on horizontal and vertical as-built SLM samples.

Table 6.10 Tensile properties of the selected alloy in different states.

	YS (MPa)	UTS (MPa)	A%
As-cast	225	445	40
As-built by SLM (horizontal)	520	600	40
As-built by SLM (vertical)	490	525	35

It is satisfying to see that each set of tests shows a good reproducibility. Both for "horizontal" and "vertical" orientations, differences in yield stress are below 5 MPa between specimens. The samples constructed horizontally show a yield strength (YS) and tensile strength (UTS) of 520 MPa and 600 MPa respectively, which is slightly higher than those constructed vertically which have a YS of 490 MPa and UTS of 525 MPa. This difference may be due to the slight anisotropy of the cellular dendrite microstructure of the samples, as explained by Amato *et al.* [379]. The difference in the ductility and tensile strength can also be due to the fact that metallurgical defects are more easily introduced into the bonding area between two consecutive layers leading to somewhat inferior tensile properties [380]. Moreover, the crystalline texture inherited from the directional solidification is a possible explanation for the anisotropic mechanical behavior. However, this difference between construction directions is moderate, around 30 MPa

on average, approaching a material with quasi-isotropic behavior. It is not surprising to note that for both types of samples, “horizontal” and “vertical”, the YS and UTS are higher than that of the same material in the as-cast state which are around 225 and 455 MPa respectively (see Figure 6.3). Let us also note that this result is in agreement with the hardness measurements shown above. Several authors have reported a similar behavior in materials built by SLM such as Al-alloys [381] and stainless steels [107], [152]. Wang *et al.* [270] demonstrated that the cellular structures, with average submicron sizes that could develop during SLM, are a possible reason of increase of yield strength compared to as-cast equivalents. It can be attributed to the Hall-Petch effect, taking into consideration the fine-grained substructure within the bigger grains, creating an effective resistance to dislocation glide. Such a fine-grained substructure with a high density of small-angle grain boundaries was indeed observed in our specimens by EBSD imaging (Figure 6.13).

It is also interesting to note that a strong difference exists between work hardening in as-cast and as-built by SLM materials. It is moderate for the latter since, for a high uniform elongation (for instance, about 30 % for “horizontal” samples), the difference between YS and UTS is of only 80 MPa, while it reaches 220 MPa in the as-cast material. This feature may be explained by a high density of dislocations in the as-built by SLM material. A similar behavior of some austenitic HEAs from the CrFeMnNi family has been observed by Olszewska [355] in hot forged materials.

Elongation to fracture (A%) of the tested pieces, up to 50 %, is quite satisfactory and comparable to values currently measured in austenitic materials obtained from conventional manufacturing. These values indicate a good quality of construction and a probably negligible effect of porosity. In the case of “horizontally” cut samples, the stress-strain curves are quite reproducible. In “vertically” cut samples, and contrarily to mechanical resistance (YS and UTS), elongation to fracture shows strong discrepancies between different tests. For the three tests performed, the total elongation to fracture varies from 19 % (green curve, Figure 6.16) to almost 50 % (purple curve). Such a phenomenon can be attributed to the defects in the material, due to its local microstructure. An explanation should be sought in microscopic observations of fracture surfaces.

The fracture surfaces of the tensile specimens were observed by SEM. Typical images are shown in Figure 6.17. In all samples, ductile fracture is observed, in agreement with mechanical characteristics. The observed microvoids (dimples, shown by red arrows on Figure 6.17 a) are typical of a fracture consecutive to plastic deformation.

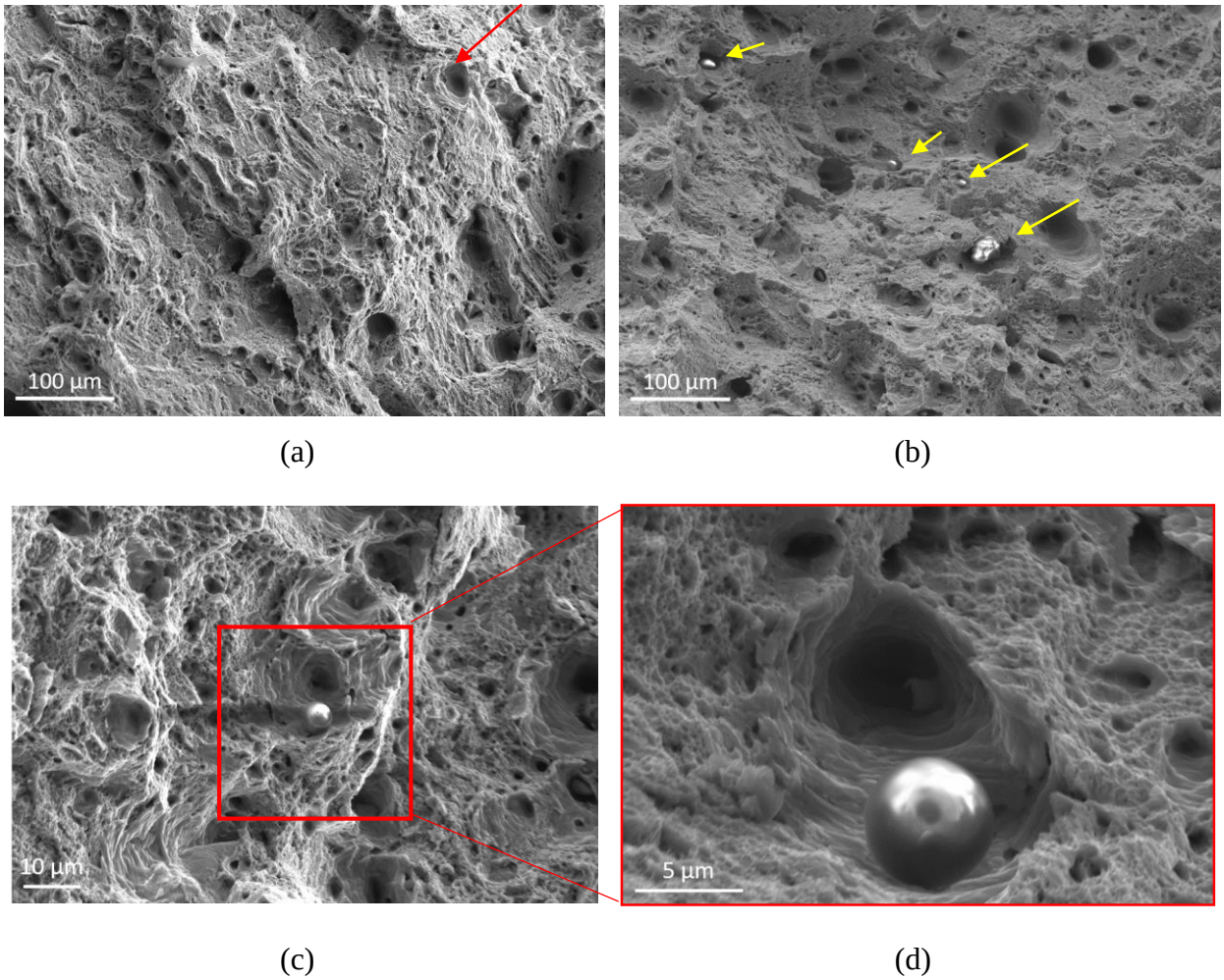

Figure 6.17 SE images of the fracture surface of tensile specimens, showing spherical inclusions. Where a-c-d) is a horizontally built sample, represented by the red curve in fig. 6.16 and b) is a vertically built sample represented by the blue curve in fig. 6.16.

Nevertheless, small spherical inclusions were often observed, as for example on Figure 6.17 b, c and d. The EDS analysis of these inclusions suggests that they mostly contain Al and O (see Figure 6.18). These inclusions were not detected with SEM imaging of the powder.

It is possible to explain the formation of these spherical inclusions thermodynamically. Indeed, Al has a much higher oxygen affinity compared to other alloying elements found in the alloy. According to Ellingham diagram for oxides [382] the standard Gibbs free energy changes for Al_2O_3 is more negative than that for oxides of Cr, Co, Ni, Mn and Fe at all temperatures. This implies that Al will preferentially react with oxygen, if present, inside the powder or in the atmosphere of the laser chamber. Al_2O_3 has a high melting point of around 2070 °C, but during SLM the temperature might reach even higher values depending on the processing parameters. It is also possible that such particles are the result of spattering, as explained in section 1.1.5. On the

other hand, Thermo-Calc equilibrium calculation suggests that Al_2O_3 can form in the alloy under 2050 °C, but in a very negligible amount; between 0.2-0.3% for an oxygen concentration in the range 300-500 ppm, which is higher than what we measured in our material in both the powder as well as the SLM samples. Therefore, these inclusions are most probably due to contamination during the process.

Finally, a better control of the powder processing and storage conditions, in addition to the oxygen content inside the SLM chamber and limiting possible contamination from different materials used with the same machine, might help decrease the content of such inclusions.

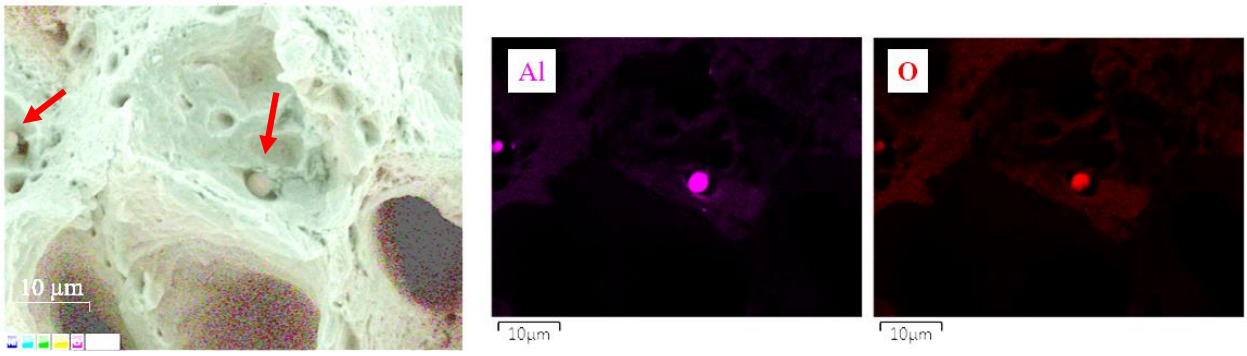

Figure 6.18 Right: EDS maps for Al and O of the inclusions referred to with red arrows on the left SEM image.

6.4 Conclusion

In this chapter, the microstructural and mechanical properties of the selected alloy (S_A) were investigated. The alloy was studied in three different fabrication states: as-cast, as-atomized and as-built by SLM.

The evaluation of the as-cast S_A confirmed our expectations:

- the alloy does in fact show an austenitic single-phased structure;
- the expansion behavior of the material shows that although the CTE of the selected alloy is slightly higher than that of 316L, the difference is not significant enough to cause strong differences in the AM building process.

After characterizing the properties of the as-cast material, the selected alloy was fabricated in powder form. Although the analyzed chemical composition of the powder evidenced a deviation from the nominal designed composition, a re-evaluation of the design properties showed no major difference. The evaluation of the powder indicated that:

- the powder is mainly spherical in shape with a fine size distribution, which is important for the flowability during SLM building;
- around 4% of internal porosity is observed inside the powder particles. The spherical shape of the majority of pores can be attributed to the entrapment of Ar bubbles from the atomization process;
- the powder contains a main FCC phase with a small percentage (~3%) of BCC. The presence of ferrite, absent in the as-cast material, is most probably due to the cooling rate difference between the two processes.

Overall, the powder was said to fulfil the specifications and validated for SLM processing. Finally, the evaluation of the as-built material by SLM showed that:

- the roughness of printed surfaces is very low;
- the observed surfaces are crack-free, and no signs of hot cracking were observed;
- the porosity level of printed samples is in the satisfactory range of 1 to 2%;
- the material displays a single FCC phase, as confirmed by both EBSD and X-ray measurements
- the material is chemically homogeneous with no apparent segregation of elements;
- the alloy exhibits very good ductility with a uniform elongation of 40% for horizontal samples and 35% for vertical samples and a UTS of 600 and 525 MPa respectively. These values are similar to those of 316L built by SLM.

Finally, even though the evaluation results of the S_A alloy do not show a clear superiority with respect to 316L or 304, the material being tried for the first time with minimal adjustment of processing parameters, results can be considered as good. Overall, once printed, the new alloy shows a very good surface quality with no evident distortions, no cracking, a rather low porosity, a composition that is consistent with the targeted one, a fully austenitic structure and fair mechanical properties.

General conclusion

The presented study focused on the design and optimization of new iron-based austenitic materials adapted to the process of additive manufacturing. A numerical method of alloy design, based on a set of selected criteria and constraints to be optimized, was used. A genetic algorithm was used to optimize alloys. One original chemical composition was selected for experimental validation of the models and evaluation of the material.

The aim was to propose new compositions with improved printability and robustness in the additive manufacturing process. To achieve this goal, a thorough analysis of the most commonly observed defects in AM parts was performed. The defects include solidification cracking, porosity, residual stresses and geometrical distortions, balling and surface roughness, etc…

The origins of defects have been associated to different physical phenomena and the effects of material composition on each of them were analyzed in order to propose a set of requirements and material-dependent criteria. The optimization has been performed in a large composition base, containing twelve chemical elements: eleven metals to which a constant small content (200 wt. ppm) of carbon was associated.

The microstructure stability after solidification was the first criterion to be considered. It was discussed in two steps. The first was to set a constraint for the feasibility of the researched alloys: based on the Hull diagram, a fully austenitic structure after solidification and cooling was sought. Secondly, the solidification conditions were evaluated using the Scheil-Gulliver model, searching for an “FA” (ferrite-austenite) solidification mode. Alloys solidifying in any other mode were considered infeasible. The Scheil-Gulliver simulation also allowed to calculate the critical temperature range (CTR), which was set as an objective to be minimized to avoid hot cracking. To ensure a good mechanical strength, and a better resistance to thermal strains, the solid solution hardening of the alloy, estimated from the Labusch model, was set as an objective to be maximized. To ensure a low level of residual stresses in the final component, we aimed at minimizing the coefficient of thermal expansion of the material. It was calculated using a rule of mixtures (linear combination of the CTE of alloying elements).

To improve the meltpool behavior and the surface quality (by decreasing roughness), several properties were taken into consideration. Vaporization fluxes play a significant role in controlling AM processes. Through keyholing, it can lead to the entrapment of gas bubbles within the meltpool and therefore induce porosity in the final component. For this reason, the average vaporization flux of the elements within the meltpool, calculated from the partial vapor pressures of the compositional elements, was set to be minimized. Similarly, we aimed at minimizing the distribution of vaporization between different elements, as to avoid a change in chemical composition of the built part.

Finally, the surface tension of the designed alloys was considered. To ensure a higher fluidity and avoid phenomena such as balling or swelling, the surface tension was set to be minimized. Its value was estimated using a Gaussian process regression model that was developed in the frame of this work.

The combination of all the different predictive tools (CALPHAD, machine learning model, physical and linear models) with the genetic algorithm NSGA-II allowed a multi-objective optimization of austenitic materials compositions and led to identification of a set of non-dominated solutions. The originality of proposed solutions comes from the fact that the optimized alloys lie between conventional stainless steels and complex concentrated alloys. From the whole set of one hundred of alloys, one composition was selected to be experimentally evaluated. Selection was assisted by a multi-criteria decision algorithm. The alloy was studied in three different fabrication states: as-cast, as-atomized and as-built by SLM.

The microstructural and mechanical properties of the selected alloy confirm the expected properties and characteristics. An austenitic, single-phased structure was obtained in the as-cast state. The material shows a convenient strength and ductility (HV = 115, tensile room temperature YS = 455 MPa, elongation to fracture 50 %), not surprising for a non-optimized microstructure. The thermal expansion coefficient (CTE) was shown to be slightly higher than that of 316L grade, yet the difference is not high enough to cause significant changes in the AM building process.

The powder of the selected composition was produced by gas atomization under Ar. Mainly spherical particles, with a medium size distribution (d_{50} = 22.1 µm), convenient for the SLM process, were obtained. Although a relatively high (~ 4%) internal porosity was observed, the majority of the observed pores are spherical in shape and attributed to the entrapment of Ar bubbles from the atomization process. Contrarily to the as-cast material, a minor (~ 3%) BCC phase was observed, according to XRD results. The difference may most probably be attributed to the cooling rate difference between the two processes.

Finally, the powder was used to build samples by Selective Laser Melting. Due to limited time for performing this part of the study, the process parameters have been chosen mainly on the basis of existing experience of the laboratory, gained in the frame of previous projects on classical stainless steels. Yet, the microstructural and mechanical analysis of the samples built by SLM showed satisfactory results. The observed surfaces were all crack-free, and no signs of hot cracking could be detected. Overall, the porosity of printed samples is limited to 1-2%, at an acceptable level, currently encountered for printed austenitic stainless steels. Given that process parameters have not been adjusted specifically for this material, this can be seen as an excellent result. The selected alloy built by SLM is characterized by a single FCC phase, in agreement with expectations. Furthermore, the material is chemically homogeneous with no apparent segregation of elements as shown by the SEM-EDS measurements. The tensile tests of printed specimens showed that the selected alloy exhibits a good ductility with an elongation of 40% for horizontal samples and 35% for vertical samples, and with a UTS of 600 and 525 MPa respectively. These values are very

similar to that of 316L built with SLM, where the UTS varies between 370 and 760 MPa and elongation varies between 9 and 66%. It was shown that the building orientation has an effect on the tensile properties, yet for both building directions, the values were higher for as-built SLM samples than for the equivalent as-cast sample. It is believed that the tensile properties can be further improved by controlling the impurities level during the gas atomization process as well as the SLM process.

The presented work brings new insight into the tailored design of austenitic materials for additive manufacturing, yet, several areas of the study could be further improved.

Future steps could include incorporating different additional criteria that were not taken into account in our study, such as the cost of the material, its density [229], or criteria on recyclability, ecological impact or geo-political risks [220].

Due to the constraint of time, the experimental assessment part of the optimized material was limited in several aspects. In our study only one composition was experimentally produced, whereas different other compositions associated with diverse selection scenarios would have brought insight on the effect of various criteria on the final properties of the product. Additionally, the processing of the selected composition by SLM was somewhat restricted by time as well; otherwise, further optimization of the process parameters would have been possible. Similarly, further characterization of the material built by SLM would have been interesting. This includes some properties that were considered in the design criteria, such as residual stresses, but also others, like fatigue behavior, corrosion resistance, effect of temperature on properties, among others.

Finally, in this study we have focused solely on the material composition aspect in the design process. Nevertheless, considering process dependent parameters for future work would open a wide perspective. The combination of material and process dependent criteria could provide a better description of the overall design method. Nevertheless, the present work aimed at demonstrating the feasibility of the method, which seems globally attained. But of course, aiming for a specific application would constitute an interesting industrial perspective.

Appendix A: Non-Sorting Genetic Algorithm

In order to start a genetic optimization, the first step would be to generate a random population P_0 with a specific size and must cover a large scale in the search space. This is what we call *initialization*, and it is only done at the beginning.

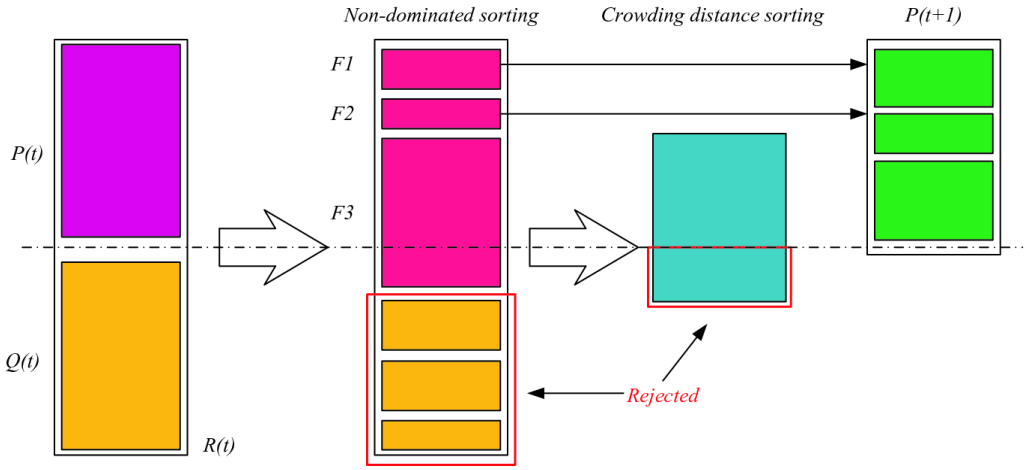

Figure A.0.1 Schematic summary of the GA algorithm

To describe how the algorithm works starting from here, consider the scheme Figure A.0.1. During each successive generation, several steps are taken, and repeated until the end of the optimization:

I- Selection

A proportion of the existing population, P(t), is selected and used as parents to breed a new generation. Individual solutions are selected through a fitness-based process; fitter solutions are more likely to be selected. The idea is that "the better an individual is; the higher its chance of being a parent" [383]. In single-objective problems this is easily done by comparing the objective value, whereas in multi-objective problems this is determined according to a concept of dominance, which will be further detailed later in the text.

II- Reproduction

The use of the selection process determines the parents used in the crossover to produce a new offspring. Once parents are selected, a process of crossover (recombination) and/or mutation is applied to produce a new generation of offsprings, Q(t).

(a) Crossover

Crossover is implemented by selecting a random point on the chromosome where the parents' parts exchange happens. The crossover then brings up a new offspring based on the exchange point chosen with particular parts of the parents. There are different types of crossover techniques, from these we can namely mention: one-point crossover, two-point crossover, and multi-point crossover. An example of one-point crossover is shown in Figure A.0.2 a.

(b) Mutation

After crossover is done, mutation takes place. This operator applies the changes randomly to one or more "genes" to produce anew offspring. For example, in binary encoding, one or more randomly chosen bits can be switched from 0 to 1 or from 1 to 0. This creates new adaptive solutions and helps to avoid local optima. The mutation operator is used to ease this problem by creating a new offspring slightly different from parents, and this encourages diversity in the population. Some 'alleles' are slightly changed; an example is shown in Figure A.0.2 b.

The setting of these parameters, like other genetic operators is usually tuned and experimented with by trial and error until the performance of the algorithm is optimized, and better solutions of the problem are found.

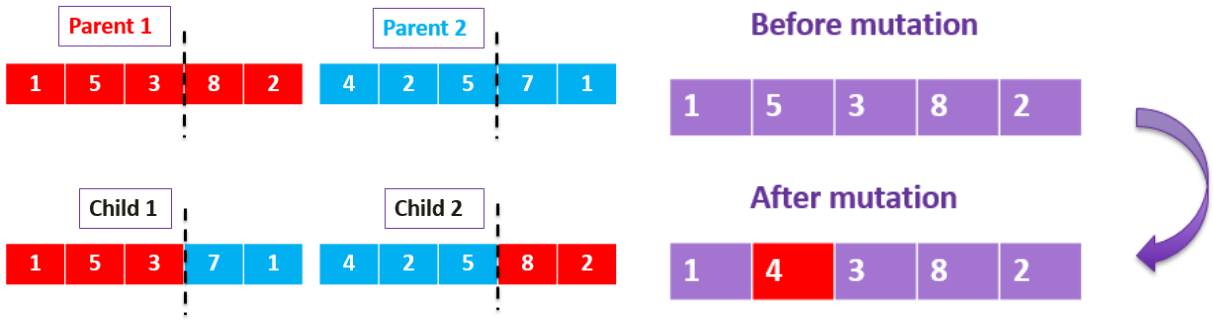

(a) (b)

Figure A.0.2 Example of a) one-point crossover and b) allele mutation

III- Evaluation

Once a new generation of offspring Q(t) is created, an evaluation step is necessary to proceed. All individuals in R(t) (P(t) U R(t)) must be evaluated based on the defined set of objectives, which will allow to sort the individuals. To do this, one must calculate the different non-dominated fronts starting from the first non-dominated front F_1 up to F_n. This step is necessary to create the new set of ranked individuals, which will allow us to reach the new population of the successive iteration, P(t) as shown in Figure A.0.1. The individuals belonging to the first fronts must be selected to constitute the next generation, and other individuals will be eliminated or rejected to keep the initial size of the population. Therefore, some selection must be operated to decide which individuals of the first fronts can be included in the population of size N. Hence, the individuals of the non-dominated fronts are sorted according to their crowding distance: this value estimates

the average distance of an individual with its neighbors. Individuals located in low population density will be pushed up, and individuals located in highly crowded areas will be penalized.

To summarize, every individual p in the population has two attributes:

- Non-domination rank (p-rank)
- Crowding distance (p-distance)

And solution i is preferred over solution j if:

$$i\text{-}rank < j\text{-}rank$$

$$OR$$

$$(rank\ of\ i = rank\ of\ j)\ AND\ (i\text{-}distance < j\text{-}distance)$$

To do this, it will be necessary to revisit the concept of dominance and how to find the different non-dominated fronts, as well as the diversity preservation operators:

IV- Concept of Dominance

In a Multi-Objective Genetic Algorithm (MOGA), an individual A is said to be better than an individual B if A dominates B. This domination occurs if both conditions below are true:

- The solution A is no worse than B in all objectives
- The solution A is strictly better than B in at least one objective.

Among a set of solutions P, the non-dominated set of solutions P' are those that are not dominated by any member of the set P. The non-dominated set of the entire feasible search space S is the globally Pareto-optimal set.

For every population, we need to find the different dominating fronts. Therefore, for every individual p, two values are defined:

- Domination count (n_p): how many individuals dominate p
- Domination list (S_p): list of individuals that p dominates

In the presence of constraints, each solution can be either feasible or infeasible. Three situations can be met:

1) If both solutions are feasible then the dominating solution is selected

2) If one is feasible and other is not, then the feasible is selected

3) If both are infeasible then choose the solution with the smaller overall constraint violation

To find the first non-dominated front F1, it is enough to look at individuals with zero domination count. To find the individuals in the next non-dominated front, solutions of F1 are discounted temporarily and the above procedure is repeated until all fronts are defined. For a simple example, see Figure A.0.3.

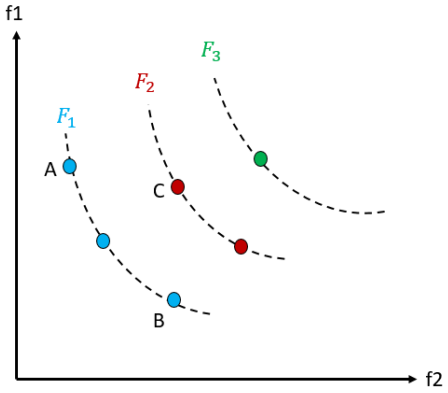

Figure A.0.3 Scheme showing the different Pareto fronts F_n in a two objectives (f1 anf f2-- to be minimzed) problem

V- Diversity Preservation

The density estimation is used to estimate density of solutions surrounding a particular solution in the population. For each objective, the crowding distance for a solution i, is defined as the difference of the objective function value for neighbors i+1 and i-1, as illustrated in Figure A.0.4. For example, the crowding distance of the ith solution in Figure A.0.4 in its front (solid circles) is the average side length of the cuboid (shown with a dashed box).

Then, this distance is normalized by the maximal difference of the objective function for the whole set. For boundaries, as neighbors on one of the two sides are missing, the value is directly set to infinity to ensure the selection of these points. Finally, to calculate the overall crowding distance of the solution, this value is summed over all objectives.

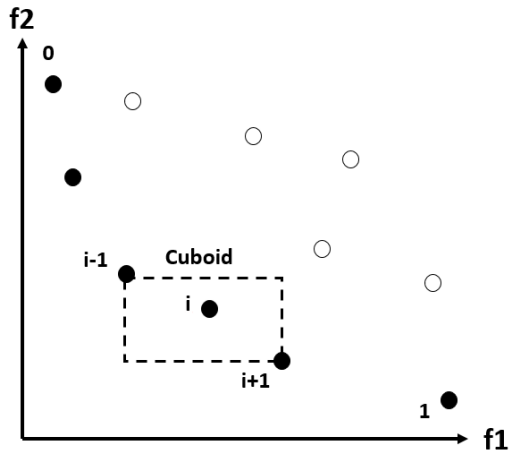

Figure A.0.4 Schematic of a Pareto curve showing a set of dominant solutions

The calculation of the crowding distance will allow to define the p-distance for every individual p. This value, along with the p-rank, will help to be used to sort and select individuals that are preserved for the next generation, in population P(t+1).

Appendix B: Surface roughness microscopic images

P=120 V=1000	P=126 V=1000
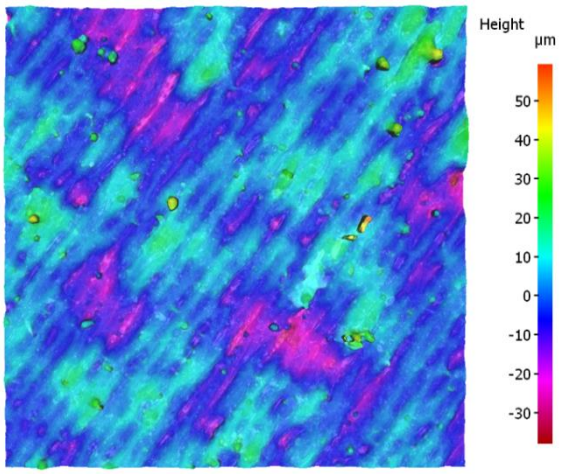	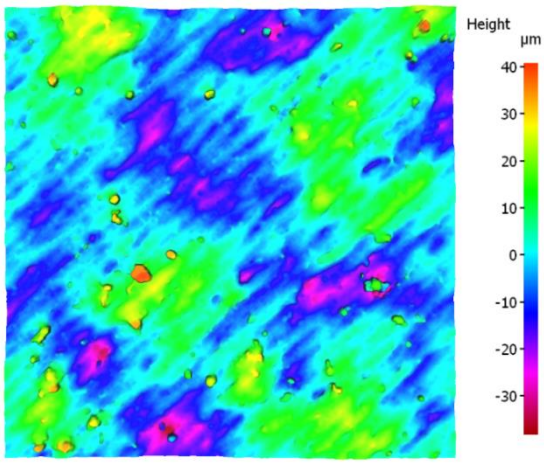
P=132 V=1000	P=144 V=1000
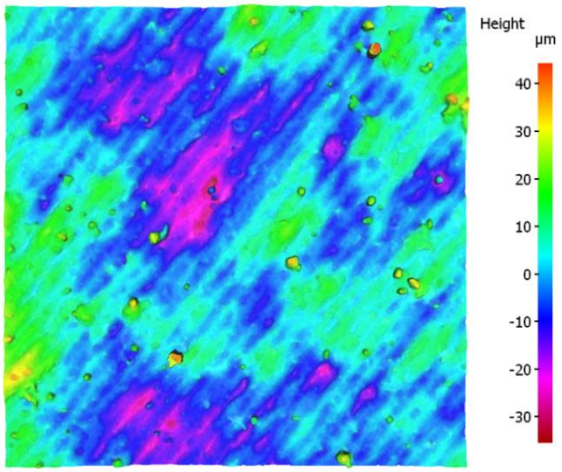	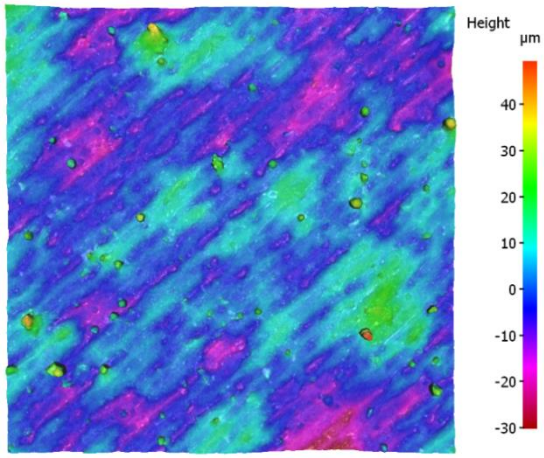
P=150 V=1000	P=204 V=1000
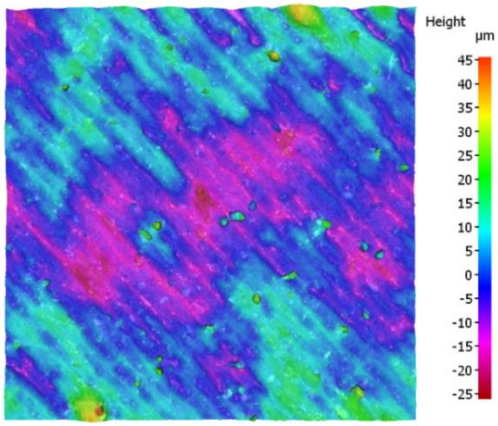	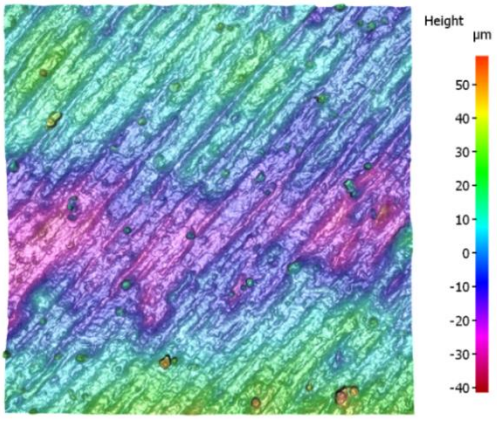

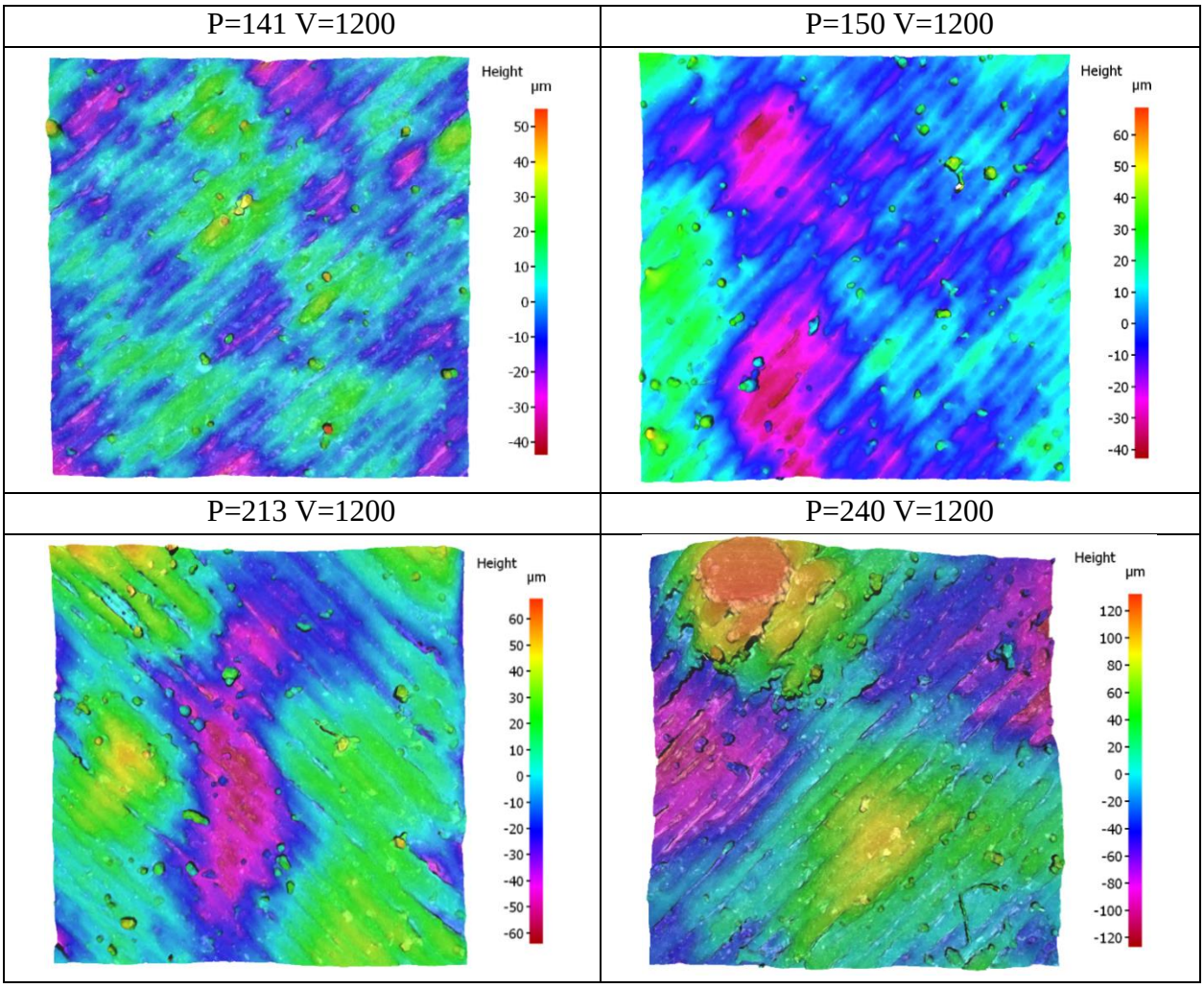

Figure B.1 Microscopic images showing the effect of the process parameters on the surface roughness of different as-printed samples where V is laser velocity in mm/s, P is laser power in W and f is the focal distance in = 60mm/10

Appendix C: Machine learning-based model of surface tension of liquid metals: a step in designing multicomponent alloys for additive manufacturing

Mariam ASSI[1*], Julien FAVRE[1], Anna FRACZKIEWICZ[1*] and Franck TANCRET[2]

1: Mines Saint-Etienne, Univ Lyon, CNRS, UMR 5307 LGF, Centre SMS, F - 42023, Saint-Etienne, France

2 : Nantes Université, CNRS, Institut des Matériaux de Nantes Jean Rouxel (IMN), 44000 Nantes, France

Abstract: The surface tension (ST) of metallic alloys is a key property in many processing techniques. Notably, the ST value of liquid metals is crucial in additive manufacturing processes as it has a direct effect on the stability of the meltpool. Although several theoretical models have been proposed to describe the ST, mainly in binary systems, both experimental studies and existing theoretical models focus on simple systems. This study presents a machine learning model based on Gaussian process regression to predict the surface tension of multi-component metallic systems. The model is built and tested on available experimental data from literature. It is shown that the model accurately predicts the ST value of binaries and ternaries with high precision, and that identifying certain trends in the ST values as a function of alloy composition is possible. The ability of the model to extrapolate to higher-order systems, especially novel concentrated alloys (high entropy alloys, HEA), is discussed.

Keywords: surface tension, liquid metal, machine learning, data science, Gaussian Process Regression, high entropy alloys, stainless steels

*Corresponding authors: Mariam-assi@hotmail.com, anna.fraczkiewicz@emse.fr

1. Introduction

In recent years, the development of innovatory processes like Additive Manufacturing (AM) has open new possibilities in modern metallurgy. However, the available set of conventional alloys currently known to be reliably processable by AM remains quite limited, and there exist very few materials that are optimized for these processes [384]. Designing new, "AM-dedicated alloys" is challenging [17], [385]–[388]: in such materials, minimization of the defects in final products (like hot cracking, porosity, surface roughness, balling, residual stresses and distortions) is expected. AM processes involve liquid metal, so different properties of materials in this state are of practical importance and need to be studied. Among them, the surface tension (ST) is crucial, as two different effects involving this characteristics may be feared: (i) the ST value influences the conditions of wetting of the previously deposited solid phase by the liquid one; (ii) the absolute ST value and its variation with temperature contributes to the control of the meltpool stability and shape [275].

It is currently admitted that the ST value depends on the temperature of the liquid, pressure and chemical composition of the alloy [283], [284]. Generally, for a wide range of materials, the ST decreases with temperature [285]–[288]. There is no general rule about alloying effects on ST in comparison to pure elements. Typical values in metals and alloys range from $0.4\ N.m^{-1}$ (e.g. Li at 453 K) to $2.5\ N.m^{-1}$ (e.g. W at 3650 K) [284].

Experimental measurement of surface tension in metallic alloys faces many challenges and is subjected to numerous sources of error. The difficulties come from several features. First, the measurements need to be performed in the liquid state, at high temperatures, facing an obvious and difficult to avoid risk of contamination (oxidation). Moreover, real alloys currently contain impurities; some of them (S, O) have a significant effect on ST, decreasing its value even for very low content in the alloy [289]–[293]. Several methods of experimental assessment of surface tension exist; their details have been reviewed [298]. The Sessile Drop Method (SD), and the pendant drop method (PD) similarly present the advantage of providing values of ST over wide ranges of temperatures [389]; however, the use of reference surfaces and/or capillary tubes respectively is a source of significant error [298]. Surface contamination effects are much less pronounced in the Maximum Bubble Pressure Method (MBPM) in which consecutive measurements are done on a freshly formed surface [390], [391]. Finally, the Electromagnetic Levitation (EL) method provides an enhanced accuracy as it eliminates persistent sources of contamination as mentioned above [298].

Theoretical description of surface tension, based on alloys thermodynamics, started at the beginning of 20^{th} century, with the first approaches proposed by Gibbs [294] and improved by Guggenheim [295], [296]. Finally, the Butler model proposed in 1932 [297] became the most known and used model to estimate the ST values from the chemical composition of the alloy.Although it provides a fair estimation, the Butler model remains inaccurate in many cases, probably due to neglecting the atomic structure of liquid alloy surfaces [298]. Recently, Vermot

des Roches *et al.* [299] have compared the results of ST calculations by Butler model to available experimental data on binary alloys : it was shown that the Butler model fails to accurately predict almost 40% of them.

In an attempt to alleviate some of the limitations of the Butler model, Wynblatt *et al.* [300] presented an approach that is built on the same assumption of the equality of chemical potentials between surface and bulk but instead of a monolayer, the surface was considered to be made of multilayers. Although more general, this model could not really improve the prediction of certain systems such as the Al-Ni system. Egry *et al.* [29], [30] proposed an analytical model extended from the ideal solution approach. It was able to significantly enhance the predictions of several systems, for example the Al-Ni and Fe-Ni systems. Yet, a general model that would be able to describe all the existing alloys is still missing.

Some authors proposed models relating the ST value in a given metallic matrix to the presence of different surface-active elements. An interesting approach was presented by Ghebiri *et al.* who proposed a semi-empirical model describing the oxygen content effect in different metallic liquids [303].

Although several theoretical models have been proposed to describe the ST, mainly in binary systems [295], [297], [300], [304], and some authors have used them to estimate the ST values and evolution for ternaries and multi-element alloys [305]–[307], both experimental studies and existing theoretical models focus on simple systems. Rare are the results coming from alloys containing three or more elements, except experimental measurements in several grades of industrial alloys like austenitic stainless steels [308]–[310] and Ni-based superalloys [311], [312]. Besides, the lack of models for multicomponent systems is due to the difficulty in physical modeling the complicated behavior of ST, when several elements are included and the large number of parameters is required to assess.

In this work, a general machine learning-based (ML) model is proposed to predict the surface tension of metallic alloys. The model is based on a Bayesian algorithm, specifically Gaussian Process Regression (GPR). The ambition of the ML-GPR model is to enlarge its application field to multicomponent alloys. Thus, after its training and validation on existing experimental data, the ability of the model to predict surface tension in more complex compositions (like classical stainless steels) and some innovatory concentrated alloys (austenitic single phase HEA alloys from the CoCrFeMnNi family) will be tested.

2. Methods

2.1 Data Processing

The data used to build, train and develop the model come from existing bibliography. Its exhaustive list is referenced and the list of exploited systems is given in Table C.4. A large panel of metallic systems (pure metals, binaries, ternaries as well as some multicomponent systems like industrial alloy grades) have been taken into account, in the limits of our best knowledge. All

measurement techniques were considered. However, ST data for alloys containing elements such as Na, K, Rb, Cs, Bi and Pb were not considered. In most of the cases, these elements were studied as additives [392] and their low content does not permit a comprehensive extrapolation.

In total, around 2200 data points were collected from approximately 70 scientific articles. The data considered consists of purely experimental data. The elements considered are: Ag, Al, Au, C, Co, Cr, Cu, Fe, Ge, Li, Mg, Mn, Mo, Nb, Ni, Si, Sn, Ta, Ti, W, Zn, and Zr. The data points are measurements recorded at different temperatures, for which around 520 points are for pure elements, 1257 for binary systems, 350 for ternary systems, and less than 140 points for quaternary and higher order systems. Impurities such as oxygen, sulfur and phosphorus, as mentioned in section 1, behave differently and require a different approach. Moreover, in most cases the content of these elements is not specified but rather approximated. Hence, they were not included in the composition vector.

Within the considered alloys and alloying elements, the construction of the database highly depended on the availability of measurements in literature, so that not all elements or materials are represented evenly. This will be discussed later. In addition to the amount of data, another issue lies in the measured values themselves. Each measurement is subjected to an error, whether experimental or due to the purity of the material studied, both which could vary between different sources. Therefore, a discrepancy in the values is inevitable. For example, Fig. 1 a) shows different values of ST for pure zirconium as reported by different authors and compared by Paradis *et al*. [393]. The discrepancy in the measurements reaches up to around 0.15 $N.m^{-1}$ at the melting temperature. The authors also showed similar comparisons for pure niobium and pure titanium. Similarly, measurements of ST for pure Fe could vary significantly between different sources. Monma *et al.* [394] reported a value of around 1.65 $N.m^{-1}$ for pure Fe at 1823 K, while a value of around 1.9 $N.m^{-1}$ was reported by Brillo *et al.* [395]. Likewise, two sets of values for the Fe-Ti system are shown in Fig. 1b, which will be discussed later. Such scatter in data may largely originate in differences between the various measurement methods mentioned in the introduction. However, in our study all the sets of different values were used, assuming that the statistical nature of the used ML tool (GPR) will allow to smooth out the scatter and extract correct trends. Such an ability was for instance illustrated by the learning of phase formation in multicomponent alloys, from highly scattered data, with large differences coming from a wide diversity of experimental conditions and methods [169]. The resulting model was then trusted, and successfully used for alloy design [170], demonstrating its ability to learn relevant trends from highly noisy data. It was thus chosen here to use all available data (i.e. both old and recent, coming from different measurement techniques). Indeed, on one hand there would not have been a systematic and rational way of deciding what data are good or wrong or better than others, and on the other hand removing all the data appearing scattered would have led to an extremely limited applicability of the model (number of elements, concentration spans).

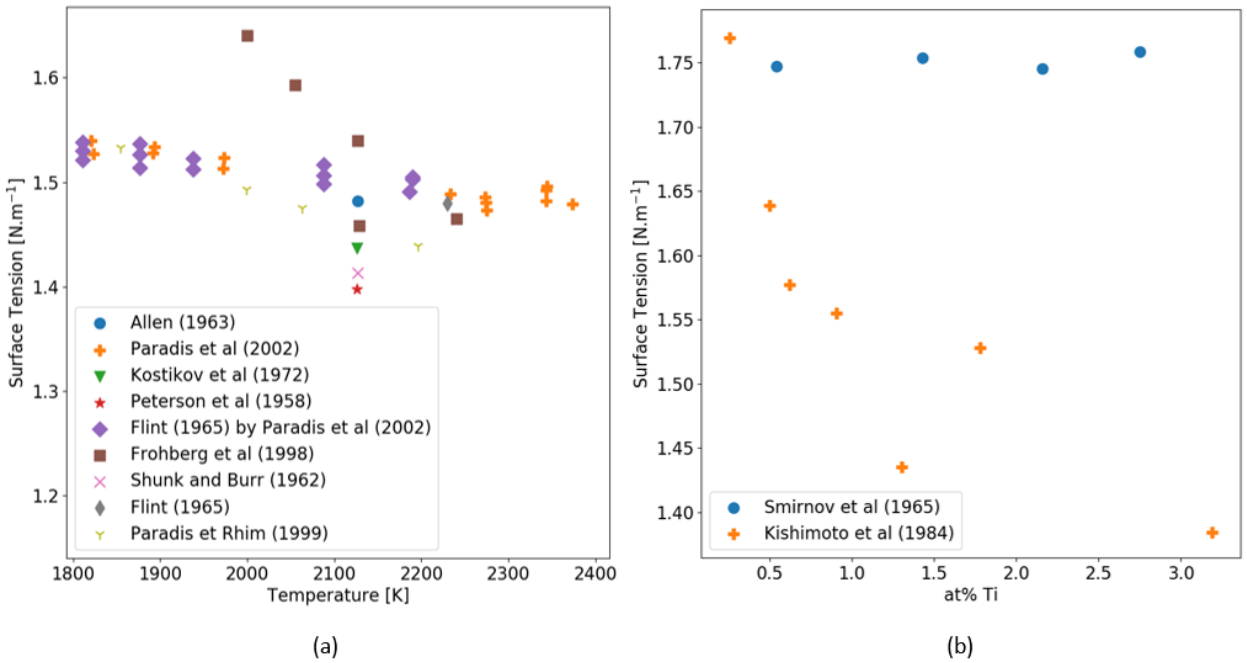

Figure C.1 Examples of surface tension data discrepancy for a) pure Zirconium at different temperatures [391],b) Fe-Ti at 1823 K [396], [397]

2.2 Machine Learning Model

Machine Learning (ML) algorithms currently serve as an excellent exploitation tool for available experimental data in the field of materials science [398]–[404]. Although the earliest use of informatics in materials science goes back to the integration of thermodynamic databases into thermochemical computations to map phase stability in binary and ternary alloys [399], with the advancement of the computing power and the different ML algorithms, the use of ML in materials science became more present.

In this study, the proposed model is based on Gaussian Processes Regression (GPR), a Bayesian algorithm that has been successfully used to solve nonlinear prediction problems. Bailer-Jones *et al.* [405] were among the first to utilize this method in the domain of metallurgy, where they presented a Gaussian Process model for the empirical modelling of austenite formation during the continuous heating of steels. More recently, this method has been used by several authors to predict material properties [169], [406], [407].

GPR mainly defines a distribution over functions such that for every two or more points chosen, the output of these points follows a joint multivariate Gaussian distribution [209]. A more detailed explanation of the model can be found in Appendix C.2. One of the main advantages of using the ML-GPR method is that in addition to predicting a mean value, it also provides a variance for the predicted distribution. In this study, GPR available in the open-source Python package Scikit-learn was used [210].

What is referred to as Gaussian process training is usually the selection of a covariance function (kernel) and its parameters. For this model, the RBF (Radial Basis Function, also known as squared-exponential) kernel was chosen and the lengthscale values were optimized through fitting. The final lengthscales could be insightful as they can provide information on the influence of the input parameters. Usually, the lower the value of the lengthscale, the higher can be the influence of the respective feature, whereas large lengthscales would prohibit steep variations. Lengthscales are optimized such that the model remains smooth and any over-complexity is avoided. This is ensured by the addition of a hyper-parameter indicating the noise level. To ensure that the selection is optimal, a GridSearch technique was applied and repeated for different parameter intervals.

The predictability and the ability of generalization of the ML-GPR algorithm is evaluated by cross-validation to avoid overfitting. The evaluation metrics considered are the most commonly used values for regression and numerical problems, i.e: the Mean Squared Error and Root Mean Squared Error (MSE and RMSE, respectively), Mean Absolute Error (MAE) and R-squared (R^2).

The model hyper-parameters are adjusted to obtain a large R^2, a small MSE and a small RMSE. The variation of these metrics for the different cross-validation folds is discussed hereafter.

3. Results and discussion

3.1. Building the model

The model was first trained and fit on all collected experimental data. The average values of the evaluation metrics for both the training and the testing sets computed with the 10-fold cross-validation method are shown in Table C.1. It can be seen that the overall performance of the model is very good with an MSE average of around 0.02 and an R^2 value of 0.97. Fig. 2 shows the cross-validation prediction results as well as the final prediction results of the model after training as a function of the real measurements. The majority of the points lie on the line with slope 1 indicating a generally high prediction accuracy. Nevertheless, there remains a few data points at which the model shows a relatively high error in prediction, especially in the cross-validation test results. Several of these points can be explained by the insufficiency of data to well describe a particular material. For example, Mg and W-based alloys are only described with 14 data points each. Hence, it is unavoidable that the model fails to correctly predict these points when they lie within the testing set. The same could be said about Li and Zn, which are represented with 10 and 24 points respectively, especially that these points are located on the extremes of the database. Li and Mg have some of the lowest ST values of 0.39 and 0.55 $N.m^{-1}$ respectively at their melting temperatures, compared to 3 $N.m^{-1}$ for W. It is also normal to observe that the predicted value for the mentioned points is correct when the model is trained on the whole dataset, as shown in Fig. 2 b. Of course, due to data discrepancy discussed in section 3, there remain a few points that still show a higher error even after training.

Table C.1 Average and standard deviation values for different evaluation metrics using the 10-fold cross validation method

	test R^2	train R^2	test MSE	train MSE	test MAE	train MAE
Average	0.9783	0.9950	0.0237	0.0050	0.0581	0.0419
Standard deviation	0.0294	0.0003	0.0369	0.0003	0.0091	0.0008

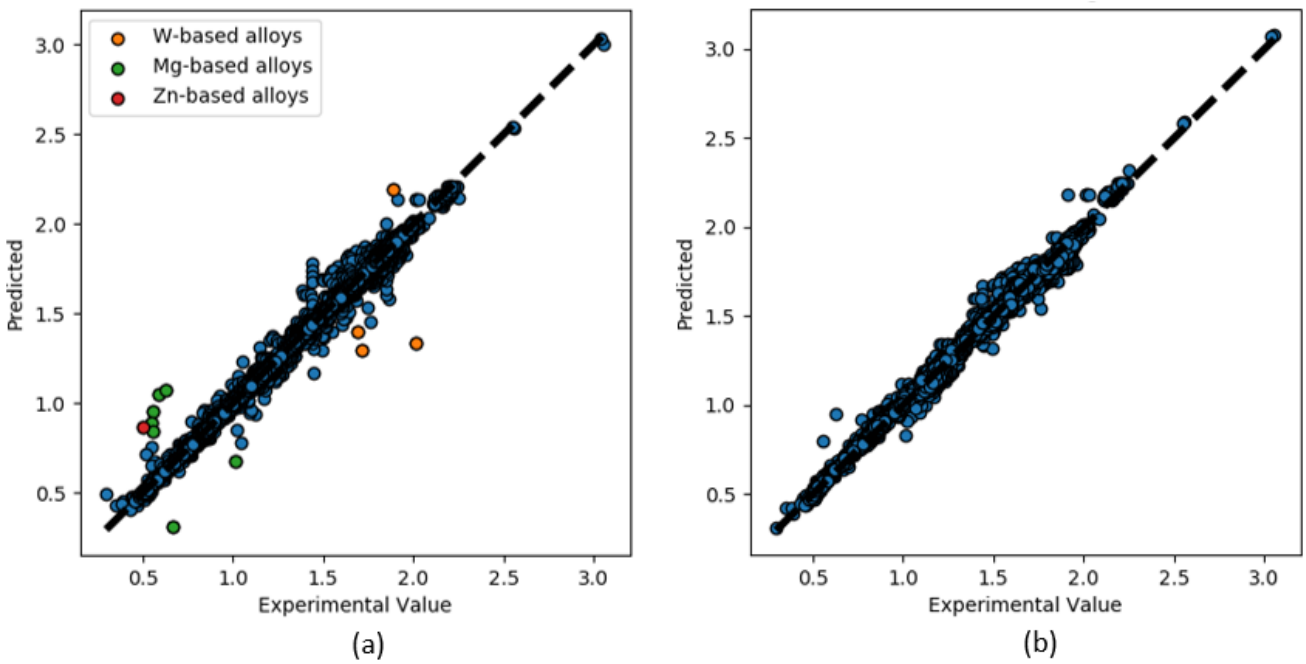

Figure C. 1 Predicted surface tension values in [N.m^{-1}] as function of the experimental values from literature for a) 10-fold cross validation b) the final trained model on the whole dataset

3.2 Model validation: surface tension in binary systems; comparison between experimental values and ML-GPR model prediction

Based on the so built and trained model, the evaluation of surface tension in selected binary systems has been performed. The obtained results have been systematically compared with existing data. Only a few examples of studied systems will be presented and commented on in this paragraph. A complete set of data, for about 20 different binaries, mainly Fe-, Al- and Ni-based, is presented in Appendix C.1.

For well-documented binary alloys, the ML-GPR model of surface tension shows its ability to correctly reproduce the trends in ST in binary alloys, as a function of the content of elements. This is the case of Fe-based alloys in which the ST is quite independent of alloying element content (ex: Fe-Cr at 2073 K, Fe-Ni at 1773 K, Fe-Co at 1823 K), as shown in Fig. 3, but also in the case where the addition of an alloying element changes the ST value, as seen in the Fe-Al system at 1233 K (Fig. 3 d).

Also, Al-based alloys are generally well described, as shown in examples in Fig. 4. Let us note that in these materials, any alloying increases the ST value, as the surface tension for pure aluminum is low, of about 0.9 $N.m^{-1}$, and slightly decreasing with temperature. In all these systems, the accuracy of prediction is quite satisfactory, with the 95% confidence interval currently below 0.2 $N.m^{-1}$.

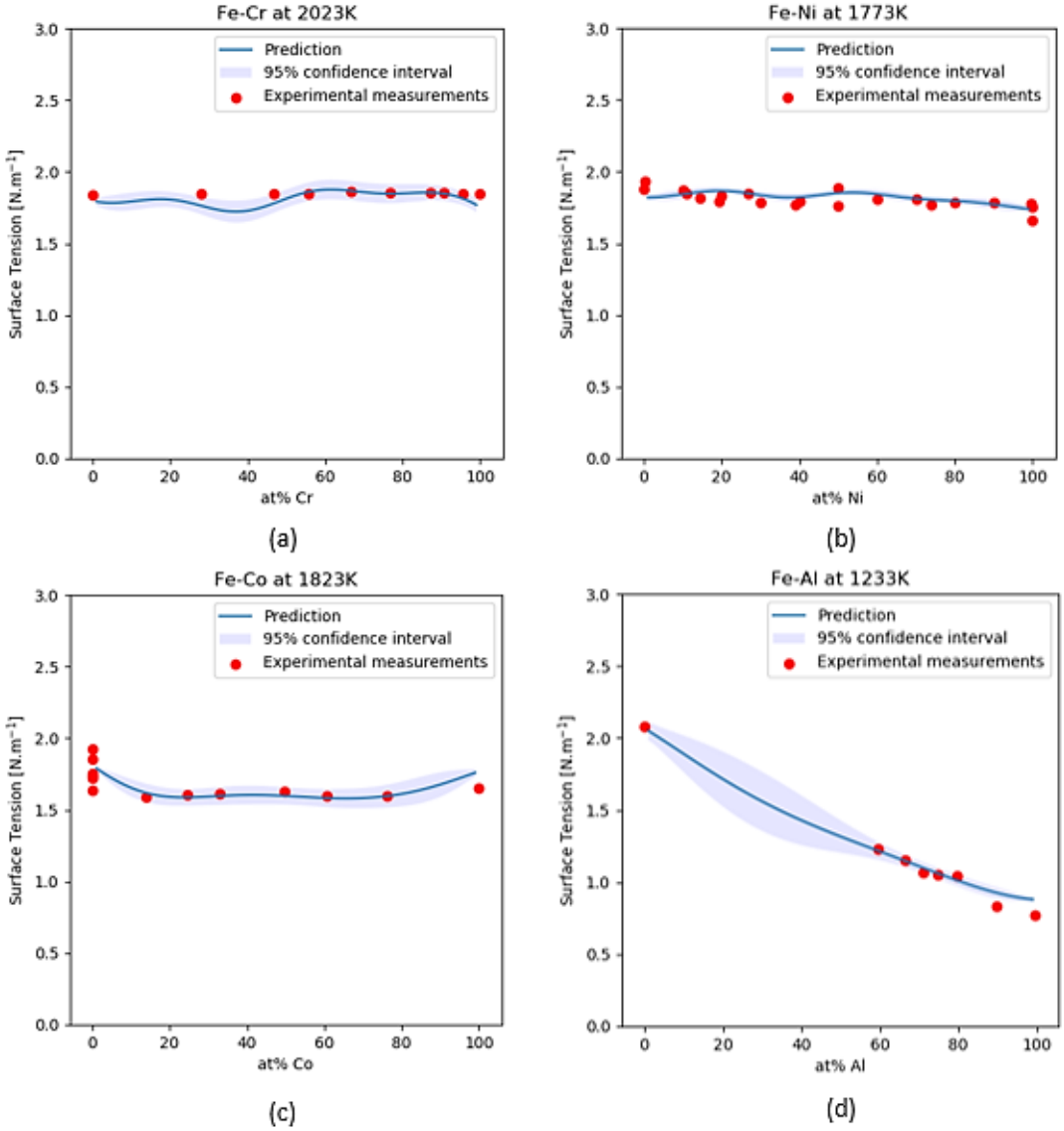

Figure C.2 Surface tension prediction for a) Fe-Cr at 2023 K, b) Fe-Ni at 1873 K c) Fe-Co at 1823 K and d) Fe-Al at 1233 K

Several singular points need to be stressed on. Fig. 3 b and Fig. 4 a (Fe-Ni, Al-Cu, respectively) show the cases of well-documented alloys, with a wide experimental data set, coming from several research groups and sometimes, obtained by different experimental methods, and leading naturally to some differences in measured values. Obviously, the model prediction in such a situation should choose an "average" value, best optimized in the sense of existing trend, as observed in the figures. Another case is shown in Fig. 3 c (Fe-Co): for the studied temperature (1823 K), different ST values for pure Fe have been measured, with differences as large as 0.35 $N.m^{-1}$. It is reassuring to note that the model prediction of ST follows the data coming from the same bibliographic reference as the major part of data describing the whole Fe-Co binary system. Finally, the "bad" prediction of ST in Al-Ni system (Fig. 4 b) for almost equimolar alloys may be surprising. In fact, an almost constant ST value was measured for alloys containing between 45 and 75 at. % Ni [408] while the model indicates a continuous increase of ST with increasing Ni content. It may be hypothesized that the congruent solidification of NiAl B2-ordered phase and the associated liquid demixing in the vicinity of the equimolar composition [409] can change the liquid behavior; a phenomenon that would be at the origin of modified ST behavior, but not detected by the model, trained on homogeneous liquid behavior. Finally, we can see that the ST trends are successfully represented in the cases of Al-Cr at 2073 K and Al-Co at 1873 K (Fig. 4 c and d).

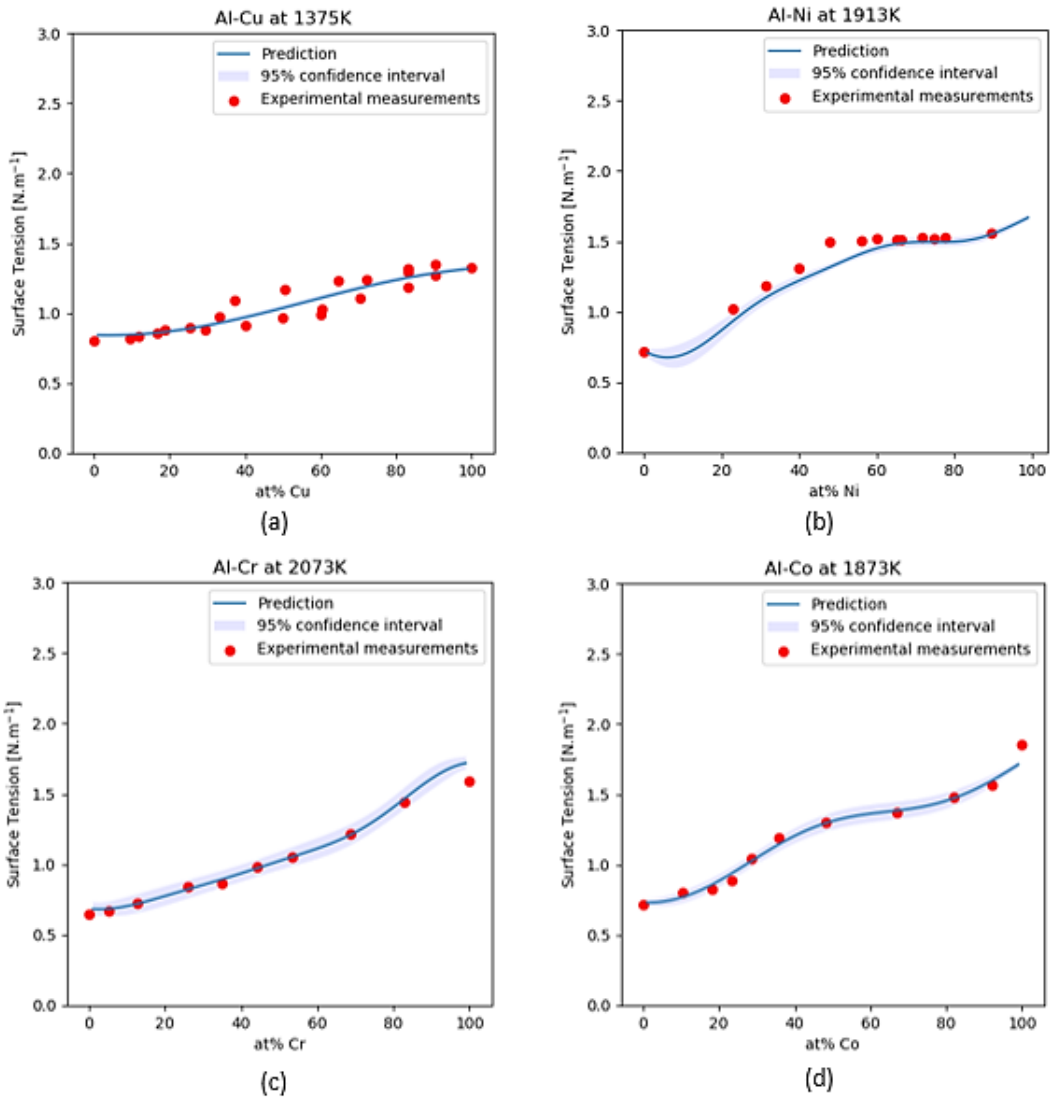

Figure C. 3 Surface tension prediction for a) Al-Cu at 1375 K b) Al-Ni at 1913 K c) Al-Cr at 2073 K and d) Al-Co at 1873 K

It is not surprising to find that the quality of predictions (measured by the standard deviation of predicted ST value) decreases in binary alloys if – for a large range of chemical compositions – experimental data is missing. Several cases are observed. In the Fe-Al binary system (Fig. 3d), experimental data are missing for alloys containing more than 40 at. % of Fe. The model satisfactorily describes the Al-rich alloys; for the alloys containing more iron, the prediction follows an almost linear increase of ST, with an increase of standard deviation when compositions far from known experimental points are of concern. Yet, in all cases, the standard deviation is below 0.25 $N.m^{-1}$ and so, remains satisfactory. The same rule of increase of standard deviation far from experimental points may be clearly observed in the Fe-Mo system, Fig. 5a, with similar

values of maximal standard deviation and so, a prediction that remains sufficient for applicative purposes. However, a more complicated situation has to be described in the Fe-Ti system (Fig. 5b). Only scarce experimental data, limited to Ti content as low as 3 at. %, (already discussed in §3.1), are available. Lack of reference points leads to a peculiar behavior of the ML-GPR model: a deep minimum of ST for about 20 % of Ti and standard deviations higher than 0.5 $N.m^{-1}$.

This is one of the rare cases in which the proposed model seems to extrapolate with a very low level of confidence, towards areas not sufficiently covered by the database, although the description of actual data appears correct in the corresponding range. Somewhat similar although less dramatic situations have been also seen in Fe-Mo. In doubt of the validity of the model in the Fe-Ti system beyond ~3% Ti, it would be preferable not to use the model in Fe-based alloys containing more than a few percent titanium. Fortunately, very high concentrations of such elements are almost never used for alloys of this class of engineering materials.

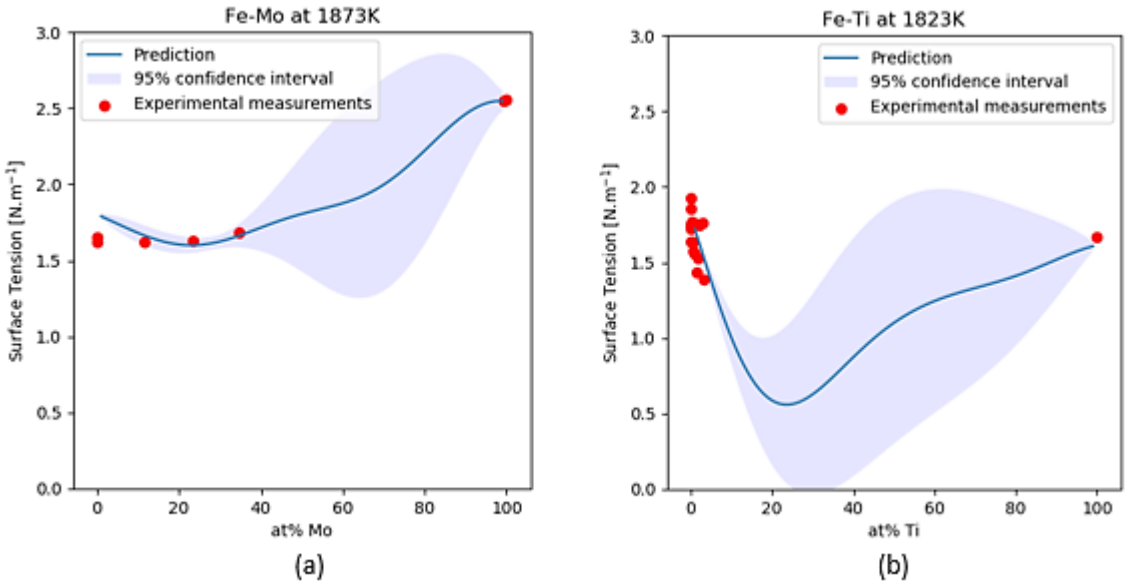

Figure C. 4 Surface tension prediction for a) Fe-Mo at 1873K and b) Fe-Ti at 1823K

3.3 Model evaluation: surface tension in ternary systems; comparison between experimental values and ML-GPR model prediction.

The ML-GPR model allows to evaluate the ST value for complete ternary maps in isothermal conditions. This permits a clear visualization of trends and the effect of different elements on ST values. In Fig. 6 ternary maps to describe the ST in several ternary systems are shown. The color code is used to identify the contours of ST value ($N.m^{-1}$). Unfortunately, the limited availability of data for ternary systems makes it difficult to evaluate the performance of the ML-GPR model globally. Although this is the case with binary systems as well, the evaluation of ternaries remains

harder simply due to the fact that a higher number of points is needed to describe the space. Nevertheless, there has been some proposed thermodynamical models in the literature which predicted the ST for certain ternary systems. For example, Costa *et al.* [410] analyzed the energies of mixing in liquid Co–Cr, Cr–Ni and Co–Ni systems and extended the results to predict the surface tension properties of the Co-Cr-Ni system. Compared to experimental data found in literature for the systems Cr-Ni and Co-Ni, their model predicts overestimated values of surface tension. Usually, this is explained by the high reactivity of alloy components and adsorption of oxygen on the liquid surface, which leads to a decrease in the surface tension and therefore a lower measured value compared to the theoretical prediction. Fig. 6 a. shows the surface tension prediction of the ML-GPR model for the Co-Cr-Ni system at 1873 K. Compared to the abovementioned thermodynamic model, the prediction of the ML-GPR model shows a slightly larger range of variation but similar trends. The difference in the exact values is explained by the fact that the model is trained on a set of experimental data; data that already include a certain range of error coming from material contamination, or experimental setup, etc. Similarly, Mehta *et al.* [411] studied the surface properties of the Fe-Cu-Si ternary system. They compared the results of four different models: Chou *et al.* [412], Toop [413], Kohler [414] and Butler [297], which seem to be in agreement. Among the three components, pure silicon has the lowest surface tension value, and iron the highest. The surface tension of the ternary alloy changes non-linearly when viewed from the corners. The ML-GPR model's prediction for the Fe-Cu-Si system at 1773 K is shown in Fig. 6 b. The predictions are in excellent agreement with the results of [411], starting with a value around 1.7 $N.m^{-1}$ for the composition of $Si_5Cu_5Fe_{90}$, and decreasing as the content of Si and Cu increases, to reach a value around 0.9 $N.m^{-1}$ for the composition of $Si_{45}Cu_{45}Fe_{10}$, indicating the ability of the GPR model to interpolate/extrapolate surface tension values for ternary systems.

The main advantage of the machine learning model lies in its ability to generalize, without the need to study the exact systems involved and analyze the components that might be formed by the involved elements.

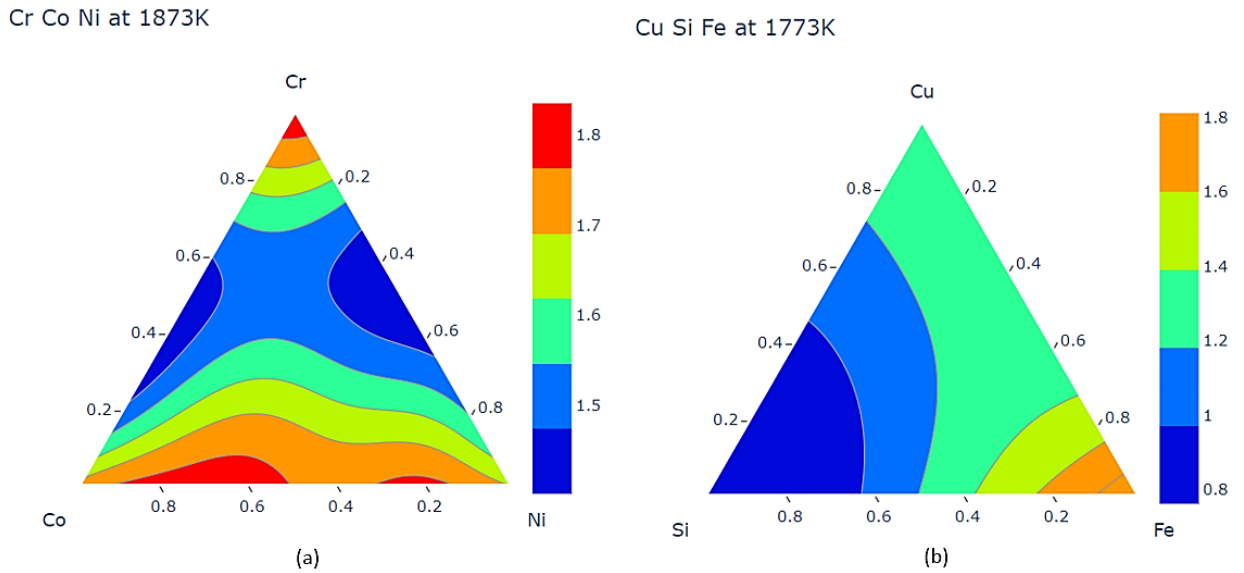

Figure C. 5 ML-GPR Prediction of Surface Tension [N.m^{-1}] for a) Cr-Co-Ni at 1873K and b) Cu-Si-Fe at 1773K

3.4. Efficiency of the ML-GPR model to describe multicomponent systems: comparison with existing data.

The next part of the work consisted in testing the ML-GPR model's ability to extrapolate towards multi-component (containing at least three elements) systems behavior, on the basis of data coming from simpler ones, since it has been built mainly from pure elements or binary systems, and to a minor extent from higher-order systems. To this purpose, training the ML-GPR model again on solely pure materials and binary alloys was done (~1770 data points). Then, the available experimental ST values of several ternaries and higher-order systems were used as test points. The results of model prediction in comparison with the experimental data from literature are shown in Fig. 7. To simplify, alloys from the same family; e.g., Al-Cu-Ag alloys, or Sn-Cu-Ag materials, were grouped by the same color. Due to the importance of stainless steels, and the existence of data for different grades of this class of materials, associated data take a significant place among available studies, and they are divided into several classes for a better graphical representation in Fig. 7b. The exact chemical compositions of several grades of stainless steels [308] are summarized in Table C.2 and used to build the graph in Fig. 7b.

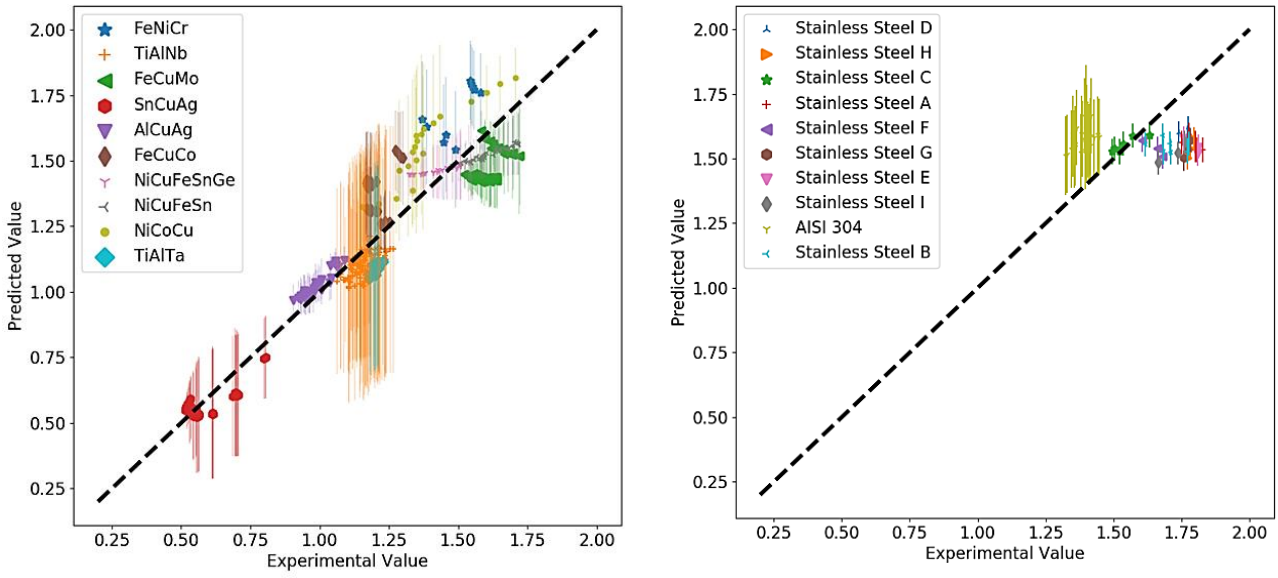

(a) (b)

Figure C. 6 ML-GPR model prediction vs experimental values of ST [N.m^{-1}] for several higher order system including several stainless steels grades (stainless steels A to I [40], AISI 304 [308]*), when the model is learnt solely from pure metals and binary alloys*

In general, it can be seen that the accuracy of prediction of ST by the ML-GPR model is satisfactory. For the ternary systems, like Al-Cu-Ag and Sn-Cu-Ag systems, the prediction accuracy is quite high. It is worth noting that the binaries of these systems are well represented in the database, compared to the other cases. Several datasets from literature describe both the effect of chemical composition and temperature for the Ag-Cu, Sn-Cu and Ag-Sn systems. As for the prediction of the quaternary CuFeNi$_{85}$Sn (purple) and quinary CuFeGeNi$_{80}$Sn (red), although the ML-GPR model correctly predicts the ST value, the predicted variation of temperature effects on ST seems unsatisfactory. By looking at the ST values of different binary systems containing germanium, one can see that this element usually strongly decreases the ST value as it has low ST value itself, around 0.6 N.m^{-1} at melting temperature. For example, a Ni-Ge alloy with 5% of Ge at 1873 K has an ST of 1.6 N.m^{-1}, compared to 1.75 N.m^{-1} for pure Ni. Similarly, for Fe-Ge at 1823 K, an addition of 20% of Ge can decrease the ST value to 1.3 N.m^{-1} compared to an average value of 1.8 N.m^{-1} for pure Fe. This data allows the model to give a proper estimation of the ST but is not enough for a satisfactory estimation of the temperature effect. As for the Ni-Co-Cu system, an opposite behavior is observed. The predicted values slightly overestimate the measured ST value. In fact, for the Ni-Co binary system we saw that there is little to no effect of composition on ST. In the case of Ni-Cu and Co-Cu, the addition of Cu decreases the ST. The results are therefore somewhat surprising, as the model does not succeed to predict the effect of Cu, especially when it is present in low contents.

For different stainless steel compositions studied by Li *et al.* [308], Table C.2, and the Fe-Cu-Mo system studied in [415], the ML-GPR model slightly underestimates the ST value. The opposite is seen for some data concerning an AISI 304 steel measured by the maximum bubble method. Let

us note that for the same alloy measured with sessile drop method, we do not observe a high error for the model predictions. This part of the study intended to assess whether a model built only from low order systems (unaries and binaries) would be able to give fair values and/or trends for higher order systems, i.e. ternaries or even more complex alloys. Let us stress on the fact that, even if the trends are slightly degraded for commercial alloys (eg.: stainless steels), good value ranges are obtained for all alloys.

Table C.2 Composition of different grades of stainless steel in weight % [308]

Steel	C	Si	Mn	Al	Cr	Ti
A	0.0435	0.287	0.189	0.1288	16.198	0.0044
B	0.0847	0.298	0.596	0.089	15.995	0.0056
C	0.0689	0.316	0.572	0.0042	16.232	0.0028
D	0.0084	0.464	0.35	0.0562	10.858	0.2211
E	0.0056	0.126	0.141	0.0504	16.199	0.293
F	0.0053	0.092	0.112	0.0806	17.346	0.2741
G	0.0059	0.145	0.131	0.052	18.67	0.1541
H	0.0153	0.555	0.149	0.0216	19.105	0.0082
I	0.0076	0.467	0.124	0.0293	21.511	0.0042

Therefore, it may be reasonably expected that no further significant degradation of prediction would come for the complete model and it seems possible to extend the model to higher-order systems, as long as the compositional space of the lower order systems involved is sufficiently well described. The range to which it can be extrapolated could be individually discussed based on the statistical representation of the system on topic, but also with the help of the error bars provided by the algorithm. Consequently, the model learnt using all available data should be able to provide fair predictions of the ST in the case of multicomponent alloys, which is attempted in the next section.

3.5 Use of the ML-GPR model to predict ST in complex alloys: application to austenitic HEA alloys

Table C.3 Predicted surface tension values for some HEA alloys at their melting point

Alloy	$T_{liquidus}$ in K	Surface Tension [$N.m^{-1}$]
CuCrFeMoNi	1816	1.39
Al0.5CrCuFeNi2	1561	1.47
Al0.5CrCuFeNi	1657	1.34
CoCrFeMnNi	1596	1.2
CoCrFeNi	1713	1.4
CrFeMnNi	1574	1.0
CoCuFeMnNi	1555	1.12
CoCrCuFeNi	1648	1.23
CrCuFeMoNi	1817	1.39
Al0.5CoCrCu0.5FeNi	1607	1.3
Al0.3CoCrCuFeNi	1620	1.28
Al0.5CoCrCuFeNi	1599	1.27
Al0.5CoCrCu0.5Fe2Ni	1644	1.22
Al0.5CoCrCu0.5Fe3Ni	1670	1.21
Al0.5CoCrCu0.5Fe3.5Ni	1680	1.22
CoCrFeMo0.3Ni	1674	1.4
Al0.3CoCrFeMo0.1Ni	1654	1.37
Al0.2CrCuFeNi2	1589	1.48
Al0.6CrCuFeNi2	1552	1.46
Al0.25CoCrFeNi	1674	1.37
Al0.3CoCrFeNi	1666	1.36
Al0.375CoCrFeNi	1652	1.35

In the next part of the study, the ML-GPR model, learnt from all available data (retrained on the whole database), was used to predict the surface tension of several alloys for which experimental data are still missing. Such an approach, even if it would come along with a high level of uncertainty on the predicted values, is valuable in the framework of alloy design. Indeed, decreasing the ST value may be of interest in some specific processes such as welding or additive manufacturing, to help the stabilization of the meltpool. However little knowledge of the trend of ST variations with composition is known in the case of highly alloyed systems. This section provides a quick glance of possible variations to foresee some possible research directions where

ST at the liquidus could be possibly minimized. This investigation will give further insight into the effect of several elements on the value of the ST, as well as the behavior of the material at different temperatures. In Table C.3 the surface tension for several face-centered cubic (FCC) high entropy alloys (HEA) [416] is given at their liquidus temperatures estimated using ThermoCalc software (TCHEA4 database). It is clear that the range of variation seems to be limited. It has been mentioned that certain elements can have a similar effect on the trend of the ST value in a specific system, such as the behavior of transition metal elements in a binary system with iron [299]. Nevertheless, the results show that by varying the content of one element or the other, it is possible to optimize the value of ST depending on the desired outcome. For example, changing the composition of the CoCuFeNi equimolar alloy by decreasing the amount of either nickel or cobalt, could help achieve a minimum in the ST value. Similarly, for the CoCrFeNi equimolar alloy, introducing a small amount of aluminum could also decrease slightly the value of ST.

An example of ML-GPR model predictions is given in Fig. 8 for the CoCrFeMnNi equimolar alloy (also known as Cantor alloy). The effect of the different elements on the ST value of the alloy is presented by considering that the element is added to an equimolar quaternary alloy. The square points represent the surface tension values for the quaternary alloys CoCrFeNi (in red), CrFeMnNi (in blue), CoFeMnNi (in green), CoCrFeMn (in pink) and CoCrMnNi (in orange). The predicted ST value for the Cantor alloy is in fact surprisingly low, not far from the minimum value obtained for a major part of studied compositions. One explanation could be come from a high amount of manganese in Cantor alloy: as presented in Fig. 8, this element has a strong effect on ST values in the studied system. More generally, Mn is the first predominant factor driving the global ST variations. When Mn content increases, the ST value decreases progressively. For the other elements, the trend is opposed, because it results in a lower Mn fraction. However, a second predominant factor is the liquidus temperature, which is also affected by composition. For instance, the addition of Fe results in an increase of liquidus temperature from 1277°C for CoCrMnNi to 1538°C for pure Fe. For these elements, the temperature results in a decrease of ST value according to the ST database. Therefore, the variation from Cantor to a pure element should result in a higher liquidus temperature, and a lower ST. The competition between these two opposite effects may eventually result in a sag point, as it is the case for Fe curve. On the other hand, in the case of Ni content (denominated “x” in the following), the CoCrFeMn alloy has a liquidus at 1373°C, and the variation of liquidus is only of 82°C when x changes from 0 to 100. Therefore, liquidus has a limited impact on ST in this case, and ST is mostly driven by Mn content, with a continuous decrease when x tends toward 0. This explains the peculiar behavior of Ni curve at low x values.

These preliminary results are based on the information acquired from the existing database. The extrapolation of the model to multicomponent alloys induces a relatively large variance interval of more than 0.3 $N.m^{-1}$, as the predicted systems are farther from trained input samples in the composition space. Of course, the more data is added to the training database, the better the model performs on the different aspects discussed. Nevertheless, this model represents a simple method

to estimate a range for the ST value and trend without the complication of manually calculating physical parameters for the elements and their interactions. This is especially useful in cases where the aim is to optimize the property rather than achieve a specific value.

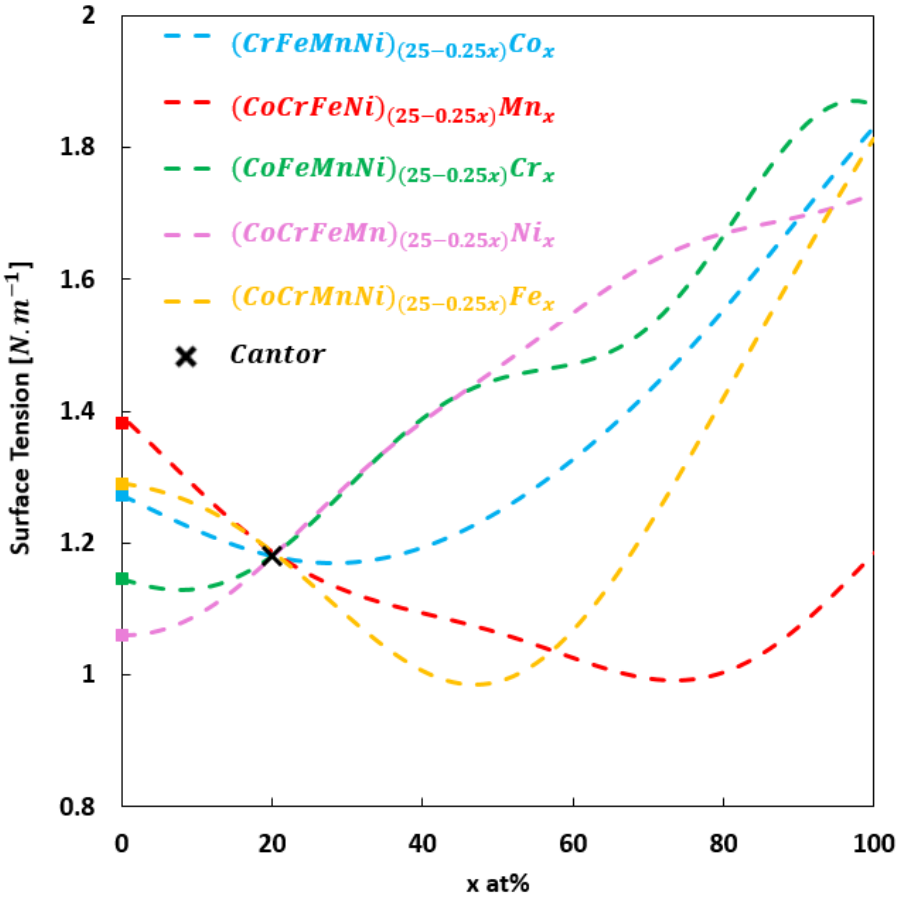

Figure C. 7 ML-GPR model prediction of surface tension values, showing the independent effects of elements on the equimolar alloy CoCrFeMnNi (Cantor alloy) behavior. Calculations performed at melting temperature of each alloy, estimated from ThermoCalc data.

4. Conclusion

1. With a long-term purpose of improvement of criteria of alloy design for innovating processes like additive manufacturing, a Machine-Learning model based on Gaussian Process Regression (ML-GPR) was developed for predicting the surface tension values in metallic alloys. The model is built on the basis of the data coming from experimental measurements found. Analysis of more than 70 papers and textbooks allowed the creation of a database containing more than 2200 experimental points. An interesting perspective would be to incorporate data obtained by atomistic simulation.

2. The model's database comes mainly from pure elements and simple alloys, mostly binary and, less commonly, containing three or more chemical elements. A good agreement between prediction and experiments was generally observed in binary and ternary alloys when enough

experimental data exist. The confidence range of prediction is generally lower than 0.2 $N.m^{-1}$. There are rare cases in which the model seems to extrapolate with a very low level of confidence, towards areas not sufficiently covered by the database, such as in Fe-Ti or Fe-Mo systems.

3. On the basis of results for simple alloys, the possibilities of extension of predictions by ML-GPR model to multi-element alloys have been assessed.

4. The tentative of using the ML-GPR model to predict the surface tension in novel concentrated alloys, namely austenitic HEAs from the CoCrFeMnNi family, remains a challenging task. Yet, significant variations in ST could be identified when changing the contents in certain elements. Especially, a strong effect of Mn, decreasing the ST values, was shown.

Appendix C.1: References of surface tension values

Alloy	Ref	Method	Alloy	Ref	Method	Alloy	Ref	Method
Fe-Cr	[417], [418]	LD,SD	Ni-Al	[419], [420], [421]	EL,OD	Al-Li	[392]	MGBP
Fe-Cu	[419], [417]	EL, SD	Ni-Cr	[418], [422]	SD, SD*	Al-Ti	[423]	EL
Fe-Sn	[417]	LD	Ni-Sn	[417]	LD	Al-Cu	[424], [425]	--, SD
Fe-Al	[421]	EL, OD	Ni-Co	[422]	SD*	Al-Si	[426],[427]	EL, OD, SD
Fe-Co	[394]	SD	Ni-W	[422]	SD*	Al-Zn	[428], [429] by [299]	--
Fe-Mo	[394],[299]	SD	Ni-Cu	[417]	LD, SD	Au-Si	[430]	Large drop
Fe-W	[394]	SD	Ni-Mo	[394]	SD	Al-Au	[431]	EL
Fe-Si	[432]	SD, PD	Ni-Ge	[433]	--	Al-Mg	[434], [429] by [299]	MGBP,SD
Fe-Ge	Zamarev *et al.* 1976 by [299]	--	Ni-Si	[435] by [299]	--	Mn-Sn	[436]	SD
Fe-Ti	[397], [396] by [299]	--	Zn-Li	[392]	MGBP	Sn-Cu	[437]	CD
Fe-Ni	[438], [418] , [439], [395], [394]	--,SD, SD, EL, SD	Cu-Co	[440]	EL	Sn-Ag	[441], [437]	SD, CD
Zr	[393], [101], [104]–[107]	--	Cu-Ge	[433]	--	Au-Ge	[430]	Large drop
Nb	[393], [101], [102]	--	Cu-Ti	[442], [443]	SD, EL	Au-Sn	[444]	SD
Co	[445]	OD+EL	Cu-Zr	[446]	Large drop	Si-Ge	[447]	PD
Ni	[445]	OD+EL	Ta	[408], [448]	PD	Sn-Ge	[433]	--
Ti	[393], [449]–[451]	--				Mn-Ge	[433]	--

(a)

Alloy	Ref	Method	Alloy	Ref	Method
Fe-Cr-Mn-Ni	[452]	MGBP, SD	Ni-Cu-Fe-Sn-Ge	[305]	EL
AISI 304 steel	[452]	MGBP, SD, EL	Fe-Cu-Mo	[415]	EL
Ni-Cu-Fe-Sn	[305]	EL	Fe-Ni-Cr	[418]	SD
Al-Cu-Ag	[453]	EL	Fe-Cr-S	[454]	SD
Ti-Al-Nb	[455]	EL	Fe-Cr-Mo	[452]	MGBP, SD
Ti-Al-Ta	[455]	PD, SD	Fe-C-Si	[432]	SD
Ag-Au-Cu	[456]	SD	Ni-Cu-Fe	[305]	EL
Ti-Al-V	[457]	PF	Fe-Cr-Ni-S	[454]	SD

(b)

Alloy	Ref	Method	Alloy	Ref	Method	Alloy	Ref	Method
Bi-Sn	[428]	SD	Se-Na	[392]	MGBP	In-Na	[392]	MGBP
Bi-Pb	[428]	SD	Bi-Na	[392]	MGBP	Cs-Sb	[428]	SD

In-K	[392]	MGBP	Bi-K	[392]	MGBP	Pb-Sn	[428]	SD
Cs-Na	[392]	MGBP	Pb-Li	[392]	MGBP	In-Li	[392]	MGBP
Co-O	[458]	--	Fe-O	[458]	--	Ni superalloy CMSX-4	[311], [459]	SD, SD+
Cu-O	[458]	--	Ni-O	[458]	--	Ni superalloy CMSX-10	[459]	SD+
Fe-O-N	[293]	SD	Cu-Bi	[460]	--	Ni-alloy MM247LC	[457]	PF

(c)

Table C.4 Complete database for development of the ML-GPR model. Systems and bibliographic references. (c) includes systems that were not taken into consideration. The abbreviations describe the experimental method used by the authors: SD= Sessile Drop, SD= improved SD, SD+= modified SD, CSD=Constrained SD, PF=Parabolic Flight, PD= Pendant Drop, MGBP=Maximum Gas Bubble Pressure, EL= Electromagnetic Levitation, OD= Oscillating Drop technique*

Appendix C.2 Gaussian process regression

To explain the main mathematical principles behind Gaussian processes, let us consider a database D made of N measurements of a property (output) y, as a function of L variables (inputs), x^m, as m varies from 1 to L. The input data $[X_N]$ can then be defined as N L-dimensional input line vectors with $[X_N]= \{ \vec{x}_1 , \vec{x}_2, \dots , \vec{x}_N \}$. The output column vector is $\vec{y}_M=\{ y_1 , y_2, \dots , y_N\}$. Within the frame of alloy modelling, each line would correspond to an alloy, the x^m values could be the concentrations in alloying elements and the output *y* would be the property to be modelled or predicted.

Now, to predict an output y_{N+1} for a new input vector $\vec{x}_{N+1}$, e.g. the property of a new alloy, the Gaussian process (GP) assumes that the joint probability distribution of the new point and the N points in the database D, $P(y_{N+1} | \vec{x}_{N+1} , D)$ is a multivariate Gaussian:

$$P(y_{N+1} \mid \vec{x}_{N+1} , D) = \frac{1}{\sqrt{2\pi}\sigma_{\hat{y}}} \exp[-\frac{(y_{N+1} - \hat{y})^2}{2\sigma_{\hat{y}}^2}] \qquad 0.1$$

where $\hat{y}$ and $\sigma_{\hat{y}}^2$ are its corresponding mean and standard deviation respectively; the way to determine them will be exposed below. Statistically, the mean gives the most probable value of the output, predicted for the new set of inputs, and starting from known information contained in the database. With this being said, $\hat{y}$ is therefore the value we want to predict and $\sigma_{\hat{y}}$ provides an estimate of a predictive error. $\hat{y}$ is defined as:

$$\hat{y} = \vec{k}^T [C_N]^{-1} \vec{y}_N \qquad 0.2$$

where $\vec{k}$ is a column vector defined as:

$$\vec{k} = [C(\vec{x}_1, \vec{x}_{N+1}), C(\vec{x}_2, \vec{x}_{N+1}), \dots, C(\vec{x}_N, \vec{x}_{N+1})] \qquad 0.3$$

where $[C_N]$ is the covariance matrix which is a function of $[X_N]$. The elements of the covariance matrix, $C(\vec{x}_i, \vec{x}_j)$, are defined by the covariance function. The latter defines how strongly any input can impact the value of the output. There exist several forms for this function. In the present case, the radial-basis function (RBF), also known as squared-exponential, is used and can be defined as follows:

$$C(\vec{x}_i, \vec{x}_j) = \theta . exp\left[-\frac{1}{2}\sum_{l=1}^{L} \frac{(x_i^l - x_j^l)^2}{r_l^2}\right] + \omega \qquad 0.4$$

Where θ , ω (not detailed here) and r_l are a set of parameters referred to as hyper-parameters, and are usually unknown initially; therefore, they need to be inferred and optimized from the data during the learning process. Note that the covariance function gives the covariance between two data points i and j, and is written as a function of their corresponding inputs $\vec{x}_i$ and $\vec{x}_j$ (x_i^l and x_j^l being the corresponding coordinates in the l^{th} dimension). r_l is the lengthscale which specifies the smoothness of the interpolant in the l^{th} dimension [461], i.e. the output cannot vary steeply in the l^{th} dimension if l is large. In other words, the lower the value of the lengthscale, the higher is the potential influence of the respective feature, and vice versa. And, roughly speaking, in the case of the prediction of a property of an alloy, the shape of the covariance function indicates that an alloy with a composition close to alloys of the database would have chances to have similar properties, whereas a correlation between the properties of alloys with very different compositions should not be relevant.

In fact, to get the best performance out of any machine learning model, a tuning of the hyper-parameters (finding the hyper-parameter values that provide the best predictive capacity) is needed. The method used here to achieve this is by applying a Gridsearch: constructing a grid containing the parameters one wishes to optimize. This works by defining a list of the parameters as well as a range for the search. The model is then tested with different combinations of these parameters and the results are finally compared to choose the best model, i.e. the one with the highest prediction accuracy. Of course, this method is not optimal as the obtained optimal combination of parameters still depends on the manually set ranges of search. The effect of this issue can be lessened by simply increasing the number of values to be evaluated. Bearing in mind that this significantly increases the computational time, a compromise must be made. Finally, the parameters are adjusted as to obtain the best possible description of data.

Additionally, even if the Bayesian nature of GPs normally automatically avoids overfitting, i.e. they avoid fitting noise using complex variations instead of just capturing the actuals trends embedded in the data, it is nevertheless preferable to check the predictive capacity of the model using what is called cross-validation. The latter consists in training the model on a part of the database, and to test it on the remaining part, in order to check the ability of the model to generalize properly or, in other words, to be able to make correct predictions in cases it has not seen at the learning stage. One way to do this is using the K-fold cross validation method.

Appendix D: Complete set of optimized alloys

	Composition in wt%											
Alloy	Fe	Cr	Ni	Co	Mn	Mo	Al	Nb	Si	Ti	W	C
1	40.1	31.2	21.6	5.1	0.1	1.6	0.2	0.0	0.1	0.0	0.0	0.02
2	45.4	28.1	12.1	14.0	0.3	0.0	0.0	0.0	0.0	0.0	0.0	0.02
3	39.8	17.8	18.4	19.8	0.7	0.0	3.3	0.0	0.0	0.0	0.0	0.02
4	31.5	17.9	12.2	12.0	23.4	0.0	1.8	0.0	1.1	0.0	0.0	0.02
5	47.9	18.9	13.8	13.1	0.1	2.6	2.4	0.0	0.5	0.0	0.7	0.02
6	42.5	31.2	19.6	5.1	0.1	1.1	0.0	0.0	0.3	0.0	0.0	0.02
7	37.1	29.9	19.5	8.0	4.5	0.0	0.3	0.0	0.8	0.0	0.0	0.02
8	35.6	15.4	12.1	11.8	22.9	0.0	2.2	0.0	0.0	0.0	0.0	0.02
9	43.8	15.2	15.2	19.4	0.3	2.5	2.8	0.1	0.0	0.0	0.7	0.02
10	39.2	15.2	12.1	11.7	20.4	0.1	1.3	0.0	0.0	0.0	0.0	0.02
11	33.2	18.1	12.2	12.1	21.4	0.0	1.8	0.0	1.0	0.1	0.0	0.02
12	38.6	29.2	13.3	13.3	5.2	0.0	0.2	0.0	0.1	0.0	0.0	0.02
13	44.4	26.9	12.5	14.7	0.4	0.0	0.8	0.2	0.1	0.0	0.0	0.02
14	30.0	17.7	15.6	13.6	20.1	0.1	2.1	0.0	0.9	0.0	0.0	0.02
15	38.5	23.0	13.7	12.1	11.0	0.3	1.4	0.0	0.0	0.0	0.0	0.02
16	41.9	15.2	13.7	14.9	11.7	0.1	2.3	0.0	0.0	0.0	0.1	0.02
17	30.9	31.2	21.6	13.2	0.1	1.6	1.4	0.0	0.1	0.0	0.0	0.02
18	53.9	15.2	14.1	11.7	2.8	0.1	2.2	0.0	0.0	0.0	0.0	0.02
19	30.0	23.6	15.1	14.8	13.9	0.0	1.3	0.0	1.0	0.0	0.4	0.02
20	30.0	16.2	19.2	10.4	22.1	0.0	2.1	0.0	0.0	0.0	0.0	0.02
21	34.3	26.1	15.0	8.9	15.2	0.4	0.1	0.0	0.0	0.0	0.0	0.02
22	42.5	22.2	14.0	8.8	10.7	0.3	0.7	0.0	0.0	0.0	0.7	0.02
23	30.9	18.0	12.6	15.3	19.1	0.0	2.4	0.1	0.8	0.0	0.7	0.02
24	30.0	25.2	16.4	12.7	15.8	0.0	0.0	0.0	0.0	0.0	0.0	0.02
25	37.0	30.7	19.2	7.9	3.9	1.1	0.0	0.0	0.0	0.1	0.0	0.02
26	40.9	21.8	18.2	13.1	0.2	2.6	2.4	0.0	0.0	0.0	0.7	0.02
27	43.9	30.3	19.3	4.8	0.5	1.1	0.1	0.0	0.0	0.0	0.0	0.02
28	44.3	21.0	16.3	13.1	0.2	2.6	2.4	0.0	0.0	0.0	0.1	0.02
29	30.0	29.2	19.4	10.4	10.8	0.0	0.2	0.0	0.0	0.0	0.0	0.02
30	30.2	18.0	11.9	15.1	21.4	0.0	2.4	0.0	0.8	0.1	0.0	0.02
31	45.2	28.1	12.1	14.1	0.3	0.0	0.0	0.0	0.0	0.1	0.1	0.02
32	30.0	16.7	17.4	14.1	19.6	0.0	2.2	0.0	0.0	0.0	0.0	0.02
33	47.5	17.8	16.3	11.8	0.6	2.5	2.5	0.0	0.3	0.0	0.7	0.02

34	41.1	18.0	15.2	19.4	0.1	2.6	2.8	0.1	0.0	0.0	0.7	0.02
35	32.6	17.5	14.6	12.1	17.5	2.8	2.2	0.0	0.6	0.0	0.0	0.02
36	31.0	24.1	12.7	14.1	15.7	0.0	1.6	0.0	0.9	0.0	0.0	0.02
37	37.4	29.6	18.2	9.8	4.8	0.1	0.0	0.0	0.0	0.0	0.1	0.02
38	34.9	29.2	19.4	5.5	10.8	0.1	0.2	0.0	0.0	0.0	0.0	0.02
39	46.7	18.3	16.3	13.1	0.2	2.5	2.5	0.0	0.2	0.0	0.0	0.02
40	39.9	17.8	17.7	19.8	0.3	1.2	3.3	0.0	0.1	0.0	0.1	0.02
41	40.9	18.3	15.2	19.4	0.1	2.6	2.8	0.0	0.0	0.0	0.7	0.02
42	48.2	18.3	13.8	13.1	0.3	2.6	2.4	0.0	0.5	0.0	0.7	0.02
43	31.1	18.0	15.7	12.8	19.4	1.2	1.4	0.0	0.0	0.1	0.3	0.02
44	31.1	18.0	11.9	15.2	19.7	0.8	2.4	0.0	0.8	0.0	0.0	0.02
45	46.0	18.4	16.3	13.2	0.5	2.6	2.4	0.0	0.0	0.0	0.8	0.02
46	45.8	17.8	14.2	18.4	0.4	0.7	2.5	0.2	0.1	0.0	0.0	0.02
47	31.7	17.5	14.6	12.1	18.0	2.8	2.5	0.0	0.6	0.0	0.0	0.02
48	42.1	22.8	14.1	14.8	4.1	0.3	1.7	0.0	0.0	0.0	0.0	0.02
49	31.7	18.0	13.6	12.0	21.9	0.0	1.7	0.0	0.8	0.0	0.2	0.02
50	30.0	18.0	18.7	10.0	21.6	0.0	1.7	0.0	0.0	0.0	0.0	0.02
51	46.8	27.0	12.5	11.7	1.8	0.0	0.1	0.0	0.0	0.0	0.0	0.02
52	36.2	30.7	19.2	7.9	4.8	1.1	0.0	0.0	0.0	0.0	0.0	0.02
53	35.1	15.5	12.1	11.8	22.7	0.0	2.0	0.0	0.8	0.0	0.0	0.02
54	30.0	30.4	19.1	10.2	10.2	0.0	0.0	0.0	0.0	0.0	0.1	0.02
55	36.5	18.6	19.6	20.1	0.3	1.2	3.5	0.0	0.0	0.0	0.3	0.02
56	46.5	17.9	14.2	18.0	0.4	0.4	2.5	0.1	0.1	0.0	0.0	0.02
57	34.0	30.5	16.3	13.3	4.8	0.1	0.3	0.0	0.7	0.0	0.1	0.02
58	44.3	18.4	14.1	14.8	4.0	2.6	1.7	0.0	0.0	0.0	0.0	0.02
59	44.2	30.3	19.3	4.8	0.2	1.1	0.0	0.0	0.0	0.0	0.0	0.02
60	39.3	17.9	13.7	11.7	15.3	0.2	2.0	0.0	0.0	0.0	0.0	0.02
61	34.6	16.0	12.2	11.8	22.5	0.1	2.0	0.0	0.8	0.0	0.0	0.02
62	39.3	28.2	13.0	13.6	5.2	0.1	0.3	0.0	0.3	0.0	0.0	0.02
63	30.0	18.1	11.9	15.1	21.4	0.0	2.4	0.0	1.0	0.1	0.0	0.02
64	54.6	22.2	12.1	8.8	0.4	0.3	0.7	0.0	0.1	0.0	0.7	0.02
65	30.5	29.8	19.1	10.2	10.2	0.0	0.1	0.0	0.0	0.0	0.1	0.02
66	35.7	29.9	19.2	8.6	4.8	1.1	0.0	0.0	0.5	0.0	0.0	0.02
67	49.7	23.1	13.4	12.1	0.1	0.0	1.4	0.0	0.0	0.2	0.1	0.02
68	41.9	15.3	13.7	12.2	11.7	2.8	2.3	0.0	0.0	0.1	0.0	0.02
69	30.7	26.8	13.3	11.7	17.5	0.1	0.0	0.0	0.0	0.0	0.0	0.02
70	47.2	18.0	11.8	18.5	0.4	0.8	2.3	0.0	0.9	0.0	0.0	0.02
71	47.0	27.0	13.8	10.4	0.7	0.0	0.5	0.0	0.2	0.0	0.3	0.02
72	30.3	18.2	12.2	13.3	23.0	0.0	1.8	0.0	1.0	0.0	0.0	0.02

73	34.7	17.7	15.6	8.9	20.1	0.1	2.1	0.0	0.9	0.0	0.0	0.02
74	41.0	23.1	13.4	5.3	17.0	0.0	0.2	0.0	0.0	0.0	0.0	0.02
75	51.1	18.3	16.4	9.8	0.5	0.7	2.4	0.0	0.0	0.0	0.8	0.02
76	30.0	26.9	16.1	9.0	18.0	0.0	0.0	0.0	0.0	0.0	0.0	0.02
77	49.2	21.0	16.3	8.1	0.2	2.6	2.4	0.0	0.1	0.0	0.0	0.02
78	41.1	29.2	13.2	13.3	3.0	0.0	0.0	0.0	0.1	0.0	0.0	0.02
79	30.0	17.5	16.1	13.4	19.9	0.0	1.9	0.0	0.7	0.0	0.5	0.02
80	31.5	18.0	12.5	14.9	19.1	0.1	2.3	0.1	0.8	0.0	0.6	0.02
81	57.1	15.4	12.1	11.8	1.4	0.0	2.2	0.0	0.0	0.0	0.0	0.02
82	39.8	17.8	18.3	19.8	0.7	0.2	3.3	0.0	0.0	0.0	0.0	0.02
83	39.9	17.8	18.3	19.8	0.7	0.2	3.3	0.0	0.0	0.0	0.0	0.02
84	32.7	18.1	12.7	12.1	21.4	0.0	1.8	0.0	1.0	0.1	0.0	0.02
85	49.5	23.9	11.8	9.8	4.8	0.1	0.0	0.0	0.0	0.0	0.1	0.02
86	41.0	29.6	19.2	4.7	4.8	0.5	0.0	0.0	0.2	0.0	0.0	0.02
87	31.8	23.1	13.4	13.3	17.0	0.0	1.4	0.0	0.0	0.0	0.0	0.02
88	30.0	24.7	15.8	12.2	17.3	0.0	0.0	0.0	0.0	0.0	0.0	0.02
89	34.7	18.7	11.3	10.7	21.9	0.0	1.6	0.0	1.0	0.0	0.0	0.02
90	35.1	29.5	16.5	13.3	4.1	0.1	1.4	0.0	0.0	0.0	0.1	0.02
91	32.3	18.6	14.1	11.7	20.1	0.3	2.1	0.0	0.9	0.0	0.0	0.02
92	30.0	17.9	13.5	14.7	17.9	2.6	2.2	0.1	0.7	0.0	0.4	0.02
93	35.4	15.4	12.1	11.7	22.9	0.3	2.2	0.0	0.0	0.0	0.0	0.02
94	34.4	16.0	12.2	11.8	22.5	0.1	2.0	0.0	0.8	0.0	0.1	0.02
95	33.1	18.7	11.3	11.8	22.5	0.0	1.7	0.0	0.8	0.0	0.0	0.02
96	30.0	18.1	15.9	12.8	19.4	2.1	1.4	0.0	0.0	0.0	0.3	0.02
97	30.0	18.1	12.1	13.3	24.0	0.0	1.7	0.0	0.9	0.0	0.0	0.02
98	38.1	29.2	13.7	13.3	5.2	0.0	0.2	0.0	0.0	0.0	0.1	0.02
99	41.7	15.4	13.7	14.9	11.7	0.1	2.3	0.0	0.0	0.1	0.0	0.02
100	33.3	23.1	13.4	12.7	16.1	0.0	1.4	0.0	0.0	0.0	0.0	0.02

References

[1] M. Bayat, W. Dong, J. Thorborg, A. C. To, and J. H. Hattel, "A review of multi-scale and multi-physics simulations of metal additive manufacturing processes with focus on modeling strategies," *Addit. Manuf.*, vol. 47, p. 102278, Nov. 2021, doi: 10.1016/j.addma.2021.102278.

[2] ASTM, "ASTM F2792-10e1: Standard Terminology for Additive Manufacturing Technologies," 2012.

[3] H. B. Cary and S. C. Helzer, *Modern Welding Technology*. Pearson/Prentice Hall, 2005.

[4] J. E. Greene, "Review Article: Tracing the recorded history of thin-film sputter deposition: From the 1800s to 2017," *J. Vac. Sci. Technol. A Vacuum, Surfaces, Film.*, vol. 35, no. 5, p. 05C204, 2017, doi: 10.1116/1.4998940.

[5] R. N. Leyden *et al.*, "EP0852536 (A1): Selective deposition modeling method and apparatus for forming three-dimensional objects and supports," 1998.

[6] C. W. Hull and J. P. Partanen, "EP1946910 (A2): Imager assembly and method for solid imaging," 2008.

[7] P. F. Jacobs, C. W. Hull, D. R. Smalley, and J. W. Allison, "EP0681906 (A2): Stereolithographic construction techniques.," 1995.

[8] C. W. Hull, "EP0171069 (A2): Method and apparatus for production of three-dimensional objects by stereolithography.," 1986.

[9] T. D. Ngo, A. Kashani, G. Imbalzano, K. T. Q. Nguyen, and D. Hui, "Additive manufacturing (3D printing): A review of materials, methods, applications and challenges," *Compos. Part B Eng.*, vol. 143, pp. 172–196, Jun. 2018, doi: 10.1016/j.compositesb.2018.02.012.

[10] P. Kocovic, *3D Printing and Its Impact on the Production of Fully Functional Components. Chapter 1*. IGI Global, 2017.

[11] M. Javaid, A. Haleem, R. P. Singh, R. Suman, and S. Rab, "Role of additive manufacturing applications towards environmental sustainability," *Adv. Ind. Eng. Polym. Res.*, vol. 4, no. 4, pp. 312–322, Oct. 2021, doi: 10.1016/j.aiepr.2021.07.005.

[12] D. Wang, S. Wu, Y. Bai, H. Lin, Y. Yang, and C. Song, "Characteristics of typical geometrical features shaped by selective laser melting," *J. Laser Appl.*, vol. 29, no. 2, p. 022007, 2017, doi: 10.2351/1.4980164.

[13] P. Peyre and É. Charkaluk, *La fabrication additive des alliages métalliques*. ISTE editions, 2022.

[14] A. Bandyopadhyay, Y. Zhang, and S. Bose, "Recent developments in metal additive manufacturing," *Curr. Opin. Chem. Eng.*, vol. 28, pp. 96–104, 2020, doi: 10.1016/j.coche.2020.03.001.

[15] L. A. Dobrzanski, A. D. Dobrzanska-Danikiewicz, A. Achtelik-Franczak, L. B. Dobrzanski, M. Szindler, and T. G. Gawel, “Porous Selective Laser Melted Ti and Ti6Al4V Materials for Medical Applications,” in *Powder Metallurgy - Fundamentals and Case Studies*, InTech, 2017.

[16] A. Mostafaei *et al.*, “Defects and anomalies in powder bed fusion metal additive manufacturing,” *Curr. Opin. Solid State Mater. Sci.*, vol. 26, no. 2, p. 100974, Apr. 2022, doi: 10.1016/j.cossms.2021.100974.

[17] T. DebRoy *et al.*, “Additive manufacturing of metallic components – Process, structure and properties,” *Prog. Mater. Sci.*, vol. 92, pp. 112–224, 2018, doi: 10.1016/j.pmatsci.2017.10.001.

[18] L. Thijs, F. Verhaeghe, T. Craeghs, J. Van Humbeeck, and J.-P. Kruth, “A study of the microstructural evolution during selective laser melting of Ti–6Al–4V,” *Acta Mater.*, vol. 58, no. 9, pp. 3303–3312, May 2010, doi: 10.1016/j.actamat.2010.02.004.

[19] A. Yadollahi, N. Shamsaei, S. M. Thompson, and D. W. Seely, “Effects of process time interval and heat treatment on the mechanical and microstructural properties of direct laser deposited 316L stainless steel,” *Mater. Sci. Eng. A*, vol. 644, pp. 171–183, Sep. 2015, doi: 10.1016/j.msea.2015.07.056.

[20] D. Wang, “Evaluation for Solidification Cracking Susceptibility of Type 310S Stainless Steel using Laser Trans-Varestraint Test and Prediction of Solidification,” 2016.

[21] J. R. Trelewicz, G. P. Halada, O. K. Donaldson, and G. Manogharan, “Microstructure and Corrosion Resistance of Laser Additively Manufactured 316L Stainless Steel,” *JOM*, vol. 68, no. 3, pp. 850–859, Mar. 2016, doi: 10.1007/s11837-016-1822-4.

[22] V. D. Manvatkar, A. A. Gokhale, G. Jagan Reddy, A. Venkataramana, and A. De, “Estimation of Melt Pool Dimensions, Thermal Cycle, and Hardness Distribution in the Laser-Engineered Net Shaping Process of Austenitic Stainless Steel,” *Metall. Mater. Trans. A*, vol. 42, no. 13, pp. 4080–4087, Dec. 2011, doi: 10.1007/s11661-011-0787-8.

[23] B. Zheng, Y. Zhou, J. E. Smugeresky, J. M. Schoenung, and E. J. Lavernia, “Thermal Behavior and Microstructure Evolution during Laser Deposition with Laser-Engineered Net Shaping: Part II. Experimental Investigation and Discussion,” *Metall. Mater. Trans. A*, vol. 39, no. 9, pp. 2237–2245, Sep. 2008, doi: 10.1007/s11661-008-9566-6.

[24] S. Gorsse, C. Hutchinson, M. Gouné, and R. Banerjee, “Additive manufacturing of metals: a brief review of the characteristic microstructures and properties of steels, Ti-6Al-4V and high-entropy alloys,” *Sci. Technol. Adv. Mater.*, vol. 18, no. 1, pp. 584–610, 2017, doi: 10.1080/14686996.2017.1361305.

[25] P. D. Nezhadfar, M. Masoomi, S. Thompson, N. Phan, and N. Shamsaei, “Mechanical properties of 17-4 PH stainless steel additively manufactured under Ar and N2 shielding gas,” *Solid Free. Fabr. 2018 Proc. 29th Annu. Int. Solid Free. Fabr. Symp. - An Addit. Manuf. Conf. SFF 2018*, no. December, pp. 1301–1310, 2020.

[26] H. Amano *et al.*, “Effect of a helium gas atmosphere on the mechanical properties of Ti-6Al-4V alloy built with laser powder bed fusion: A comparative study with argon gas,”

Addit. Manuf., vol. 48, p. 102444, Dec. 2021, doi: 10.1016/j.addma.2021.102444.

[27] Y. Liu, Y. Yang, and D. Wang, "Investigation into the shrinkage in Z-direction of components manufactured by selective laser melting (SLM)," *Int. J. Adv. Manuf. Technol.*, vol. 90, no. 9–12, pp. 2913–2923, 2017, doi: 10.1007/s00170-016-9596-y.

[28] A. Almabrouk Mousa, "Experimental investigations of curling phenomenon in selective laser sintering process," *Rapid Prototyp. J.*, vol. 22, no. 2, pp. 405–415, Mar. 2016, doi: 10.1108/RPJ-12-2013-0132.

[29] E. Yasa, J. Deckers, T. Craeghs, M. Badrossamay, and J.-P. Kruth, "Investigation on occurance of elevated edges in selective laser melting," 2009, pp. 180–192.

[30] M. F. Zäh and S. Lutzmann, "Modelling and simulation of electron beam melting," *Prod. Eng.*, vol. 4, no. 1, pp. 15–23, Feb. 2010, doi: 10.1007/s11740-009-0197-6.

[31] R. Morgan, C. J. Sutcliffe, and W. O'Neill, "Density analysis of direct metal laser re-melted 316L stainless steel cubic primitives," *J. Mater. Sci.*, vol. 39, no. 4, pp. 1195–1205, Feb. 2004, doi: 10.1023/B:JMSC.0000013875.62536.fa.

[32] E. O. Olakanmi, R. F. Cochrane, and K. W. Dalgarno, "Densification mechanism and microstructural evolution in selective laser sintering of Al–12Si powders," *J. Mater. Process. Technol.*, vol. 211, no. 1, pp. 113–121, Jan. 2011, doi: 10.1016/j.jmatprotec.2010.09.003.

[33] Q. Jia and D. Gu, "Selective laser melting additive manufacturing of TiC/Inconel 718 bulk-form nanocomposites: Densification, microstructure, and performance," *J. Mater. Res.*, vol. 29, no. 17, pp. 1960–1969, Sep. 2014, doi: 10.1557/jmr.2014.130.

[34] H. D. Carlton, A. Haboub, G. F. Gallegos, D. Y. Parkinson, and A. A. MacDowell, "Damage evolution and failure mechanisms in additively manufactured stainless steel," *Mater. Sci. Eng. A*, vol. 651, pp. 406–414, Jan. 2016, doi: 10.1016/j.msea.2015.10.073.

[35] W. E. King *et al.*, "Observation of keyhole-mode laser melting in laser powder-bed fusion additive manufacturing," *J. Mater. Process. Technol.*, vol. 214, no. 12, pp. 2915–2925, 2014, doi: 10.1016/j.jmatprotec.2014.06.005.

[36] A. Kaplan, "A model of deep penetration laser welding based on calculation of the keyhole profile," *J. Phys. D. Appl. Phys.*, vol. 27, no. 9, pp. 1805–1814, 1994, doi: 10.1088/0022-3727/27/9/002.

[37] C. Zhao *et al.*, "Real-time monitoring of laser powder bed fusion process using high-speed X-ray imaging and diffraction," *Sci. Rep.*, vol. 7, no. 1, p. 3602, Dec. 2017, doi: 10.1038/s41598-017-03761-2.

[38] A. A. Martin *et al.*, "Ultrafast dynamics of laser-metal interactions in additive manufacturing alloys captured by in situ X-ray imaging," *Mater. Today Adv.*, vol. 1, p. 100002, Mar. 2019, doi: 10.1016/j.mtadv.2019.01.001.

[39] K. Q. Le, C. Tang, and C. H. Wong, "On the study of keyhole-mode melting in selective laser melting process," *Int. J. Therm. Sci.*, vol. 145, no. June, 2019, doi: 10.1016/j.ijthermalsci.2019.105992.

[40] J. W. Elmer, J. Vaja, H. D. Carlton, and R. Pong, “The effect of Ar and N2 shielding gas on laser weld porosity in steel, stainless steels, and nickel,” *Weld. J.*, vol. 94, no. 10, pp. 313s-325s, 2015.

[41] S. Dong *et al.*, “Research on metallurgical bonding of selective laser melted AlSi10Mg alloy,” *Mater. Res. Express*, vol. 7, no. 2, 2020, doi: 10.1088/2053-1591/ab6dae.

[42] W. J. Sames, F. Medina, W. H. Peter, S. S. Babu, and R. R. Dehoff, “Effect of Process Control and Powder Quality on Inconel 718 Produced Using Electron Beam Melting,” in *8th International Symposium on Superalloy 718 and Derivatives*, Hoboken, NJ, USA: John Wiley & Sons, Inc., 2014, pp. 409–423.

[43] T. Mukherjee, J. S. Zuback, A. De, and T. DebRoy, “Printability of alloys for additive manufacturing,” *Sci. Rep.*, vol. 6, pp. 1–8, 2016, doi: 10.1038/srep19717.

[44] K. Darvish, Z. W. Chen, and T. Pasang, “Reducing lack of fusion during selective laser melting of CoCrMo alloy: Effect of laser power on geometrical features of tracks,” *Mater. Des.*, vol. 112, pp. 357–366, Dec. 2016, doi: 10.1016/j.matdes.2016.09.086.

[45] G. Strano, L. Hao, R. M. Everson, and K. E. Evans, “Surface roughness analysis, modelling and prediction in selective laser melting,” *J. Mater. Process. Technol.*, vol. 213, no. 4, pp. 589–597, Apr. 2013, doi: 10.1016/j.jmatprotec.2012.11.011.

[46] J. P. Kruth, L. Froyen, J. Van Vaerenbergh, P. Mercelis, M. Rombouts, and B. Lauwers, “Selective laser melting of iron-based powder,” *J. Mater. Process. Technol.*, vol. 149, no. 1–3, pp. 616–622, 2004, doi: 10.1016/j.jmatprotec.2003.11.051.

[47] R. Li, J. Liu, Y. Shi, L. Wang, and W. Jiang, “Balling behavior of stainless steel and nickel powder during selective laser melting process,” *Int. J. Adv. Manuf. Technol.*, vol. 59, no. 9–12, pp. 1025–1035, 2012, doi: 10.1007/s00170-011-3566-1.

[48] S. Pal *et al.*, “As-fabricated surface morphologies of Ti-6Al-4V samples fabricated by different laser processing parameters in selective laser melting,” *Addit. Manuf.*, vol. 33, p. 101147, May 2020, doi: 10.1016/j.addma.2020.101147.

[49] V. Gunenthiram, “Compréhension de la formation de porosités en fabrication additive (LBM). Analyse expérimentale de l ’ interaction laser - lit de poudre - bain liquide. PhD Thesis ENSAM, École doctorale n° 432,” 2018.

[50] M. Yakout, M. A. Elbestawi, and S. C. Veldhuis, “A study of thermal expansion coefficients and microstructure during selective laser melting of Invar 36 and stainless steel 316L,” *Addit. Manuf.*, vol. 24, pp. 405–418, Dec. 2018, doi: 10.1016/j.addma.2018.09.035.

[51] M. Simonelli *et al.*, “A Study on the Laser Spatter and the Oxidation Reactions During Selective Laser Melting of 316L Stainless Steel, Al-Si10-Mg, and Ti-6Al-4V,” *Metall. Mater. Trans. A*, vol. 46, no. 9, pp. 3842–3851, Sep. 2015, doi: 10.1007/s11661-015-2882-8.

[52] J. Liu and P. Wen, “Metal vaporization and its influence during laser powder bed fusion process,” *Mater. Des.*, vol. 215, p. 110505, 2022, doi: 10.1016/j.matdes.2022.110505.

[53] H. . Niu and I. T. . Chang, “Instability of scan tracks of selective laser sintering of high

speed steel powder," *Scr. Mater.*, vol. 41, no. 11, pp. 1229–1234, Nov. 1999, doi: 10.1016/S1359-6462(99)00276-6.

[54] Q. Huang, N. Hu, X. Yang, R. Zhang, and Q. Feng, "Microstructure and inclusion of Ti–6Al–4V fabricated by selective laser melting," *Front. Mater. Sci.*, vol. 10, no. 4, pp. 428–431, Dec. 2016, doi: 10.1007/s11706-016-0354-8.

[55] Y. N. Zhang, X. Cao, P. Wanjara, and M. Medraj, "Oxide films in laser additive manufactured Inconel 718," *Acta Mater.*, vol. 61, no. 17, pp. 6562–6576, 2013, doi: 10.1016/j.actamat.2013.07.039.

[56] J. Dawes, R. Bowerman, and R. Trepleton, "Introduction to the Additive Manufacturing Powder Metallurgy Supply Chain," *Johnson Matthey Technol. Rev.*, vol. 59, no. 3, pp. 243–256, Jul. 2015, doi: 10.1595/205651315X688686.

[57] H. Taheri, M. R. B. M. Shoaib, L. W. Koester, T. A. Bigelow, P. C. Collins, and L. J. Bond, "Powder-based additive manufacturing - a review of types of defects, generation mechanisms, detection, property evaluation and metrology," *Int. J. Addit. Subtractive Mater. Manuf.*, vol. 1, no. 2, p. 172, 2017, doi: 10.1504/IJASMM.2017.088204.

[58] S. Singh, S. Ramakrishna, and R. Singh, "Material issues in additive manufacturing: A review," *J. Manuf. Process.*, vol. 25, pp. 185–200, Jan. 2017, doi: 10.1016/j.jmapro.2016.11.006.

[59] C. Pleass and S. Jothi, "Influence of powder characteristics and additive manufacturing process parameters on the microstructure and mechanical behaviour of Inconel 625 fabricated by Selective Laser Melting," *Addit. Manuf.*, vol. 24, pp. 419–431, Dec. 2018, doi: 10.1016/j.addma.2018.09.023.

[60] J. H. Tan, W. L. E. Wong, and K. W. Dalgarno, "An overview of powder granulometry on feedstock and part performance in the selective laser melting process," *Addit. Manuf.*, vol. 18, pp. 228–255, Dec. 2017, doi: 10.1016/j.addma.2017.10.011.

[61] S. Vock, B. Klöden, A. Kirchner, T. Weißgärber, and B. Kieback, "Powders for powder bed fusion: a review," *Prog. Addit. Manuf.*, vol. 4, no. 4, pp. 383–397, Dec. 2019, doi: 10.1007/s40964-019-00078-6.

[62] Q. B. Nguyen, M. L. S. Nai, Z. Zhu, C.-N. Sun, J. Wei, and W. Zhou, "Characteristics of Inconel Powders for Powder-Bed Additive Manufacturing," *Engineering*, vol. 3, no. 5, pp. 695–700, Oct. 2017, doi: 10.1016/J.ENG.2017.05.012.

[63] B. H. Rabin, G. R. Smolik, and G. E. Korth, "Characterization of entrapped gases in rapidly solidified powders," *Mater. Sci. Eng. A*, vol. 124, no. 1, pp. 1–7, Apr. 1990, doi: 10.1016/0921-5093(90)90328-Z.

[64] N. Kouraytem, S. T. Thoroddsen, and J. O. Marston, "Penetration in bimodal, polydisperse granular material," *Phys. Rev. E*, vol. 94, no. 5, p. 052902, Nov. 2016, doi: 10.1103/PhysRevE.94.052902.

[65] P. Moghimian *et al.*, "Metal powders in additive manufacturing: A review on reusability and recyclability of common titanium, nickel and aluminum alloys," *Addit. Manuf.*, vol. 43, p. 102017, Jul. 2021, doi: 10.1016/j.addma.2021.102017.

[66] X. Yang, F. Gao, F. Tang, X. Hao, and Z. Li, “Effect of Surface Oxides on the Melting and Solidification of 316L Stainless Steel Powder for Additive Manufacturing,” *Metall. Mater. Trans. A Phys. Metall. Mater. Sci.*, vol. 52, no. 10, pp. 4518–4532, 2021, doi: 10.1007/s11661-021-06405-3.

[67] P. Vora, K. Mumtaz, I. Todd, and N. Hopkinson, “AlSi12 in-situ alloy formation and residual stress reduction using anchorless selective laser melting,” *Addit. Manuf.*, vol. 7, pp. 12–19, Jul. 2015, doi: 10.1016/j.addma.2015.06.003.

[68] V. V. Popov, A. Katz-Demyanetz, A. Koptyug, and M. Bamberger, “Selective electron beam melting of Al0.5CrMoNbTa0.5 high entropy alloys using elemental powder blend,” *Heliyon*, vol. 5, no. 2, p. e01188, Feb. 2019, doi: 10.1016/j.heliyon.2019.e01188.

[69] I. A. Radulov *et al.*, “Production of net-shape Mn-Al permanent magnets by electron beam melting,” *Addit. Manuf.*, vol. 30, p. 100787, Dec. 2019, doi: 10.1016/j.addma.2019.100787.

[70] A. Koptyug *et al.*, “Compositionally-tailored steel-based materials manufactured by electron beam melting using blended pre-alloyed powders,” *Mater. Sci. Eng. A*, vol. 771, p. 138587, Jan. 2020, doi: 10.1016/j.msea.2019.138587.

[71] M. Fischer, D. Joguet, G. Robin, L. Peltier, and P. Laheurte, “In situ elaboration of a binary Ti–26Nb alloy by selective laser melting of elemental titanium and niobium mixed powders,” *Mater. Sci. Eng. C*, vol. 62, pp. 852–859, May 2016, doi: 10.1016/j.msec.2016.02.033.

[72] L. Yan, X. Chen, W. Li, J. Newkirk, and F. Liou, “Direct laser deposition of Ti-6Al-4V from elemental powder blends,” *Rapid Prototyp. J.*, vol. 22, no. 5, pp. 810–816, Aug. 2016, doi: 10.1108/RPJ-10-2015-0140.

[73] M. Fischer, “Elaboration in situ d’alliages de titane et de structures architecturées par fabrication additive – Application aux dispositifs médicaux implantables. PhD Thesis, Université de Lorraine,” 2017.

[74] A. Vafadar, F. Guzzomi, A. Rassau, and K. Hayward, “Advances in Metal Additive Manufacturing: A Review of Common Processes, Industrial Applications, and Current Challenges,” *Appl. Sci.*, vol. 11, no. 3, p. 1213, Jan. 2021, doi: 10.3390/app11031213.

[75] R. R. Dehoff *et al.*, “Site specific control of crystallographic grain orientation through electron beam additive manufacturing,” *Mater. Sci. Technol.*, vol. 31, no. 8, pp. 931–938, Jun. 2015, doi: 10.1179/1743284714Y.0000000734.

[76] W. Xu, E. W. Lui, A. Pateras, M. Qian, and M. Brandt, “In situ tailoring microstructure in additively manufactured Ti-6Al-4V for superior mechanical performance,” *Acta Mater.*, vol. 125, pp. 390–400, Feb. 2017, doi: 10.1016/j.actamat.2016.12.027.

[77] A. Wimmer *et al.*, “Investigations on the influence of adapted metal-based alloys on the process of laser beam melting,” *J. Laser Appl.*, vol. 32, no. 2, p. 022029, May 2020, doi: 10.2351/7.0000071.

[78] H. Jia, H. Sun, H. Wang, Y. Wu, and H. Wang, “Scanning strategy in selective laser melting (SLM): a review,” *Int. J. Adv. Manuf. Technol.*, vol. 113, no. 9–10, pp. 2413–2435, 2021, doi: 10.1007/s00170-021-06810-3.

[79] M. Van Elsen, *Complexity of Selective Laser Melting: a new optimisation approach*. 2007.

[80] L. N. Carter, C. Martin, P. J. Withers, and M. M. Attallah, "The influence of the laser scan strategy on grain structure and cracking behaviour in SLM powder-bed fabricated nickel superalloy," *J. Alloys Compd.*, vol. 615, pp. 338–347, Dec. 2014, doi: 10.1016/j.jallcom.2014.06.172.

[81] H. Gong, K. Rafi, N. V. Karthik, T. Starr, and B. Stucker, "Defect morphology in Ti-6Al-4V parts fabricated by Selective Laser Melting and Electron Beam Melting," *24th Int. SFF Symp. - An Addit. Manuf. Conf. SFF 2013*, pp. 440–453, 2013.

[82] H. Gong, "Generation and detection of defects in metallic parts fabricated by selective laser melting and electron beam melting and their effects on mechanical properties. Electronic Theses and Dissertations. Paper 515," 2013.

[83] J. V. Gordon *et al.*, "Defect structure process maps for laser powder bed fusion additive manufacturing," *Addit. Manuf.*, vol. 36, p. 101552, 2020, doi: 10.1016/j.addma.2020.101552.

[84] M. Saunders, "How process parameters drive successful metal AM part - Metal Additive Manufacturing Magazine Vol.4 No. 2," *available at: https://issuu.com/inovar-communications/docs/mam_summer_2018_sp?e=32443561/63203285*, pp. 127–135, 2018.

[85] M. J. Heiden, S. C. Jensen, J. R. Koepke, D. J. Saiz, S. M. Dickens, and B. H. Jared, "Process and feedstock driven microstructure for laser powder bed fusion of 316L stainless steel," *Materialia*, vol. 21, no. August 2021, p. 101356, 2022, doi: 10.1016/j.mtla.2022.101356.

[86] Y. Brif, M. Thomas, and I. Todd, "The use of high-entropy alloys in additive manufacturing," *Scr. Mater.*, vol. 99, pp. 93–96, 2015, doi: 10.1016/j.scriptamat.2014.11.037.

[87] E. A. Périgo, J. Jacimovic, F. García Ferré, and L. M. Scherf, "Additive manufacturing of magnetic materials," *Addit. Manuf.*, vol. 30, p. 100870, Dec. 2019, doi: 10.1016/j.addma.2019.100870.

[88] V. Chaudhary, S. A. Mantri, R. V. Ramanujan, and R. Banerjee, "Additive manufacturing of magnetic materials," *Prog. Mater. Sci.*, vol. 114, p. 100688, Oct. 2020, doi: 10.1016/j.pmatsci.2020.100688.

[89] C. Teng *et al.*, "Simulating Melt Pool Shape and Lack of Fusion Porosity for Selective Laser Melting of Cobalt Chromium Components," *J. Manuf. Sci. Eng.*, vol. 139, no. 1, Jan. 2017, doi: 10.1115/1.4034137.

[90] B. Richter *et al.*, "High-speed X-ray investigation of melt dynamics during continuous-wave laser remelting of selective laser melted Co-Cr alloy," *CIRP Ann.*, vol. 68, no. 1, pp. 229–232, 2019, doi: 10.1016/j.cirp.2019.04.110.

[91] R. K. Enneti, R. Morgan, and S. V. Atre, "Effect of process parameters on the Selective Laser Melting (SLM) of tungsten," *Int. J. Refract. Met. Hard Mater.*, vol. 71, pp. 315–319, Feb. 2018, doi: 10.1016/j.ijrmhm.2017.11.035.

[92] A. Iveković *et al.*, “Selective laser melting of tungsten and tungsten alloys,” *Int. J. Refract. Met. Hard Mater.*, vol. 72, pp. 27–32, Apr. 2018, doi: 10.1016/j.ijrmhm.2017.12.005.

[93] D. Zhang *et al.*, “Metal Alloys for Fusion-Based Additive Manufacturing,” *Adv. Eng. Mater.*, vol. 20, no. 5, pp. 1–20, 2018, doi: 10.1002/adem.201700952.

[94] T. M. Pollock, A. J. Clarke, and S. S. Babu, “Design and Tailoring of Alloys for Additive Manufacturing,” *Metall. Mater. Trans. A Phys. Metall. Mater. Sci.*, vol. 51, no. 12, pp. 6000–6019, 2020, doi: 10.1007/s11661-020-06009-3.

[95] *ASM Specialty Handbook: Stainless Steels*. ASM International, 1994.

[96] M. K. Alam, M. Mehdi, R. J. Urbanic, and A. Edrisy, “Mechanical behavior of additive manufactured AISI 420 martensitic stainless steel,” *Mater. Sci. Eng. A*, vol. 773, p. 138815, Jan. 2020, doi: 10.1016/j.msea.2019.138815.

[97] C.-O. . Olsson and D. Landolt, “Passive films on stainless steels—chemistry, structure and growth,” *Electrochim. Acta*, vol. 48, no. 9, pp. 1093–1104, Apr. 2003, doi: 10.1016/S0013-4686(02)00841-1.

[98] B. Al-mangour, *Powder metallurgy of stainless steel: State-of-the art, challenges, and development*, no. January 2015. 2016.

[99] J. Suryawanshi, K. G. Prashanth, and U. Ramamurty, “Mechanical behavior of selective laser melted 316L stainless steel,” *Mater. Sci. Eng. A*, vol. 696, pp. 113–121, Jun. 2017, doi: 10.1016/j.msea.2017.04.058.

[100] E. Yasa and J.-P. Kruth, “Microstructural investigation of Selective Laser Melting 316L stainless steel parts exposed to laser re-melting,” *Procedia Eng.*, vol. 19, pp. 389–395, 2011, doi: 10.1016/j.proeng.2011.11.130.

[101] H. Yu, J. Yang, J. Yin, Z. Wang, and X. Zeng, “Comparison on mechanical anisotropies of selective laser melted Ti-6Al-4V alloy and 304 stainless steel,” *Mater. Sci. Eng. A*, vol. 695, pp. 92–100, May 2017, doi: 10.1016/j.msea.2017.04.031.

[102] Y. Zhong, L. Liu, S. Wikman, D. Cui, and Z. Shen, “Intragranular cellular segregation network structure strengthening 316L stainless steel prepared by selective laser melting,” *J. Nucl. Mater.*, vol. 470, no. December 2017, pp. 170–178, Mar. 2016, doi: 10.1016/j.jnucmat.2015.12.034.

[103] A. Riemer, S. Leuders, M. Thöne, H. A. Richard, T. Tröster, and T. Niendorf, “On the fatigue crack growth behavior in 316L stainless steel manufactured by selective laser melting,” *Eng. Fract. Mech.*, vol. 120, pp. 15–25, Apr. 2014, doi: 10.1016/j.engfracmech.2014.03.008.

[104] T. Niendorf, S. Leuders, A. Riemer, H. A. Richard, T. Tröster, and D. Schwarze, “Highly Anisotropic Steel Processed by Selective Laser Melting,” *Metall. Mater. Trans. B*, vol. 44, no. 4, pp. 794–796, Aug. 2013, doi: 10.1007/s11663-013-9875-z.

[105] A. Röttger *et al.*, “Microstructure and mechanical properties of 316L austenitic stainless steel processed by different SLM devices,” *Int. J. Adv. Manuf. Technol.*, vol. 108, no. 3, pp. 769–783, 2020, doi: 10.1007/s00170-020-05371-1.

[106] P. Bajaj, A. Hariharan, A. Kini, P. Kürnsteiner, D. Raabe, and E. A. Jägle, "Steels in additive manufacturing: A review of their microstructure and properties," *Mater. Sci. Eng. A*, vol. 772, no. October 2019, 2020, doi: 10.1016/j.msea.2019.138633.

[107] A. Röttger, K. Geenen, M. Windmann, F. Binner, and W. Theisen, "Comparison of microstructure and mechanical properties of 316 L austenitic steel processed by selective laser melting with hot-isostatic pressed and cast material," *Mater. Sci. Eng. A*, vol. 678, pp. 365–376, Dec. 2016, doi: 10.1016/j.msea.2016.10.012.

[108] A. B. Spierings, N. Herres, and G. Levy, "Influence of the particle size distribution on surface quality and mechanical properties in AM steel parts," *Rapid Prototyp. J.*, vol. 17, no. 3, pp. 195–202, Apr. 2011, doi: 10.1108/13552541111124770.

[109] N. Guo and M. C. Leu, "Additive manufacturing: technology, applications and research needs," *Front. Mech. Eng.*, vol. 8, no. 3, pp. 215–243, Sep. 2013, doi: 10.1007/s11465-013-0248-8.

[110] A. Mertens *et al.*, "Mechanical properties of alloy Ti-6Al-4V and of stainless steel 316L processed by selective laser melting: Influence of out-of-equilibrium microstructures," *Powder Metall.*, vol. 57, no. 3, pp. 184–189, 2014, doi: 10.1179/1743290114Y.0000000092.

[111] R. Casati, J. Lemke, and M. Vedani, "Microstructure and Fracture Behavior of 316L Austenitic Stainless Steel Produced by Selective Laser Melting," *J. Mater. Sci. Technol.*, vol. 32, no. 8, pp. 738–744, Aug. 2016, doi: 10.1016/j.jmst.2016.06.016.

[112] H. H. Alsalla, C. Smith, and L. Hao, "Effect of build orientation on the surface quality, microstructure and mechanical properties of selective laser melting 316L stainless steel," *Rapid Prototyp. J.*, vol. 24, no. 1, pp. 9–17, Jan. 2018, doi: 10.1108/RPJ-04-2016-0068.

[113] I. Tolosa, F. Garciandía, F. Zubiri, F. Zapirain, and A. Esnaola, "Study of mechanical properties of AISI 316 stainless steel processed by 'selective laser melting', following different manufacturing strategies," *Int. J. Adv. Manuf. Technol.*, vol. 51, no. 5–8, pp. 639–647, Nov. 2010, doi: 10.1007/s00170-010-2631-5.

[114] M. Montero-Sistiaga, S. Nardone, C. Hautfenne, and J. Humbeeck, "Effect of heat treatment of 316L stainless steel produced by Selective Laser Melting (SLM)," in *Solid Freeform Fabrication 2016: Proceedings of the 27th Annual International Solid Freeform Fabrication Symposium – An Additive Manufacturing Conference*, 2016.

[115] J. Yu, M. Rombouts, and G. Maes, "Cracking behavior and mechanical properties of austenitic stainless steel parts produced by laser metal deposition," *Mater. Des.*, vol. 45, pp. 228–235, Mar. 2013, doi: 10.1016/j.matdes.2012.08.078.

[116] M. Ziętala *et al.*, "The microstructure, mechanical properties and corrosion resistance of 316L stainless steel fabricated using laser engineered net shaping," *Mater. Sci. Eng. A*, vol. 677, pp. 1–10, Nov. 2016, doi: 10.1016/j.msea.2016.09.028.

[117] A. L. Greer, "Confusion by design," *Nature*, vol. 366, no. 6453, pp. 303–304, Dec. 1993, doi: 10.1038/366303a0.

[118] J.-W. Yeh *et al.*, "Nanostructured High-Entropy Alloys with Multiple Principal Elements:

Novel Alloy Design Concepts and Outcomes," *Adv. Eng. Mater.*, vol. 6, no. 5, pp. 299–303, May 2004, doi: 10.1002/adem.200300567.

[119] B. Cantor, I. T. H. Chang, P. Knight, and A. J. B. Vincent, "Microstructural development in equiatomic multicomponent alloys," *Mater. Sci. Eng. A*, vol. 375–377, no. 1-2 SPEC. ISS., pp. 213–218, 2004, doi: 10.1016/j.msea.2003.10.257.

[120] R. A. Swalin and S. A. Rice, "Thermodynamics of Solids," *Phys. Today*, vol. 16, no. 1, pp. 72–74, Jan. 1963, doi: 10.1063/1.3050727.

[121] J.-W. Yeh, "Recent progress in high-entropy alloys," *Ann. Chim. Sci. des Matériaux*, vol. 31, no. 6, pp. 633–648, Dec. 2006, doi: 10.3166/acsm.31.633-648.

[122] F. Otto, Y. Yang, H. Bei, and E. P. George, "Relative effects of enthalpy and entropy on the phase stability of equiatomic high-entropy alloys," *Acta Mater.*, vol. 61, no. 7, pp. 2628–2638, Apr. 2013, doi: 10.1016/j.actamat.2013.01.042.

[123] M. G. Poletti and L. Battezzati, "Electronic and thermodynamic criteria for the occurrence of high entropy alloys in metallic systems," *Acta Mater.*, vol. 75, pp. 297–306, Aug. 2014, doi: 10.1016/j.actamat.2014.04.033.

[124] D. Ma, B. Grabowski, F. Körmann, J. Neugebauer, and D. Raabe, "Ab initio thermodynamics of the CoCrFeMnNi high entropy alloy: Importance of entropy contributions beyond the configurational one," *Acta Mater.*, vol. 100, pp. 90–97, Nov. 2015, doi: 10.1016/j.actamat.2015.08.050.

[125] Y. J. Zhou, Y. Zhang, F. J. Wang, and G. L. Chen, "Phase transformation induced by lattice distortion in multiprincipal component CoCrFeNiCuxAl1−x solid-solution alloys," *Appl. Phys. Lett.*, vol. 92, no. 24, p. 241917, Jun. 2008, doi: 10.1063/1.2938690.

[126] M. C. Troparevsky, J. R. Morris, P. R. C. Kent, A. R. Lupini, and G. M. Stocks, "Criteria for Predicting the Formation of Single-Phase High-Entropy Alloys," *Phys. Rev. X*, vol. 5, no. 1, p. 011041, Mar. 2015, doi: 10.1103/PhysRevX.5.011041.

[127] C.-J. Tong *et al.*, "Microstructure characterization of Al x CoCrCuFeNi high-entropy alloy system with multiprincipal elements," *Metall. Mater. Trans. A*, vol. 36, no. 4, pp. 881–893, Apr. 2005, doi: 10.1007/s11661-005-0283-0.

[128] S. Guo, C. Ng, and C. T. Liu, "Anomalous solidification microstructures in Co-free AlxCrCuFeNi2 high-entropy alloys," *J. Alloys Compd.*, vol. 557, pp. 77–81, Apr. 2013, doi: 10.1016/j.jallcom.2013.01.007.

[129] S. Guo and C. T. Liu, "Phase stability in high entropy alloys: Formation of solid-solution phase or amorphous phase," *Prog. Nat. Sci. Mater. Int.*, vol. 21, no. 6, pp. 433–446, 2011, doi: 10.1016/S1002-0071(12)60080-X.

[130] B. Ren, Z. X. Liu, D. M. Li, L. Shi, B. Cai, and M. X. Wang, "Effect of elemental interaction on microstructure of CuCrFeNiMn high entropy alloy system," *J. Alloys Compd.*, vol. 493, no. 1–2, pp. 148–153, Mar. 2010, doi: 10.1016/j.jallcom.2009.12.183.

[131] L. Liu, J. B. Zhu, L. Li, J. C. Li, and Q. Jiang, "Microstructure and tensile properties of FeMnNiCuCoSnx high entropy alloys," *Mater. Des.*, vol. 44, pp. 223–227, Feb. 2013, doi:

10.1016/j.matdes.2012.08.019.

[132] L. Liu, J. B. Zhu, C. Zhang, J. C. Li, and Q. Jiang, "Microstructure and the properties of FeCoCuNiSnx high entropy alloys," *Mater. Sci. Eng. A*, vol. 548, pp. 64–68, Jun. 2012, doi: 10.1016/j.msea.2012.03.080.

[133] Y.-F. Kao, T.-J. Chen, S.-K. Chen, and J.-W. Yeh, "Microstructure and mechanical property of as-cast, -homogenized, and -deformed AlxCoCrFeNi (0≤x≤2) high-entropy alloys," *J. Alloys Compd.*, vol. 488, no. 1, pp. 57–64, Nov. 2009, doi: 10.1016/j.jallcom.2009.08.090.

[134] M.-R. Chen, S.-J. Lin, J.-W. Yeh, S.-K. Chen, Y.-S. Huang, and C.-P. Tu, "Microstructure and Properties of Al0.5CoCrCuFeNiTix (x=0–2.0) High-Entropy Alloys," *Mater. Trans.*, vol. 47, no. 5, pp. 1395–1401, 2006, doi: 10.2320/matertrans.47.1395.

[135] C. Li, J. C. Li, M. Zhao, and Q. Jiang, "Effect of alloying elements on microstructure and properties of multiprincipal elements high-entropy alloys," *J. Alloys Compd.*, vol. 475, no. 1–2, pp. 752–757, May 2009, doi: 10.1016/j.jallcom.2008.07.124.

[136] Y. J. Zhou, Y. Zhang, Y. L. Wang, and G. L. Chen, "Microstructure and compressive properties of multicomponent Alx(TiVCrMnFeCoNiCu)100−x high-entropy alloys," *Mater. Sci. Eng. A*, vol. 454–455, pp. 260–265, Apr. 2007, doi: 10.1016/j.msea.2006.11.049.

[137] O. N. Senkov, G. B. Wilks, J. M. Scott, and D. B. Miracle, "Mechanical properties of Nb25Mo25Ta25W25 and V20Nb20Mo20Ta20W20 refractory high entropy alloys," *Intermetallics*, vol. 19, no. 5, pp. 698–706, May 2011, doi: 10.1016/j.intermet.2011.01.004.

[138] O. N. Senkov, J. M. Scott, S. V. Senkova, F. Meisenkothen, D. B. Miracle, and C. F. Woodward, "Microstructure and elevated temperature properties of a refractory TaNbHfZrTi alloy," *J. Mater. Sci.*, vol. 47, no. 9, pp. 4062–4074, May 2012, doi: 10.1007/s10853-012-6260-2.

[139] M.-H. Chuang, M.-H. Tsai, W.-R. Wang, S.-J. Lin, and J.-W. Yeh, "Microstructure and wear behavior of AlxCo1.5CrFeNi1.5Tiy high-entropy alloys," *Acta Mater.*, vol. 59, no. 16, pp. 6308–6317, Sep. 2011, doi: 10.1016/j.actamat.2011.06.041.

[140] P. Chen *et al.*, "Fatigue behavior of high-entropy alloys: A review," *Sci. China Technol. Sci.*, vol. 61, no. 2, pp. 168–178, Feb. 2018, doi: 10.1007/s11431-017-9137-4.

[141] Y. Shi, B. Yang, and P. Liaw, "Corrosion-Resistant High-Entropy Alloys: A Review," *Metals (Basel).*, vol. 7, no. 2, p. 43, Feb. 2017, doi: 10.3390/met7020043.

[142] Y. Kuzminova *et al.*, "The effect of the parameters of the powder bed fusion process on the microstructure and mechanical properties of CrFeCoNi medium-entropy alloys," *Intermetallics*, vol. 116, p. 106651, Jan. 2020, doi: 10.1016/j.intermet.2019.106651.

[143] A. Gali and E. P. George, "Tensile properties of high- and medium-entropy alloys," *Intermetallics*, vol. 39, pp. 74–78, Aug. 2013, doi: 10.1016/j.intermet.2013.03.018.

[144] R. Zhou *et al.*, "Microstructures and mechanical properties of C-containing FeCoCrNi high-entropy alloy fabricated by selective laser melting," *Intermetallics*, vol. 94, pp. 165–171, Mar. 2018, doi: 10.1016/j.intermet.2018.01.002.

[145] T. Fujieda *et al.*, "Mechanical and corrosion properties of CoCrFeNiTi-based high-entropy alloy additive manufactured using selective laser melting," *Addit. Manuf.*, vol. 25, no. November 2018, pp. 412–420, 2019, doi: 10.1016/j.addma.2018.10.023.

[146] R. Li, P. Niu, T. Yuan, P. Cao, C. Chen, and K. Zhou, "Selective laser melting of an equiatomic CoCrFeMnNi high-entropy alloy: Processability, non-equilibrium microstructure and mechanical property," *J. Alloys Compd.*, vol. 746, pp. 125–134, May 2018, doi: 10.1016/j.jallcom.2018.02.298.

[147] S. Chen, Y. Tong, and P. K. Liaw, "Additive manufacturing of high-entropy alloys: A review," *Entropy*, vol. 20, no. 12, 2018, doi: 10.3390/e20120937.

[148] A. T. Clare *et al.*, "Alloy design and adaptation for additive manufacture," *J. Mater. Process. Technol.*, vol. 299, 2022, doi: 10.1016/j.jmatprotec.2021.117358.

[149] S. Thapliyal *et al.*, "Design of heterogeneous structured Al alloys with wide processing window for laser-powder bed fusion additive manufacturing," *Addit. Manuf.*, vol. 42, no. April, p. 102002, 2021, doi: 10.1016/j.addma.2021.102002.

[150] M. A. Ackers, O. M. D. M. Messé, and U. Hecht, "Novel approach of alloy design and selection for additive manufacturing towards targeted applications," *J. Alloys Compd.*, vol. 866, p. 158965, 2021, doi: 10.1016/j.jallcom.2021.158965.

[151] H. E. Sabzi and P. E. J. J. Rivera-Díaz-del-Castillo, "Defect Prevention in Selective Laser Melting Components: Compositional and Process Effects," *Materials (Basel).*, vol. 12, no. 22, p. 3791, Nov. 2019, doi: 10.3390/ma12223791.

[152] H. E. Sabzi, S. Maeng, X. Liang, M. Simonelli, N. T. Aboulkhair, and P. E. J. Rivera-Díaz-del-Castillo, "Controlling crack formation and porosity in laser powder bed fusion: Alloy design and process optimisation," *Addit. Manuf.*, vol. 34, no. March, p. 101360, 2020, doi: 10.1016/j.addma.2020.101360.

[153] F. Tancret, "Computational thermodynamics and genetic algorithms to design affordable γ'-strengthened nickel–iron based superalloys," *Model. Simul. Mater. Sci. Eng.*, vol. 20, no. 4, p. 45012, May 2012, doi: 10.1088/0965-0393/20/4/045012.

[154] J. Zander, R. Sandström, and L. Vitos, "Modelling mechanical properties for non-hardenable aluminium alloys," *Comput. Mater. Sci.*, vol. 41, no. 1, pp. 86–95, Nov. 2007, doi: 10.1016/j.commatsci.2007.03.013.

[155] H. Sieurin, J. Zander, and R. Sandström, "Modelling solid solution hardening in stainless steels," *Mater. Sci. Eng. A*, vol. 415, no. 1–2, pp. 66–71, 2006, doi: 10.1016/j.msea.2005.09.031.

[156] M. Walbrühl, D. Linder, J. Ågren, and A. Borgenstam, "Modelling of solid solution strengthening in multicomponent alloys," *Mater. Sci. Eng. A*, vol. 700, pp. 301–311, 2017, doi: 10.1016/j.msea.2017.06.001.

[157] N. Saunders, X. Li, A. P. Miodownik, and J.-P. Schillé, "Modelling of the Thermo-Physical and Physical Properties for Solidification of Al-Alloys," in *Essential Readings in Light Metals*, Cham: Springer International Publishing, 2016, pp. 519–524.

[158] Z. Guo and W. Sha, “Modelling the correlation between processing parameters and properties of maraging steels using artificial neural network,” *Comput. Mater. Sci.*, vol. 29, no. 1, pp. 12–28, Jan. 2004, doi: 10.1016/S0927-0256(03)00092-2.

[159] J. Xiong, S.-Q. Shi, and T.-Y. Zhang, “A machine-learning approach to predicting and understanding the properties of amorphous metallic alloys,” *Mater. Des.*, vol. 187, p. 108378, Feb. 2020, doi: 10.1016/j.matdes.2019.108378.

[160] C.-T. Wu *et al.*, “Machine learning recommends affordable new Ti alloy with bone-like modulus,” *Mater. Today*, vol. 34, pp. 41–50, Apr. 2020, doi: 10.1016/j.mattod.2019.08.008.

[161] J. J. Möller, W. Körner, G. Krugel, D. F. Urban, and C. Elsässer, “Compositional optimization of hard-magnetic phases with machine-learning models,” *Acta Mater.*, vol. 153, pp. 53–61, Jul. 2018, doi: 10.1016/j.actamat.2018.03.051.

[162] C. Shen, C. Wang, X. Wei, Y. Li, S. van der Zwaag, and W. Xu, “Physical metallurgy-guided machine learning and artificial intelligent design of ultrahigh-strength stainless steel,” *Acta Mater.*, vol. 179, pp. 201–214, 2019, doi: 10.1016/j.actamat.2019.08.033.

[163] H. Zhang *et al.*, “Dramatically Enhanced Combination of Ultimate Tensile Strength and Electric Conductivity of Alloys via Machine Learning Screening,” *Acta Mater.*, vol. 200, pp. 803–810, Nov. 2020, doi: 10.1016/j.actamat.2020.09.068.

[164] K. Kaufmann and K. S. Vecchio, “Searching for high entropy alloys: A machine learning approach,” *Acta Mater.*, vol. 198, pp. 178–222, Oct. 2020, doi: 10.1016/j.actamat.2020.07.065.

[165] Y. Wang *et al.*, “Accelerated design of Fe-based soft magnetic materials using machine learning and stochastic optimization,” *Acta Mater.*, vol. 194, pp. 144–155, Aug. 2020, doi: 10.1016/j.actamat.2020.05.006.

[166] N. Khatavkar, S. Swetlana, and A. K. Singh, “Accelerated prediction of Vickers hardness of Co- and Ni-based superalloys from microstructure and composition using advanced image processing techniques and machine learning,” *Acta Mater.*, vol. 196, pp. 295–303, Sep. 2020, doi: 10.1016/j.actamat.2020.06.042.

[167] F. Ren *et al.*, “Accelerated discovery of metallic glasses through iteration of machine learning and high-throughput experiments,” *Sci. Adv.*, vol. 4, no. 4, Apr. 2018, doi: 10.1126/sciadv.aaq1566.

[168] M. K. Tripathi, S. Ganguly, P. Dey, and P. P. Chattopadhyay, “Evolution of glass forming ability indicator by genetic programming,” *Comput. Mater. Sci.*, vol. 118, pp. 56–65, Jun. 2016, doi: 10.1016/j.commatsci.2016.02.037.

[169] F. Tancret, I. Toda-Caraballo, E. Menou, and P. E. J. Rivera Díaz-Del-Castillo, “Designing high entropy alloys employing thermodynamics and Gaussian process statistical analysis,” *Mater. Des.*, vol. 115, pp. 486–497, 2017, doi: 10.1016/j.matdes.2016.11.049.

[170] E. Menou *et al.*, “Evolutionary design of strong and stable high entropy alloys using multi-objective optimisation based on physical models, statistics and thermodynamics,” *Mater. Des.*, vol. 143, pp. 185–195, Apr. 2018, doi: 10.1016/j.matdes.2018.01.045.

[171] E. Menou, G. Ramstein, E. Bertrand, and F. Tancret, “Multi-objective constrained design of nickel-base superalloys using data mining- and thermodynamics-driven,” *Model. Simul. Mater. Sci. Eng.*, vol. 055001, 2016, doi: 10.1088/0965-0393/24/5/055001.

[172] F. Tancret, “Computational thermodynamics, Gaussian processes and genetic algorithms: Combined tools to design new alloys,” *Model. Simul. Mater. Sci. Eng.*, vol. 21, no. 4, 2013, doi: 10.1088/0965-0393/21/4/045013.

[173] F. Tancret, “Materials Design: Computational Alloy Design by Combinatorial Optimization,” in *Encyclopedia of Materials: Metals and Alloys*, Elsevier, 2022, pp. 596–608.

[174] W. Xu, P. E. J. Rivera-Díaz-del-Castillo, and S. van der Zwaag, “Genetic alloy design based on thermodynamics and kinetics,” *Philos. Mag.*, vol. 88, no. 12, pp. 1825–1833, Apr. 2008, doi: 10.1080/14786430802322180.

[175] C. Zhang, F. Zhang, S. Chen, and W. Cao, “Computational Thermodynamics Aided High-Entropy Alloy Design,” *JOM*, vol. 64, no. 7, pp. 839–845, Jul. 2012, doi: 10.1007/s11837-012-0365-6.

[176] W. Xu, P. E. J. R. D. del Castillo, and S. van der Zwaag, “A combined optimization of alloy composition and aging temperature in designing new UHS precipitation hardenable stainless steels,” *Comput. Mater. Sci.*, vol. 45, no. 2, pp. 467–473, Apr. 2009, doi: 10.1016/j.commatsci.2008.11.006.

[177] L. Kaufman and H. Bernstein, *Computer calculation of phase diagrams With special reference to refractory metals*. 1970.

[178] N. Saunders and A. P. Miodownik, *CALPHAD (Calculation of Phase Diagrams): A Comprehensive Guide*. Elsevier Science Ltd, 1998.

[179] L. Kaufman and J. Ågren, “CALPHAD, first and second generation – Birth of the materials genome,” *Scr. Mater.*, vol. 70, pp. 3–6, Jan. 2014, doi: 10.1016/j.scriptamat.2012.12.003.

[180] G. Bracq, M. Laurent-Brocq, L. Perrière, R. Pirès, J.-M. Joubert, and I. Guillot, “The fcc solid solution stability in the Co-Cr-Fe-Mn-Ni multi-component system,” *Acta Mater.*, vol. 128, pp. 327–336, Apr. 2017, doi: 10.1016/j.actamat.2017.02.017.

[181] J.-M. Joubert, “Crystal chemistry and Calphad modeling of the σ phase,” *Prog. Mater. Sci.*, vol. 53, no. 3, pp. 528–583, Mar. 2008, doi: 10.1016/j.pmatsci.2007.04.001.

[182] T. Rieger, J.-M. Joubert, M. Laurent-Brocq, L. Perrière, I. Guillot, and J.-P. Couzinié, “Study of the FCC+L12 two-phase region in complex concentrated alloys based on the Al–Co–Cr–Fe–Ni–Ti system,” *Materialia*, vol. 14, p. 100905, Dec. 2020, doi: 10.1016/j.mtla.2020.100905.

[183] B. Hallstedt and Z.-K. Liu, “Software for thermodynamic and kinetic calculation and modelling,” *Calphad*, vol. 33, no. 2, p. 265, Jun. 2009, doi: 10.1016/j.calphad.2009.04.002.

[184] “FactSage: https://www.factsage.com/.” [Online]. Available: https://www.factsage.com/.

[185] “Thermo-Calc Software: https://thermocalc.com/.” [Online]. Available:

https://thermocalc.com/.

[186] “CompuTherm for Materials Design: https://computherm.com/.” [Online]. Available: https://computherm.com/.

[187] B. Sundman, U. R. Kattner, M. Palumbo, and S. G. Fries, “OpenCalphad - a free thermodynamic software,” *Integr. Mater. Manuf. Innov.*, vol. 4, no. 1, pp. 1–15, Dec. 2015, doi: 10.1186/s40192-014-0029-1.

[188] “OpenCalphad: http://www.opencalphad.com/.” [Online]. Available: http://www.opencalphad.com/.

[189] “PyCalphad Computational Thermodynamics: https://pycalphad.org/docs/latest/.” [Online]. Available: https://pycalphad.org/docs/latest/.

[190] “Thermochimica: https://nuclear.ontariotechu.ca/piro/thermochimica/index.php.” [Online]. Available: https://nuclear.ontariotechu.ca/piro/thermochimica/index.php.

[191] J. Zhang *et al.*, “A novel crack-free Ti-modified Al-Cu-Mg alloy designed for selective laser melting,” *Addit. Manuf.*, vol. 38, p. 101829, Feb. 2021, doi: 10.1016/j.addma.2020.101829.

[192] Z. Lu and L. Zhang, “Thermodynamic description of the quaternary Al-Si-Mg-Sc system and its application to the design of novel Sc-additional A356 alloys,” *Mater. Des.*, vol. 116, pp. 427–437, Feb. 2017, doi: 10.1016/j.matdes.2016.12.034.

[193] J.-G. Jung, Y.-H. Cho, J.-M. Lee, H.-W. Kim, and K. Euh, “Designing the composition and processing route of aluminum alloys using CALPHAD: Case studies,” *Calphad*, vol. 64, pp. 236–247, Mar. 2019, doi: 10.1016/j.calphad.2018.12.010.

[194] Z. Lu, L. Zhang, J. Wang, Q. Yao, G. Rao, and H. Zhou, “Understanding of strengthening and toughening mechanisms for Sc-modified Al-Si-(Mg) series casting alloys designed by computational thermodynamics,” *J. Alloys Compd.*, vol. 805, pp. 415–425, Oct. 2019, doi: 10.1016/j.jallcom.2019.07.069.

[195] R. Shi and A. A. Luo, “Applications of CALPHAD modeling and databases in advanced lightweight metallic materials,” *Calphad*, vol. 62, pp. 1–17, Sep. 2018, doi: 10.1016/j.calphad.2018.04.009.

[196] A. Shafiei, “Design of Eutectic High Entropy Alloys in Al–Co–Cr–Fe–Ni System,” *Met. Mater. Int.*, vol. 27, no. 1, pp. 127–138, Jan. 2021, doi: 10.1007/s12540-020-00655-3.

[197] S. Yang, J. Lu, F. Xing, L. Zhang, and Y. Zhong, “Revisit the VEC rule in high entropy alloys (HEAs) with high-throughput CALPHAD approach and its applications for material design-A case study with Al–Co–Cr–Fe–Ni system,” *Acta Mater.*, vol. 192, pp. 11–19, Jun. 2020, doi: 10.1016/j.actamat.2020.03.039.

[198] H. Hyer *et al.*, “Composition-dependent solidification cracking of aluminum-silicon alloys during laser powder bed fusion,” *Acta Mater.*, vol. 208, p. 116698, Apr. 2021, doi: 10.1016/j.actamat.2021.116698.

[199] H. Zhang *et al.*, “High-strength NbMoTaX refractory high-entropy alloy with low stacking fault energy eutectic phase via laser additive manufacturing,” *Mater. Des.*, vol. 201, p.

109462, Mar. 2021, doi: 10.1016/j.matdes.2021.109462.

[200] C. Wen *et al.*, "Machine learning assisted design of high entropy alloys with desired property," *Acta Mater.*, vol. 170, pp. 109–117, 2019, doi: 10.1016/j.actamat.2019.03.010.

[201] Y. Yan, D. Lu, and K. Wang, "Accelerated discovery of single-phase refractory high entropy alloys assisted by machine learning," *Comput. Mater. Sci.*, vol. 199, no. March, p. 110723, 2021, doi: 10.1016/j.commatsci.2021.110723.

[202] W.-M. Choi *et al.*, "Computational design of V-CoCrFeMnNi high-entropy alloys: An atomistic simulation study," *Calphad*, vol. 74, p. 102317, Sep. 2021, doi: 10.1016/j.calphad.2021.102317.

[203] A. Raturi, J. Aditya C, N. P. Gurao, and K. Biswas, "ICME approach to explore equiatomic and non-equiatomic single phase BCC refractory high entropy alloys," *J. Alloys Compd.*, vol. 806, pp. 587–595, Oct. 2019, doi: 10.1016/j.jallcom.2019.06.387.

[204] P. Lu *et al.*, "Computational design and initial corrosion assessment of a series of non-equimolar high entropy alloys," *Scr. Mater.*, vol. 172, pp. 12–16, Nov. 2019, doi: 10.1016/j.scriptamat.2019.07.003.

[205] W. Li, L. Li, S. Antonov, and Q. Feng, "Effective design of a Co-Ni-Al-W-Ta-Ti alloy with high γ′ solvus temperature and microstructural stability using combined CALPHAD and experimental approaches," *Mater. Des.*, vol. 180, p. 107912, Oct. 2019, doi: 10.1016/j.matdes.2019.107912.

[206] H. S. Rao and A. Mukherjee, "Artificial neural networks for predicting the macromechanical behaviour of ceramic-matrix composites," *Comput. Mater. Sci.*, vol. 5, no. 4, pp. 307–322, Apr. 1996, doi: 10.1016/0927-0256(95)00002-X.

[207] Y. Reich and N. Travitzky, "Machine learning of material behaviour knowledge from empirical data," *Mater. Des.*, vol. 16, no. 5, pp. 251–259, 1995, doi: 10.1016/0261-3069(96)00007-6.

[208] H. Bhadeshia, "Neural Networks in Materials Science," *ISIJ Int.*, vol. 39, no. 10, pp. 966–979, 1999.

[209] C. E. Rasmussen and C. K. I. Williams, *Gaussian Processes for Machine Learning. The MIT Press.* Massachusetts Institute of Technology., 2006.

[210] F. Pedregosa *et al.*, "Scikit-learn: Machine Learning in Python," *J. Mach. Learn. Res.*, vol. 12, pp. 2825–2830, 2011.

[211] M. Mahfouf, M. Jamei, and D. A. Linkens, "Optimal design of alloy steels using multiobjective genetic algorithms," *Mater. Manuf. Process.*, vol. 20, no. 3, pp. 553–567, 2005, doi: 10.1081/AMP-200053580.

[212] J. Tenner, "Optimisation of the heat treatment of steel using neural networks. PhD Thesis, University of Sheffield.," no. October, 1999.

[213] P. Das, S. Mukherjee, S. Ganguly, B. K. Bhattacharyay, and S. Datta, "Genetic algorithm based optimization for multi-physical properties of HSLA steel through hybridization of

neural network and desirability function," *Comput. Mater. Sci.*, vol. 45, no. 1, pp. 104–110, Mar. 2009, doi: 10.1016/j.commatsci.2008.03.050.

[214] N. S. Reddy, J. Krishnaiah, H. B. Young, and J. S. Lee, "Design of medium carbon steels by computational intelligence techniques," *Comput. Mater. Sci.*, vol. 101, pp. 120–126, Apr. 2015, doi: 10.1016/j.commatsci.2015.01.031.

[215] M. Joo, J. Ryu, and H. K. D. H. Bhadeshia, "Domains of Steels with Identical Properties," *Mater. Manuf. Process.*, vol. 24, no. 1, pp. 53–58, Dec. 2008, doi: 10.1080/10426910802543657.

[216] W. Xu and S. van der Zwaag, "Property and Cost Optimisation of Novel UHS Stainless Steels via a Genetic Alloy Design Approach," *ISIJ Int.*, vol. 51, no. 6, pp. 1005–1010, 2011, doi: 10.2355/isijinternational.51.1005.

[217] S. Chatterjee, M. Murugananth, and H. K. D. H. Bhadeshia, "δ TRIP steel," *Mater. Sci. Technol.*, vol. 23, no. 7, pp. 819–827, Jul. 2007, doi: 10.1179/174328407X179746.

[218] Q. Lu, S. van der Zwaag, and W. Xu, "High-throughput design of low-activation, high-strength creep-resistant steels for nuclear-reactor applications," *J. Nucl. Mater.*, vol. 469, pp. 217–222, Feb. 2016, doi: 10.1016/j.jnucmat.2015.11.052.

[219] Y. Sun, W. D. Zeng, Y. F. Han, X. Ma, and Y. Q. Zhao, "Optimization of chemical composition for TC11 titanium alloy based on artificial neural network and genetic algorithm," *Comput. Mater. Sci.*, vol. 50, no. 3, pp. 1064–1069, Jan. 2011, doi: 10.1016/j.commatsci.2010.11.002.

[220] M. Bignon, "Contribution à la conception computationnelle d'alliages de titane ou à haute entropie Prédiction de l'occurrence de la transformation martensitique de trempe ou de déformation. PhD Thesis, Université de Nantes," Université de Nantes, 2020.

[221] A. Dreano, J. Favre, C. Desrayaud, P. Chanin-Lambert, A. Wimmer, and M. F. Zaeh, "Computational design of a crack-free aluminum alloy for additive manufacturing," *Addit. Manuf.*, vol. 55, p. 102876, Jul. 2022, doi: 10.1016/j.addma.2022.102876.

[222] J. Blank and K. Deb, "Pymoo: Multi-Objective Optimization in Python," *IEEE Access*, vol. 8, pp. 89497–89509, 2020, doi: 10.1109/ACCESS.2020.2990567.

[223] G. Munda, "Multiple Criteria Decision Analysis: State of the Art Surveys," in *Environmental Sciences*, vol. 78, no. 23, 2005, pp. 163–189.

[224] J. P. Brans and P. Vincke, "A Preference Ranking Organisation Method: (The PROMETHEE Method for Multiple Criteria Decision-Making)," *Manage. Sci.*, vol. 31, no. 6, pp. 647–656, Feb. 1985.

[225] S. R. Maity and S. Chakraborty, "Tool steel material selection using PROMETHEE II method," *Int. J. Adv. Manuf. Technol.*, vol. 78, no. 9–12, pp. 1537–1547, Jun. 2015, doi: 10.1007/s00170-014-6760-0.

[226] P. Chatterjee and S. Chakraborty, "Material selection using preferential ranking methods," *Mater. Des.*, vol. 35, pp. 384–393, Mar. 2012, doi: 10.1016/j.matdes.2011.09.027.

[227] L. Anojkumar, M. Ilangkumaran, and V. Sasirekha, “Comparative analysis of MCDM methods for pipe material selection in sugar industry,” *Expert Syst. Appl.*, vol. 41, no. 6, pp. 2964–2980, May 2014, doi: 10.1016/j.eswa.2013.10.028.

[228] A.-H. Peng and X.-M. Xiao, “Material selection using PROMETHEE combined with analytic network process under hybrid environment,” *Mater. Des.*, vol. 47, pp. 643–652, May 2013, doi: 10.1016/j.matdes.2012.12.058.

[229] E. Menou, “Conception d’alliages par optimisation combinatoire multiobjectifs : thermodynamique prédictive, fouille de données, algorithmes génétiques et analyse décisionnelle. PhD Thesis, Université de Nantes,” Université de Nantes, 2016.

[230] P. Bajaj, J. Wright, I. Todd, and E. A. Jägle, “Predictive process parameter selection for Selective Laser Melting Manufacturing: Applications to high thermal conductivity alloys,” *Addit. Manuf.*, vol. 27, pp. 246–258, 2019, doi: 10.1016/j.addma.2018.12.003.

[231] F. Sciammarella, M. Gonser, and M. Styrcula, “Laser Additive Manufacturing of Pure Copper,” 2013.

[232] S. R. Pogson, P. Fox, C. J. Sutcliffe, and W. O’Neill, “The production of copper parts using DMLR,” *Rapid Prototyp. J.*, vol. 9, no. 5, pp. 334–343, Dec. 2003, doi: 10.1108/13552540310502239.

[233] M. R. Alkahari, T. Furumoto, T. Ueda, A. Hosokawa, R. Tanaka, and M. S. Abdul Aziz, “Thermal conductivity of metal powder and consolidated material fabricated via selective laser melting,” *Key Eng. Mater.*, vol. 523–524, pp. 244–249, 2012, doi: 10.4028/www.scientific.net/KEM.523-524.244.

[234] A. L. Schaeffler, “Constitution diagram for stainless steel weld metal.,” *Met. Prog.*, 1949.

[235] W. T. Delong, “Ferrite in Austenitic Stainless Steel Weld Metal,” *Weld. J.*, pp. 273–286, 1974.

[236] R. G. Faulkner, J. A. Williams, E. Gonzalez Sanchez, and A. W. Marshall, “Influence of Co, Cu and W on microstructure of 9%Cr steel weld metals,” *Mater. Sci. Technol.*, vol. 19, no. 3, pp. 347–354, 2003, doi: 10.1179/026708303225009652.

[237] R. H. Kaltenhauser, *Improving the Engineering Properties of Ferritic Stainless Steels*. Defense Technical Information Center.

[238] B. Y. D. J. Kotecki, “WRC-1992 Constitution Diagram for Stainless Steel Weld Metals : A Modification of the WRC-1988 Diagram,” pp. 171–178, 1992.

[239] H. EZAKI, M. MORINAGA, K. KUSUNOKI, and Y. TSUCHIDA, “Electronic Approach to the Prediction of Phase Stability in Cr-Mo Ferritic Steels,” *Tetsu-to-Hagane*, vol. 78, no. 8, pp. 1377–1382, 1992, doi: 10.2355/tetsutohagane1955.78.8_1377.

[240] M. C. Balmforth and J. C. Lippold, “New ferritic-martensitic stainless steel constitution diagram,” *Weld. J. (Miami, Fla)*, vol. 79, no. 12, pp. 339-s, 2000.

[241] S. H. Ryu and J. Yu, “A new equation for the Cr equivalent in 9 to 12 pct Cr steels,” *Metall. Mater. Trans. A Phys. Metall. Mater. Sci.*, vol. 29, no. 6, pp. 1573–1578, 1998, doi:

10.1007/s11661-998-0080-7.

[242] F. C. Hull, “Delta Ferrite and Martensite Formation in Stainless Steels.,” *Weld. J. (Miami, Fla)*, vol. 52, no. 5, 1973.

[243] E. Salama, M. M. Eissa, and A. S. Tageldin, “Distinct properties of tungsten austenitic stainless alloy as a potential nuclear engineering material,” *Nucl. Eng. Technol.*, vol. 51, no. 3, pp. 784–791, 2019, doi: 10.1016/j.net.2018.12.021.

[244] J. E. Indacochea, “Performance of a Steel/Oxide Composite Waste Form for Combined Waste Steams from Advanced Electrochemical Processes Fuel Cycle Research and Development. Technical report, University of Illinois at Chicago,” 2017.

[245] C. Qiu, H. Chen, Q. Liu, S. Yue, and H. Wang, “On the solidification behaviour and cracking origin of a nickel-based superalloy during selective laser melting,” *Mater. Charact.*, vol. 148, no. November 2018, pp. 330–344, 2019, doi: 10.1016/j.matchar.2018.12.032.

[246] Z. Sun, X. P. Tan, M. Descoins, D. Mangelinck, S. B. Tor, and C. S. Lim, “Revealing hot tearing mechanism for an additively manufactured high-entropy alloy via selective laser melting,” *Scr. Mater.*, vol. 168, pp. 129–133, 2019, doi: 10.1016/j.scriptamat.2019.04.036.

[247] M. L. Montero-Sistiaga, M. Godino-Martinez, K. Boschmans, J. P. Kruth, J. Van Humbeeck, and K. Vanmeensel, “Microstructure evolution of 316L produced by HP-SLM (high power selective laser melting),” *Addit. Manuf.*, vol. 23, pp. 402–410, 2018, doi: 10.1016/j.addma.2018.08.028.

[248] J. C. Lippold and D. J. Kotecki, *Welding Metallurgy and Weldability of Stainless Steels*. John Wiley & Sons, Inc., Hoboken, New Jersey, 2005.

[249] G. Mathers, *The welding of aluminium and its alloys*. Woodhead Publishing Limited, 2002.

[250] M. Rappaz, J. M. Drezet, and M. Gremaud, “A new hot-tearing criterion,” *Metall. Mater. Trans. A Phys. Metall. Mater. Sci.*, vol. 30, no. 2, pp. 449–455, 1999, doi: 10.1007/s11661-999-0334-z.

[251] J. Campbell, *Castings*. Butterworth-Heinemann, 1991.

[252] J. A. Brooks and A. W. Thompson, “Microstructural development and solidification cracking susceptibility of austenitic stainless steel welds,” *Int. Mater. Rev.*, vol. 36, no. 1, pp. 16–44, Jan. 1991, doi: 10.1179/imr.1991.36.1.16.

[253] N. Suutala, T. Takalo, and T. Moisio, “Ferritic-austenitic solidification mode in austenitic stainless steel welds,” *Metall. Trans. A*, vol. 11, no. 5, pp. 717–725, May 1980, doi: 10.1007/BF02661201.

[254] A. Yamada, T. Umeda, and Y. Kimura, “Calculation of Liquidus and Solidus Surfaces of Iron-rich Corner of Fe-Cr-Ni System,” *Tetsu-to-Hagane*, vol. 76, no. 12, pp. 2137–2143, 1990, doi: 10.2355/tetsutohagane1955.76.12_2137.

[255] H. Inoue and T. Koseki, “Solidification mechanism of austenitic stainless steels solidified with primary ferrite,” *Acta Mater.*, vol. 124, pp. 430–436, Feb. 2017, doi:

10.1016/j.actamat.2016.11.030.

[256] N. Suutala, “Effect of Manganese and Nitrogen on the Solidification Mode in Austenitic Stainless Steel Welds.,” *Metall. Trans. A, Phys. Metall. Mater. Sci.*, vol. 13 A, no. 12, pp. 2121–2130, 1982, doi: 10.1007/BF02648382.

[257] Y. Arata, F. Matsuda, and S. Katayama, “Solidification crack susceptibility in weld metals of fully austenitic stainless steels. I. Fundamental investigation on solidification behavior of fully austenitic and duplex microstructures and effect of ferrite on microsegregation,” *Trans. JWRI*, 1976.

[258] V. Kujanpaa, N. Suutala, T. Takalo, and T. Moisio, “Correlation Between Solidification Cracking and Microstructure in Austenitic and Austenitic-Ferritic Stainless Steel Welds.,” *Weld. Res. Int.*, vol. 9, no. 2, pp. 55–76, 1979.

[259] V. P. Kujanpää, S. A. David, and C. L. White, “Formation of hot cracks in austenitic stainless steel welds-solidification cracking,” *Weld. J.*, vol. 65, no. 8, pp. 203–212, 1986.

[260] F. MATSUDA, H. NAKAGAWA, T. UEHARA, S. KATAYAMA, and Y. ARATA, “A New Explanation for Role of Delta-Ferrite Improving Weld Solidification Crack Susceptibility in Austenitic Stainless Steel(Materials, Metallurgy, Weldability).pdf,” *Trans. JWRI*, vol. 8, no. 1, pp. 105–112, 1979.

[261] K. Nishimoto and H. Mori, “Hot cracking susceptibility in laser weld metal of high nitrogen stainless steels,” *Sci. Technol. Adv. Mater.*, vol. 5, no. 1–2, pp. 231–240, 2004, doi: 10.1016/j.stam.2003.10.006.

[262] V. M. Radhakrishnan, “Hot cracking in austenitic stainless steel weld metals,” *Sci. Technol. Weld. Join.*, vol. 5, no. 1, pp. 40–44, 2000, doi: 10.1179/stw.2000.5.1.40.

[263] N. Suutala, “Effect of solidification conditions on the solidification mode in austenitic stainless steels,” *Metall. Trans. A*, vol. 14, no. 1, pp. 191–197, 1983, doi: 10.1007/BF02651615.

[264] T. Böllinghaus, H. Herold, C. E. Cross, and J. C. Lippold, *Hot cracking phenomena in welds II*. 2008.

[265] V. Shankar, T. P. S. S. Gill, S. L. Mannan, S. Sundarlsan, and S. Sundaresan, “Solidification cracking in austenitic stainless steel welds,” *Sadhana*, vol. 28, no. August, pp. 359–382, 2003, doi: 10.1007/BF02706438.

[266] R. Scherer, G. Riedrich, and H. HOUGARDY, “US Patent 2 240 672,” 1941.

[267] R. Saluja and K. M. Moeed, “Assessment of Delta ferrite for SA 240 Type 304L Austenitic Weld Metal using Different Filler Materials,” *Int. J. Sci. Eng. Res.*, vol. 7, no. 2, pp. 493–498, 2016.

[268] R. Saluja and K. Moeed, “‘ Formation , Quantification and Significance of Delta Ferrite for 300 Series Stainless Steel Weldments ,’” no. September 2015, 2018.

[269] K. Abd-Elghany and D. L. Bourell, “Property evaluation of 304L stainless steel fabricated by selective laser melting,” *Rapid Prototyp. J.*, vol. 18, no. 5, pp. 420–428, Jul. 2012, doi:

10.1108/13552541211250418.

[270] D. Wang, C. Song, Y. Yang, and Y. Bai, “Investigation of crystal growth mechanism during selective laser melting and mechanical property characterization of 316L stainless steel parts,” *Mater. Des.*, vol. 100, pp. 291–299, 2016, doi: 10.1016/j.matdes.2016.03.111.

[271] W. E. King *et al.*, “Laser powder bed fusion additive manufacturing of metals; physics, computational, and materials challenges,” *Appl. Phys. Rev.*, vol. 2, no. 4, p. 041304, Dec. 2015, doi: 10.1063/1.4937809.

[272] X. He, T. DebRoy, and P. W. Fuerschbach, “Alloying element vaporization during laser spot welding of stainless steel,” *J. Phys. D. Appl. Phys.*, vol. 36, no. 23, pp. 3079–3088, 2003, doi: 10.1088/0022-3727/36/23/033.

[273] C. B. Alcock, V. P. Itkin, and M. K. Horrigan, “Vapour Pressure Equations for the Metallic Elements: 298–2500K,” *Can. Metall. Q.*, vol. 23, no. 3, pp. 309–313, Jul. 1984, doi: 10.1179/cmq.1984.23.3.309.

[274] W. M. Haynes, “CRC Handbook of Chemistry and Physics (Internet Version),” *Taylor Fr. Boca Rat. FL*, p. 0, 2016.

[275] T. Fuhrich, P. Berger, and H. Hügel, “Marangoni effect in laser deep penetration welding of steel,” *J. Laser Appl.*, vol. 13, no. 5, pp. 178–186, 2001, doi: 10.2351/1.1404412.

[276] P.-G. de Gennes, F. Brochard-Wyart, and D. Quéré, *Capillarity and wetting phenomena: drops, bubbles, pearls, waves*. Springer, 2004.

[277] M. Bayat *et al.*, “Keyhole-induced porosities in Laser-based Powder Bed Fusion (L-PBF) of Ti6Al4V: High-fidelity modelling and experimental validation,” *Addit. Manuf.*, vol. 30, no. July, p. 100835, 2019, doi: 10.1016/j.addma.2019.100835.

[278] S. A. Khairallah, A. T. Anderson, A. Rubenchik, and W. E. King, “Laser powder-bed fusion additive manufacturing: Physics of complex melt flow and formation mechanisms of pores, spatter, and denudation zones,” *Acta Mater.*, vol. 108, pp. 36–45, 2016, doi: 10.1016/j.actamat.2016.02.014.

[279] A. A. Martin *et al.*, “Dynamics of pore formation during laser powder bed fusion additive manufacturing,” *Nat. Commun.*, vol. 10, no. 1, pp. 1–10, 2019, doi: 10.1038/s41467-019-10009-2.

[280] L. Aucott *et al.*, “Revealing internal flow behaviour in arc welding and additive manufacturing of metals,” *Nat. Commun.*, vol. 9, no. 1, p. 5414, Dec. 2018, doi: 10.1038/s41467-018-07900-9.

[281] E. Ahmadi and A. R. Ebrahimi, “Welding of 316L Austenitic Stainless Steel with Activated Tungsten Inert Gas Process,” *J. Mater. Eng. Perform.*, vol. 24, no. 2, pp. 1065–1071, 2015, doi: 10.1007/s11665-014-1336-6.

[282] T.-N. Le and Y.-L. Lo, “Effects of sulfur concentration and Marangoni convection on melt-pool formation in transition mode of selective laser melting process,” *Mater. Des.*, vol. 179, p. 107866, Oct. 2019, doi: 10.1016/j.matdes.2019.107866.

[283] M. D. L. Christian Wohlfarth, B. Wohlfarth, *Surface Tension of Pure Liquids and Binary Liquid Mixtures*. Springer, 1997.

[284] C. J. Smithells, "Metals reference book," *J. Less Common Met.*, vol. 51, no. 2, pp. 354–355, 1977, doi: 10.1016/0022-5088(77)90096-0.

[285] K. C. Mills and Y. C. Su, "Review of surface tension data for metallic elements and alloys: Part 1 - Pure metals," *Int. Mater. Rev.*, vol. 51, no. 6, pp. 329–351, 2006, doi: 10.1179/174328006X102510.

[286] B. J. Keene, "Review of data for the surface tension of pure metals," *Int. Mater. Rev.*, vol. 38, no. 4, pp. 157–192, 1993, doi: 10.1179/imr.1993.38.4.157.

[287] A. Kasama, A. McLean, W. A. Miller, Z. Morita, and M. J. Ward, "Surface tension of liquid iron and iron-oxygen alloys," *Can. Metall. Q.*, vol. 22, no. 1, pp. 9–17, 1983, doi: 10.1179/cmq.1983.22.1.9.

[288] H. M. Lu and Q. Jiang, "Surface tension and its temperature coefficient for liquid metals," *J. Phys. Chem. B*, vol. 109, no. 32, pp. 15463–15468, 2005, doi: 10.1021/jp0516341.

[289] P. Sahoo, T. Debroy, and M. J. McNallan, "Surface tension of binary metal-surface active solute systems under conditions relevant to welding metallurgy," *Metall. Trans. B*, vol. 19, no. 2, pp. 483–491, 1988, doi: 10.1007/BF02657748.

[290] B. J. Keene, K. C. Mills, J. W. Bryant, and E. D. Hondros, "Effects of interaction between surface active elements on the surface tension of iron," *Can. Metall. Q.*, vol. 21, no. 4, pp. 393–403, 1982, doi: 10.1179/cmq.1982.21.4.393.

[291] F. A. Halden and W. D. Kingery, "Surface tension at elevated temperatures. II. Effect of C, N, O and S on liquid iron surface tension and interfacial energy with Al2O3," *J. Phys. Chem.*, vol. 59, no. 6, pp. 557–559, 1955, doi: 10.1021/j150528a018.

[292] H. G. Kim, J. Choe, T. Inoue, S. Ozawa, and J. Lee, "Surface Tension of Super-Cooled Fe-O Liquid Alloys," *Metall. Mater. Trans. B Process Metall. Mater. Process. Sci.*, vol. 47, no. 4, pp. 2079–2081, 2016, doi: 10.1007/s11663-016-0712-z.

[293] J. Zhu and K. Mukai, "The surface tension of liquid iron containing nitrogen and oxygen," *ISIJ Int.*, vol. 38, no. 10, pp. 1039–1044, 1998, doi: 10.2355/isijinternational.38.1039.

[294] J. W. Gibbs, "The collected works of J. Williard Gibbs," vol. 1, pp. 219–331, 1928.

[295] E. A. Guggenheim, "Statistical thermodynamics of the surface of a regular solution," *Trans. Faraday Soc.*, vol. 41, p. 150, 1945, doi: 10.1039/tf9454100150.

[296] E. A. Guggenheim and N. K. Adam, "The thermodynamics of adsorption at the surface of solutions," *Proc. R. Soc. London. Ser. A, Contain. Pap. a Math. Phys. Character*, vol. 139, no. 837, pp. 218–236, Jan. 1933, doi: 10.1098/rspa.1933.0015.

[297] J. A. V Butler and P. R. S. L. A, "The thermodynamics of the surfaces of solutions," *Proc. R. Soc. London. Ser. A, Contain. Pap. a Math. Phys. Character*, vol. 135, no. 827, pp. 348–375, Mar. 1932, doi: 10.1098/rspa.1932.0040.

[298] I. Takamichi and I. L. G. Roderick, *The Thermophysical Properties of Metallic Liquids*

Volume 2: Predictive Models. Oxford University Press, 2015.

[299] M. Vermot des Roches, A. E. Gheribi, and P. Chartrand, "A versatile multicomponent database for the surface tension of liquid metals," *Calphad Comput. Coupling Phase Diagrams Thermochem.*, vol. 65, no. April, pp. 326–339, Jun. 2019, doi: 10.1016/j.calphad.2019.04.002.

[300] P. Wynblatt, A. Saúl, and D. Chatain, "The effects of prewetting and wetting transitions on the surface energy of liquid binary alloys," *Acta Mater.*, vol. 46, no. 7, pp. 2337–2347, Apr. 1998, doi: 10.1016/S1359-6454(98)80015-3.

[301] I. Egry, "The surface tension of binary alloys: Simple models for complex phenomena," *Int. J. Thermophys.*, vol. 26, no. 4, pp. 931–939, 2005, doi: 10.1007/s10765-005-6675-y.

[302] I. Egry, E. Ricci, R. Novakovic, and S. Ozawa, "Surface tension of liquid metals and alloys — Recent developments," *Adv. Colloid Interface Sci.*, vol. 159, no. 2, pp. 198–212, Sep. 2010, doi: 10.1016/j.cis.2010.06.009.

[303] A. E. Gheribi, M. Vermot des Roches, and P. Chartrand, "Modelling the surface tension of liquid metals as a function of oxygen content," *J. Non. Cryst. Solids*, vol. 505, no. July 2018, pp. 154–161, 2019, doi: 10.1016/j.jnoncrysol.2018.10.006.

[304] G. Kaptay, "Improved Derivation of the Butler Equations for Surface Tension of Solutions," *Langmuir*, vol. 35, no. 33, pp. 10987–10992, 2019, doi: 10.1021/acs.langmuir.9b01892.

[305] J. Chang, H. P. Wang, K. Zhou, and B. Wei, "Surface tension measurement of undercooled liquid Ni-based multicomponent alloys," *Philos. Mag. Lett.*, vol. 92, no. 9, pp. 428–435, 2012, doi: 10.1080/09500839.2012.685768.

[306] A. Dogan and H. Arslan, "Thermophysical properties of Cu–In–Sn liquid Pb-free alloys: viscosity and surface tension," *Philos. Mag.*, vol. 98, no. 1, pp. 37–53, 2018, doi: 10.1080/14786435.2017.1392053.

[307] Z. Guo, M. Hindler, W. Yuan, and A. Mikula, "The density and surface tension of In-Sn and Cu-In-Sn alloys," *Monatshefte fur Chemie*, vol. 142, no. 6, pp. 579–584, 2011, doi: 10.1007/s00706-011-0501-y.

[308] Z. Li, K. Mukai, M. Zeze, and K. C. Mills, "Determination of the surface tension of liquid stainless steel," *J. Mater. Sci.*, vol. 40, pp. 2191–2195, 2005.

[309] J. Choe *et al.*, "Surface tension measurements of 430 stainless steel," *ISIJ Int.*, vol. 54, no. 9, pp. 2104–2108, 2014, doi: 10.2355/isijinternational.54.2104.

[310] Y. Su, Z. Li, and K. C. Mills, "Equation to estimate the surface tensions of stainless steels," *J. Mater. Sci.*, vol. 40, no. 9–10, pp. 2201–2205, 2005, doi: 10.1007/s10853-005-1933-8.

[311] M. Hayashi, A. Jakobsson, T. Tanaka, and S. Seetharaman, "Surface tension of the nickel-based superalloy CMSX-4," *High Temp. - High Press.*, vol. 35–36, no. 4, pp. 441–445, 2003, doi: 10.1068/htjr123.

[312] R. K. Wunderlich, H. J. Fecht, and G. Lohöfer, "Surface Tension and Viscosity of the Ni-Based Superalloys LEK94 and CMSX-10 Measured by the Oscillating Drop Method on

Board a Parabolic Flight," *Metall. Mater. Trans. B Process Metall. Mater. Process. Sci.*, vol. 48, no. 1, pp. 237–246, 2017, doi: 10.1007/s11663-016-0847-y.

[313] M. Assi, J. Favre, A. Fraczkiewicz, and F. Tancret, "Machine learning-based model of surface tension of liquid metals: a step in designing multicomponent alloys for additive manufacturing," *J. Mater. Sci.*, 2022, doi: 10.1007/s10853-022-07441-z.

[314] S. Kou, *Welding Metallurgy*. 2003.

[315] J. A. Goldak and M. Akhlaghi, *Computational Welding Mechanics*. Library of Congress Cataloging-in-Publicaton Data, 2005.

[316] R. Martukanitz *et al.*, "Toward an integrated computational system for describing the additive manufacturing process for metallic materials," *Addit. Manuf.*, vol. 1–4, pp. 52–63, Oct. 2014, doi: 10.1016/j.addma.2014.09.002.

[317] R. Magana Carranza, J. Robinson, I. Ashton, P. Fox, C. Sutcliffe, and E. Patterson, "A novel device for in-situ force measurements during laser powder bed fusion (L-PBF)," *Rapid Prototyp. J.*, vol. 27, no. 7, pp. 1423–1431, Aug. 2021, doi: 10.1108/RPJ-12-2020-0305.

[318] P. Mercelis and J. Kruth, "Residual stresses in selective laser sintering and selective laser melting," *Rapid Prototyp. J.*, vol. 12, no. 5, pp. 254–265, Oct. 2006, doi: 10.1108/13552540610707013.

[319] J. P. Kruth, J. Deckers, E. Yasa, and R. Wauthlé, "Assessing and comparing influencing factors of residual stresses in selective laser melting using a novel analysis method," *Proc. Inst. Mech. Eng. Part B J. Eng. Manuf.*, vol. 226, no. 6, pp. 980–991, 2012, doi: 10.1177/0954405412437085.

[320] L. van Belle, G. Vansteenkiste, and J. C. Boyer, "Investigation of Residual Stresses Induced during the Selective Laser Melting Process," *Key Eng. Mater.*, vol. 554–557, pp. 1828–1834, Jun. 2013, doi: 10.4028/www.scientific.net/KEM.554-557.1828.

[321] J. Hunt, F. Derguti, and I. Todd, "Selection of steels suitable for additive layer manufacturing," *Ironmak. Steelmak.*, vol. 41, no. 4, pp. 254–256, 2014, doi: 10.1179/0301923314Z.000000000269.

[322] H. D.P.H., "Thermal Stress Resistance Parameters for Brittle Refractory Ceramics: a compendium," *Bull. Amer. Ceram. Soc.*, vol. 49, no. 12, pp. 1033–1037, 1970.

[323] I. Toda-Caraballo, E. I. Galindo-Nava, and P. E. J. Rivera-Díaz-Del-Castillo, "Unravelling the materials genome: Symmetry relationships in alloy properties," *J. Alloys Compd.*, vol. 566, pp. 217–228, 2013, doi: 10.1016/j.jallcom.2013.02.148.

[324] "CES EduPack software, Granta Design Limited, Cambridge, UK,." 2009.

[325] G. P. M. Leyson and W. A. Curtin, "Friedel vs . Labusch : the strong / weak pinning transition in solute strengthened metals," *Philos. Mag.*, vol. 93, no. February 2015, pp. 2428–2444, 2013, doi: 10.1080/14786435.2013.776718.

[326] C. R. LaRosa, M. Shih, C. Varvenne, and M. Ghazisaeidi, "Solid solution strengthening theories of high-entropy alloys," *Mater. Charact.*, vol. 151, no. October 2018, pp. 310–317,

2019, doi: 10.1016/j.matchar.2019.02.034.

[327] J. Friedel, *Dislocations*, vol. 1,2,4. Pergamon Press Ltd., 1964.

[328] R. L. Fleischer, "Solution Hardening," *Acta Metall.*, vol. 9, 1961.

[329] R. L. Fleischer, "Substitutional solution hardening," *Acta Metall.*, vol. 11, no. 3, pp. 203–209, 1963, doi: 10.1016/0001-6160(63)90213-X.

[330] N. F. Mott, "A Theory of World'-hardening of Metal Crystals," *London, Edinburgh, Dublin Philos. Mag. J. Sci. Ser. 7*, pp. 1151–1178, 1952, doi: 10.1080/14786441108521024.

[331] R. Labusch, "A Statistical Theory of Solid Solution Hardening," vol. 659, pp. 659–669, 1970.

[332] R. Labusch, "Statistische Theorien Der Mischkristallhartung," *Acta Metall.*, vol. 20, 1972.

[333] A. Akhtar and E. Teghtsoonian, "Substitutional solution hardening of magnesium single crystals," *Philos. Mag.*, no. June 2013, pp. 37–41, 1971.

[334] C. H. Cáceres and D. M. Rovera, "Solid solution strengthening in concentrated Mg ± Al alloys," *J. Light Met.*, vol. 1, pp. 151–156, 2001.

[335] L. A. Gypen and A. Deruyttere, "Multi-component solid solution hardening Part 2 Agreement with experimental results," *J. Mater. Sci.*, vol. 12, pp. 1034–1038, 1977.

[336] L. Cizek, "Solid solution hardening of copper crystals," *J. Mater. Sci.*, vol. 9, pp. 1517–1520, 1974.

[337] C. Pohl, J. Schatte, and H. Leitner, "A Solid solution hardening of molybdenum – hafnium alloys : Experiments and Modeling," *Mater. Sci. Eng. A*, vol. 559, pp. 643–650, 2013, doi: 10.1016/j.msea.2012.09.004.

[338] I. Toda-Caraballo, "A general formulation for solid solution hardening effect in multicomponent alloys," *Scr. Mater.*, vol. 127, pp. 113–117, 2017, doi: 10.1016/j.scriptamat.2016.09.009.

[339] J. Zander and R. Sandström, "One parameter model for strength properties of hardenable aluminium alloys," *Mater. Des.*, vol. 29, no. 8, pp. 1540–1548, Jan. 2008, doi: 10.1016/j.matdes.2008.02.001.

[340] A. R. Denton and N. W. Ashcroft, "Vegard's law," *Phys. Rev. A*, vol. 43, no. 6, pp. 3161–3164, Mar. 1991, doi: 10.1103/PhysRevA.43.3161.

[341] H. M. Ledbetter and E. R. Naimon, "Elastic Properties of Metals and Alloys. II. Copper," *J. Phys. Chem. Ref. Data*, vol. 3, no. 4, pp. 897–935, Oct. 1974, doi: 10.1063/1.3253150.

[342] P. Lukáč, "Solid solution hardening in Mg-Cd single crystals," *Phys. Status Solidi*, vol. 131, no. 2, pp. 377–390, Jun. 1992, doi: 10.1002/pssa.2211310212.

[343] H. E. Friedrich and B. L. Mordike, *Magnesium Technology: Metallurgy, Design, Data, Applications*. Springer-Verlag Berlin Heidelberg, 2006.

[344] D. J. Dever, "Temperature dependence of the elastic constants in α-iron single crystals:

relationship to spin order and diffusion anomalies," *J. Appl. Phys.*, vol. 43, no. 8, pp. 3293–3301, Aug. 1972, doi: 10.1063/1.1661710.

[345] J. R. Neighbours, F. W. Bratten, and C. S. Smith, "The Elastic Constants of Nickel," *J. Appl. Phys.*, vol. 23, no. 4, pp. 389–393, Apr. 1952, doi: 10.1063/1.1702218.

[346] I. Toda-Caraballo and P. E. J. Rivera-Díaz-del-Castillo, "Modelling solid solution hardening in high entropy alloys," *Acta Mater.*, vol. 85, pp. 14–23, Feb. 2015, doi: 10.1016/j.actamat.2014.11.014.

[347] W. Martienssen and H. Warlimont, *Springer Handbook of Condensed Matter and Materials Data*. 2005.

[348] J. Carvill, "Engineering materials," in *Mechanical Engineer's Data Handbook*, Elsevier, 1993, pp. 218–266.

[349] K. Deb, A. Pratap, S. Agarwal, and T. Meyarivan, "A fast and elitist multiobjective genetic algorithm: NSGA-II," *IEEE Trans. Evol. Comput.*, vol. 6, no. 2, pp. 182–197, Apr. 2002, doi: 10.1109/4235.996017.

[350] J. Blank and K. Deb, "A Running Performance Metric and Termination Criterion for Evaluating Evolutionary Multi- and Many-objective Optimization Algorithms," in *2020 IEEE Congress on Evolutionary Computation (CEC)*, 2020, pp. 1–8, doi: 10.1109/CEC48606.2020.9185546.

[351] J. Blank and K. Deb, "Pymoo: termination criterion https://pymoo.org/interface/termination.html." [Online]. Available: https://pymoo.org/interface/termination.html.

[352] R. Venkata Rao and B. K. Patel, "Decision making in the manufacturing environment using an improved PROMETHEE method," *Int. J. Prod. Res.*, vol. 48, no. 16, pp. 4665–4682, Aug. 2010, doi: 10.1080/00207540903049415.

[353] B. Murty, J. Yeh, and S. Ranganathan, *High-Entropy Alloys*. 2014.

[354] M. Laurent-Brocq *et al.*, "Insights into the phase diagram of the CrMnFeCoNi high entropy alloy," *Acta Mater.*, vol. 88, pp. 355–365, 2015, doi: 10.1016/j.actamat.2015.01.068.

[355] J. Olszewska, "Conception et développement d'une nuance d'alliage de type HEA (High Entropy Alloys) de la famille CrFeMnNi à résistance mécanique élevée. PhD Thesis, Mines Saint-Etienne," 2019.

[356] "MatWeb datasheets, AISI 316 Cast Stainless Steel, EN 10088-3." [Online]. Available: https://matweb.com/search/DataSheet.aspx?MatGUID=6894e11c936f42eb9c0d0e0903c3ae38&ckck=1.

[357] S. Irukuvarghula, H. Hassanin, C. Cayron, M. Aristizabal, M. M. Attallah, and M. Preuss, "Effect of powder characteristics and oxygen content on modifications to the microstructural topology during hot isostatic pressing of an austenitic steel," *Acta Mater.*, vol. 172, pp. 6–17, 2019, doi: 10.1016/j.actamat.2019.03.038.

[358] C. Meier, R. Weissbach, J. Weinberg, W. A. Wall, and A. J. Hart, "Critical influences of

particle size and adhesion on the powder layer uniformity in metal additive manufacturing," *J. Mater. Process. Technol.*, vol. 266, pp. 484–501, Apr. 2019, doi: 10.1016/j.jmatprotec.2018.10.037.

[359] R. Cunningham, S. P. Narra, C. Montgomery, J. Beuth, and A. D. Rollett, "Synchrotron-Based X-ray Microtomography Characterization of the Effect of Processing Variables on Porosity Formation in Laser Power-Bed Additive Manufacturing of Ti-6Al-4V," *Jom*, vol. 69, no. 3, pp. 479–484, 2017, doi: 10.1007/s11837-016-2234-1.

[360] A. M. Beese and B. E. Carroll, "Review of Mechanical Properties of Ti-6Al-4V Made by Laser-Based Additive Manufacturing Using Powder Feedstock," *Jom*, vol. 68, no. 3, pp. 724–734, 2016, doi: 10.1007/s11837-015-1759-z.

[361] N. Ciftci, N. Ellendt, G. Coulthard, E. Soares Barreto, L. Mädler, and V. Uhlenwinkel, "Novel Cooling Rate Correlations in Molten Metal Gas Atomization," *Metall. Mater. Trans. B*, vol. 50, no. 2, pp. 666–677, Apr. 2019, doi: 10.1007/s11663-019-01508-0.

[362] S. Relave, "Caractérisation et prédiction de la microstructure obtenue par fabrication additive. Application aux aciers inoxydables. Soutenue," École des Mines de Saint-Étienne, 2019.

[363] D. Wang, Y. Liu, Y. Yang, and D. Xiao, "Theoretical and experimental study on surface roughness of 316L stainless steel metal parts obtained through selective laser melting," *Rapid Prototyp. J.*, vol. 22, no. 4, pp. 706–716, Jun. 2016, doi: 10.1108/RPJ-06-2015-0078.

[364] J. Delgado, J. Ciurana, and C. A. Rodríguez, "Influence of process parameters on part quality and mechanical properties for DMLS and SLM with iron-based materials," *Int. J. Adv. Manuf. Technol.*, vol. 60, no. 5–8, pp. 601–610, May 2012, doi: 10.1007/s00170-011-3643-5.

[365] Y. Deng, Z. Mao, N. Yang, X. Niu, and X. Lu, "Collaborative optimization of density and surface roughness of 316L stainless steel in selective laser melting," *Materials (Basel).*, vol. 13, no. 7, 2020, doi: 10.3390/ma13071601.

[366] "Organisation Internationale de Métrologie Légale: International alcoholometric tables." .

[367] E. Yasa, T. Craeghs, M. Badrossamay, and J.-P. Kruth, "Rapid Manufacturing Research at the Catholic University of Leuven," *RapidTech 2009*, no. Lc, pp. 1–10, 2009.

[368] A. B. Spierings and G. Levy, "Comparison of density of stainless steel 316L parts produced with selective laser melting using different powder grades," in *SFF Symposium*, 2009.

[369] E. Yasa, "Investigation of Sectoral Scanning in Selective Laser Melting.," in *Proceedings of 10th Biennial ASME Conference on Engineering Systems, Design and Analysis*, 2010, pp. 695–703.

[370] I. Yadroitsev and I. Smurov, "Selective laser melting technology: From the single laser melted track stability to 3D parts of complex shape," *Phys. Procedia*, vol. 5, pp. 551–560, 2010, doi: 10.1016/j.phpro.2010.08.083.

[371] J. P. Kruth, M. Badrossamay, E. Yasa, J. Deckers, L. Thijs, and J. Van Humbeeck, "Part and material properties in selective laser melting of metals," *16th Int. Symp.*

Electromachining, ISEM 2010, pp. 3–14, 2010.

[372] E. Yasa, J.-P. Kruth, and J. Deckers, "Manufacturing by combining Selective Laser Melting and Selective Laser Erosion/laser re-melting," *CIRP Ann.*, vol. 60, no. 1, pp. 263–266, 2011, doi: 10.1016/j.cirp.2011.03.063.

[373] B. Liu, R. Wildman, C. Tuck, I. Ashcroft, and R. Hague, "Investigaztion the effect of particle size distribution on processing parameters optimisation in selective laser melting process," *22nd Annu. Int. Solid Free. Fabr. Symp. - An Addit. Manuf. Conf. SFF 2011*, no. mm, pp. 227–238, 2011.

[374] S. Dadbakhsh, L. Hao, and N. Sewell, "Effect of selective laser melting layout on the quality of stainless steel parts," *Rapid Prototyp. J.*, vol. 18, no. 3, pp. 241–249, Apr. 2012, doi: 10.1108/13552541211218216.

[375] A. Laohaprapanon *et al.*, "Optimal Scanning Condition of Selective Laser Melting Processing with Stainless Steel 316L Powder," *Adv. Mater. Res.*, vol. 341–342, pp. 816–820, Sep. 2011, doi: 10.4028/www.scientific.net/AMR.341-342.816.

[376] Z. Sun, X. Tan, S. B. Tor, and C. K. Chua, "Simultaneously enhanced strength and ductility for 3D-printed stainless steel 316L by selective laser melting," *NPG Asia Mater.*, vol. 10, no. 4, pp. 127–136, Apr. 2018, doi: 10.1038/s41427-018-0018-5.

[377] M. Ghasri-Khouzani *et al.*, "Fabrication of aluminum/stainless steel bimetallic composites through a combination of additive manufacturing and vacuum-assisted melt infiltration casting," *J. Manuf. Process.*, vol. 69, pp. 320–330, Sep. 2021, doi: 10.1016/j.jmapro.2021.07.047.

[378] T. de Terris *et al.*, "Optimization and comparison of porosity rate measurement methods of Selective Laser Melted metallic parts," *Addit. Manuf.*, vol. 28, no. June, pp. 802–813, 2019, doi: 10.1016/j.addma.2019.05.035.

[379] K. N. Amato *et al.*, "Microstructures and mechanical behavior of Inconel 718 fabricated by selective laser melting," *Acta Mater.*, vol. 60, no. 5, pp. 2229–2239, 2012, doi: 10.1016/j.actamat.2011.12.032.

[380] M. Ma, Z. Wang, M. Gao, and X. Zeng, "Layer thickness dependence of performance in high-power selective laser melting of 1Cr18Ni9Ti stainless steel," *J. Mater. Process. Technol.*, vol. 215, no. 1, pp. 142–150, 2015, doi: 10.1016/j.jmatprotec.2014.07.034.

[381] N. Read, W. Wang, K. Essa, and M. M. Attallah, "Selective laser melting of AlSi10Mg alloy: Process optimisation and mechanical properties development," *Mater. Des.*, vol. 65, pp. 417–424, 2015, doi: 10.1016/j.matdes.2014.09.044.

[382] D. E. Laughlin and D. R. Gaskell, "Introduction to the Thermodynamics of Materials, Fifth Edition." p. 618, 2008.

[383] A. Shukla, H. M. Pandey, and D. Mehrotra, "Comparative review of selection techniques in genetic algorithm," in *2015 International Conference on Futuristic Trends on Computational Analysis and Knowledge Management (ABLAZE)*, 2015, pp. 515–519, doi: 10.1109/ABLAZE.2015.7154916.

[384] N. T. Aboulkhair, M. Simonelli, L. Parry, I. Ashcroft, C. Tuck, and R. Hague, "3D printing of Aluminium alloys: Additive Manufacturing of Aluminium alloys using selective laser melting," *Prog. Mater. Sci.*, vol. 106, no. July, p. 100578, 2019, doi: 10.1016/j.pmatsci.2019.100578.

[385] E. O. Olakanmi, R. F. Cochrane, and K. W. Dalgarno, "A review on selective laser sintering/melting (SLS/SLM) of aluminium alloy powders: Processing, microstructure, and properties," *Prog. Mater. Sci.*, vol. 74, pp. 401–477, 2015, doi: 10.1016/j.pmatsci.2015.03.002.

[386] C. Y. Yap *et al.*, "Review of selective laser melting: Materials and applications," *Appl. Phys. Rev.*, vol. 2, no. 4, 2015, doi: 10.1063/1.4935926.

[387] D. Herzog, V. Seyda, E. Wycisk, and C. Emmelmann, "Additive manufacturing of metals," *Acta Mater.*, vol. 117, pp. 371–392, 2016, doi: 10.1016/j.actamat.2016.07.019.

[388] W. J. Sames, F. A. List, S. Pannala, R. R. Dehoff, and S. S. Babu, "The metallurgy and processing science of metal additive manufacturing," *Int. Mater. Rev.*, vol. 61, no. 5, pp. 315–360, 2016, doi: 10.1080/09506608.2015.1116649.

[389] A. J. B. Milne, B. Defez, M. Cabrerizo-Vílchez, and A. Amirfazli, "Understanding (sessile/constrained) bubble and drop oscillations," *Adv. Colloid Interface Sci.*, vol. 203, pp. 22–36, 2014, doi: 10.1016/j.cis.2013.11.006.

[390] V. B. Fainerman and R. Miller, "The maximum bubble pressure tensiometry," in *Drops and bubbles in interfacial research*, D. MÖbius and R. Miller, Eds. Elsevier, 1998, pp. 279–326.

[391] V. B. Fainerman and R. Miller, "Maximum bubble pressure tensiometry—an analysis of experimental constraints," *Adv. Colloid Interface Sci.*, vol. 108–109, pp. 287–301, May 2004, doi: 10.1016/j.cis.2003.10.010.

[392] B. B. Alchagirov, R. K. Arkhestov, F. F. Dyshekova, and T. M. Taova, "Surface tension of alloys with additives of alkali metals," *High Temp.*, vol. 51, no. 2, pp. 183–196, 2013, doi: 10.1134/S0018151X13020016.

[393] P. F. Paradis, T. Ishikawa, and S. Yoda, "Non-Contact Measurements of Surface Tension and Viscosity of Niobium, Zirconium, and Titanium Using an Electrostatic Levitation Furnace," *Int. J. Thermophys.*, vol. 23, no. 3, pp. 825–842, 2002, doi: 10.1023/A:1015459222027.

[394] K. Monma and H. Suto, "Experimental Studies on the Surface Tension of Molten Metals and Alloys," *Trans. JIM*, vol. 1, no. 2, pp. 69–76, 1960, doi: 10.2320/matertrans1960.1.69.

[395] J. Brillo and I. Egry, "Surface tension of nickel , copper , iron," *Calphad Comput. Coupling Phase Diagrams Thermochem.*, vol. 0, pp. 2213–2216, 2005.

[396] B. V. T. L.A. Smirnov, S.I. Popel, "Izvestiya vysshikh uchebnykh zavedenii," *Chern. Met.*, vol. 8, pp. 10–14, 1965.

[397] M. Kishimoto, K. Mori, and Y. Kawai, "Surface Tension of Liquid Fe－Ti and Fe-C-Ti Systems under H2 Atmosphere," *J. Japan Inst. Met.*, vol. 48, pp. 413–417, 1984.

[398] S. Chibani and F. X. Coudert, “Machine learning approaches for the prediction of materials properties,” *APL Mater.*, vol. 8, no. 8, 2020, doi: 10.1063/5.0018384.

[399] K. Rajan, “Materials informatics,” *Mater. Today*, vol. 8, no. 10, pp. 38–45, 2005, doi: 10.1016/S1369-7021(05)71123-8.

[400] Y. Liu, T. Zhao, W. Ju, S. Shi, S. Shi, and S. Shi, “Materials discovery and design using machine learning,” *J. Mater.*, vol. 3, no. 3, pp. 159–177, 2017, doi: 10.1016/j.jmat.2017.08.002.

[401] H. Yamada *et al.*, “Predicting Materials Properties with Little Data Using Shotgun Transfer Learning,” *ACS Cent. Sci.*, vol. 5, no. 10, pp. 1717–1730, 2019, doi: 10.1021/acscentsci.9b00804.

[402] G. Pilania, C. Wang, X. Jiang, S. Rajasekaran, and R. Ramprasad, “Accelerating materials property predictions using machine learning,” *Sci. Rep.*, vol. 3, no. 1, p. 2810, Dec. 2013, doi: 10.1038/srep02810.

[403] L. Ward, A. Agrawal, A. Choudhary, and C. Wolverton, “A general-purpose machine learning framework for predicting properties of inorganic materials,” *npj Comput. Mater.*, vol. 2, no. 1, p. 16028, Nov. 2016, doi: 10.1038/npjcompumats.2016.28.

[404] Z.-L. Wang and Y. Adachi, “Property prediction and properties-to-microstructure inverse analysis of steels by a machine-learning approach,” *Mater. Sci. Eng. A*, vol. 744, pp. 661–670, Jan. 2019, doi: 10.1016/j.msea.2018.12.049.

[405] C. A. L. Bailer-Jones, H. K. D. H. Bhadeshia, and D. J. C. MacKay, “Gaussian process modelling of austenite formation in steel,” *Mater. Sci. Technol.*, vol. 15, no. 3, pp. 287–294, Mar. 1999, doi: 10.1179/026708399101505851.

[406] S. Bishnoi, R. Ravinder, H. S. Grover, H. Kodamana, and N. M. A. Krishnan, “Scalable Gaussian processes for predicting the optical, physical, thermal, and mechanical properties of inorganic glasses with large datasets,” *Mater. Adv.*, vol. 2, no. 1, pp. 477–487, 2021, doi: 10.1039/D0MA00764A.

[407] H. Rappel, L. A. A. Beex, L. Noels, and S. P. A. Bordas, “Identifying elastoplastic parameters with Bayes’ theorem considering output error, input error and model uncertainty,” *Probabilistic Eng. Mech.*, vol. 55, pp. 28–41, Jan. 2019, doi: 10.1016/j.probengmech.2018.08.004.

[408] V. Eremenko, Y. N. Ivashchenko, and P. Marsenyuk, “Free surface energy and density of liquid vanadium, niobium, and tantalum at the melting point,” *High Temp.*, vol. 22, no. 4, pp. 705–708, 1984.

[409] F. Baras and O. Politano, “Molecular dynamics simulations of nanometric metallic multilayers: Reactivity of the Ni-Al system,” *Phys. Rev. B*, vol. 84, no. 2, p. 024113, Jul. 2011, doi: 10.1103/PhysRevB.84.024113.

[410] C. Costa, S. Delsante, G. Borzone, D. Zivkovic, and R. Novakovic, “Thermodynamic and surface properties of liquid Co-Cr-Ni alloys,” *J. Chem. Thermodyn.*, vol. 69, pp. 73–84, 2014, doi: 10.1016/j.jct.2013.09.034.

[411] U. Mehta, S. K. Yadav, I. Koirala, R. P. Koirala, G. K. Shrestha, and D. Adhikari, “Study of surface tension and viscosity of Cu–Fe–Si ternary alloy using a thermodynamic approach,” *Heliyon*, vol. 6, no. 8, p. e04674, Aug. 2020, doi: 10.1016/j.heliyon.2020.e04674.

[412] K. C. Chou, “A general solution model for predicting ternary thermodynamic properties,” *Calphad*, vol. 19, no. 3, pp. 315–325, 1995, doi: 10.1016/0364-5916(95)00029-E.

[413] G. W. Toop, “Predicting ternary activities using binary data,” *Trans Met. Soc AIME*, vol. 233, no. 5, pp. 850–855, 1965.

[414] F. Kohler, “Daten eines ternären Systems aus den zugehörigen binären Systemen,” *Monatshefte für Chemie*, vol. 91, no. 4, pp. 738–740, 1960, doi: 10.1007/BF00899814.

[415] H. P. Wang, B. C. Luo, T. Qin, J. Chang, and B. Wei, “Surface tension of liquid ternary Fe-Cu-Mo alloys measured by electromagnetic levitation oscillating drop method,” *J. Chem. Phys.*, vol. 129, no. 12, 2008, doi: 10.1063/1.2981833.

[416] Y. F. Ye, Q. Wang, J. Lu, C. T. Liu, and Y. Yang, “High-entropy alloy: challenges and prospects,” *Mater. Today*, vol. 19, no. 6, pp. 349–362, 2016, doi: 10.1016/j.mattod.2015.11.026.

[417] K. Nogi, W. B. Chung, A. McLean, and W. A. Miller, “Surface Tension of Liquid Fe-(Cu,Sn,Cr) and Ni-(Cu,Sn) Binary Alloys,” *Mater. Trans.*, vol. 32, pp. 164–168, 1991.

[418] K. Mori, M. Kishimoto, T. Shimose, and Y. Kawai, “Surface Tension of Liquid Iron-Nickel-Chromium Alloy System,” *J. Japan Inst. Met.*, vol. 39, no. 12, pp. 1301–1307, 1975, doi: 10.2320/jinstmet1952.39.12_1301.

[419] I. I. Egry and J. J. Brillo, “Surface Tension and Density of Liquid Metallic Alloys Measured by Electromagnetic Levitation,” *J. Chem. Eng. Data*, vol. 54, no. 9, pp. 2347–2352, Sep. 2009, doi: 10.1021/je900119n.

[420] D. Giuranno, A. Tuissi, R. Novakovic, and E. Ricci, “Surface tension and density of Al-Ni alloys,” *J. Chem. Eng. Data*, vol. 55, no. 9, pp. 3024–3028, 2010, doi: 10.1021/je901055j.

[421] I. Egry, J. Brillo, D. Holland-Moritz, and Y. Plevachuk, “The surface tension of liquid aluminium-based alloys,” *Mater. Sci. Eng. A*, vol. 495, no. 1–2, pp. 14–18, Nov. 2008, doi: 10.1016/j.msea.2007.07.104.

[422] F. Xiao, L. xiao Liu, R. hui Yang, H. kai Zhao, L. Fang, and C. Zhang, “Surface tension of molten Ni-(Cr, Co, W) alloys and segregation of elements,” *Trans. Nonferrous Met. Soc. China (English Ed.*, vol. 18, no. 5, pp. 1184–1188, 2008, doi: 10.1016/S1003-6326(08)60202-2.

[423] J. J. Wessing and J. Brillo, “Density, Molar Volume, and Surface Tension of Liquid Al-Ti,” *Metall. Mater. Trans. A Phys. Metall. Mater. Sci.*, vol. 48, no. 2, pp. 868–882, Feb. 2017, doi: 10.1007/s11661-016-3886-8.

[424] J. Schmitz, J. Brillo, I. Egry, and R. Schmid-Fetzer, “Surface tension of liquid Al–Cu binary alloys,” vol. 100, no. 11, pp. 1529–1535, doi: 10.3139/146.110221.

[425] P. Laty, J. C. Joud, P. Desré, and G. Lang, “Tension superficielle d’alliages liquides aluminium-cuivre,” *Surf. Sci.*, vol. 69, no. 2, pp. 508–520, 1977, doi: 10.1016/0039-6028(77)90130-3.

[426] H. Kobatake, J. Brillo, J. Schmitz, and P. Y. Pichon, “Surface tension of binary Al–Si liquid alloys,” *J. Mater. Sci.*, vol. 50, no. 9, pp. 3351–3360, 2015, doi: 10.1007/s10853-015-8883-6.

[427] I. F. Bainbridge and J. A. Taylor, “The surface tension of pure aluminum and aluminum alloys,” *Metall. Mater. Trans. A Phys. Metall. Mater. Sci.*, vol. 44, no. 8, pp. 3901–3909, 2013, doi: 10.1007/s11661-013-1696-9.

[428] J. . Taylor, “The surface tensions of liquid-metal solutions,” *Acta Metall.*, vol. 4, no. 5, pp. 460–468, 1956, doi: 10.1016/0001-6160(56)90042-6.

[429] A. Schneider and E. K. Stoll, “Zeitschrift für Elektrochemie und angewandte physikalische Chemie,” 1941, doi: https://doi.org/10.1002/bbpc.19410470709.

[430] Y. V. Naidich, V. M. Perevertailo, and L. P. Obushchak, “Density and surface tension of alloys of the systems Au-Si and Au-Ge,” *Sov. Powder Metall. Met. Ceram.*, vol. 14, no. 5, pp. 403–404, 1975, doi: 10.1007/BF00807814.

[431] J. Brillo and G. Kolland, “Surface tension of liquid Al–Au binary alloys,” *J. Mater. Sci.*, vol. 51, no. 10, pp. 4888–4901, 2016, doi: 10.1007/s10853-016-9794-x.

[432] Y. Kawai, K. Mori, M. Kishimoto, K. Ishikura, and T. Shimada, “Surface Tension of Liquid Fe-C-Si Alloys,” *Tetsu-to-Hagane*, vol. 60, no. 1, pp. 29–37, 1974, doi: 10.2355/tetsutohagane1955.60.1_29.

[433] V. M. Perevertailo, O. B. Loginova, and S. A. Lysovenko, “On the criteria for the surface activity and classification of the surface tension isotherms from the data on the melt structure,” *J. Superhard Mater.*, vol. 37, no. 4, pp. 234–241, 2015, doi: 10.3103/S1063457615040036.

[434] C. Garcia-Cordovilla, E. Louis, and A. Pamies, “The surface tension of liquid pure aluminium and aluminium-magnesium alloy,” *J. Mater. Sci.*, vol. 21, no. 8, pp. 2787–2792, 1986, doi: 10.1007/BF00551490.

[435] L. M. Shergin, S. I. Popel’, and B. V. Tsarevsky, “Temperature dependence between densities and surface tension of cobalt–silicon and nickel–silicon melts,” *Phys. Chem. Metall. Melts*, vol. 25, p. 50, 1971.

[436] V. I. Nizhenko and Y. I. Smirnov, “Surface properties of manganese - TiN liquid alloys,” *Powder Metall. Met. Ceram.*, vol. 42, no. 9–10, pp. 517–522, 2003, doi: 10.1023/B:PMMC.0000013225.95000.c6.

[437] J. Lee, W. Shimoda, and T. Tanaka, “Surface tension and its temperature coefficient of liquid Sn-X (X=Ag, Cu) alloys,” *Mater. Trans.*, vol. 45, no. 9, pp. 2864–2870, 2004, doi: 10.2320/matertrans.45.2864.

[438] I. Seyhan and I. Egry, “Surface tension of undercooled binary iron and nickel alloys and the effect of oxygen on the surface tension of Fe and Ni,” *Int. J. Thermophys.*, vol. 20, no. 4,

pp. 1017–1028, 1999, doi: 10.1023/A:1022638400507.

[439] A. Sharan and A. W. Cramb, “Surface tension and wettability studies of liquid Fe-Ni-O alloys,” *Metall. Mater. Trans. B*, vol. 28, no. 3, pp. 465–472, 1997, doi: 10.1007/s11663-997-0113-4.

[440] I. Egry *et al.*, “Surface Tension, Phase Separation, and Solidification of Undercooled Cobalts-Copper Alloys,” *Adv. Eng. Mater.*, vol. 5, no. 11, pp. 819–823, 2003, doi: 10.1002/adem.200320508.

[441] P. Fima, “Surface tension and density of liquid Sn-Ag alloys,” *Appl. Surf. Sci.*, vol. 257, no. 8, pp. 3265–3268, 2011, doi: 10.1016/j.apsusc.2010.11.002.

[442] V. Krasovskyy and Y. Naidich, “Surface tension and specific volume of copper-titanium melts measured by the sessile drop method,” *J. Adhes. Sci. Technol.*, vol. 18, no. 4, pp. 465–471, 2004, doi: 10.1163/156856104323016360.

[443] S. Amore, J. Brillo, I. Egry, and R. Novakovic, “Surface tension of liquid Cu-Ti binary alloys measured by electromagnetic levitation and thermodynamic modelling,” *Appl. Surf. Sci.*, vol. 257, no. 17, pp. 7739–7745, 2011, doi: 10.1016/j.apsusc.2011.04.019.

[444] S. . Kaufman and T. . Whalen, “The surface tension of liquid gold, liquid tin, and liquid gold-tin binary solutions,” *Acta Metall.*, vol. 13, no. 7, pp. 797–805, Jul. 1965, doi: 10.1016/0001-6160(65)90144-6.

[445] X. J. Han, N. Wang, and B. Wei, “Thermophysical properties of undercooled liquid cobalt,” *Philos. Mag. Lett.*, vol. 82, no. 8, pp. 451–459, Aug. 2002, doi: 10.1080/09500830210144382.

[446] V. P. Krasovskyy, Y. V. Naidich, and N. A. Krasovskaya, “Surface tension and density of copper-zirconium alloys in contact with fluoride refractories,” *J. Mater. Sci.*, vol. 40, no. 9–10, pp. 2367–2369, 2005, doi: 10.1007/s10853-005-1960-5.

[447] E. Ricci *et al.*, “Surface tension and density of Si-Ge melts,” *J. Chem. Phys.*, vol. 140, no. 21, 2014, doi: 10.1063/1.4879775.

[448] T. Ishikawa, P. F. Paradis, R. Fujii, Y. Saita, and S. Yoda, “Thermophysical property measurements of liquid and supercooled iridium by containerless methods,” *Int. J. Thermophys.*, vol. 26, no. 3, pp. 893–904, 2005, doi: 10.1007/s10765-005-5585-3.

[449] O. Flint, “Surface tension of liquid metals,” *J. Nucl. Mater.*, vol. 16, no. 3, pp. 16–260, Jul. 1965, doi: 10.1016/0022-3115(65)90113-3.

[450] K. Zhou, H. P. Wang, J. Chang, and B. Wei, “Experimental study of surface tension, specific heat and thermal diffusivity of liquid and solid titanium,” *Chem. Phys. Lett.*, vol. 639, pp. 105–108, 2015, doi: 10.1016/j.cplett.2015.09.014.

[451] J. Tille and J. C. Kelly, “The surface tension of liquid titanium,” *Br. J. Appl. Phys.*, vol. 14, no. 10, pp. 717–719, 1963, doi: 10.1088/0508-3443/14/10/332.

[452] T. Dubberstein, H. P. Heller, J. Klostermann, R. Schwarze, and J. Brillo, “Surface tension and density data for Fe–Cr–Mo, Fe–Cr–Ni, and Fe–Cr–Mn–Ni steels,” *J. Mater. Sci.*, vol.

50, no. 22, pp. 7227–7237, 2015, doi: 10.1007/s10853-015-9277-5.

[453] J. Brillo, Y. Plevachuk, and I. Egry, “Surface tension of liquid Al-Cu-Ag ternary alloys,” *J. Mater. Sci.*, vol. 45, no. 19, pp. 5150–5157, 2010, doi: 10.1007/s10853-010-4512-6.

[454] Z. Li, M. Zeze, and K. Mukai, “Surface Tension and Wettability of Liquid Fe-16mass%Cr-S Alloy with Alumina,” *Mater. Trans.*, vol. 44, no. 10, pp. 2108–2113, 2003, doi: 10.2320/matertrans.44.2108.

[455] R. Nowak *et al.*, “Surface tension of γ-TiAl-based alloys,” *J. Mater. Sci.*, vol. 45, no. 8, pp. 1993–2001, 2010, doi: 10.1007/s10853-009-4061-z.

[456] R. Pajarre, P. Koukkari, T. Tanaka, and J. Lee, “Computing surface tensions of binary and ternary alloy systems with the Gibbsian method,” *Calphad*, vol. 30, no. 2, pp. 196–200, Jun. 2006, doi: 10.1016/j.calphad.2005.08.003.

[457] R. Aune *et al.*, “Surface tension and viscosity of industrial alloys from parabolic flight experiments - Results of the ThermoLab project,” *Microgravity Sci. Technol.*, vol. 15, no. 1, pp. 11–14, 2005, doi: 10.1007/bf02945937.

[458] T. Tanaka and S. Hara, “Thermodynamic evaluation of surface tension of liquid metal-oxygen systems,” *Steel Res.*, vol. 72, no. 11–12, pp. 439–445, 2001, doi: 10.1002/srin.200100149.

[459] Z. Li, K. C. Mills, M. McLean, and K. Mukai, “Measurement of the density and surface tension of Ni-based superalloys in the liquid and mushy states,” *Metall. Mater. Trans. B Process Metall. Mater. Process. Sci.*, vol. 36, no. 2, pp. 247–254, 2005, doi: 10.1007/s11663-005-0026-z.

[460] B. Oleksiak, J. Łabaj, J. Wieczorek, A. Blacha-Grzechnik, and R. Burdzik, “Surface tension of Cu - Bi alloys and wettability in a liquid alloy - Refractory material - Gaseous phase system,” *Arch. Metall. Mater.*, vol. 59, no. 1, pp. 281–285, 2014, doi: 10.2478/amm-2014-0046.

[461] D. K. Duvenaud, “Automatic Model Construction with Gaussian Processes. PhD Thesis, Pembroke College, University of Cambridge,” Pembroke College, University of Cambridge, 2014.

École Nationale Supérieure des Mines
de Saint-Étienne

NNT : 2022EMSEM022

Mariam ASSI

Alloy design for additive manufacturing

Speciality : Materials Science and Engineering

Keywords : alloy design, additive manufacturing, stainless steel, high entropy alloys, selective laser melting, machine learning

Abstract :

The recent developments in the field of metallic additive manufacturing (AM) processes for the production of high-performance industrial products remains restricted by the limited availability of reliably processable or printable alloys. So far, most of the alloys being printed by AM are commercial alloys which have been previously optimized for different processing techniques. One of the ambitions of the domain would therefore be to design new alloys that are specifically adapted to such processes, allowing to minimize the defects in final products and optimize their properties. This means an optimization of certain material characteristics which should allow to reduce the presence of defects currently seen in AM-fabricated parts such as hot cracking, porosity, surface roughness, residual stresses and distortions, etc.
Within the scope of this thesis, a computational design of new austenitic alloy compositions, optimized specifically for AM is proposed. This method is based on a set of computational tools including Bayesian machine learning (ML) algorithms combined with calculation of phase diagrams (CALPHAD) and physical models, integrated in a multi-objective genetic algorithm (GA). In this context, several material-dependent criteria are reviewed and their effect on the mentioned defects is identified. Then, the implementation of a genetic algorithm yields a set of optimal alloys. Experimental validation is carried out on one selected composition. The selected alloy was investigated in the as-cast condition, as an atomized powder and as specimens built by Selective Laser Melting (SLM). The printability of the alloy is assessed and compared to existing commercial alloys.

École Nationale Supérieure des Mines
de Saint-Étienne

NNT : 2022EMSEM022

Mariam ASSI

Conception d’alliages pour la fabrication additive

Spécialité: Sciences et Génie des Matériaux

Mots clefs : conception d’alliages, fabrication additive, acier inoxydables, alliages à haute entropie, fusion laser sélective, machine learning

Résumé :

Les développements récents dans le domaine des procédés de fabrication additive (FA) métallique pour la production de produits industriels à hautes performances restent limités par la disponibilité d'alliages pouvant être traités ou imprimables de manière fiable. Jusqu'à présent, la plupart des alliages imprimés par FA sont des alliages commerciaux qui ont été préalablement optimisés pour différents procédés de fabrication. L'une des ambitions du domaine serait donc de concevoir de nouveaux alliages spécifiquement adaptés aux procédés de FA, permettant de minimiser les défauts des produits finaux et d'optimiser leurs propriétés. Ceci impliquerait une optimisation de certaines caractéristiques du matériau permettant de réduire la présence des défauts actuellement observés tels que la fissuration à chaud, la porosité, la rugosité de surface, les contraintes et distorsions résiduelles, etc.
Dans le cadre de cette thèse, une conception de nouvelles nuances d’alliages austénitiques, optimisées spécifiquement pour la FA, est proposée. La démarche repose sur un ensemble d'outils de calcul comprenant des algorithmes bayésiens d'apprentissage automatique combinés à des calculs de diagrammes de phases par la méthode CALPHAD et à des modèles physiques, intégrés dans un algorithme génétique multi-objectifs. Dans ce contexte, plusieurs critères dépendants du matériau sont examinés et leur effet sur les défauts mentionnés est étudié. Ensuite, la mise en œuvre d'un algorithme génétique a produit un ensemble d'alliages optimaux. Une validation expérimentale est alors réalisée sur une composition sélectionnée. L'alliage sélectionné est étudié à l'état coulé puis de poudre atomisée, et sous forme d’échantillons construits par fusion laser sélective (SLM). L'imprimabilité de l'alliage est évaluée et comparée aux alliages commerciaux existants.